UM HE 80-19

The Magnetic Moment of the Cascade-Zero Hyperon

PETER TIMOTHY COX

May 1980

Supported in part by:
National Science Foundation

Department of Physics, The University of Michigan

UM HE 80-19

THE MAGNETIC MOMENT OF THE CASCADE-ZERO HYPERON

by
Peter Timothy Cox

A dissertation submitted in partial fulfillment
of the requirements for the degree of
Doctor of Philosophy
(Physics)
in The University of Michigan
1980

Doctoral Committee :

Professor Oliver E. Overseth, Chairman
Professor Gordon L. Kane
Professor Wilfred Kaplan
Professor Michael J. Longo
Professor Jens C. Zorn

ABSTRACT

THE MAGNETIC MOMENT OF
THE CASCADE-ZERO HYPERON

by

Peter Timothy Cox

Chairman : Oliver E. Overseth

The magnetic moment of the cascade-zero hyperon (Ξ^0) has been measured to be -1.236 ± 0.014 nuclear magnetons (n m). In the Neutral Hyperon Beam at Fermilab a quarter of a million $\Xi^0\rightarrow\Lambda\pi^0$ decays were detected, by identifying the subsequent $\Lambda\rightarrow p\pi^-$ and $\pi^0\rightarrow 2\gamma$ decays in a multiwire proportional chamber magnetic spectrometer and an array of lead glass. The Ξ^0's were produced inclusively by 400 GeV protons, at angles of 0, ±2, ±4, ±7.6, and ±10 mrad, and had momenta between 60 and 380 GeV/c. The measured Ξ^0 polarization is presented as a function of the tranverse momentum of the parent Ξ^0, for each production angle. The average polarization was -0.108 ± 0.006. This polarization was precessed through angles as large as 320^0.

The helicity of the decay Λ from the $\Xi^0\rightarrow\Lambda\pi^0$ decay (α_{Ξ^0}) was also measured, giving the value $\alpha_\Lambda\alpha_{\Xi^0} = -0.264\pm0.005$.

An independent sample of a third of a million inclusively - produced Λ's gave a new value for the magnetic moment of the lambda hyperon, -0.598 ± 0.015 n m.

ACKNOWLEDGEMENTS

I would like to thank Oliver Overseth for introducing me to experimental high energy physics, and for his tolerant and continuous support as my thesis adviser.

Many current and ex- members of the Neutral Hyperon Group at Fermilab contributed to this experiment. Bob Handler was an inexhaustible source of ideas, and his committment and devotion to the running, and the later analysis, of the experiment were invaluable. Ken Heller's superhuman efforts and enthusiastic attention to detail were contributed, and appreciated, at all stages of the experiment. In addition to the aforementioned, I would particularly stress the importance I attach to arguments, conversations, differences of opinion, and discussions with, and criticisms, demonstrations, explanations, and lectures from : Gerry Bunce, Tom Devlin, Jay Dworkin, Ralph Edwards, Lee Pondrom, Marleigh Sheaff, and Lindsay Schachinger.

Much of the equipment was designed and built by E. Behr, J. Jaske, G. Ott, and S. Fraser.

This experiment would not have been possible without the cooperation and efforts of the staff of Fermilab, and in particular those of the Meson Laboratory.

TABLE OF CONTENTS

LIST OF FIGURES

LIST OF TABLES

CHAPTER 1

INTRODUCTION

1.1 Spin And Magnetic Moments

The intrinsic magnetic moment of a particle is a static property, closely related to its spin (a purely quantum concept), which describes how the system interacts with an electromagnetic field. The study of spin properties of subatomic particles has been a fruitful path towards deeper understanding of their structure, as exemplified by the highly successful description of the quantum electrodynamic (QED) behavior of the photon and the leptons (the electron, muon, and neutrino). The classical magnetic moment of a spin system is

$$\vec{\mu} = g \frac{e}{2mc} \vec{s}$$

where $\vec{s}$ is a vector representing the angular momentum of the system, m and e are the mass and charge, respectively,

of the system, c is the speed of light, and g is a proportionality constant known as the "g-factor". According to Dirac theory of spin 1/2 particles, a pointlike charged particle should have a value of g=2; a neutral one g=0. The close agreement of the experimental values of g for the muon and electron with the value of 2 is one of the great successes of the Dirac theory. Deviations from the predicted g values ("anomalous" values) point to some internal structure or a non-pointlike nature. By inclusion of the higher order quantum electrodynamic corrections, (due to virtual photon loops etc., which give the leptons non-pointlike structure) the theoretical values for the lepton moments agree with the experimental values to the precision to which they have been calculated. This impressive agreement validates both QED and the Dirac theory.

Magnetic moments are expressed in terms of magnetons, units of $e\hbar/(2mc)$. These are <u>intrinsic</u> magnetons when the mass of the particle is used (and e is the particle's charge), <u>Bohr</u> magnetons (μ_B) when the mass of the electron is used, and <u>nuclear</u>, or proton, magnetons (μ_N) when the proton mass is used. Table 1 shows the values for the measured octet baryon, and lepton, moments, as of April 1978 [1,2] when this experiment was conceived. It is conventional to express baryon moments in nuclear magnetons

(n m). The large anomalous moments of the baryons presumably reflect their internal structure, and should be explicable in terms of their underlying composition by any theory attempting to explain this structure.

Rather surprisingly a simple quark model in which there are three spin 1/2 quarks describes these moments with some success. The quantum numbers of these quarks are shown in Table 2 . In an SU(6) quark model, baryons are formed from combinations of three quarks (three flavors), with wave functions which reflect the color singlet nature which seems to be required of observable particles, and thus obey the antisymmetric permutation properties required of fermions. Like any observable in quantum mechanics, the magnetic moment of a baryon is obtained by forming

$$\mu = \sum_i \langle B | \mu_i | B \rangle$$

where $|B\rangle$ represents the wave function of the baryon, μ_i is the magnetic moment operator for a quark of flavor i, and the sum is over all flavors of quark in the baryon [3].

For exact SU(6) symmetry, and with the assumption of g=2 for quarks,

$$\mu_i = \frac{q_i \hbar}{2mc} = q_i \mu_0 \qquad (1.1.1)$$

for i=u, d, s, the baryon moments can all be related to one input number, usually chosen to be the measured proton

moment. The results are shown in Table 3 ; note that the predicted neutron moment agrees with experiment to within 3% (the ratio of $\mu(p)/\mu(n)=-1.5$ [4,5]), which is quite remarkable. However the predictions disagreed with the measured hyperon moments. This was further supported by a precise measurement of the Λ magnetic moment [2,6],

$$\mu_\Lambda = -0.6138 \pm 0.0047 \text{ n m},$$

obtained by our Neutral Hyperon Beam Collaboration (Michigan - Rutgers - Wisconsin) at Fermilab. This disagrees with the naive prediction by 30%. The discrepancy can be reduced by breaking the perfect SU(6) symmetry assumed.

Since the magnetic moment definition of Eq. (1.1.1) can be inverted to give a <u>definition</u> of the quark "mass", this breaking can be implemented by allowing different masses for u, d and s quarks. The question of how such a quark mass is related to the mass of the hadron of which the quark is a constituent is still largely unanswered. Ignoring this problem, the quark moments can be expressed by

$$\mu_i = \frac{q_i \hbar}{2 m_i c}$$

where m_i is the mass, and q_i the charge, of a quark of flavor i=u, d, s.

This leads to the predictions

$$\mu(p) = \tfrac{4}{3}\mu_u - \tfrac{1}{3}\mu_d$$

$$\mu(n) = \tfrac{4}{3}\mu_d - \tfrac{1}{3}\mu_u$$

$$\mu(\Lambda) = \mu_s .$$

If it is assumed that $m_u = m_d$, these can be rewritten to define μ_u, μ_d, and μ_s in terms of two parameters, which can be taken to be the experimentally determined $\mu(p)$ and $\mu(\Lambda)$. Notice that $\mu(p)/\mu(n) = -1.5$ still. Alternatively a prediction can be made for $\mu(\Lambda)$ if an estimate of the ratio m_u/m_s is known, using the relation

$$\mu(\Lambda) = -\frac{(m_u)}{(m_s)}\,\frac{\mu(p)}{3} = -0.93\,\frac{(m_u)}{(m_s)}.$$

Several authors have obtained estimates for this ratio, e.g. from the simple assumption $m_u = m(p)/3 = 313$ MeV and $m_s = m(\Lambda) - 2m_u = 490$ MeV, which gives the value $\mu(\Lambda) = -0.59\,\mu_N$. Quantum chromodynamic arguments have led to similar predictions [7], and by judicious choice of multiplet splittings (which can be taken to reflect the amount of SU(6)-breaking) the value $\mu(\Lambda) = -0.61\,\mu_N$ can even be obtained [8]. Bag models predict similar values [9]. The question outstanding is whether or not this agreement is significant. Predicted baryon moments are shown in Table 3; comparison with Table 1 shows that the existing experimental values for the hyperons were not sufficiently well known to test these predictions. In simple quark models, all baryon moments are determined by three

parameters at most, corresponding to three quarks. These parameters are chosen to be the three most precisely measured moments. A fourth precise measurement would then test the model.

It was realized that we could make a precision determination of the magnetic moment of the Ξ^0 hyperon in our neutral hyperon beam at Fermilab. This moment had never been measured. Although Ξ^0 production occurs only 1 % as often as Λ production, with modification of the detection apparatus used in the determination of the Λ moment we proposed an experiment which would increase the world sample of Ξ^0 decays by a factor of 20 and would allow a determination of the Ξ^0 moment to a few percent. During the design of the experiment a study was made of background Λ events from our precision Λ magnetic moment experiment, to select those which could be daughter Λ's from $\Xi^0 \rightarrow \Lambda\pi^0$ decays. This separation appeared successful, and yielded the value

$$\mu(\Xi^0) = -1.20 \pm 0.06 \ \mu_N$$

from a sample of 42 000 Λ events [10]. This measured value is over 3σ from the broken SU(6) prediction of -1.39.

In this first μ_{Ξ^0} measurement the analysis was complicated by the impossibility of explicit Ξ^0 reconstruction, since there was no π^0 detection in the

experiment. An experiment specifically designed to measure μ_Ξ, with high precision, and involving different backgrounds, appeared opportune. Moreover, since our first determination disagreed significantly with theoretical expectation it became particularly desirable to perform this experiment as carefully and as accurately as possible.

1.2 Measurement Of A Magnetic Moment

In the rest frame of a charged spin system moving in a magnetic field $\vec{B}$, the equation of motion of the system is:

$$\frac{d\vec{s}}{dt} = \frac{ge}{2mc}\vec{s} \times \vec{B}$$

where m is the mass of the particle, e is the magnitude of the particle's charge, and the g-factor is defined by this expression. The magnetic moment of the system is $\mu = ge/(2mc)$. A <u>neutral</u> system which possesses a magnetic moment has an analogous equation of motion

$$\frac{d\vec{s}}{dt} = \frac{\mu}{\hbar}\vec{s} \times \vec{B}.$$

The relativistic quantum mechanical treatment leads to a much more complicated expression for the general case of a particle moving in an electromagnetic field in the Lab. For a neutral spin system moving in a homogeneous magnetic field $\vec{B}$, the equation reduces to the classical equation of motion in which the spin vector $\vec{s}$ precesses in the Lab:

$$\frac{d\vec{s}}{dt} = \vec{s} \times \vec{\Omega}$$

$$\text{with } \vec{\Omega} = \frac{\mu}{\hbar}\left[\vec{B} - \frac{(\gamma-1)}{\gamma}(\vec{B}\cdot\hat{p})\hat{p}\right]$$

which can be deduced from the general expression given by Bargmann, Michel, and Telegdi [11]. For the special case in which the momentum $\vec{p}$ is perpendicular to the field direction $\vec{B}$, this becomes:

$$\frac{d\vec{s}}{dt} = \frac{\mu}{\hbar}\vec{s} \times \vec{B},$$

in terms of Lab quantities. For a spin 1/2 particle, this means that the spin vector $\vec{s}$ precesses about the field direction with an angular velocity $\vec{w}$ given by:

$$\vec{w} = \frac{2\mu\vec{B}}{\hbar}.$$

For the case in which the motion of the spin is always perpendicular to the field this equation may be integrated to obtain the <u>precession angle</u> through which the spin is rotated due to its motion through the field:

$$\phi = \frac{2\mu}{\hbar c\beta}\int B\,dl \qquad (1.2.1)$$

where the velocity of the particle v is given by $v=\beta c$. This equation leads to a direct method of measuring the magnetic moment of a neutral hyperon (which is a spin 1/2 particle).

1.3 Hyperon Beams And Inclusive Polarization

At energies ~200 GeV a hyperon with a lifetime $\sim 10^{-10}$ sec travels about 10 m before it decays. Hyperons of these energies are produced copiously in the collisions of 400 GeV protons with target nuclei. By using a magnetic field to deflect the charged particles out of the beam, neutral hyperons can be separated from the collision fragments, thus intense beams of neutral hyperons can be realized which travel significant distances in the laboratory before decaying. This forms the basis for the Neutral Hyperon Beam facility at Fermilab.

The Neutral Hyperon Collaboration discovered in 1976 that lambda (Λ) hyperons produced in such an "inclusive" reaction, $p+Be \rightarrow \Lambda + X$ where X represents everything else produced in the collision, showed appreciable polarization [12]. An inclusive reaction is one in which only <u>one</u> particle type is examined out of the possibly enormous number produced in the reaction, ignoring the fact that they may have originated in very different processes. Polarization of a sample of particles with spin means that there is an overall nonzero spin component in some direction. This implies a coherent interference between the amplitudes describing the competing production

mechanisms for the particle type under investigation, which seems intuitively unreasonable in a cataclysmic process at high energies. Presumably this coherence reflects an underlying simplicity in the dynamics of the production, although no model has succeeded in describing convincingly the features of the polarization seen by experiment [13]. Subsequent experiments have established that inclusive Λ polarization is a general property of high energy production, up the highest available energies (31 GeV in the center-of-mass of the collision), and is not a nuclear effect [14-19]. Polarization has also been searched for in inclusive $\bar{\Lambda}$ production at 400 GeV/c [15]; it is consistent with zero up to the largest available transverse momenta (~2 GeV/c) of the hyperons where the Λ polarization reaches 20%. Large transverse momentum corresponds to short-distance probing of the target (nucleus or hadron) by the incident projectile; it is expected that at higher values of the transverse momentum the actual constituents (quarks ?) are probed [20]. Experiment seems to show that inclusively-produced protons are unpolarized too [21]. However prior to our proposal of this experiment it was not known whether Ξ^0's would be produced polarized or not.

1.4 Hyperon Moment Measurement

It is clear that hyperons can be produced easily in inclusive reactions at high energies, and travel several meters before decay. Furthermore if they are polarized, so that the polarization can be precessed through large angles (~180°) by magnetic fields from conventional electromagnets, the precession angle can be found by measuring the change in direction of the polarization vector as a function of the magnetic field. Due to the parity-violating weak interaction the asymmetry of the angular distribution in a hyperon decay reveals its polarization. For high energy hyperons $\beta = p/E = 1$ very closely, so that Eq. (1.2.1) relating the precession angle to the magnetic field integral becomes

$$\phi = (18.30)\mu \int B dl \qquad (1.4.1)$$

in which ϕ is measured in degrees, $\int B dl$ in T m, and μ is in nuclear magnetons.

For a precise measurement of the magnetic moment, there are three further requirements:

1. a large number of particles be available (for good statistical precision),
2. the precessing magnetic field integral be large and known precisely, and
3. control of systematics be possible.

These requirements were met by our proposal to do this experiment in the Fermilab Neutral Hyperon Beam.

This thesis presents a 1 % measurement of the magnetic moment of the cascade-zero (Ξ^0). It also contains the inclusive polarization measurements of Ξ^0's obtained in the reaction $p + N \rightarrow \Xi^0 + X$ at 400 GeV/c, where the target nucleus N = Be, Cu, or Pb. A new measurement of α_{Ξ^0}, the helicity of the Λ in the $\Xi^0 \rightarrow \Lambda\pi^0$ decay is also given.

CHAPTER 2

APPARATUS

2.1 Introduction

The particular Ξ^0 decay mode studied in this experiment was

$$\Xi^0 \rightarrow \Lambda \begin{cases} \pi^0 \rightarrow \gamma\gamma \\ p\pi^- \end{cases} \qquad (2.1.1)$$

The charged proton and pion tracks were detected in a magnetic spectrometer, and the gamma rays required the use of some gamma-detecting devices.

This experiment was one of a series performed in the Neutral Hyperon Spectrometer at Fermiliab. Data-taking took place during July and August of 1978. The spectrometer was set up in the diffracted proton beam, the M2 line, of the Meson Laboratory. It was basically a

conventional multiwire proportional chamber (MWPC) system, used to study decay products of neutral beam components produced in a target upstream of a magnetized collimating channel (which defined the neutral beam and removed charged particles). Its detailed construction and operating characteristics for Λ inclusive production have been described elsewhere [22, 23, 24]. The basic features, shown schematically in Figs. (2.1.1) and (2.1.2) , were the production target, the collimator channel through a magnetic field, the decay volume region, and the MWPC's, separated by an analyzing magnet. In this chapter are described the various components of the magnetic spectrometer, and the experimental running conditions.

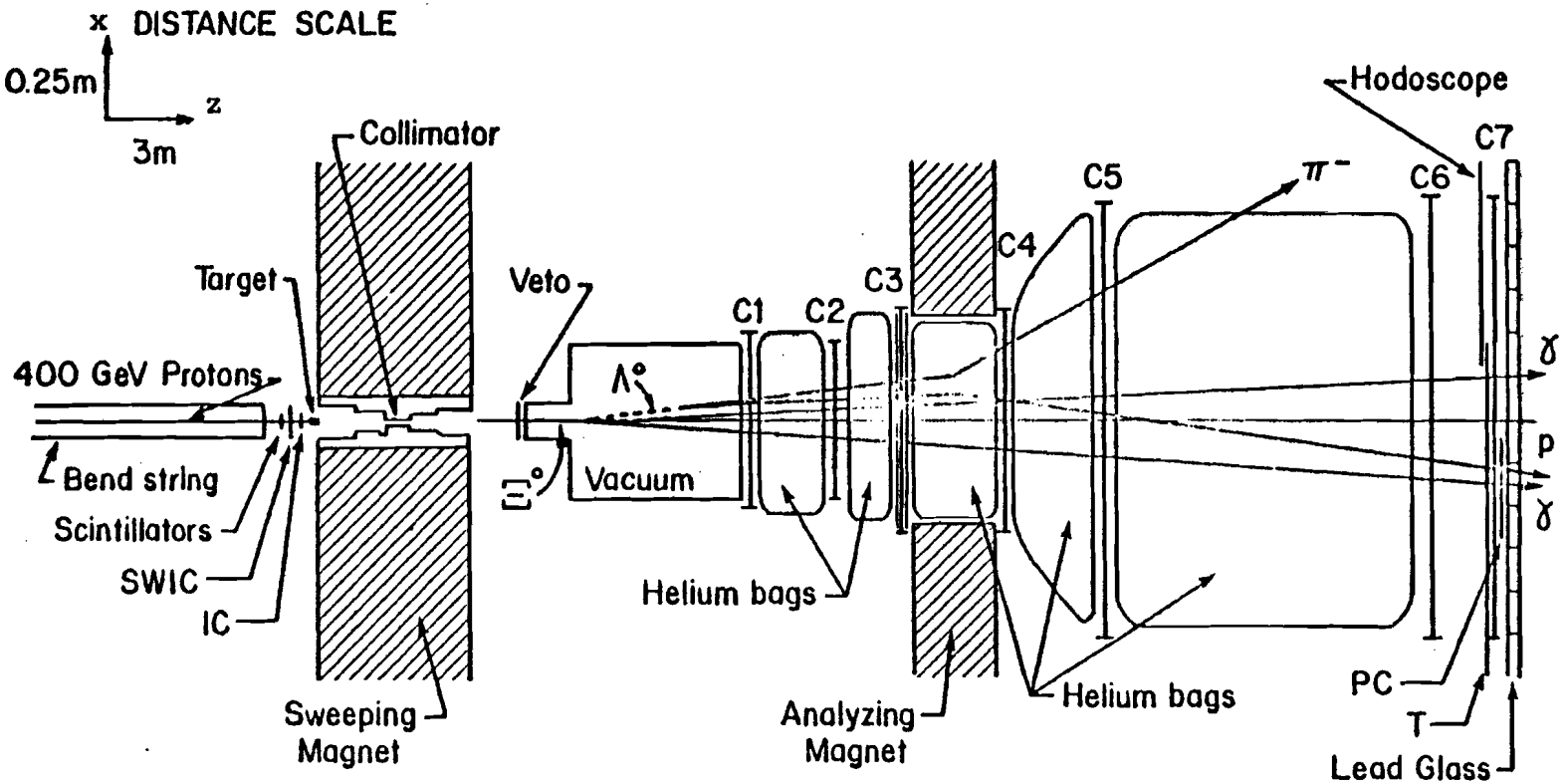

NEUTRAL HYPERON BEAM PLAN

FIGURE (2.1.1) Neutral Hyperon Spectrometer - plan

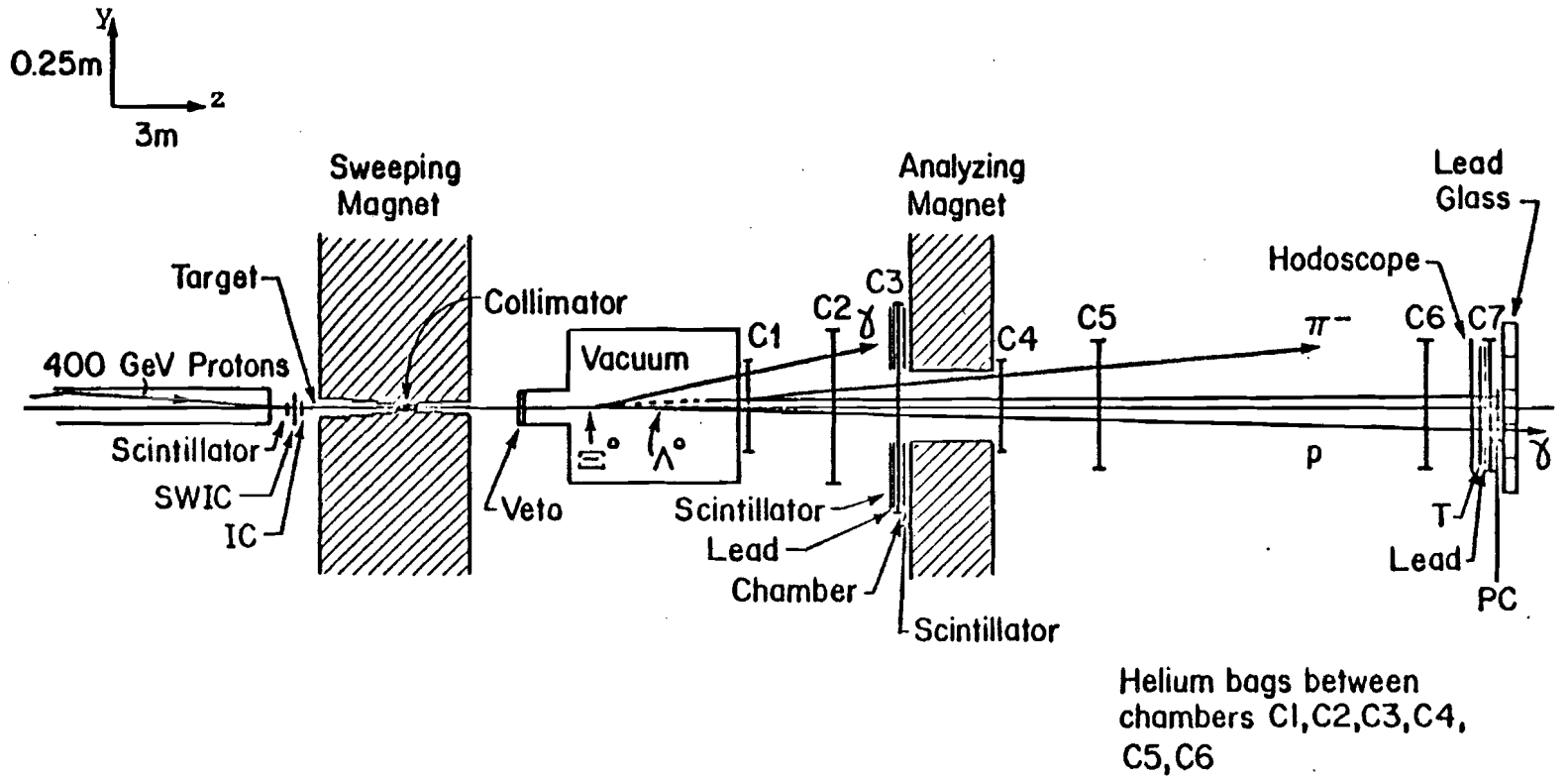

NEUTRAL HYPERON BEAM ELEVATION

Showing 1G $\Xi^0 \rightarrow \Lambda\pi^0$

FIGURE (2.1.2) Neutral Hyperon Spectrometer - elevation

2.2 The Beam Line

The Fermilab proton synchrotron was operated at an energy of 400 GeV and at intensities of approximately 2 x 10^{13} protons per machine cycle during the course of the experiment. Typically the accelerator delivered protons to the experimental areas every 15 seconds, in a burst of one second duration (called the "beam spill"). The primary accelerated proton beam was split into several subsidiary beams for delivery to the various experimental areas. The beam delivered to the Meson Laboratory was incident on the Meson beryllium target, which in turn produced several subsidiary beams for transferral to the Meson experimental areas. The diffracted proton beam component (400 GeV protons) was transported down the M2 line through a series of bending (dipole) and focussing (quadrupole) magnets, to the experimental area about 450 m downstream. Here the experiment's production target (usually 1/2-interaction length of beryllium) was aligned before the upstream aperture of the collimator, at one focus of the beam transport optical system. Typically, about 2 x 10^{9} protons per pulse were delivered onto this target, in a circular beam focus of about 2 mm full-width-half-maximum (FWHM). (The terms "upstream" and "downstream" refer to the incident proton beam direction). The final magnet in the

transporting beam-line was a string of three 3 m long dipole magnets which deflected the proton beam in the vertical plane. About two-thirds of the way between the Meson target and the experimental production target was another vertically-deflecting magnet which was used to deflect the incident proton beam from the nominal horizontal undeflected position. The beam could then be restored onto the center of the production target using the final vertical magnet string. By this means the "production angle", the angle between the incident proton direction and the outgoing hyperon direction (the collimator direction), could be varied through values between -10 and +10 mrad. The transverse momentum of the produced particles was directly related to the production angle used.

2.3 The Target Area

Immediately upstream of the production target there were three pieces of equipment used to monitor the incident proton beam. An argon-filled ionization chamber (IC), operated at about one atmosphere pressure, provided the primary intensity monitoring. It was calibrated at low proton intensities (up to about 10^6 per pulse) by using three scintillation counters 50 cm upstream of it, which

could be mechanically moved into and out of the beam. Between the scintillators and the ion chamber a segmented wire ion chamber (SWIC), with 1 mm spacing, provided a check of the beam quality ("spot-size") of the protons striking the target. The typical FWHM in both horizontal and vertical views was 2 mm. The SWIC was used to monitor, and define, the production angle, in terms of the deviation from the undeflected position of the beam (calculated from the known geometry of the beam-line magnets, and setting the corresponding magnet currents in the final bend string from their field-integral map). The target itself was mounted in a target "muff", a cylindrical piece of expanded polystyrene foam, which was mounted on a rod attached to a motor. Around the circumference of the muff were several holes, into each of which a different target was placed, so that any target could be automatically rotated into the proton beam. One hole was left empty, so that background production from sources other than the targets could be studied. Data were taken mainly using 1/2-interaction length beryllium (15.32 cm long), with some taken using 1/4-interaction length beryllium, 1/2-interaction length lead, and 1/2-interaction length copper. The targets were all cylindrical, with diameters of 0.152 cm. They were all carefully surveyed in the muff so that they were aligned with their long axes along the collimator axis, and centered on the collimator aperture.

2.4 The Collimator

Downstream of the target muff was the collimator. This was a 5.3 m long brass channel between the pole tips of a large conventional magnet. This magnet was called the "Sweeper" because it swept charged particles out of the beam of particles produced in the collision with the target. Its field was in the vertical direction, with a maximum magnitude of 2.5 T. The collimator was gravitationally level to about 0.5 mrad. The channel was composed of six blocks, each with a circular hole of fixed diameter, different for each, ranging from 4 to 20 mm, drilled through its center (see Schachinger [6] for details). The defining aperture was 4 mm in diameter, which implied a solid angle acceptance of 1.2 microsteradians. At an incident production angle of 7.6 mrad the proton beam was buried in the second block from the upstream end. The blocks were removable so that the Sweeper's magnetic field could be measured carefully. These measurements of the field integral, and field maps of the magnet, were obtained for an earlier experiment (the precision measurement of the Λ magnetic moment), and those results were used in this experiment [2,6]. It was imperative that the field integral be known precisely as it was this field which caused the precession of any

polarization associated with particles passing through it. The sweeping magnetic field was homogeneous over the length of the collimator, and was monitored continuously during the experiment by means of a nuclear magnetic resonance (NMR) probe which remained mounted in the most downstream collimator block, just below the beam position and about 110 cm from the downstream aperture. This was always the primary field monitor; a certain value of the resonance frequency defined a particular field integral. Previous measurements had proved the reliability and reproducibility of this approach; the overall precision to which the whole field integral was known (including fringe fields, which were measured with a Hall probe, and cross-calibrated directly with a flip-coil) was better than 0.2 %. (The value obtained for the magnetic moment of the Λ in this experiment also provided an independent check of the consistency of the field integral values used, by comparison with our previous experiment). Three magnitudes, and both polarities, of the field integral were used for the data-taking: 13.64 T m, 10.55 T m, and 9.05 T m, corresponding to standard fields of 2.495 T, 1.939 T, and 1.662 T respectively.

2.5 The Magnetic Spectrometer

Downstream of the collimator was the decay volume (an 11 m long evacuated pipe with a diameter of 35 cm) in which hyperons produced in the target would decay. Further downstream was the magnetic spectrometer, which consisted of six MWPC's, three before and three after a wide-aperture superconducting analyzing magnet. A 10 cm diameter scintillator veto, upstream of the decay volume and 1.9 m from the Sweeper face, defined the beginning of the decay region for neutrals. The analyzing magnet, known as "Avis", was 2.5 m long, and had a vertical field with a maximum field integral of about 2.4 T m. Operated at this field, it had a bending power of 0.96 GeV/c, i.e. a transverse momentum of 0.96 GeV/c was imparted to a charged particle traversing it. Positively-charged particles were deflected towards -x (in the coordinate system shown on Fig. (2.1.1)). Downstream of chamber C5, positive particles were always in the negative x region, and negative particles in the positive x region. The downstream aperture of Avis (61 cm horizontal x 20.3 cm vertical) was one of the geometrical apertures limiting the acceptance of the spectrometer. (The "acceptance" of a detector is a term describing the range of parameters of the particles which can be detected in it).

The MWPC's were of conventional construction [22,23] - each had two planes of signal wires, oriented orthogonally to each other, usually vertical and horizontal, except for chamber C2 which was rotated at 45 degrees relative to the others. This chamber provided some ambiguity resolution in two-track reconstruction. Chamber C1 had 256V x 128H wires, chambers C2 and C3 320V x 320H, chamber C4 316V x 128H, and chambers C6 and C7 640V x 192H wires. Chamber C3 had a third plane of signal wires oriented at 45 degrees with respect to the others for additional spatial ambiguity resolution. Chambers C2, C3, and C6 were larger than their counterparts in earlier experiments. C7 was a new addition. The signal wire spacing in all chambers was 2 mm, except for the rotated plane in C3 which was $2\sqrt{2}$ mm. They were operated using a gas mix of about 70 % argon, 30 % isobutane, and 0.3 % freon 13B1, bubbled through liquid methylal at 0 deg C, and at a plateau high-voltage of about 4.2 kV.

In the regions between the chambers were placed helium-filled polyethylene bags, in order to reduce the amount of material in the beam, which could give rise to multiple scattering, and, more importantly, to reduce the effects of γ -conversions from the neutral beam. These conversions could give rise to a large charged particle flux which would be a severe limitation on efficient MWPC

operation with high neutral beam intensities which are necessary when studying a relatively rare decay like $\Xi^0 \rightarrow \Lambda\pi^0$. With helium bags in position, and the thicknesses of scintillators and all other materials in the beam reduced to the absolute minimum (about 0.8 g/cm^2), the charged fluxes through the chambers were kept below a few MHz at the highest beam intensities. Even at these levels the effect on chamber efficiencies was apparent, reducing them to ~92 % (at worst) to ~97 % from the typical 97-99 % easily obtainable at low running intensities.

2.6 The Lead Glass Array

At the most downstream end of the spectrometer, 40 m from the downstream face of the Sweeper, was an array of lead glass. This was used for the detection of γ rays.

2.6.1 Lead glass

Lead glass is a useful material for the detection of electromagnetic showers because it has the following properties:

1. It has high transmission at optical wavelengths (which allows good sampling of energy deposited within it).

2. It has high average atomic number (which means that shower development is rapid once an electron or photon enters).

3. It has high density (so relatively small amounts can contain the electromagnetic showers of photons at these energies - typically between ~2 and ~50 GeV).

4. It can easily be adapted to modular design, and hence to designs in which useful spatial resolution information can be obtained.

Relativistic charged particles in an electromagnetic shower emit Cherenkov light which is transmitted through the glass to photomultiplier tubes, where the signal may be amplified. The total path length of particles in the shower is proportional to the energy of the incident particle, so that the total Cherenkov light is also proportional to the incident energy. Therefore lead glass may be used as an effective calorimeter for gamma rays.

2.6.2 The array

The array used here consisted of 70 lead glass blocks, each of dimensions 100 x 100 x 384 mm^3, arranged in 5 horizontal rows, and 15 vertical columns, with their long axes parallel to the beam direction. The alternate rows of 15 blocks were displaced relative to their neighbors by 1/2 a block width (5 cm) to minimize the number of nearest neighbors for each block, and the entire array shadowed the exit aperture of the analyzing magnet, Avis. These blocks were manufactured by Ohara, and by Schott, and were type SF2 glass with a radiation length of 32 mm. The array structure, together with the associated counter dimensions, is shown schematically in Fig. (2.6.1) . Three blocks were removed from the region in which protons from daughter lambda decays would strike the array, otherwise hadronic energy could leak into the neighboring blocks and interfere with recognition of gamma ray showers. At the lead glass array, the diameter of the neutral beam was about 10 cm. The central block in the array, that centered on the neutral beam line, was recessed by 38.4 cm parallel to the beam relative to the other blocks in order to prevent similar leakage from showers caused by neutral-beam interactions (accidental neutrons and gammas) in this block. The fluxes of these neutrals were several orders of

magnitude higher than those of the hyperons under investigation, and so these backgrounds could be severe. Each block was wrapped with aluminum foil (to improve the light containment) and sealed with light-proof black photographic tape except for a 5.08 cm diameter circle on the downstream end. Here a rubber O-ring was epoxied to the face of the block, which aided in securely positioning an RCA 6342A/V1 photomultiplier tube, itself mounted flush against the glass by a spring-loaded tripod framework. The whole array, blocks and tubes, was enclosed in a light-proof air-conditioned steel box (170 x 60 x 60 cm^3), mounted on a turntable which itself was mounted on a wheeled-frame. This allowed movement of the array, transverse to the beam direction, on a pair of steel rails. Before data-taking the array was carefully centered on the beam-line (the nominal line defined by the collimator axis), and fixed there for data-taking. It was convenient to move the array to three separate positions during calibration procedures (to be discussed later).

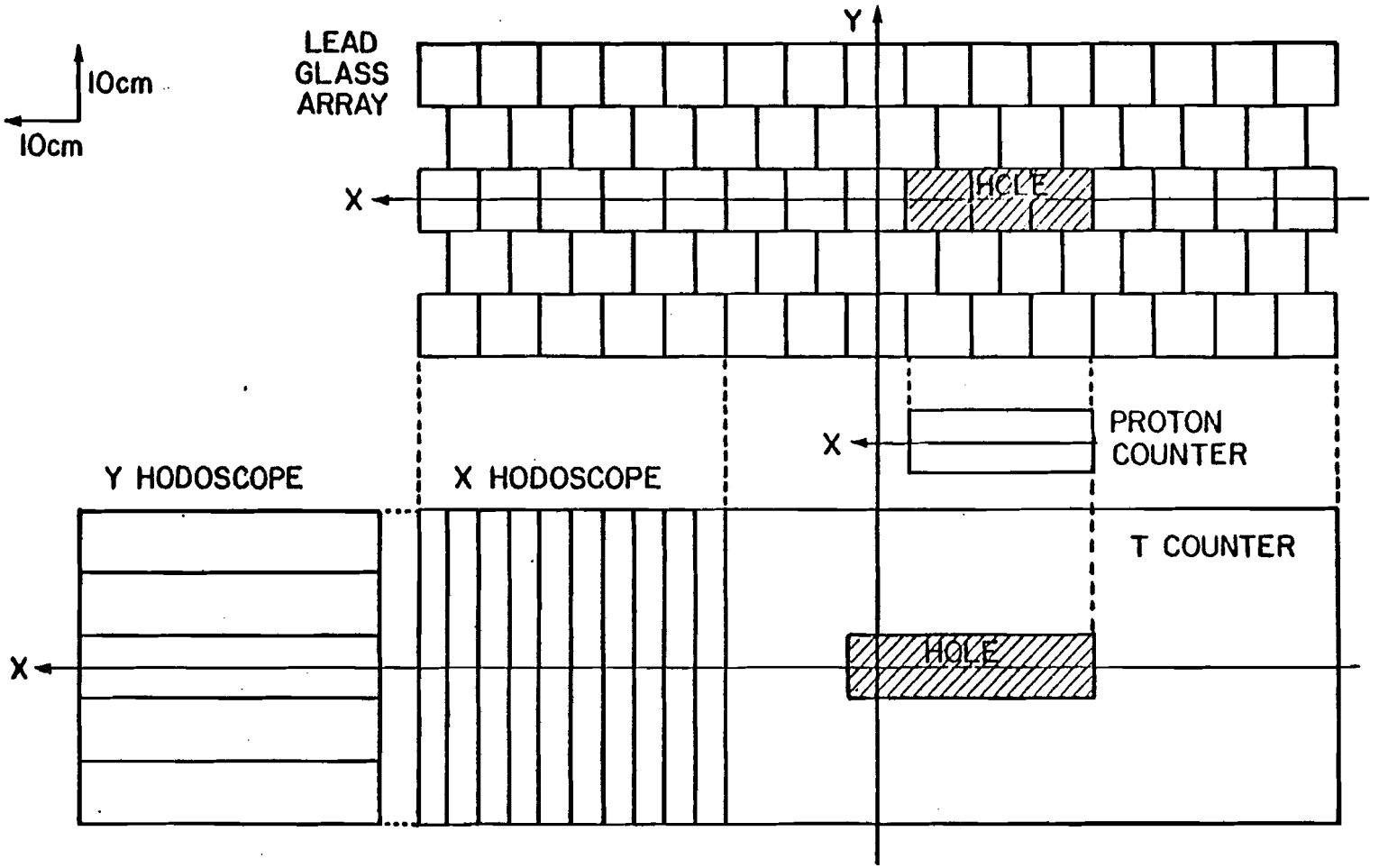

FIGURE (2.6.1) Dimensions of lead glass array and counters

2.6.3 The signals

The anode and first dynode signals from the phototube on each lead glass block were separately carried back to the electronics room in which all the signals from the apparatus were monitored and processed and the on-line computer was housed. The dynode signals were fed into part of the fast logic, to be described later, for use in defining the Ξ^0 trigger. The anode signal from each block was fed through a 16 dB attenuator, the current integrated over a 120 ns gate and digitized by an eight-bit analog-to-digital converter (ADC) unit (Lecroy model 2248). The attenuation chosen matched the phototube response to the available range of the ADC unit. The ADC range was set to 0.25 pC/count over the range 0-127 counts, and 1 pC/count over the range 128-255 (the full-scale maximum count), giving a total range of 160 pC. Since the anode signals were typically about 30 ns wide, and the signals were fed into 50Ω , the input voltage range was about 250 mV. An energy deposition of about 30 GeV (a typical mid-range γ-ray energy in this experiment) in a lead glass block corresponded to an anode pulse height of about 1.6 V, which was attenuated to 250 mV by 16 dB. All the attenuators were set to this value, and the high voltage on each phototube adjusted accordingly; this is discussed more fully in Section (2.12.1).

2.6.4 The light pulser

A piece of fiber optic light-guide was attached to each lead glass block via a small triangle of lucite glued (with an optically - transparent epoxy) to the face on which the phototube was mounted. The fiber optics were divided into four groups, each group being fed into a brass sleeve inside which a neon flash lamp was sealed. Each block could thus be fed with a light-signal from one of four lamps. Although the light was fed in through the face on which the phototube was mounted, sufficient light was totally internally reflected to be detected. This light pulser system provided a method for continuous monitoring of the operation of each of the lead glass block + phototube systems. The phototubes had 10 stages, and were run at relatively high negative voltage (around 1600 V) which kept the gain linear over a large operating range. They were usually linear over a high voltage range of 300-400 V. The negative voltage allowed dc coupling of the anode signal. Before the experiment an attempt was made to set the high voltage on each tube so that they would all have the same response to the same energy deposition in the block. This was done by testing each tube on a specific test block, with its fiber optic connection, light-bulb and pulser, under the same conditions. After stabilizing the

tubes on high voltage (and in the dark) for several hours, the voltages were set to give the same, reproducible dynode responses (800±40 mV, with rise times ~30±3 ns characteristic of the light pulser). This procedure was repeated three times at intervals of about one week. Only 7 % of the 70 tubes varied more than 10 % between readings of their dynode responses at these preset voltages. In practice the signals varied considerably more than this due primarily to variations from block to block in the fiber optic system (connections, etc.). The voltages were finally tuned for the experiment after studying the response of the blocks to electrons of known energies (see Section (2.12.1)). The actual calibrated responses of the blocks were obtained off-line from data taken with a beam containing a large proportion of electron pairs - the electron lead glass calibration data.

2.7 Scintillation Counters

The incident proton beam-monitoring scintillators, and the decay volume veto, have already been mentioned. The three-block aperture, where the protons were expected to pass through the lead glass array, was shadowed by a 30 x 10 cm^2 scintillator, and phototube, mounted flush on the front face of the steel box containing the array. This was

the proton counter (PC) since the proton from any decay was expected, and actually required, to pass through it. This counter was used as the basic timing counter in the experiment, relative to which the signal timing of all other detection equipment was referred.

Between chambers C6 and C7, 50 cm from the glass, there was a scintillator hodoscope composed of ten 5.08 x 51 cm^2 strips arranged with their long axes vertical, and five 10.16 x 51 cm^2 strips horizontal. This covered the region of the lead glass array which could be struck by charged pions from daughter lambda decays. The signals from these counters were fed to latches. (A "latch" is a flip-flop device which can be set to indicate the presence of a signal into it). This information could be used to locate crudely a pion hitting the array and was input to the γ part of the fast trigger logic in an attempt to veto such showers being considered as γ showers. Consequently it was called the "pion-killer hodoscope".

2.8 Chamber C7

To improve the position resolution of γ ray showers detected in the lead glass, a seventh MWPC was added to the spectrometer, 20 cm in front of the array. This had a two

radiation length thick piece of lead mounted in front of its active area, which itself shadowed the aperture of the glass array. Mounted immediately upstream of the lead was a scintillation counter, T, which covered that part of the chamber's active area, and that of the lead glass, which should be free of hits from charged pions. Both the counter and the lead sheet had holes 10 x 40 cm^2 cut out of them in the areas corresponding to the PC region (10 x 30 cm^2) and to the central neutral beam region. Gamma rays, or electrons, which passed through the lead usually gave rise to a small shower of charged particles which were detected in the MWPC as a small cluster of wire hits. The counter T was viewed by three phototubes, and operated as a charged particle veto. Thus the lead glass was totally covered by three scintillator systems: the hodoscope covered the π^- side, and the T veto the rest, except for the hole shadowed by PC.

2.9 Chamber C3

To be detected in the lead glass array, a gamma-ray had to pass through the aperture of the analyzing magnet. To improve the gamma ray acceptance of the basic spectrometer two scintillator-lead-MWPC-scintillator sandwiches (of dimensions 20 cm vertically and 60 cm

horizontally) were constructed on chamber C3. Pieces of scintillator and lead of these sizes were mounted on the upstream face of C3, covering the regions 60 x 20 cm^2 immediately above and below the magnet aperture, and similar sizes of scintillator completed the sandwiches on the downstream face. The lead used here was also 2 radiation lengths thick. The absence of a signal in the upstream scintillator, and the presence of a signal in the downstream scintillator, was taken to indicate a γ ray conversion. As for chamber C7 the conversion was recognized in this MWPC as a small shower of charged particle hits. The front scintillators were called A1 (top) and A2 (bottom), and the back ones A3 (top) and A4.

2.10 Data Acquisition

2.10.1 The trigger logic

A "trigger" is an essential part of a high-rate high energy physics experiment, in which thousands of events may be occurring per second. (The generic term "event" is used to refer to any example of the specific process being studied). This is a means of requiring several crucial and

well-defined criteria which are satisfied by the desired events of the experiment, but which also serve to discriminate against unwanted and background events. In this way less time is wasted during data collection ("dead-time"). Once an interesting event has been found by some means, all the relevant information pertaining to that event can be found and processed in some way.

In this experiment the relevant information was the wire hits in each MWPC, the pulse heights from the lead glass blocks, and the latched signals from the various scintillation counters. This information for each event was read into the on-line PDP-11/45 computer memory via a CAMAC interface, and written onto magnetic tape. These tapes were later analyzed off-line on Fermilab's Cyber 175 computer system, and the reconstruction of the interesting decay chains $\Xi^0 \rightarrow \Lambda\pi^0$, $\Lambda \rightarrow p\pi^-$, and $\pi^0 \rightarrow 2\gamma$ performed.

The trigger was composed of three independent sub-triggers, which were interspersed throughout the data-taking. There were two types of Ξ^0 trigger - one requiring two γ-like showers in the lead glass, and one requiring one shower in the glass and one in the chamber C3 scintillator-lead sandwich. A Λ trigger was mixed with these to provide a means of normalizing Ξ^0's to Λ's, which are much better understood from our previous experiments

and provide an independent and continuous monitoring of the experiment. Since Λ's are produced about 100 times more frequently than Ξ^0's, the Λ trigger was automatically prescaled by a factor of 128 before mixing, in order to reduce the number of Λ triggers on tape to a level comparable to that of the Ξ^0's.

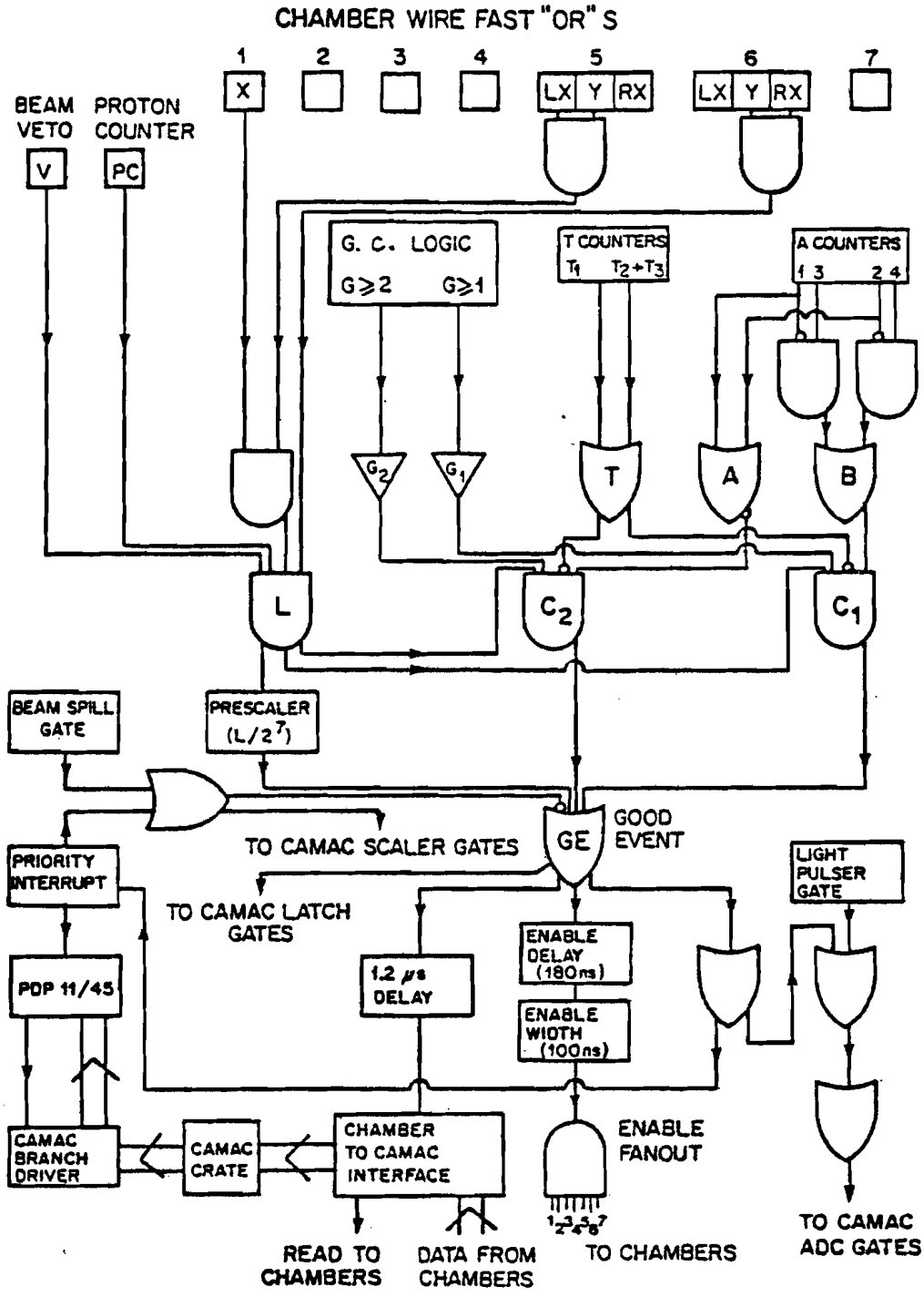

FIGURE (2.10.1) The trigger logic

2.10.2 The Λ trigger

The trigger logic is shown schematically in Fig. (2.10.1). Fast signals from the chamber signal planes provided their own triggers. Each chamber generated a fast pulse which resulted from the combination of a logical "OR" of the horizontal wires and/or an "OR" of the vertical wires. In chambers C5 and C6 the vertical wires (the horizontal coordinate) were "OR"-ed in two independent halves across the chamber centers, called "left" (+x) and "right" (-x). A fast-OR was formed at a chamber about 40 ns after a particle had passed through the active area. The Λ trigger required no signal in the veto counter V, at least one charged particle (signal) in chamber C1, a signal from the left side of chamber C5 (which means a negative particle), one from the right of C6 (positive particle), and a signal in the timing counter PC. This was called the L trigger, and written

$$L=\bar{V}.1.5L.6R.PC \qquad (2.10.1)$$

where . denotes logical "AND", and $^-$ denotes logical "NOT". This specified the basic configuration of a $\Lambda \rightarrow p\pi^-$ decay in the apparatus: a neutral particle entering the decay volume (no signal in V), a charged particle leaving the volume (signal in C1), and two separated charged particles downstream of the analyzing

magnet (signals in C5L and C6R). A signal in PC required a stiff (high momentum) positive particle, typical of the proton from a Λ decay, in which the proton, being much more massive than the pion, carries away most of the initial Λ momentum.

2.10.3 The Ξ^0 triggers

The Ξ^0 triggers were complicated by the fact that they had to specify gamma rays in some way. In order to do this a special electronic system was designed and built to identify clusters in the lead glass, fast enough that this information could be fed into the trigger logic. This device was called the "Gamma Cluster Logic" (GCL). Its function was to identify the presence of individual clusters of energy deposition in the lead glass array, and return signals, through separate outputs, according to whether there were ≥ 1, ≥ 2, and/or ≥ 3 clusters there, within about 50 ns of an event occurring. It was necessary to remove the lead glass block centered on the neutral beam from this logic, since the high rate of neutrals striking it caused confusion with real γ showers.

Using these signals the two cascade triggers, denoted C1 and C2, were defined. Both required a Λ trigger, L, as a subsidiary component. Then C2 required no signal in the veto T, and a ≥ 2 signal from GCL. C1 required a γ -like signal from the A-counters on C3 and a ≥ 1 signal from GCL. The A-counter signal could be from either the top or bottom sandwiches. These are written:

$$C2 = L.\ G\geq 2.\ \overline{T}.\ \overline{(A1+A2)} \qquad (2.10.2)$$

$$C1 = L.\ G\geq 1.\ (\overline{A1}.\ A2 + \overline{A3}.\ A4) \qquad (2.10.3)$$

The whole trigger was:

$$GE = C1 + C2 + \frac{L}{2^9} \qquad (2.10.4)$$

where "GE" stands for "Good Event", the description of an event satisfying the trigger requirements.

2.10.4 The fast gamma logic

The GCL was a cluster logic arrangement of threshold discriminators and comparators which could count the number of disjoint signal maxima occurring in a list of 70 signals fed into it. It was wired in such a way that it effectively contained a map of the 70-block lead glass array used in the experiment so that this clustering could be accomplished according to the occurrence of each signal within the 15 x 5 array structure of the glass.

A simplified block diagram is shown in Fig. (2.10.2), and a schematic of the pattern recognition in Fig. (2.10.3).

The dynode signals from each phototube on the lead glass were fed into GCL, except for those from the two blocks nearest to the neutral beam since they experienced high accidental rates. To each dynode output used, a 9 ns clip line was added in order to keep the signal into GCL about 18 ns wide. With the light pulser-originated phototube signals input, the $G \geq 1$ output signal was a short ~10 ns pulse, but without the clipping a beam particle caused GCL to update many times, giving an output pulse ~150-200 ns long. The input threshold signal level was adjustable; 45 mV was chosen as a satisfactory level at which to set each input line. This level corresponded to an energy deposition in that block of about 0.9-1.0 GeV (including the reduction due to the clip lines). It was found that there was a time-difference at the $G \geq 1$ output of up to 12 ns between that due to a small (~50 mV) input signal and that due to a large (~1.5 V) one. This was easily accounted for by the difference in rise times of the phototube pulses for signals of these magnitudes. The internal coincidence circuitry was checked to ensure that jitter of this size would not cause it to fail. Although the $G \geq 2$ efficiency was 100 % for a 1.5 V signal on one input, and a 50 mV signal on any one of the others, the

width of the output was only ~20 ns, and the time-difference effect of different signal sizes meant that the overlap region common to all inputs was only ~8 ns. Since the time-difference from channel to channel varied by as much as 9 ns (presumably due to slight differences in the threshold settings, wiring, and chip characteristics), the output width from GCL was set to 50 ns.

The relative timing of all the phototubes into GCL was checked several times, both with the light pulser system, and using electron pairs in the beam (see Section (2.12.1)). Using electrons, all the blocks were set to be within $\pm$ 3 ns of each other at the GCL inputs.

The signals from the pion-killer hodoscope were also input to GCL, so that signals in the lead glass attributable to charged particles detected in the hodoscope could be removed from the gamma cluster logic. The pion-veto was not expected to be 100 % efficient due to the effects of geometrical parallax on the comparison between hodoscope position and glass position (separated by ~50 cm along the beam direction) and because hadronic showers in the glass could spread into several blocks.

GAMMA OBSERVATION DEVICE - BLOCK DIAGRAM

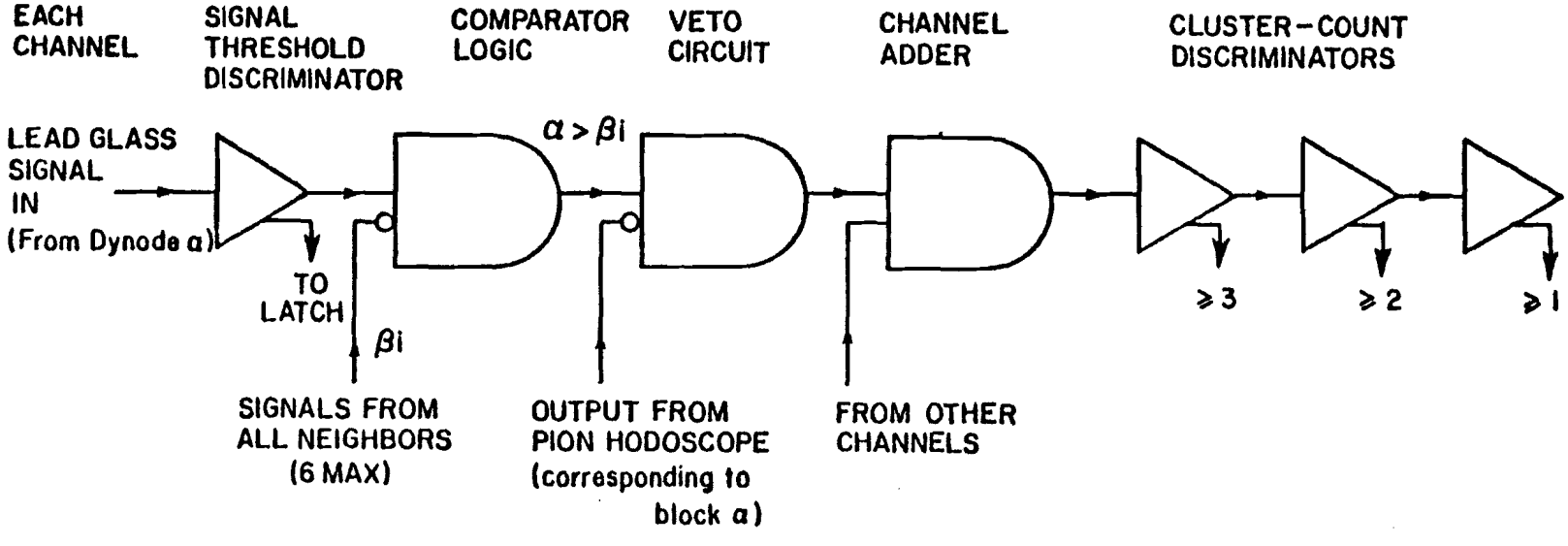

FIGURE (2,10.2) Block diagram for Gamma Cluster Logic

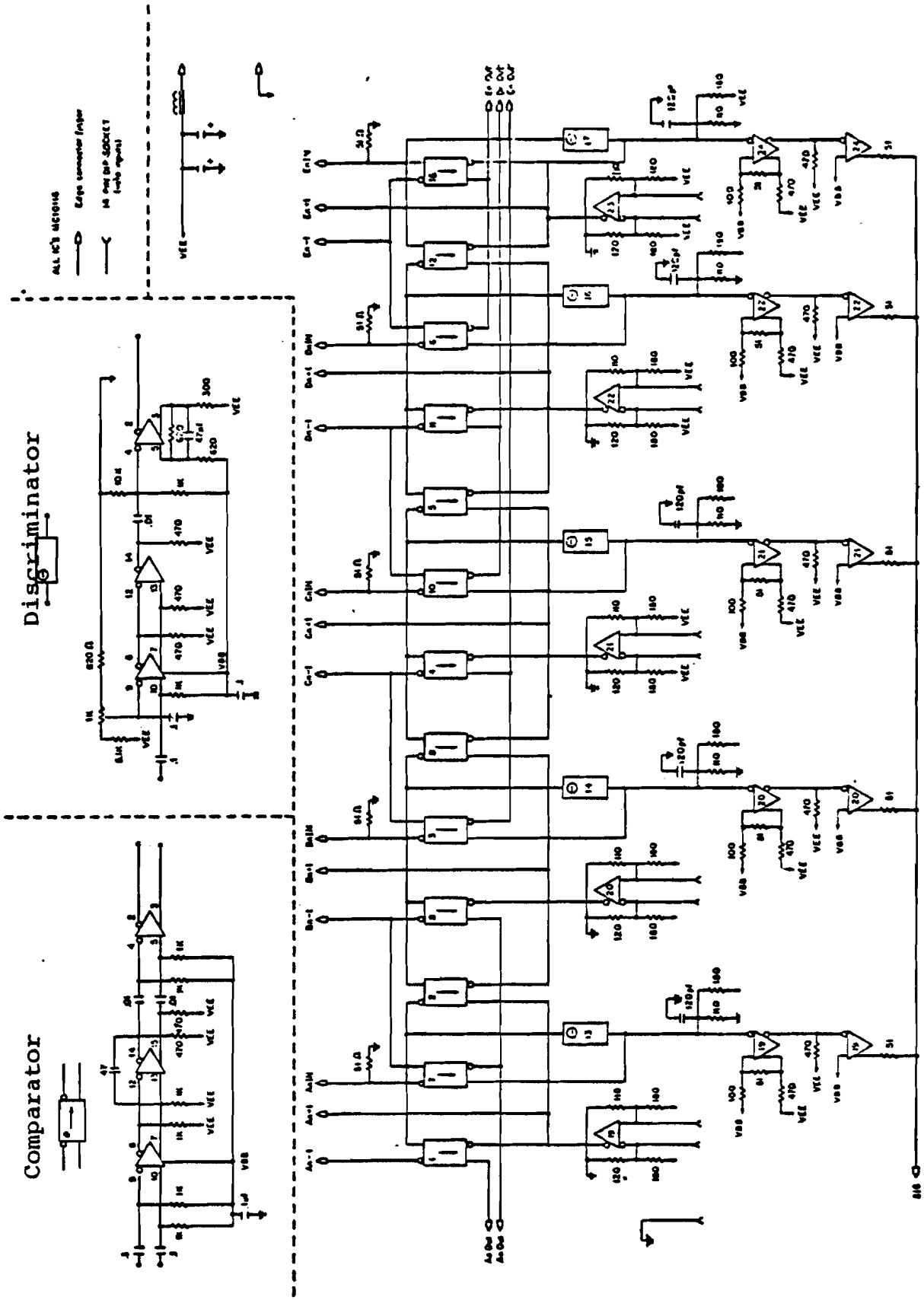

FIGURE (2.10.3) Pattern recognition schematic for Gamma Cluster Logic

2.10.5 The read-out system

When a particle passed through a chamber the signal on the hit wire (or wires) travelled to an amplifier, one per wire, where it was split into two parts, one of which contributed to the formation of the fast OR signal from the chamber. The other part was delayed electronically in order to give the system time for a trigger to be formed and examined. If the trigger was satisfied a pulse (the "enable") was sent back to each chamber where, arriving in coincidence with the delayed signal on each amplifier board, it caused a flip-flop to be set, thus storing the wire-hit information for the event. The fast OR signal took typically 150 ns to arrive at the trigger logic coincidence electronics; the internal delay generated was about 650 ns, and a typical trigger event took about 250 ns to be formed. The amplifier electronics and most of the readout system used emitter-coupled logic.

The logic simultaneously generated a "busy" logic level which prevented the system from accepting more events until the latched chamber hit information had been read out. A priority interrupt sent to the computer caused it to read the chamber hits serially through a CAMAC interface. Each hit was coded as a 16-bit data word. The

read operation reset the flip-flops as it passed; a typical event was read out in 0.5 ms. A variable number of hit wires could be read per event, up to a maximum of 156. The distribution of the total number of wire hits per event, including those due to δ ray showers in chambers C3 and C7, rose to a sharp peak at about 25 hits, and then slowly decreased to the maximum value where there was a negligible number of events. The ADC signals from the lead glass, and the latch information, were also read for each event. The computer then cleared the ADC units, and reactivated the logic to accept a new event. About 200 events per spill (of one second duration) could be handled by the computer.

Between beam spills, the computer read via CAMAC a set of scalers containing data from various scintillators and logical combinations of such signals, the ADC signals, and the IC data (which was read and reset). The ADCs at this time contained either pedestal values (the floating base-line of each ADC channel) or signals due to the light pulser system (the light pulser flashed on alternate spills).

The computer read information into core memory, which was separated into three buffers. When one buffer was filled the information was transferred to disk, while data were written into the next buffer. The core-to-disk

transfer time comprised the bulk of the dead-time in which no events could be collected. At the end of a spill the incomplete buffers were transferred to disk, and the information on disk was written onto magnetic tape. The scaler information for the spill was then written.

2.11 Monitoring

Several monitors of the behavior and operation of the experimental apparatus were used during the data-taking period. These were used to ensure proper operation of the equipment and to pinpoint specific breakdowns and failures.

The primary proton beam quality monitor was the target SWIC - the position and size of the proton beam here was kept fixed at specific well-defined operating points. The SWIC trace was continously displayed on a storage oscilloscope in the electronics room, so that these conditions could be kept as stable as possible. Any deviations from the expected target position were corrected by adjustments of the currents in the various beam-line magnets.

The field of the sweeping magnet was monitored by the NMR probe - the NMR resonance was displayed on an

oscilloscope in the electronics room. Part of the circuitry of the probe included a calibrated frequency monitor, which displayed a digital readout of the resonant frequency. The magnet's power supply also gave a voltage readout from a current shunt.

Each MWPC had a small 1 μCi Fe^{55} source attached to its frame, aimed at one signal wire which was not in the active region and had instrumentation independent of the rest of the chamber. Each radioactive source emitted 5.9 keV X rays which caused small signals on the wire; these were fed into an emitter-follower whose output could be viewed on an oscilloscope in the electronics room. The signal was a monitor of the chamber operation, including the quality of the gas-mix, the operating voltage, and background noise on the data signals.

The on-line computer displayed histograms of the wire-hits in the MWPCs, the signals in the ADCs, and other related information, on request at a storage oscilloscope. These histograms were carefully watched for the appearance of misbehavior of the apparatus, in particular bad amplifier board circuitry and problems with the readout of the chambers.

Further checks were provided by the first stage of the off-line data analysis. The chamber efficiencies were obtainable from reconstructed Λ decays since the trigger only required one hit in a chamber although there would be two from a Λ decay.

2.12 The Lead Glass Calibration Procedure

For various calibration purposes, data on electron pair events were collected. Electron pairs were produced when γ rays scattered from material in the neutral beam. Normally they appeared as Y-like tracks, in which there was apparently only one track before Avis, and two downstream of it (in one horizontal plane).

To enhance γ ray conversions, a thin piece of lead was placed in the neutral beam just downstream of the collimator exit. The e^+e^- pairs passed through the spectrometer and produced showers in the lead glass array. The incident proton beam was at 0 mrad and at relatively low intensity ($\sim 10^5$ protons/pulse). A veto scintillation counter, D, was placed on the downstream face of the Sweeper, over the exit aperture, and the lead fixed to the counter's downstream face. The normal decay-volume veto counter V was used in coincidence, and Avis was run at 1/3

of its usual full field value so that all the electrons would not be swept totally off the array. At this field the electrons satisfactorily illuminated the full width of the array. A horizontal-field magnet, with sufficient field strength to separate the pairs vertically, was placed between the Sweeper and V, so that the electrons could be swept across the vertical dimension of the array. The fringe field of the Sweeper was sufficient to split the pairs slightly in the horizontal plane, and the field directions of the Sweeper and Avis were set to opposite polarities to increase the resolution of the splitting. Each e^+e^- pair could then be reconstructed as a vee in the spectrometer, and hence their momenta, or energies, found. *The trigger required* $\overline{D}.V.12L.12R$, *which was sufficient to* tag the desired conversions. A tape of such data was taken at each of three positions of the lead glass array on its rails, and five settings of the vernier magnet current were used for each tape, in order to illuminate all the blocks uniformly. Each calibration thus resulted in three data tapes. One set of tapes was taken at the beginning of the experiment, another in the middle, and the third at the end. This simple and convenient procedure quickly enabled calibration constants for the conversion of ADC signals to energy units to be obtained off-line. The details are discussed in the next chapter (Section (3.5)).

Before the actual data-taking of the first calibration, the pulse heights from all the lead glass blocks were examined while they were illuminated with this electron beam. The anode pulses were examined directly at the phototube bases. The attenuators between the tubes and the ADC modules were set so that full-scale on the most of ADCs corresponded to the largest γ energy likely to be deposited in one block. This number was chosen to be 30 GeV, corresponding to a maximum pulse height on the anode of about 1.6 V, as mentioned in Section (2.6.3). To do this, electrons of about 15 GeV energy were picked from the beam by calculating the approximate position at the array to which they would be deflected by the analyzing magnet, and moving the array (and using the vertical vernier) to illuminate every lead glass block with electrons of this energy. It was found convenient to set the attenuators to the same value (16 dB), and the pulse heights were then set to about 0.7 - 0.8 V by slightly adjusting the applied high voltages. About 30 blocks needed this readjustment, the maximum change being about 150 V. Once this had been done the high voltages were kept fixed for the rest of the experiment.

2.13 Data-taking Conditions

Data were taken under various combinations of values of production angle and Sweeper magnetic field integral, and type of production target. Four targets were used, as described previously, although most of the data were taken using 1/2 interaction length beryllium.

As mentioned above, three magnitudes of the sweeping magnetic field were used, and two signs of the field direction: +(up) and −(down). The notation for the Sweeper field integral condition was: ± 1 corresponded to full field, 13.64 T m, $\pm 7/9$ to 7/9 of full field, 10.55 T m, and $\pm 2/3$ to 2/3 field, 9.05 T m. The varying magnitudes allowed self-consistency checks of the polarization results, and the opposite signs allowed some bias cancellation, an important feature also resulting from data-taking at two signs (+ and −) of the incident production angle. Data were taken at 0 mrad, ± 2 mrad, ± 4 mrad, ± 7.6 mrad, and ± 10 mrad.

A typical magnetic tape, or run, contained about 80 000 triggers, and took about 2 hours to complete. In all there were 142 data tapes written. The breakdown of this total into four subgroups was as follows:

1. There were 111 Ξ^0 trigger tapes.

2. There were 22 so-called "empty" tapes, in which there was no target in the beam, for background studies.

3. Three "straight-through" tapes were taken. These were used to define, and check, the centers of the MWPCs, and to relate their inherent (xy) coordinate systems to each other and to the z-axis. The Sweeper and Avis were turned off, the production target removed, and the direct proton beam at 0 mrad and low intensity ($\sim 10^5$ p/pulse) transmitted through the spectrometer. The coordinate system is described in more detail in the following chapter.

4. Three sets of lead glass calibration tapes were obtained (nine tapes in all).

CHAPTER 3

DATA ANALYSIS I : RECONSTRUCTION

3.1 The Off-line Analysis

The raw data, on the magnetic tapes written by the on-line computer, were processed through several stages of analysis off-line. Each stage performed some data-retrieval and purification of the input sample, reduced the amount of spurious and unwanted information and compacted the data for convenience and ease of further analysis. Data-compacted magnetic tapes were usually written during each level of analysis. There were three basic levels of data summary: V-reconstruction (basically Λ reconstruction from MWPC hits), and two levels of Ξ^0 reconstruction. A diagrammatic summary of the analysis is shown in Fig. (3.1.1).

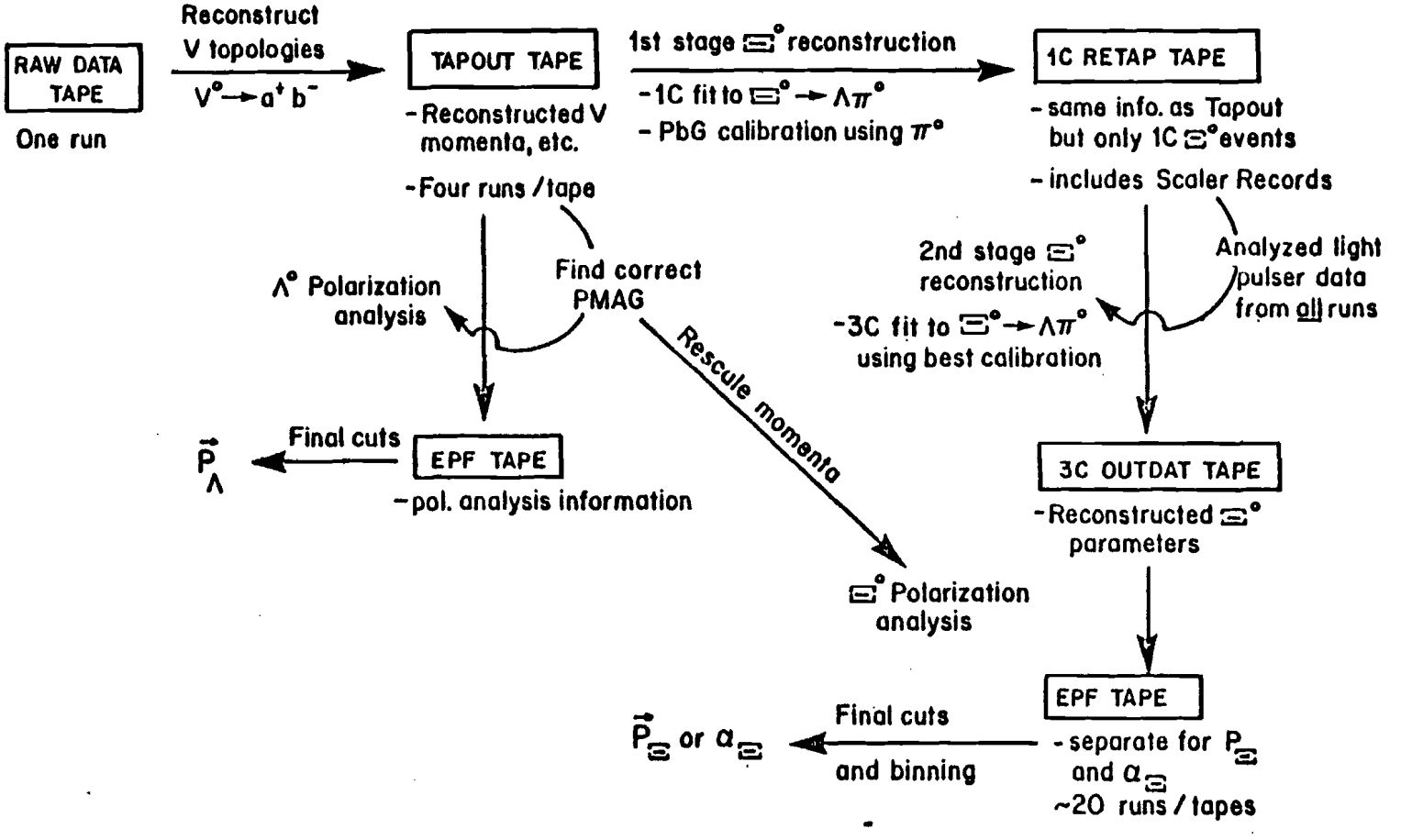

FIGURE (3.1.1) Summary of data analysis

3.2 The Coordinate System and Sign Conventions

The Lab (xyz) coordinate system was defined as follows. The positive z-axis was defined as the undeflected proton beam direction through the MWPC's when the sweeping and analyzing magnetic fields were off, with z=0 at the exit aperture of the collimator. The x=y=0 origin in each chamber was defined by the position at which this proton beam passed through it. The x and y axes were then defined in each chamber by the horizontal and vertical signal wires respectively, with a sense so that (xyz) formed a right-handed set of axes. Since the chambers were gravitationally level, this was equivalent to positive y being the upward vertical, and x being horizontal. All measurements were referred to these axes. It was found that there was less than 0.5 mrad difference between the z-axis and the collimator axis direction. The sign of the Sweeper field direction was defined so that positive magnetic field was along +y; this was equivalent to the deflection of a positive particle moving along positive z in the positive field being towards -x. The two signs of magnetic field were those with the direction of the field along + or - y. The analyzing magnetic field direction was always along +y, so positive particles were deflected to -x.

The sign of the production angle was defined positive in the following sense:

The production angle was positive when $\vec{in} \times \vec{out}$ was along +x;

The production angle was negative when $\vec{in} \times \vec{out}$ was along -x, where

$\vec{in}$ = the vector direction of the proton beam incident on the target, and

$\vec{out}$ = the vector direction of the neutral beam (collimator axis direction).

Previous experiments had shown that the axis of the neutral beam at 0 mrad production angle was in the same direction as the straight-through proton beam within 0.1 mrad, the angular resolution of the spectrometer for Λ's. The directions of the fields in all the relevant magnets had also been carefully studied [6]. Both the sweeping and analyzing magnetic fields showed no significant deviations from being purely in the y-direction. The magnet restoring the proton beam onto the target had a small bending power in x, as well as its primary bending in the (yz) plane. (This could contribute to a y-bias, but cannot affect any

magnetic moment measurements).

3.3 The Monte Carlo

For optimizing the design of a high-energy physics experiment a "Monte Carlo" is essential. This is generally a software model of the experiment, in which as many of the relevant physical parameters as possible are taken into account. Typically, hypothetical events are generated according to the kinematical laws governing the process under study, and their appearance examined in a mock-up of the experimental apparatus (i.e. the geometrical apertures, bending by magnetic fields, etc.). By assuming various momentum distributions, and considering more or less detailed specifications of the equipment, this procedure results in information which can be used for designing of the experiment and understanding its results.

A Monte Carlo of $\Xi^0 \rightarrow \Lambda\pi^0$ applied to this spectrometer showed that about five times as many γ's as passed through the Avis aperture hit the magnet face (and would be lost from detection). Therefore it was decided to build the two scintillator-lead sandwiches on the face of chamber C3. This was expected to increase the γ acceptance by about a factor of three. The Monte Carlo was

also used for deciding the optimum size for the proton counter, and the hole in the lead glass array. The distribution of γ rays from π^0 decays had greatest density around the center, near the hole, so a three-block hole (30 x 10 cm^2) was used although about 10% of the protons from the Ξ^0 decays would be outside this region in y. (The x containment of the protons in the hole was virtually total). The design of the pi-killer hodoscope also benefitted from these studies.

Once real data have been obtained, a Monte Carlo remains useful in checking that the equipment is behaving as expected, according to how well the original Monte Carlo actually simulated the experiment. A Monte Carlo is a gross simplification of the actual situation, but this is its utility - it can show just what is important, and what is less significant or irrelevant.

In the case of reconstruction or polarization analysis programs, like those central to this experiment, Monte Carlos can also test the algorithms used. Polarized events can be generated by a Monte Carlo, and these analyzed for polarization as if they were real data. This can give confidence that the program works as designed, and does not introduce spurious polarization signals!

Monte Carlos can to give quantitative information about the presence of backgrounds in data samples, once clean samples of real data are available from which one can find the correct momentum and spatial distributions with which to generate Monte Carlo events. The Monte Carlo method is the easiest way in practice of determining the acceptance of a complicated spectrometer.

The acceptance of this spectrometer has been studied in great detail for Λ's; Fig. (3.3.1) shows its momentum dependence. The lower curve shows the fraction of Λ events detected from a "flat" (momentum-independent) spectrum of $\Lambda \rightarrow p\pi^-$ decays generated at the target. This includes geometrical aperture effects, and resolution effects resulting from reconstruction. The upper curve shows just the geometrical acceptance, for $\Lambda \rightarrow p\pi^-$ decays occurring in the decay volume.

The overall Ξ^0 acceptance is shown in the lowest curve of Fig. (3.3.2) ; it is much lower than for the Λ case. Note that the acceptance drops very rapidly for Λ's of momenta lower than 100 GeV/c. To refer to cascade candidate events with one gamma detected in the lead glass and one in the chamber 3 sandwich, the notation "1G" was used; "2G" then referred to events with both gammas detected in the glass. For Ξ^0 events of momenta ~100 GeV/c

the Monte Carlo predicted that there would be about twice as many 1G Ξ^0's as 2G; at ~200 GeV/c this ratio falls to about 1:1 (see the middle two curves in Fig. (3.3.2)). The sum of these two curves gives the uppermost curve, which represents the geometric acceptance for $\Xi^0 \rightarrow \Lambda\pi^0$, and subsequent $\Lambda \rightarrow p\pi^-$, decays occurring in the decay volume. This effect has been seen in the real data.

However, finding the apparatus acceptance to sufficient precision to enable polarization - usually spatial asymmetry - measurements to be made, are usually enormous. One of the advantages of the analysis method used in this experiment is that it does not require such a one-to-one correspondence between a Monte Carlo-generated sample and each real data sample to obtain the result.

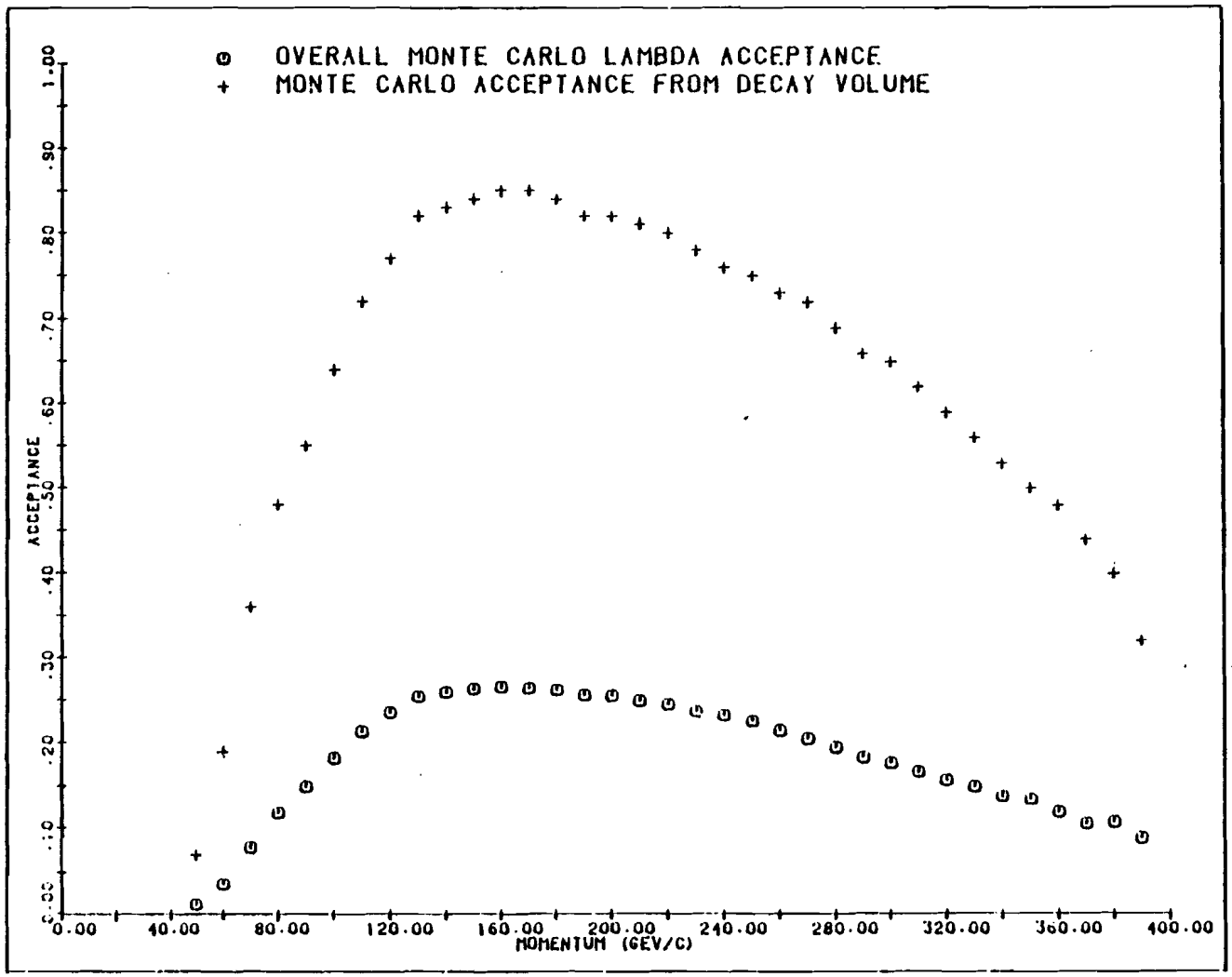

FIGURE (3.3.1) Monte carlo acceptance of spectrometer for $\Lambda \rightarrow p\pi^-$ decays

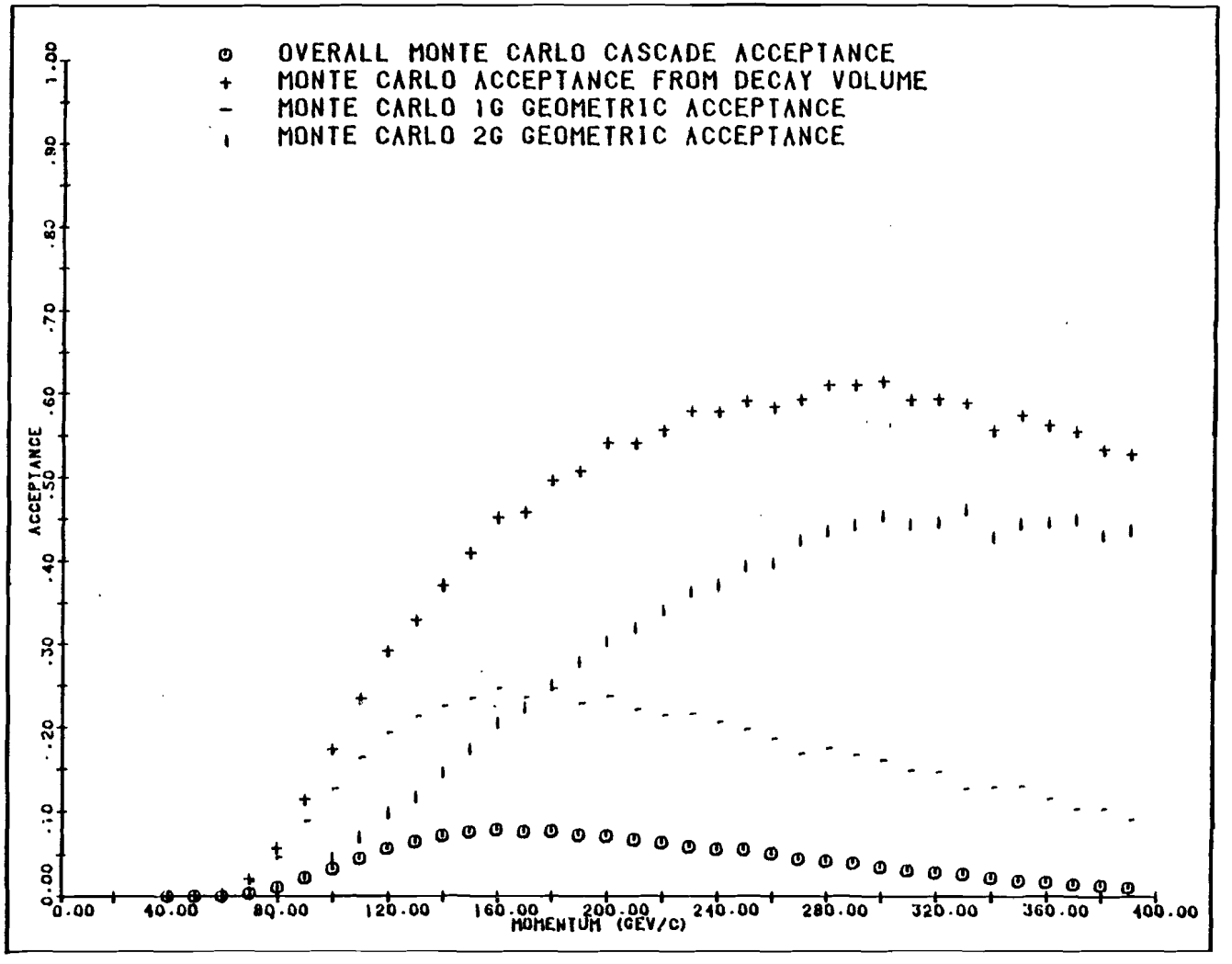

FIGURE (3.3.2) Monte carlo acceptance of spectrometer for $\Xi^0 \rightarrow \Lambda\pi^0$ decays

3.4 Vee Reconstruction

3.4.1 Pattern recognition

The MWPC wire-hit data were searched for events with the basic V-topology characteristic of a $\Lambda \rightarrow p\pi^-$ decay, i.e. two charged tracks intersecting in one point (the vertex) in the decay volume, and which are deflected through opposite angles while passing through Avis. A set of computer programs searched for such geometries, and then attempted to reconstruct each V according to one of the decay hypotheses $\Lambda \rightarrow p\pi^-$, $\bar{\Lambda} \rightarrow \bar{p}\pi^+$, $K^0_S \rightarrow \pi^+\pi^-$. The program made a reasonable attempt to identify the hits on each track by means of a least-squares fitting procedure, while requiring the x and y views to correlate with hits in the rotated chamber C2, and the track segments upstream and downstream of Avis to intersect approximately midway through the magnet. This fit resulted in slopes for both tracks in both views, the decay vertex position, and momenta for each of the tracks assuming a nominal value of 0.95 GeV/c for the field integral of Avis (the angle of bend through the magnet determined the momentum of the track). All these "V" parameters, the error matrix from

the fit, the raw wire hit information from chambers C3, C6, and C7, and the lead glass pulse height information were written to a magnetic tape for those events which satisfied the vee criteria. The scaler records were also transferred to this tape. These tapes were called "Tapout" tapes. The output of the program included diagnostic information concerning the chamber wire hit distributions and efficiencies, pulse height distributions from the lead glass, trigger latches set, and the types, qualities, and efficiencies of the reconstruction fits to the data. This provided further monitoring of the running of the experiment and was performed concurrently with the data-taking. The trigger latches gave a way of distinguishing between the vees associated with the three types of trigger-event, thus enabling comparisons between the samples to be made.

The trigger latch efficiencies were virtually 100 %, as determined from comparisons of the various sub-components of each trigger, which were themselves latched. As expected there was about 2 % cross-contamination of the L triggers by the C1 and C2's, about 15 % contamination of the C1's by the C2's, and about 10 % contamination of the C2's by C1's. Cascade reconstruction was attempted on all the cascade trigger events.

There was some ambiguity in the classification of vee-topologies into Λ's, $\bar{\Lambda}$'s, and K^0_s's. This was resolved as follows [24]. For events where the positively-charged track had the higher momentum the invariant mass was calculated assuming this track to be a proton, and the other a negative pion. The identification as a Λ was made on the basis of a comparison of this mass with the known Λ mass (1.11557 ± 0.00006 GeV/c^2), according to a mass-measurement error σ, which was calculated from the error matrix of the vee fit. If its mass was within 3σ of the known mass the event was called a Λ.

3.4.2 Calibration of the analyzing magnet

A short computer program examined only the reconstructed K^0_s events, and forced the measured $K^0_s \rightarrow \pi^+\pi^-$ invariant mass to its known value (0.49767 ± 0.00013 GeV/c^2) by iterating the Avis field integral. This gave a run-by-run calibration of this field. Its value was found to be stable to <0.3 % over the course of a run, and only varied within a few percent over the duration of the experiment, at 0.96 ± 0.01 GeV/c. This value defined the momentum scale for the experiment.

3.4.3 Typical composition of a raw data-tape

A raw data tape contained about 80 000 trigger events. At 7.6 mrad, the trigger composition was about 30 % lambda (L) triggers, 30 % C1 cascade triggers, and 40 % C2 cascade triggers. About 70% of the lambda triggers, and 60 % of the cascade triggers, were reconstructed to vees. Between 55 % and 60 % of the vees satisfied the ($p\pi^-$) mass hypothesis to be $\Lambda \rightarrow p\pi^-$ decays. In both trigger samples about 10 % were vees with very small or negligible opening angle before Avis , and 10 % totally failed to reconstruct as straight tracks. This component of both samples consisted of spurious and accidental triggers (due to backgrounds), as well as real events in which there were enough missing MWPC hits (due to chamber inefficiency and high-rate saturation effects) to cause a failure of the reconstruction pattern-finding algorithms.

At 0 mrad the relative purity (Ξ^0 content) of the trigger samples was the poorest of all the production angles. As the production angle was increased the sample purity gradually improved. This effect resulted mainly from the fact that the inclusive neutron and gamma ray (and hyperon) production spectra decrease rapidly with increasing production angle. These neutral components have

much higher fluxes than the hyperons being studied, and can give rise to backgrounds, due to interactions with material in the beam-line or accidental coincidences in the lead glass. At 300 GeV incident proton energy and a production angle of 0.6 mrad, yields in this hyperon beam have been measured to be: 400 Λ's, 45 K^0_s's, and 5 $\bar{\Lambda}$'s detected per 10^7 protons on target. Corresponding numbers for neutrons and gammas are estimated to be ~20 000 and ~30 000 respectively [22].

3.5 Lead Glass Calibration

Before $\Xi^0 \rightarrow \Lambda\pi^0$ reconstruction could proceed it was necessary to obtain the calibration constants for the lead glass ADC signals. These are the numbers, with units GeV/count, which convert the signals in counts to energies in GeV. This was done in two stages. First, the sets of lead glass calibration tapes were analyzed. The events on these tapes were mainly electron-positron pairs. These were reconstructed in the spectrometer, to give known energies and positions in the lead glass, and a least-squares fit was performed to these energies and the clustered lead glass signals (involving the unknown calibration constants) corresponding to each electron for all the events on the tapes. This involves minimizing the

quantity

$$\sum_j (E_j - \sum_i c_i s_{ij})^2 \qquad (3.5.1)$$

where

j labels events,

i labels blocks with non-zero signals for event j,

E_j =energy from spectrometer,

c_i =calibration constant for block i, and

s_{ij} =signal in arbitrary counts in block i.

This approach resulted in a set of 70 calibration constants, c_i, one for each lead glass block in the array. At the same time the energy and position resolution of electrons in the glass were studied. Using these values the first stage of Ξ^0 reconstruction could proceed and the second stage calibration was performed.

3.5.1 The GCL pattern recognition efficiency

The GCL efficiency was studied by using a software equivalent of its pattern recognition logic on electron shower data taken during the calibration runs. The pion-killer veto inputs to the GCL logic were turned off during these runs, so that the possible problem of veto inefficiency in the trigger would be avoided.

GCL's algorithm was to count as a cluster any signal which was larger than that in each of the neighboring blocks (of which there were up to six), considering only signals above the (adjustable) threshold. The threshold used for the data taking was 45 mV. This was modelled by a computer program which clustered the lead glass signals like this, and the results of applying a sequence of increasingly stringent cuts found.

The decisions made by the GCL electronics had been flagged by setting up to three latch bits, one for each of the $G\geq 1$, $G\geq 2$, $G\geq 3$ decisions. Therefore these bits contained the coded information that 0, 1, 2, or ≥ 3 clusters had been found. This latched information was compared with the software decisions, which led to inefficiencies in GCL's logic as a function of an arbitrary signal threshold c_T (in ADC counts above pedestal). The inefficiencies were defined

For $G\geq 1$, $N(1) = \frac{\text{no. of GCL says 0 decisions}}{\text{no. of software says 1 decisions}}$.

For $G\geq 2$, $N(2) = \frac{\text{no. of GCL says 0 or 1 decisions}}{\text{no. of software says 2 decisions}}$

The resulting inefficiencies were:

	Inefficiency (%)							
c_T(counts)	10	20	30	40	50	60	70	80
E_T(GeV)	0.7	1.4	2.1	2.8	3.5	4.2	4.9	5.6
N(1)	41	32	3.2	2.9	2.7	2.5	2.3	2.1
N(2)	57	39	5.3	5.0	5.0	4.7	4.9	3.2

These numbers were obtained using electrons from reconstructed e^+e^- pairs in the spectrometer. The electron momenta ranged from 2 to 60 GeV/c, with a broad peak around 15-25 GeV/c. About 30 000 events were used. No account was taken of possible hardware latch inefficiencies; these were expected to be of negligible importance once the latch modules had been checked in operation. The lead glass calibration constants were typically ~0.7 GeV/count, so the threshold counts could be converted to the approximate energy thresholds shown (E_T).

For > 2 GeV energy deposition in a one block per cluster, these results showed that GCL was over 95 % efficient.

The pion-veto section of GCL worked by vetoing the one cluster whose peak signal was in the block directly correlated spatially with the pion hit in the hodoscope. This of course could not veto the hadronic shower in the glass if the pion caused multiple clusters in surrounding blocks, or if parallax effects defeated the hard-wired logic matching the blocks with the hodoscope sectors.

3.6 1st Stage Ξ^0 Reconstruction

A set of computer programs performed a one-constraint (1C) fit to the hypothesis that a particular Ξ^0 trigger event satisfied the $\Xi^0 \rightarrow \Lambda\pi^0$ decay mode. The essential preliminary problem was the identification of gamma ray showers in the lead glass and the lead/scintillator sandwiches on chamber C3.

3.6.1 Rejection of hadron showers

Before attempting to cluster the blocks with signals in them, the charged p and π^- tracks were examined to see whether they could cause hadronic showers in the array, and consequently whether there could be spurious signals there. Both tracks were extrapolated to chambers C6 and C7 first. If hits in C6 could be clearly and unambiguously associated with a charged track the calculated slopes were modified to force the fitted tracks actually through them. All hits in C7 which could possibly be due to the charged tracks were deleted from the data. Whenever the proton track at the lead glass was not at least 5 mm from the nearest block around the edge of the hole a blanking procedure was

implemented to remove possible hadronic signals from the data. Centered on the projected position a circle of radius 7.5 cm was drawn, and the energy deposited in all blocks with centers within this circle was summed. If this was less than 2.5 GeV the lead glass data were unchanged; if it was above 2.5 GeV a second circle of radius 14.4 cm was drawn and the signals of all blocks with centers inside were set to zero. If the charged pion was identified in the C6 data, and projected to hit the lead glass (pions were usually swept totally off the array by Avis) a blanking procedure similar to that for the proton was applied. If the pion was not uniquely identified in C6, although it was expected to hit the glass, the lead glass data were left unmodified until a later stage.

3.6.2 Lead glass clustering

The lead glass data for each event were processed by a clustering algorithm which reduced them to a set of disjoint showers. A cluster was defined to be a connected spatial region bounded by either the edge of the lead glass array or by blocks without signals in them, inside which all blocks had finite energy deposited in them. The total energy of each shower was calculated using the calibration

constants from the electron calibration analysis. The x and y centers-of-gravity of each cluster were also found. From this set three types of shower were deleted:

1. Showers with centers within 2 cm of the neutral beam line. (A large number of triggers were caused by accidental coincidences between a lambda and a stable neutral beam particle (neutron or gamma) shower, with or without another gamma-like signal. These all had clusters with centers close to the neutral beam.)

2. Showers with centers within a radial distance of 15 cm from the projected charged pion hit in the glass, for the cases in which the hit had not been confirmed by the C6 data.

3. Showers composed of such a large number of blocks that they were unlikely to be due to a single electromagnetic shower of the calculated energy.

The number of remaining clusters controlled the path of further analysis. If this number was ≥ 2 the event was considered a possible $\Xi^0 \rightarrow \Lambda\pi^0$ decay with both γ rays hitting the glass; only the two most energetic showers were

considered. If this number was ≥ 1 the event was considered a possible Ξ^0 decay with only one γ hitting the glass. In the 7.6 mrad data, about 20 % of the C2 triggers ended up with no useful showers in the lead glass, 30 % with one, 30 % with two, and 15 % with three, and the rest more than three. For the C1 triggers, ~25 % had none, and 50 % one, whereas for the L triggers 45 % had none and all the rest one.

3.6.3 Use of chamber C7 data

The wire hits in chamber C7 were examined for each event in an attempt to find the x and y coordinates of any gamma ray passing through the scintillator - lead - chamber sandwich. A gamma ray passing through the thin lead sheet could cause a shower of charged particles which would appear in the chamber data. This could improve the position resolution of the gamma rays otherwise determined from the lead glass data alone. Quite often low energy wide-angle electrons produced in the shower caused large strings of wire hits (>25). There was no way of knowing where within these strings the parent γ ray actually passed. This effect was reduced by operating the chamber at a voltage lower than its plateau voltage (for minimum

ionizing particles). The following treatment was adopted in both x and y; x will be considered for definiteness. A region of width 4.3 cm on either side of the x value obtained from the lead glass clustering was examined for hits x_j in the C7 data. The lead glass array and the chamber were sufficiently close in z that there was negligible error introduced by this assumption. If no hits were found the γ position was taken directly from the lead glass data. When there was one hit, its value was taken. For more than one hit the quantities

$$\bar{x} = (1/N) \sum_j x_j \qquad (3.6.1)$$

$$\sigma^2 = (1/N) \sum_j (x_j^2 - \bar{x}^2) \qquad (3.6.2)$$

were formed, with the sums ranging over the hits within the window region. For showers with $\sigma^2 < 2.25\ cm^2$ the x value was set to $\bar{x}$. When $\sigma^2 > 2.25\ cm^2$ an attempt was made to split the hits into two disjoint regions separated by at least 9 contiguous wire-spacings where there were no hits, and $\bar{x}$ and σ^2 were redefined for these sub-regions. The procedure was repeated if possible if σ^2 were still > $2.25\ cm^2$. If such a division was impossible $\bar{x}$ was set to the lead glass value and the chamber data were ignored.

3.6.4 Use of chamber C3 data

Scintillator-lead sandwiches covered the upper and lower thirds of the active area of chamber C3. The middle third shadowed the analyzing magnet aperture, through which charged particle tracks had to pass to be momentum-analyzed. The scintillators vetoed any charged particles passing through them, so any hits in the chamber in regions behind the lead were associated with showers from neutrals passing through it. The wire hits in these regions were clustered into disjoint two-dimensional spatial regions. Since there were three planes of signal wires in this chamber (x, y, u), hits could be spatially located unambiguously, and without confusion with hits due to the proton or pion from $\Lambda \rightarrow p\pi^-$ decay. For each of these showers the center-of-gravity in x and y was also found. They were each considered as possible gamma ray showers. Events with one or more shower in C3, and one or more shower in the lead glass were considered as possible $\Xi^0 \rightarrow \Lambda\pi^0$ candidates with one gamma hitting the glass, and the other converting in C3 (and not passing through the magnet aperture). About 55 % of typical C1 triggers had no showers here, 25 % one, and 15 % three; 80 % of the C2's and 90 % of the L's had none.

3.6.5 Measurement resolution

The measurement errors were required for use in the kinematic fitting.

1. The 2 mm spacing of the signal wires of the MWPC's corresponded to a measurement of the spatial position of a charged particle within a root-mean-square (RMS) deviation σ=0.057 cm.

2. Errors associated with the energy and position measurements from the lead glass data were obtained from the electron calibration tapes.

   The spatial resolution in the lead glass was obtained from the widths of the distributions of $(x_s - x_g)$ and $(y_s - y_g)$, for electrons reconstructed in the spectrometer, where the subscript "s" denotes values from the spectrometer data, and "g" those from the lead glass data. Values of about 2.3 cm in x, and about 2.2 cm in y, were obtained for the FWHM's. Similar values were obtained using π^-'s from beam Λ's. The value σ=2.4 cm

was used for each error, where 2σ was the FWHM, since the precise values were not important.

The energy resolution of the whole lead glass array was found to be consistent with $\sigma = 0.32\sqrt{E(\text{GeV})}$, from the width of the distribution of $(E_s - E_g)$. This was the error used. There was also a long non-Gaussian tail in the distribution at high E, corresponding presumably to energy leaking out of the sides and back of the array (12 radiation lengths in depth). The value was actually found from the FWHM of the distribution $(E_g - E_s)/\sqrt{E_s}$, which should have a half-width k related to σ, according to the assumption $\sigma = k\sqrt{E}$. The FWHM of the distribution of E_g/E_s, for all electrons with momenta ≤ 30 GeV/c, was 16%.

3. For γ ray positions obtained from chamber C3 or C7 data, the corresponding σ value was used, although there was no direct experimental check of its value possible. These values ranged from 0 to 1.5 cm with about half in the 0-0.1 cm range. By examining the strings of hits in chamber C7 due to

electron conversions in the lead, and comparing with the projected tracks, the resolution was found to be about 0.7 cm in x and 0.4 cm in y. (There were usually 1-6 hit wires per string, in a range 0-1.6 cm). About 55% of the γ's in the lead glass achieved further spatial resolution from the C7 data (in x and/or y); about 45% ended with σ =2.4 cm in both x and y.

3.6.6 Kinematic fitting

The measurements of the momenta of the charged particle V, $\vec{p}_{p}$ and $\vec{p}_{\pi^-}$, with the γ ray position and (possibly) energy measurements, together with values for the probable errors in them, were used in an over-constrained kinematic fit to the hypothesis that the V and the two γ-like showers satisfied the decay chain:

$$\begin{aligned} \Xi^0 &\rightarrow \Lambda\,\pi^0 \\ \Lambda &\rightarrow p\,\pi^- \\ \pi^0 &\rightarrow 2\gamma \end{aligned} \qquad (3.6.3)$$

with the initial Ξ^0 having been formed at the production target. This used all the measured quantities, while constraining the parameters to satisfy the kinematic conservation equations appropriate to the above chain. The number of constraints is the number of measured values

minus the number of free parameters. This is 3 in the case of a Ξ^0 decay in which both γ energies are measured in the glass, and 2 if only one energy is measured. The Λ fit information from the original vee reconstruction had been carried through, but now the proton and charged pion momenta were allowed to vary within their known error ranges and the Λ mass forced as a constraint on the $\Lambda \rightarrow p\pi^-$ decay. The fit involved the minimization of a chi-squared function (χ^2) constructed to satisfy these requirements.

The chi-squared used in the Ξ^0 reconstruction was complicated by the number of parameters and constraints determining Eqs. (3.6.3). First, this fit was performed <u>without</u> constraining the gamma-ray energies (if they were known from the lead glass data), and obtaining the energies <u>from</u> the fit. This allowed the Ξ^0-events reconstructed here to be used for a direct calibration of the lead glass using actual γ rays from π^0 decays. The programs processed tapout tapes, identified topological candidate Ξ^0 decays through such a fit, and wrote the identical information from the tapout tape onto a second-stage data summary tape, called a "1C-Tape", for such candidates. This was a considerable reduction in the volume of data to be analyzed, typically by a factor of about eight, as these tapes contained only candidate Ξ^0 events. The program's

output for each tape included a set of 70 calibration constants obtained in an analogous way to those from the e^+e^- calibration, but here forcing the $\pi^0 \rightarrow 2\gamma$ decay constraint and starting from the e^+e^- calibration constants, and replacing E_S with E_{FIT} .

A typical 7.6 mrad tapout tape, containing about 50 000 vees, yielded about 7500 1C Ξ^0 candidate events, about 4000 1G's and 3500 2G's.

3.7 Final Lead Glass Calibration

The electron calibration procedure was the ideal way to obtain the calibration constants which should be used for calculating the shower energies from γ rays from π^0 decays (since the shower development should be independent of whether the incident object was an electron or a photon). However, these values can change over the course of an experiment like this one, which lasted several weeks, due to gradual changes in the properties of the lead glass + phototube + ADC system (e.g. due to radiation damage in the lead glass), or sudden transitions (e.g. due to replacement of a broken unit). The 1C Ξ^0 event calibration provided a continuous monitor of these effects, at least for those blocks which had a sufficiently large number of

γ ray hits per run. The set of calibration constants resulting from this approach agreed with that from the electron calibrations, where the sets overlapped in time. Since they were obtained from γ rays directly, they better monitored the more important blocks (the γ's of interest being there). The run-by-run IC values exhibited larger statistical fluctuations than the electron calibration constants, since there were fewer Ξ^0 events on a Ξ^0-trigger tape than there were e^+e^- pairs on an electron calibration tape. To enhance the reliability of the values of the IC calibration constants, and check their consistency with the electron values, the IC values were connected with information from the light pulser system attached to the lead glass blocks.

3.7.1 Use of the light pulser information

The light pulser system provided an independent continuous monitor of the gain of the lead glass + phototube + ADC system, for each block in the array. The ADC signals from the lead glass blocks were written into the scaler records between spills during the data-taking, alternate records being fed with the light pulser responses and the ADC pedestal values. For the light pulser signals in a particular block, x_i, where i labels the scaler record

(spill), the quantities

$$\bar{x}=(1/N)\sum_i x_i \qquad (3.7.1)$$

$$\sigma = ((1/N)\sum_i (x_i^2) - (\bar{x})^2)^{1/2} \qquad (3.7.2)$$

were formed. For a typical run there were about 200 to 300 spills, so the quantity

$$e=(1/\sqrt{N})\,\sigma/\bar{x} \qquad (3.7.3)$$

which measured the stability of the light pulser signal in a particular block over the run was typically $\leq$ 0.5%. Thus the light pulser was expected to be a good monitor of run-to-run gain changes. As long as the gain and behavior of the block+tube+ADC system remained unchanged the product of the light pulser signal and the calibration constant should remain constant for each block. An improved calibration constant for a particular block and run can be obtained from the expression:

$$C=(1/L)\langle L \times C\rangle \qquad (3.7.4)$$

where L is the mean light pulser signal over this run, and $\langle . \rangle$ denotes the mean over the <u>whole</u> experiment. This approach is valid as long as any time-dependent drifts inherent in the light pulser system have been removed, so any change in the signal is due to a gain change of the block + tube + ADC system rather than to the pulser itself. The 70 blocks were serviced by four light pulser bulbs, divided about equally amongst them, so that inherent light pulser fluctuations would appear as coherent changes in all the blocks serviced by a particular lamp. The overall

consistency of the system over the course of the data-taking also confirmed its utility. The output light spectrum of each of a sample of neon flash lamps was studied with a multichannel pulse-height analyzer before the experiment, and each lamp used was picked for its low noise and high stability characteristics. The resolution of each lamp used was better than 2% FWHM.

The details of the procedure will now be discussed.

The lead glass signals in the scaler records were examined for each block, spill, and run. There should have been alternate pedestals and light pulser signals, but occasionally one or the other might be missing, or otherwise bad.

Windows were chosen over which to average the signals in order to obtain a mean light pulser signal, for each block and each run.

Some blocks stopped operating or changed their operating characteristics suddenly during the experiment. Some blocks showed very weak light pulser signals to the extent that the pedestal-signal separation was unclear. Various alternative approaches were developed for these cases.

The light pulser signal distributions were generally non-Gaussian; although some were sharp and narrow, others were wide and flat, some had low tails, others high shoulders. The windows were chosen in order to obtain a reasonably accurate mean value. The low tails seemed to correlate directly with one of the lamps.

The signal due to the light pulser (above pedestal) was

$$S(i,j)=g(i,j)G(i)A(i) \qquad (3.7.5)$$

where

i labels the block (1,...,70),
j labels the run (1,...,133),
A(i)=the constant light pulser input,
G(i)=the constant gain of the system, and
g(i,j)=the time-dependent light pulser fluctuation.

The fluctuations g(i,j) depend on the particular lamp:

$$g(i,j)=g(k,j) \qquad (3.7.6)$$

for all blocks i serviced by lamp k (k=1,..,4). Thus 70j values were reduced to 4j values. Defining

$$\langle S(i)\rangle=\langle S(i,j)\rangle=(1/N)\sum(S(i,j)) \qquad (3.7.7)$$

where N=number of runs (=133), and

$$R(i,j)=S(i,j)/\langle S(i)\rangle$$
$$=g(k,j)G(i)A(i)/\langle S(i)\rangle \qquad (3.7.8)$$
$$D(i,j)=(1/N_b)\sum(S(i,j)/\langle S(i)\rangle)$$
$$=g(k,j)(1/N_b)\sum(G(i)A(i)/\langle S(i)\rangle \qquad (3.7.9)$$

where $\sum$ runs over the N_b blocks i on light pulser lamp k, the ratios

$$r(i,j)=R(i,j)/D(i,j) \qquad (3.7.10)$$

were formed.

In these ratios the g(k,j) factors cancel, and coherent light pulser effects have been removed from the light pulser signal S(i,j). (The ratios r(i,j) were denoted "L" in the earlier discussion).

For each block, and each run, there was an associated 1C calibration constant C(i,j). The products C(i,j)r(i,j) were formed and these products fitted by straight lines: for a particular block i,

$$y(i,j)=m(i)x(j)+c(i) \qquad (3.7.11)$$

where

y(i,j)=C(i,j)r(i,j), and
x(j)=time-dependent variable
=index of run (=1,...,133).

The linear fit was justified by its simplicity and by the fact that the first order time variation was satisfactorily removed in this way.

This resulted in a set of 70 pairs (m(i),c(i)) which carried the calibration information. The calibration constant for block i during run j was then <u>defined</u> by

$$C'(i,j)=(m(i)x(j)+c(i))/r(i,j). \qquad (3.7.12)$$

This procedure was quite successful, convenient, and consistent. It enabled the calibration constants to be interpolated between the electron calibration runs, and consistently tied to the 1C values where they existed from the 1C Ξ^0 fits.

3.8 2nd Stage Ξ^0 Reconstruction

With the calibration constants known for each block and run, the full-constraint kinematic Ξ^0 fit was performed. This is a 3C-fit for the Ξ^0 events in which both γ rays are detected in the lead glass. The fit was identical to that at the 1C level except for the constraints on the measured γ energies. If a particular event showed ≥ 2 showers in the lead glass, and ≥ 1 in chamber C3, both the 1G and 2G hypotheses were tried. The two largest showers in the glass were used for the 2G attempt, and the largest one together with each of the possible showers in C3 for the 1G. The resulting parameters from each fit were saved, and at the end the combination with the lowest χ^2 chosen to be the correct one. This approach was generally unambiguous; ~70 % of the 1G events only had one satisfactory shower in the chamber anyway. From the fit resulted several parameters associated with each Ξ^0 event, (obeying all the

conservation equations appropriate to Eq. (2.5.3)),

1. Final state momenta for $p, \pi^-, \Lambda, \pi^0, \gamma_1, \gamma_2$;

2. Ξ^0 decay vertex position $(x, y, z)_\Xi$;

3. Two chi-squared values, χ^2_Λ and χ^2_Ξ. χ^2_Λ described how well the p and π^- obeyed the $\Lambda \rightarrow p\pi^-$ hypothesis, and χ^2_Ξ described how well the Λ, with the γ data satisfied the $\Xi^0 \rightarrow \Lambda\pi^0$ hypothesis.

These fitted momenta were used in the subsequent polarization analysis. This information was written onto a third level of summary tape, called a "3C-Tape", or "Outdat" tape. The original Ξ^0 data on 111 raw-data tapes now filled six tapes. These data were subjected to the polarization analysis.

3.9 Event Parameters and Event Selection

3.9.1 Trigger samples

An important part of the data analysis of a high-statistics experiment is the clarification of the data sample - an understanding of its purity and contamination by backgrounds. "Background" events are those arising from sources other than the intended one (the production target). It is particularly important to understand these events in an experiment in which polarization or yields are being studied, since they are an unwanted confusion of the process under investigation and cause errors in the results.

To ensure that these backgrounds were kept to a satisfactorily low level during the data-taking, interspersed through the experiment data runs were taken without a target in position. Any events collected during these "empty runs" must come from the background sources. Various effects could contribute to the magnitude of such contamination, the most important one being mis-steering of the incident proton beam onto the production target in such

a way that a proportion of the data were produced from material other than the target (e.g. the collimator walls, magnet coils, etc.).

In fact these backgrounds were kept to an acceptably low level, so that their contribution to the final data sample, and their effect on the polarization results, were negligible. (At 0 mrad this background contribution to the Ξ^0 yield was about 10-12 %, but was only ~1 % at 4 mrad, and decreased to <1 % at 10 mrad, before any cuts were applied).

In the accompanying figures various lambda and cascade event parameters have been plotted for comparison purposes. It is important to notice that in this experiment there were two independent samples of Ξ^0 events obtained. This is because the acceptances for the events with two gammas detected in the lead glass (called the "2G" Ξ^0 events), and those with one in the glass and one in chamber C3 (the "1G" events) were very different, and involved different biases. This was useful when checking the consistency of results from the samples. Also Λ trigger events were prescaled into the raw data so that Λ events were available throughout the experiment for continuous monitoring of the behavior of the apparatus. In particular this enabled comparisons to be made between Λ's from Ξ^0 decays and

those in the original neutral beam (called "beam Λ's" for convenience).

3.9.2 Parameter distributions

Typical decay vertex distributions for beam Λ's and daughter Λ's from the 1G and 2G Ξ^0 samples are shown in Fig. (3.9.1). The 1G and 2G relative normalization in these, and the succeeding, figures is arbitrary. The daughter Λ's clearly show the exponential decay characteristic of a parent-daughter two-step decay process of finite lifetime; this distribution is of opposite slope to that for the beam Λ's.

Fig. (3.9.2) presents typical 1G and 2G Ξ^0 vertex distributions, showing a one-step decay process modified by acceptance (integrated over momentum).

The Λ momentum distributions (Fig. (3.9.3)) show that, as expected, daughter Λ's tend to have lower momenta that beam Λ's.

The Ξ^0 momentum distributions show that the 2G Ξ^0's have higher momenta than those in the 1G sample (Fig. (3.9.4)). Again, this was expected as the 2G events

required both γ rays to be forward in the Lab, so that they passed through the aperture of the analyzing magnet, and this implies higher momentum for the parent Ξ^0's.

The invariant mass distribution of the ($\gamma\gamma$) pair is plotted in Fig. (3.9.5) for a 2G Ξ^0 sample. The FWHM of this sample is 30 MeV, most of which is due to the energy resolution of the lead glass. No background is evident in any of these distributions. The ($\Lambda\pi^0$) mass for typical Ξ^0 events is shown in Fig. (3.9.6). The 1G and 2G samples have similar widths, although the 1G sample has a sharper peak but longer tails than the 2G sample; this is because the π^0 mass has to be assumed in the invariant mass calculation for the 1G events. The mass resolution on the cascade invariant mass can be read from these histograms; the FWHM is 32 MeV. For comparison purposes the ($p\pi^-$) invariant mass distribution for beam Λ events is shown in Fig. (3.9.7). The FWHM is 3.2 MeV after a cut of $\pm 3\sigma$ (a σ calculated from the errors involved in the fit [24]) on the invariant mass. The resolution for the Ξ^0 events was limited by the energy resolution of the lead glass.

An informative parameter for use in investigations of sample purities is the "target-pointing parameter R_Λ^2". "Target-pointing" is the process of projecting the reconstructed Λ momentum vector back to the z of the

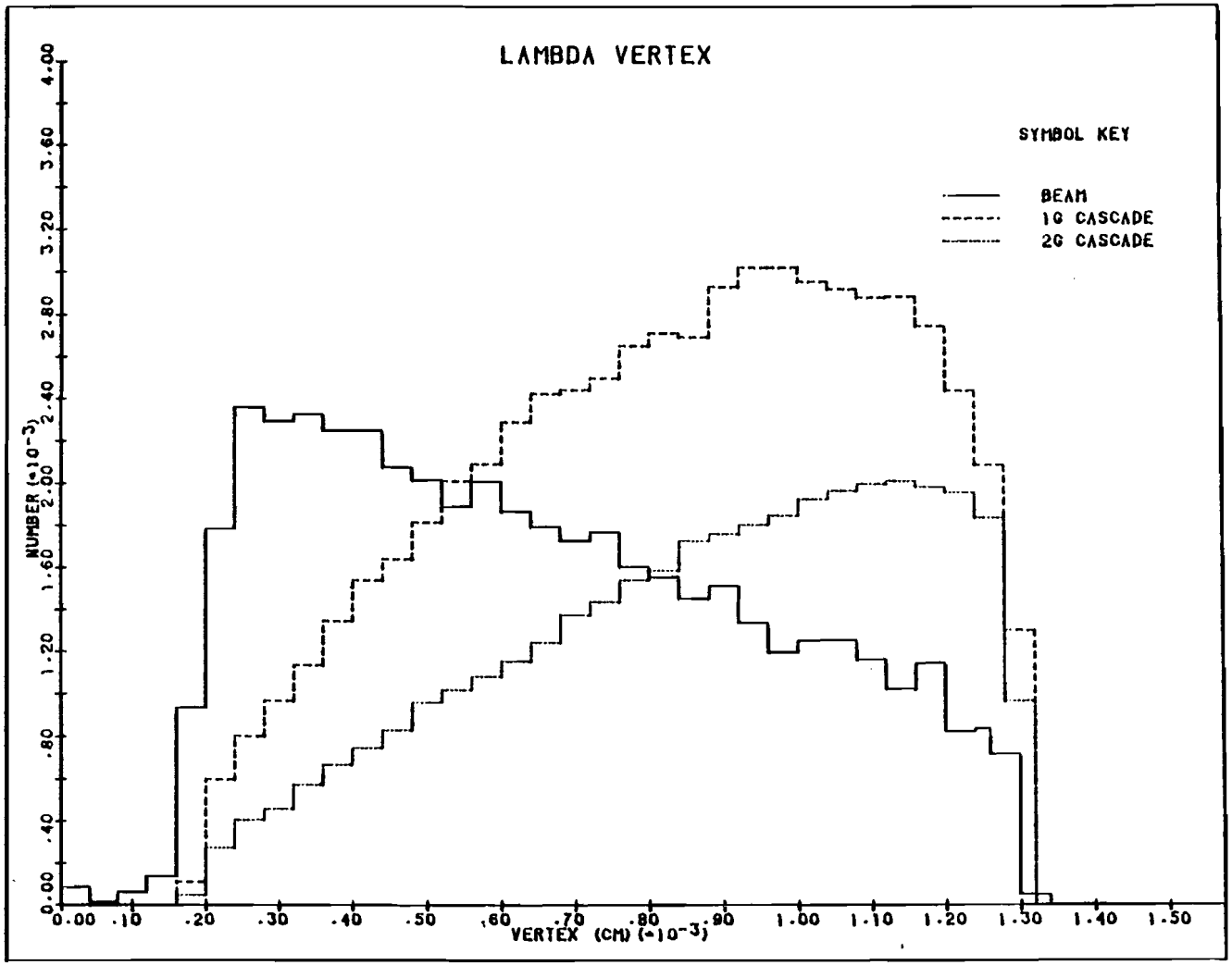

FIGURE (3.9.1) Λ vertex distributions for beam and daughter Λ's

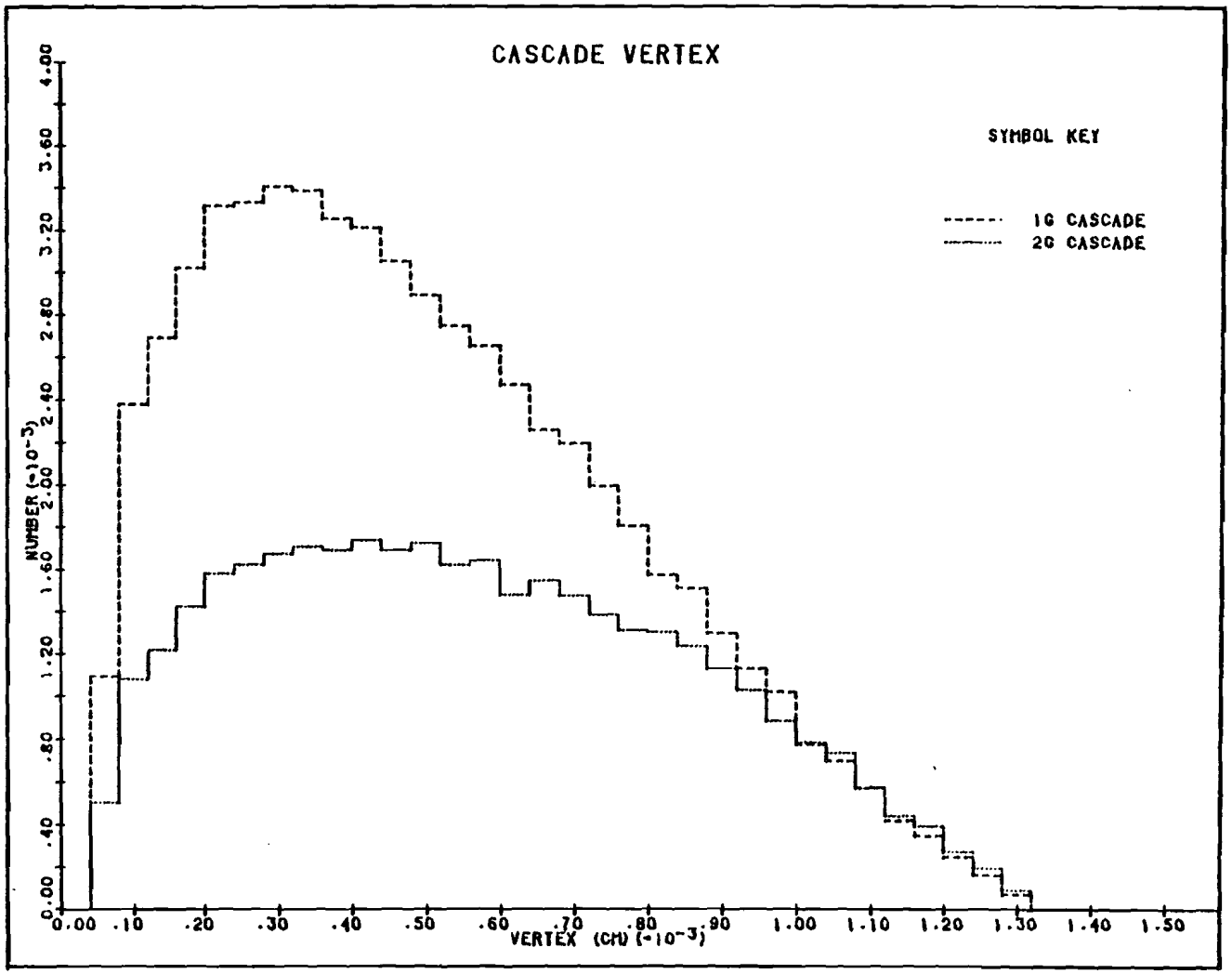

FIGURE (3.9.2) Ξ^0 vertex distributions

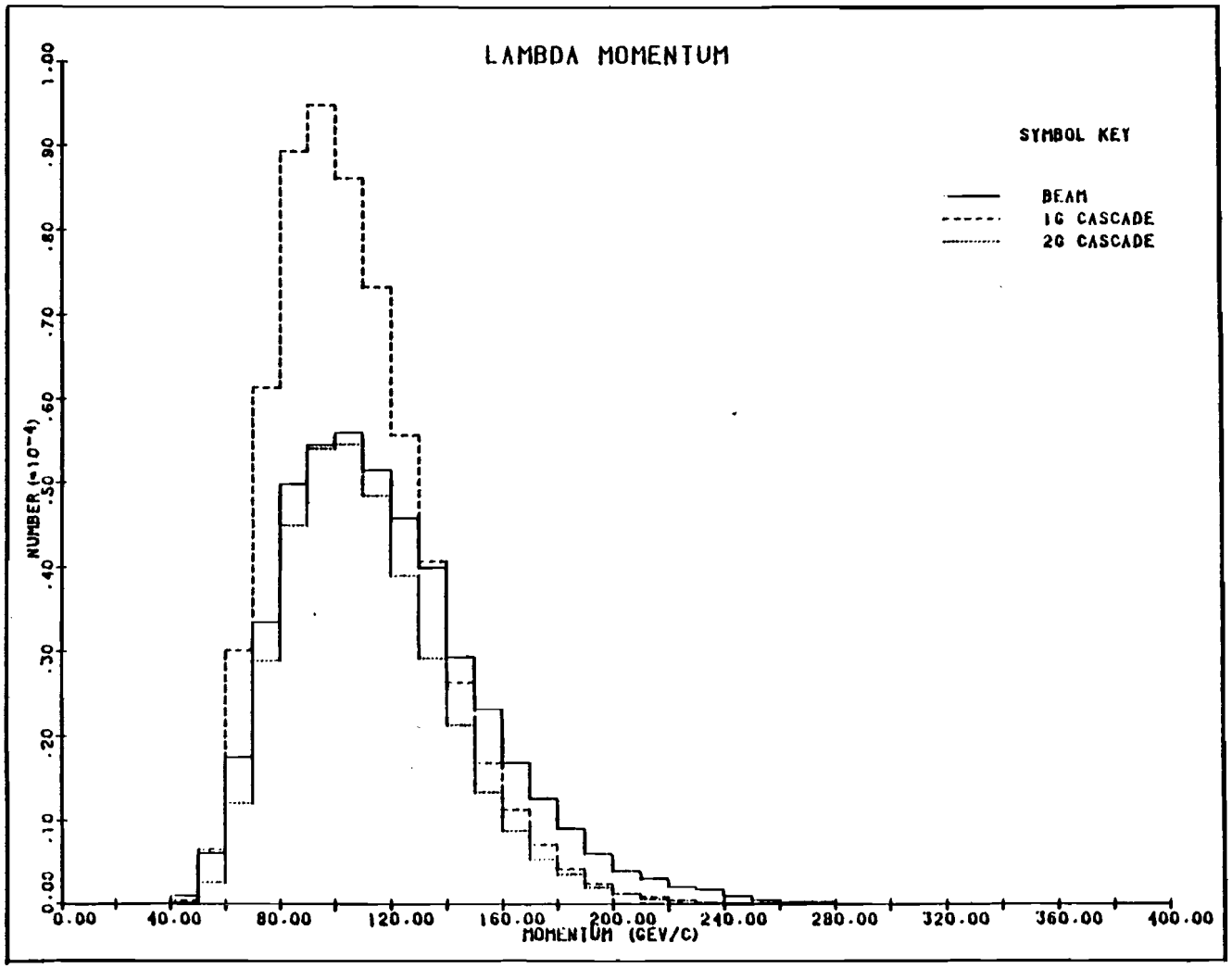

FIGURE (3.9.3) Λ momentum distributions for beam and daughter Λ's

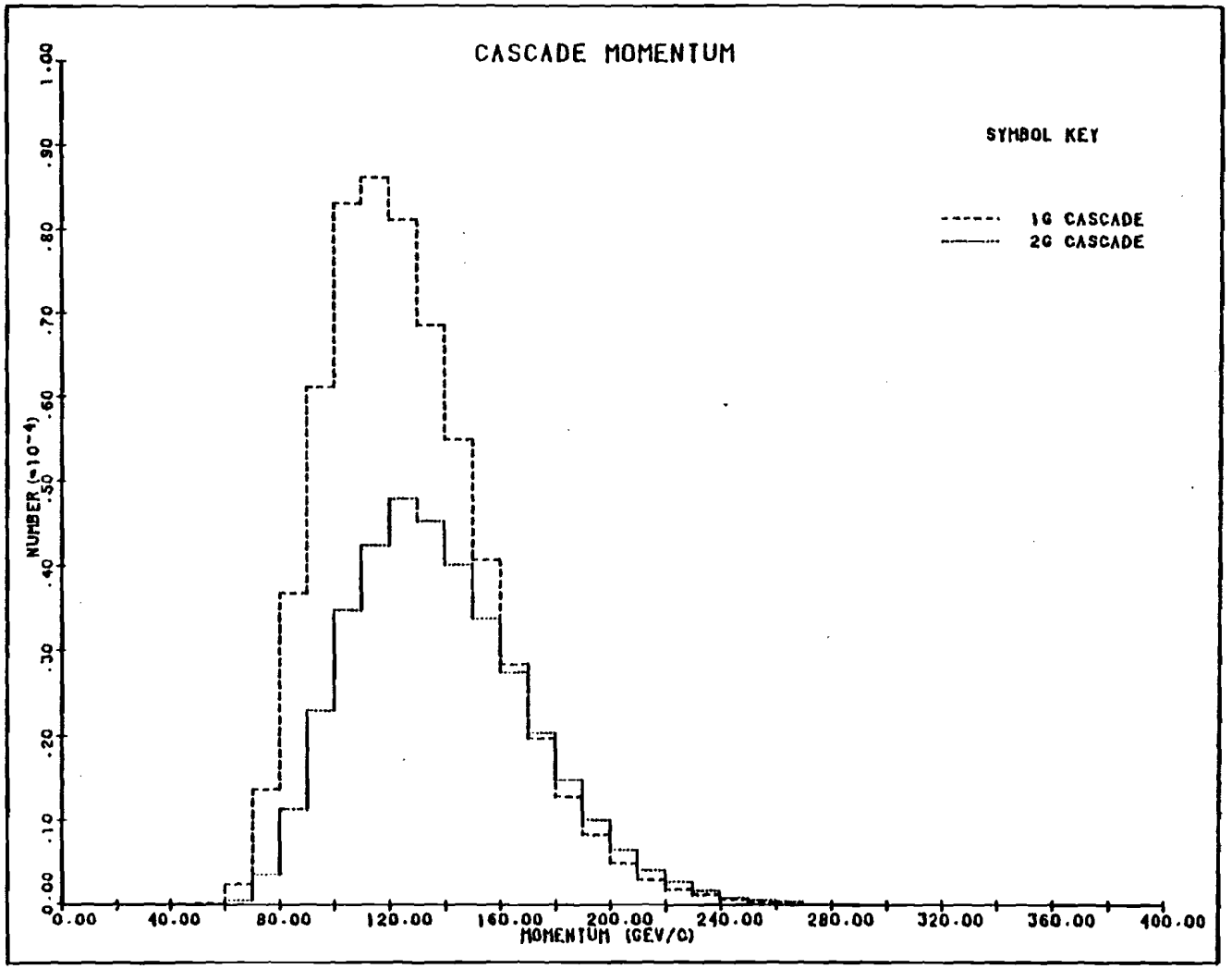

FIGURE (3.9.4) Ξ^0 momentum distributions

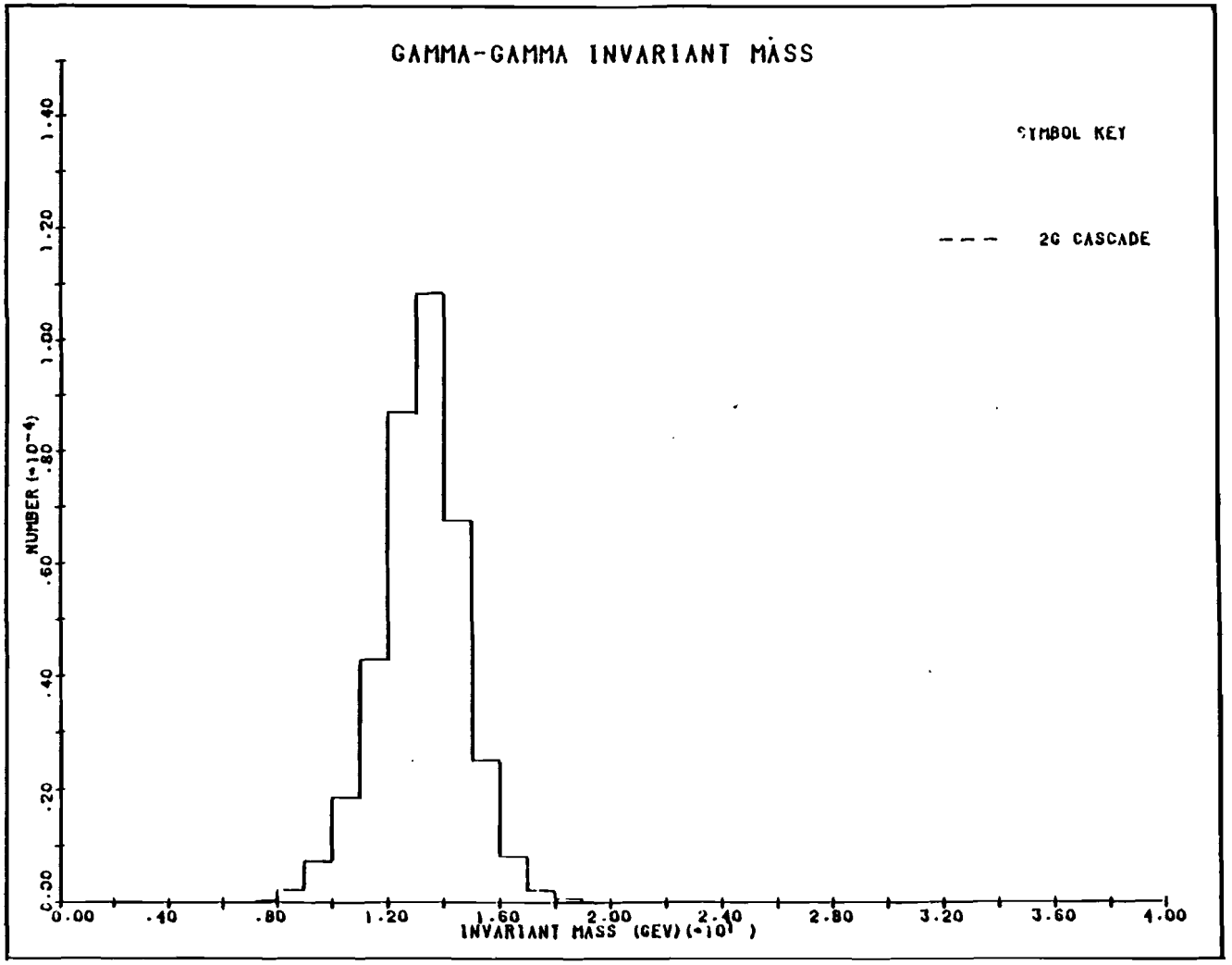

FIGURE (3.9.5) ($\gamma\gamma$) invariant mass for 2G Ξ^0's

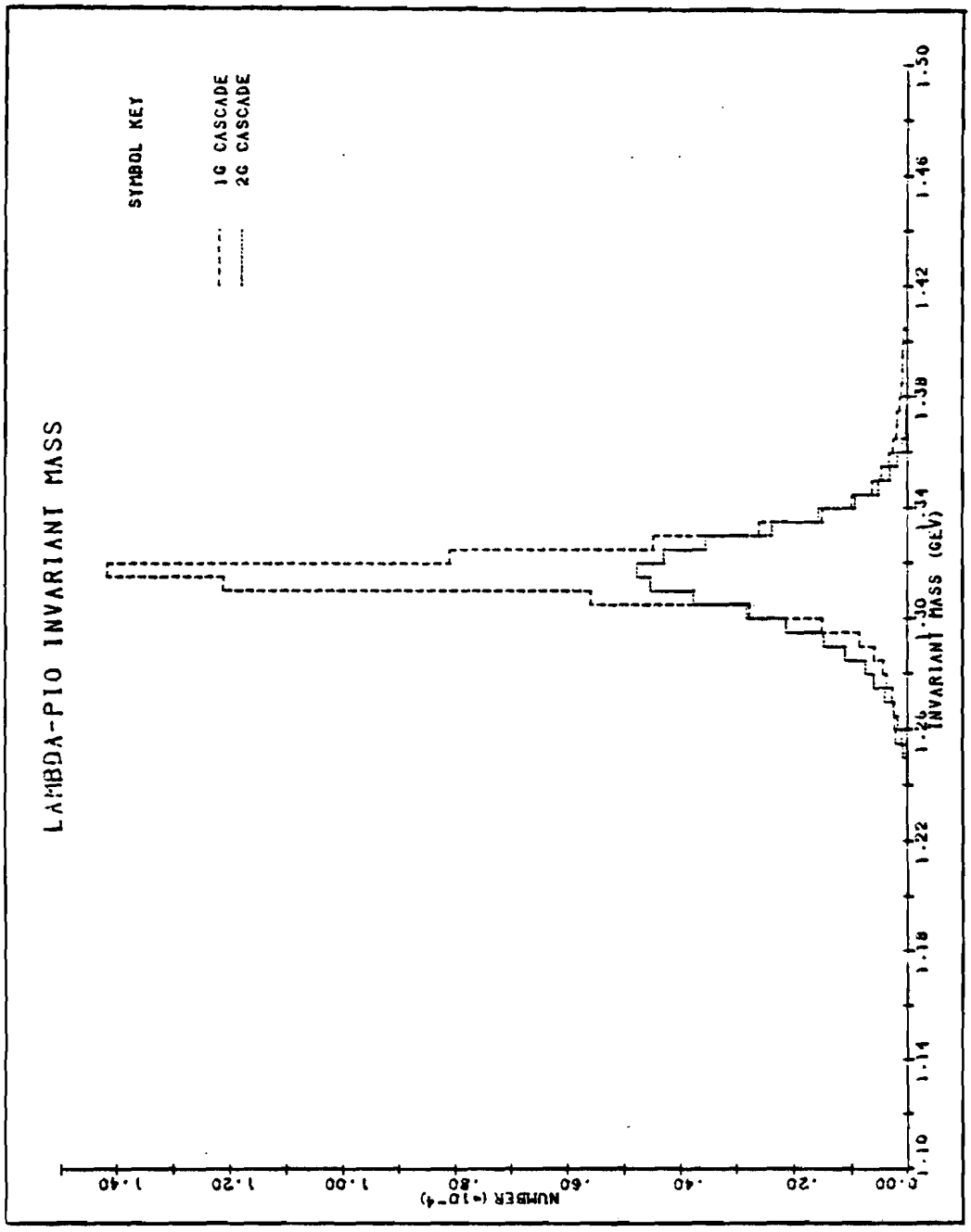

FIGURE (3.9.6) ($\Lambda\pi^0$) invariant mass for 1G and 2G Ξ^0's

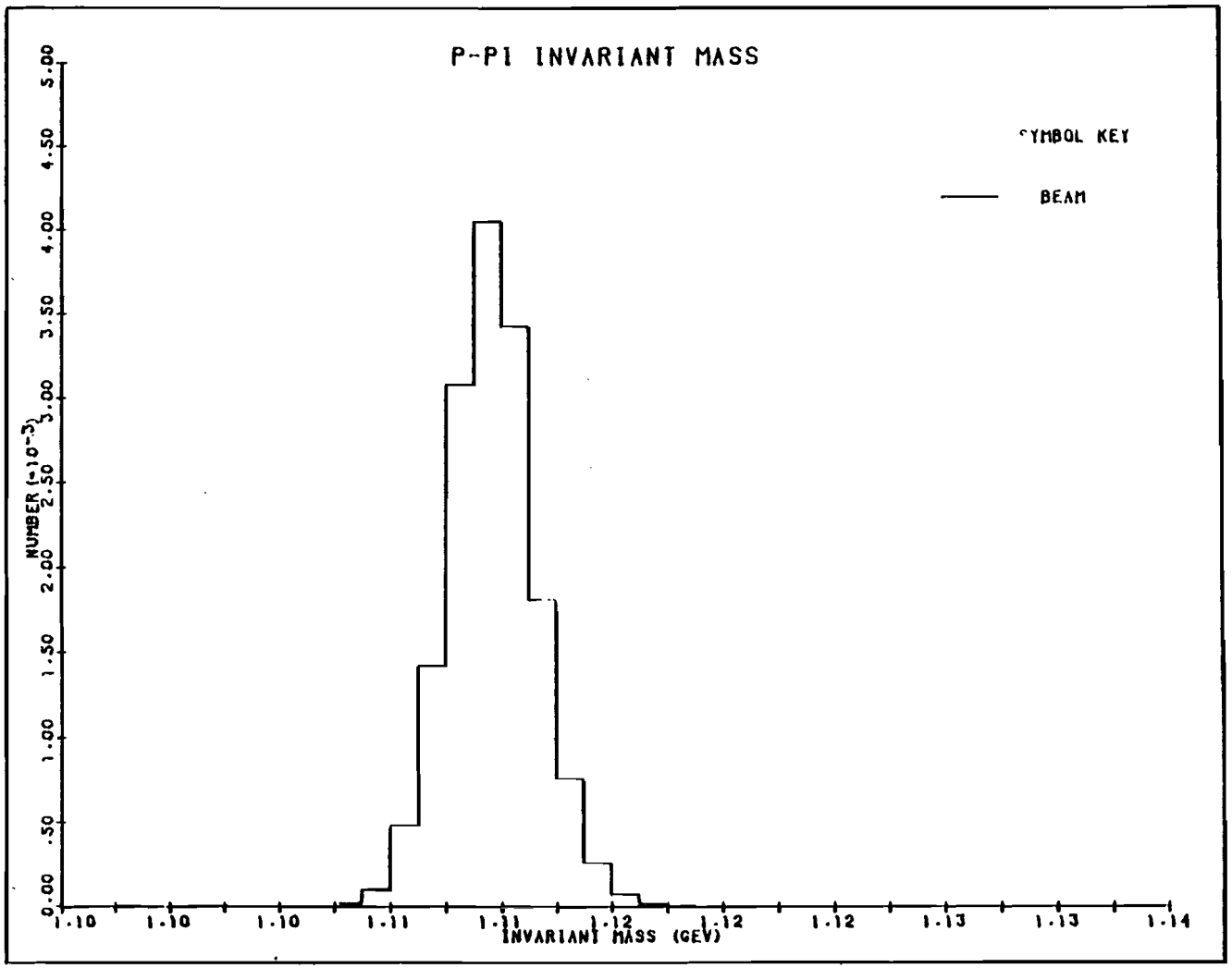

FIGURE (3.9.7) (pπ-) invariant mass for beam Λ's

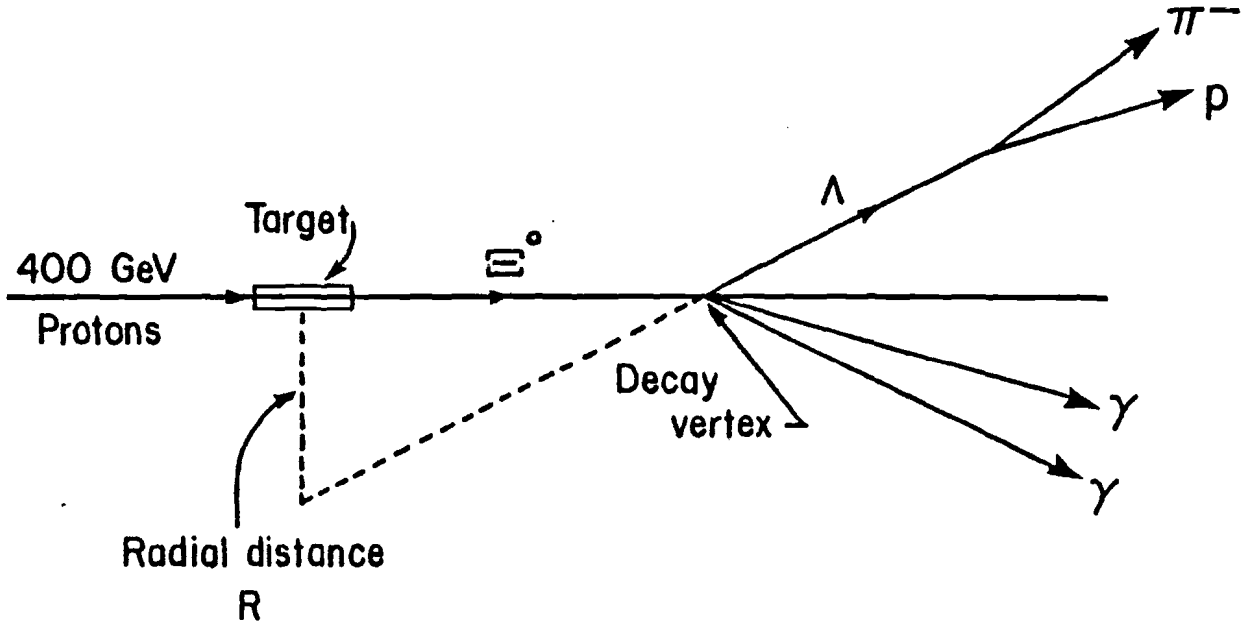

FIGURE (3.9.8) Definition of R_{Λ}^{2} parameter

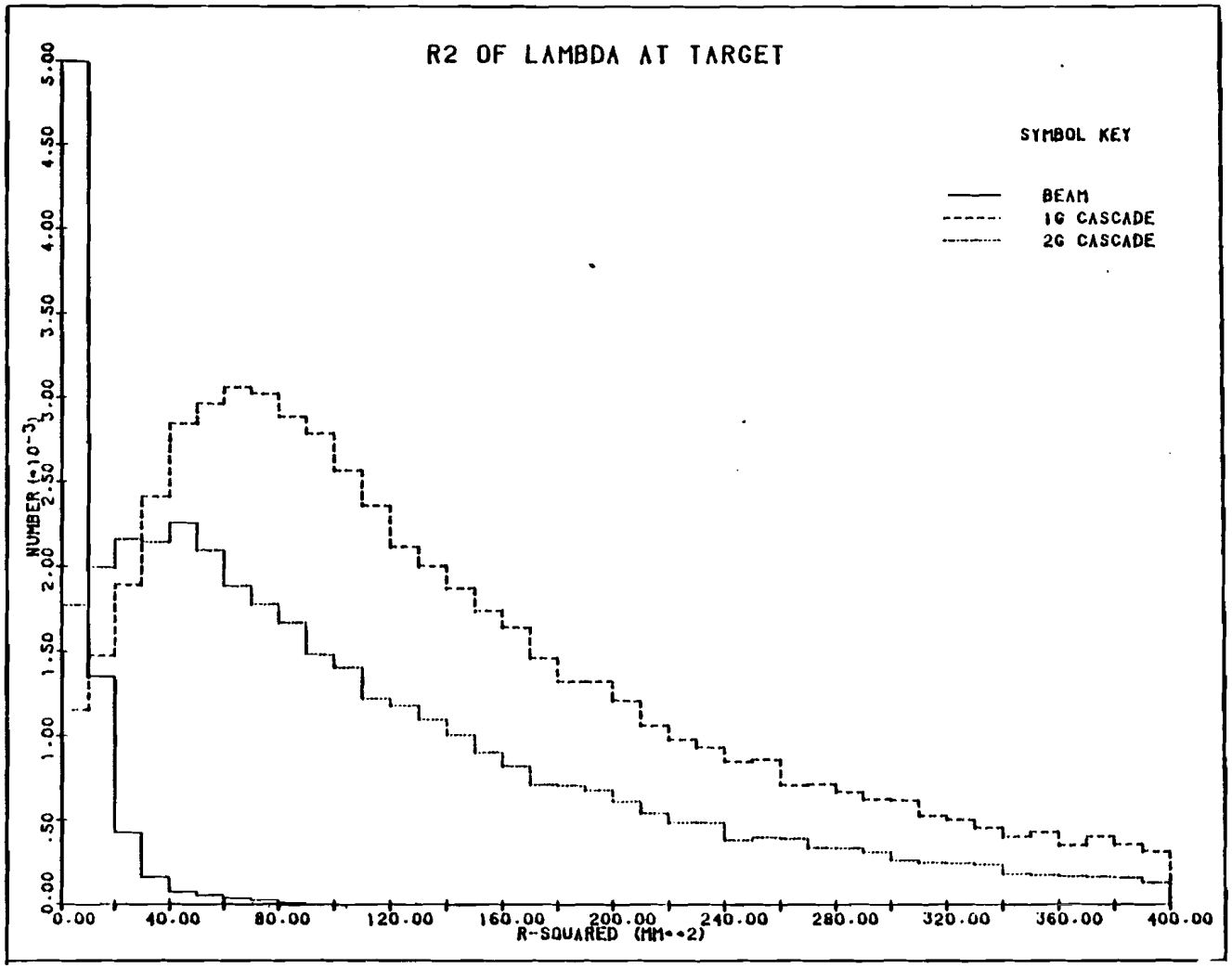

FIGURE (3.9.9) R^2_Λ at target distributions for beam and daughter Λ's

3.10 Choice of Final Data Samples

Before polarization analysis of the reconstructed Ξ^0 events, several cuts were applied to the data samples. A "cut" is some restriction in the range of possible values of a specific event parameter, which is applied in order to reduce unwanted backgrounds, or to define more precisely a particular sample of events.

3.10.1 Cuts

The cuts were chosen to be as "loose" (unrestrictive) as possible, but "tight" enough to remove events for which the subsequent analysis might be suspect. For example, Ξ^0 events with decay vertices too near the Sweeper were cut from the sample, because the magnetic field integral through which they had travelled was then not precisely defined. The set of cuts required that:

1. The Λ decay vertex was in the decay vacuum, i.e. lay between a value of z=190 and z=1300 cm;

2. The Ξ^0 vertex was outside the fringe field of the

Sweeper, i.e. at a z>60 cm;

3. The energy of any γ detected in the lead glass was $\geq$ 3 GeV;

4. The energy of any γ detected in chamber C3 was $\geq$ 1 GeV;

5. The spatial position of any γ in the lead glass was over 2 cm from the top and bottom edges of the array, and over 2 cm from the hole in the array.

6. The χ^2_C was $\leq$ 20 for 1G, and $\leq$ 30 for 2G, Ξ^0's.

These cuts were decided upon after detailed studies of their effects on the data, backgrounds, and Monte Carlo - generated events. Further cuts were additionally applied in some cases. A cut requiring the Λ momentum to be above 75 GeV/c was applied in investigations of the effects of low-momentum Λ's on the data (The spectrometer acceptance drops rapidly for Λ momenta below 100 GeV/c). For the 0 mrad data, a cut of $R^2_\Lambda \geq 30$ mm^2 was used to reduce the large background contamination there; a cut of $R^2_\Lambda \geq 20$mm^2 was used on the 2 mrad data. The data at other angles showed no evidence of backgrounds, so no R^2_Λ cut was required or applied.

Geometric cuts were made along the edges of all chambers and apertures during the polarization analysis itself, in order to eliminate regions where the detection or reconstruction efficiency was poor. The most sensitive one was that around the edges of the proton counter PC, since this was the limiting aperture on the proton acceptance. This cut eliminated about 5% of the Λ 's which would otherwise have been accepted. (The limiting aperture for π^-'s was the downstream Avis magnet aperture).

At various stages of the analysis tighter cuts were applied to investigate the stability of various results to the cuts used. These will be mentioned as appropriate.

3.10.2 Backgrounds

The χ^2_{3C} distribution was not that of a classical 3C distribution even for the 2G events, due to the possibility of systematic and non-Gaussian errors in the γ ray energy and position measurements. Some possible sources of such errors were:

- shower energy leaked out of the lead glass array (hole, back, or edges);

- the blanking procedure (for possible hadronic showers) blanked some blocks really comprising a γ shower;

- an incorrect position for a γ ray was chosen from the chamber C7 data;

- local miscalibration of the lead glass.

Misreconstruction of a Ξ^0 using an accidental γ-like signal (from e.g. hadronic showers or neutral beam interactions) might also occur. The Ξ^0-fit constrained the Ξ^0 to pass through the centroids of the beam Λ distributions at the production target and the defining aperture of the collimator, and this might not be the true physical situation. Furthermore a Ξ^0 might actually be produced by a Λ interaction within the collimator itself. These sources of possible backgrounds in the Ξ^0 events reconstructed will be discussed more quantitatively in Section (5.4).

The Ξ^0-trigger required the time-coincidence of two γ-like showers and a Λ-like vee detected in the spectrometer. If the trigger was not a Ξ^0, it was likely

that the Λ was produced in the target and the coincidence was accidental. This can be investigated by examining the R^2_Λ distributions of the Λ 's. In Figs. (3.10.1) and (3.10.2) are shown typical R^2_Λ distributions for Λ 's from Ξ^0 events with high χ^2_Ξ (low probability of being a Ξ^0), for Λ 's from Ξ^0 events with low χ^2_Ξ (high probability of being a Ξ^0), and for Λ 's from Monte Carlo Ξ^0 events. These should be compared with the typical R^2_Λ distribution of beam Λ 's shown in Fig. (3.9.9). The beam-like nature of the Λ 's in the high-χ^2_Ξ events is clearly demonstrated. By quantitative comparisons of the data with Monte Carlo results, these distributions could be used to obtain estimates of the accidental beam Λ background in the Ξ^0 sample.

3.10.3 Fool event background estimation

An alternative approach to obtaining a quantitative estimate of the background was actually followed. This involved the construction of artificial Ξ^0 events, called "Fool" events, by mixing the Λ data from one event with the γ data from another, using only real events with poor χ^2_Ξ. This information was fed through the Ξ-reconstruction programs, to obtain a sample of spurious

Ξ^0's. To increase the statistics of this sample the Λ data from each high χ^2_{Ξ} event were mixed, successively, with the γ information from the following three high χ^2_{Ξ} events. The events supplying the Λ and γ data to this procedure were presumably likely to be background triggers. Since in accidental coincidences there should be no correlation between the Λ and the γ signals, this method was expected to model them. The R^2_{Λ} distributions for Λ's from fool events and from Ξ^0 events with high χ^2_{Ξ} are shown in Figs. (3.10.3) and (3.10.4) ; they are very similar. This checks the correlation between R^2_{Λ} and χ^2_{Ξ}, and shows that the broad R^2_{Λ} distribution of the real events is not an artifact of the Ξ^0 fit. Figures (3.10.5) and (3.10.6) show the distributions of $\log(\chi^2_{\Xi})$ for real and fool events, after normalization so that they both have the same total number of events in the region $\chi^2_{\Xi} > 60.$ (1G), or 70. (2G). It is clear that the fool event distribution closely predicts the high χ^2_{Ξ} tail of the real data. With this normalization, the fool events provided a way of estimating the accidental backgrounds in the real data, by counting the number of fool events below the nominal χ^2_{Ξ} cuts (20 for 1G, 30 for 2G) used to define the samples.

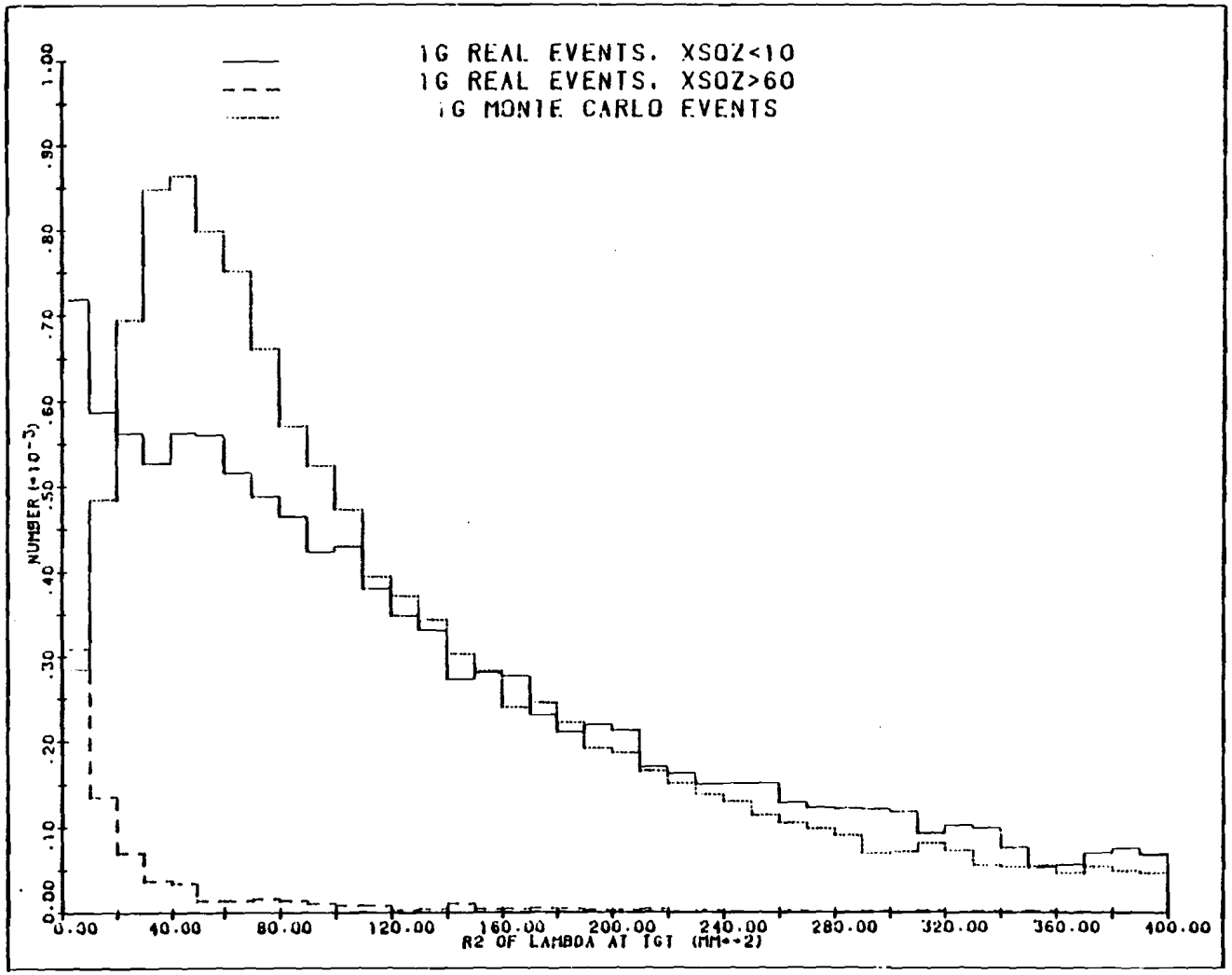

FIGURE (3.10.1) R_{Λ}^{2} for high and low χ_{Ξ}^{2} and monte carlo 1G Ξ^{0}'s

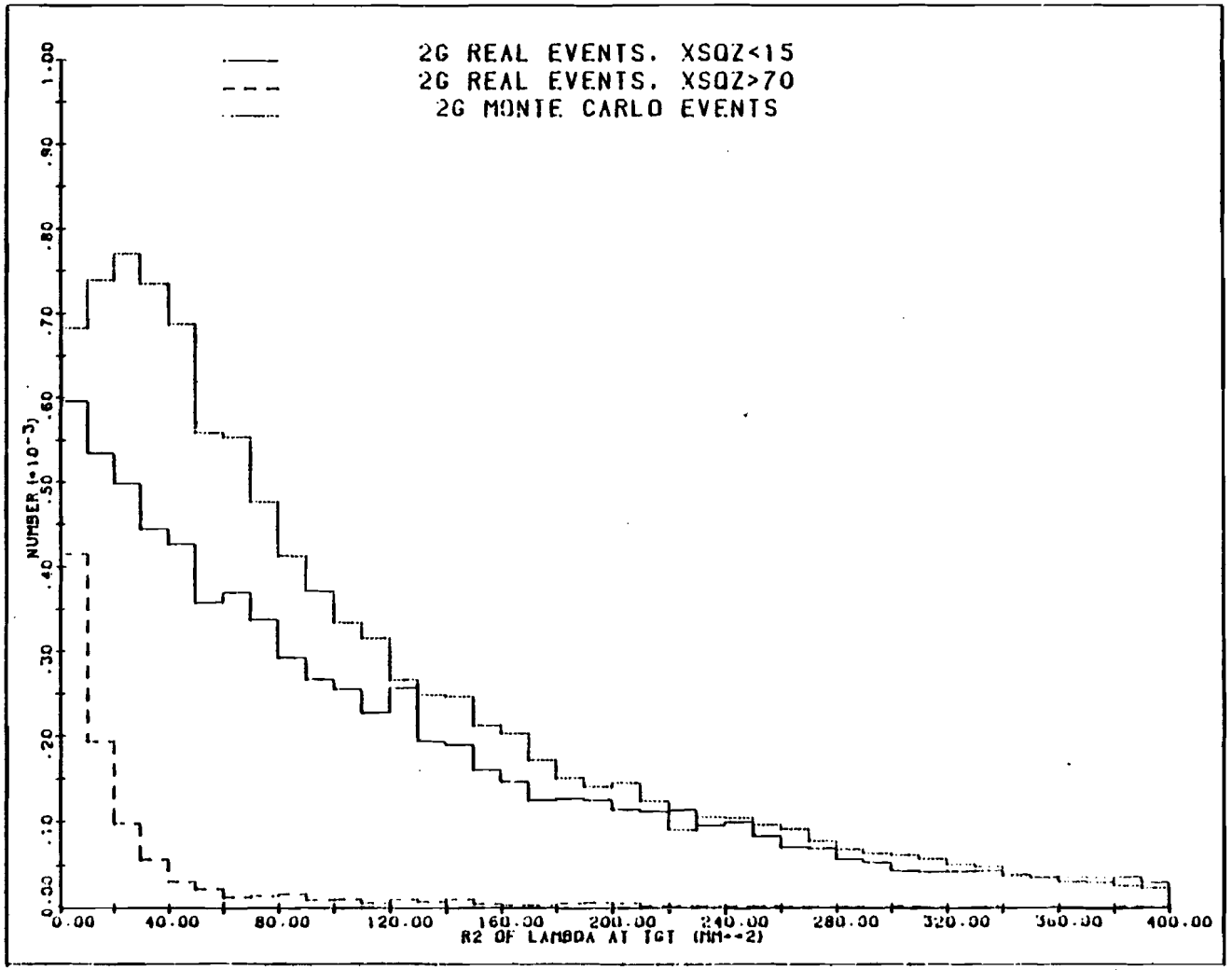

FIGURE (3.10.2) R_{Λ}^2 for high and low χ^2_{Ξ} and monte carlo 2G Ξ^0's

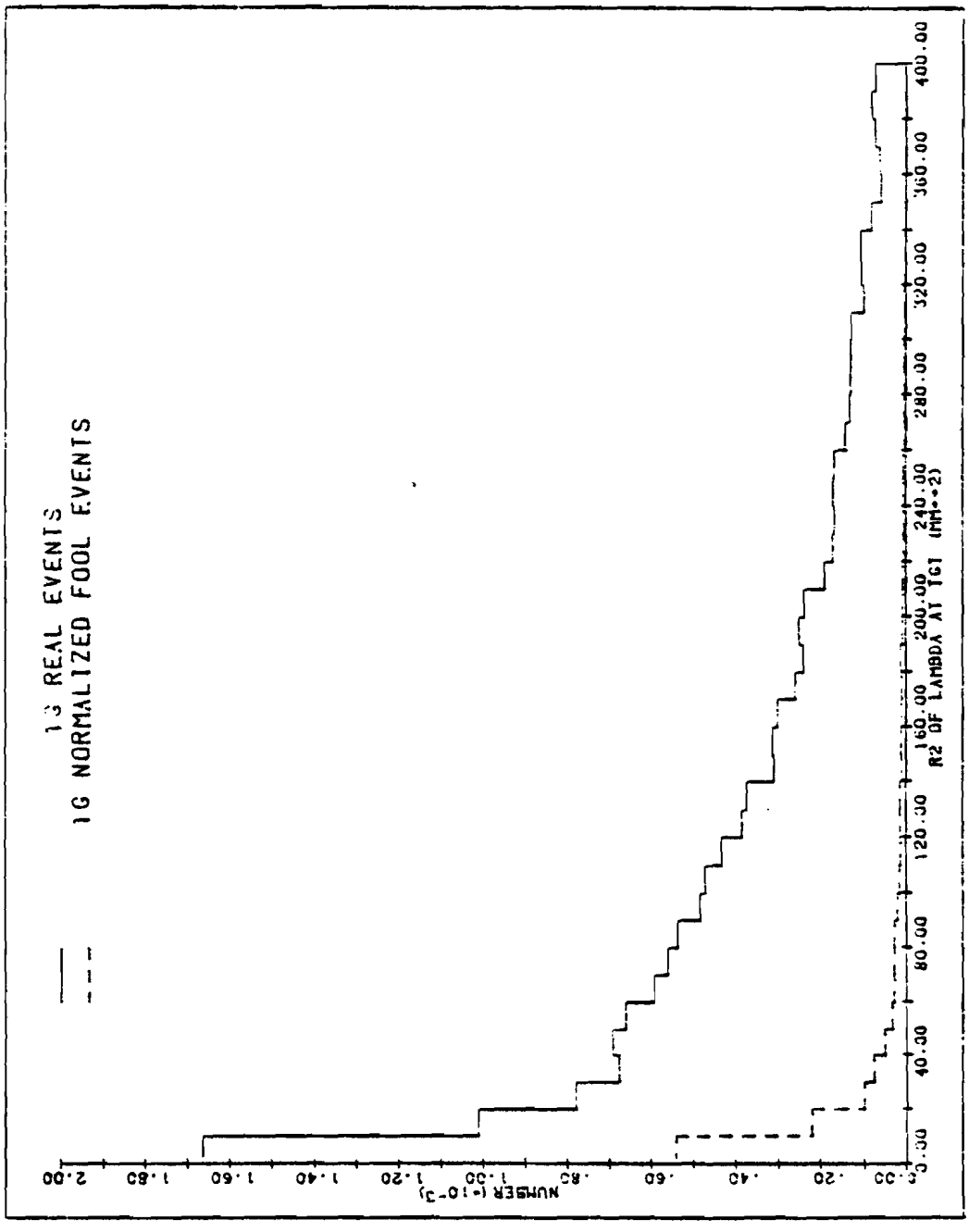

FIGURE (3.10.3) R^2_Λ for real and normalized fool 1G Ξ^0 events

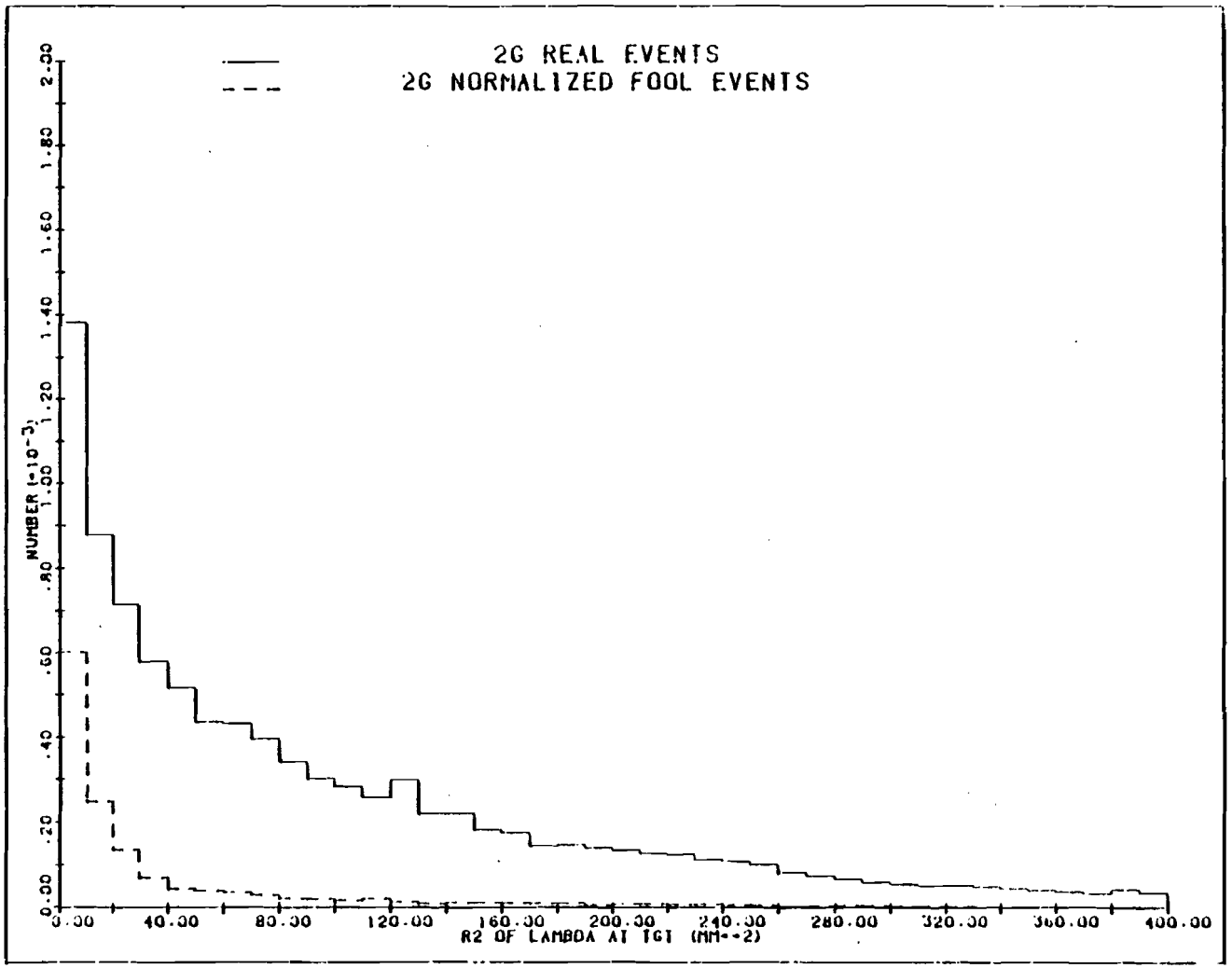

FIGURE (3.10.4) R^2_Λ for real and normalized fool 2G Ξ^0 events

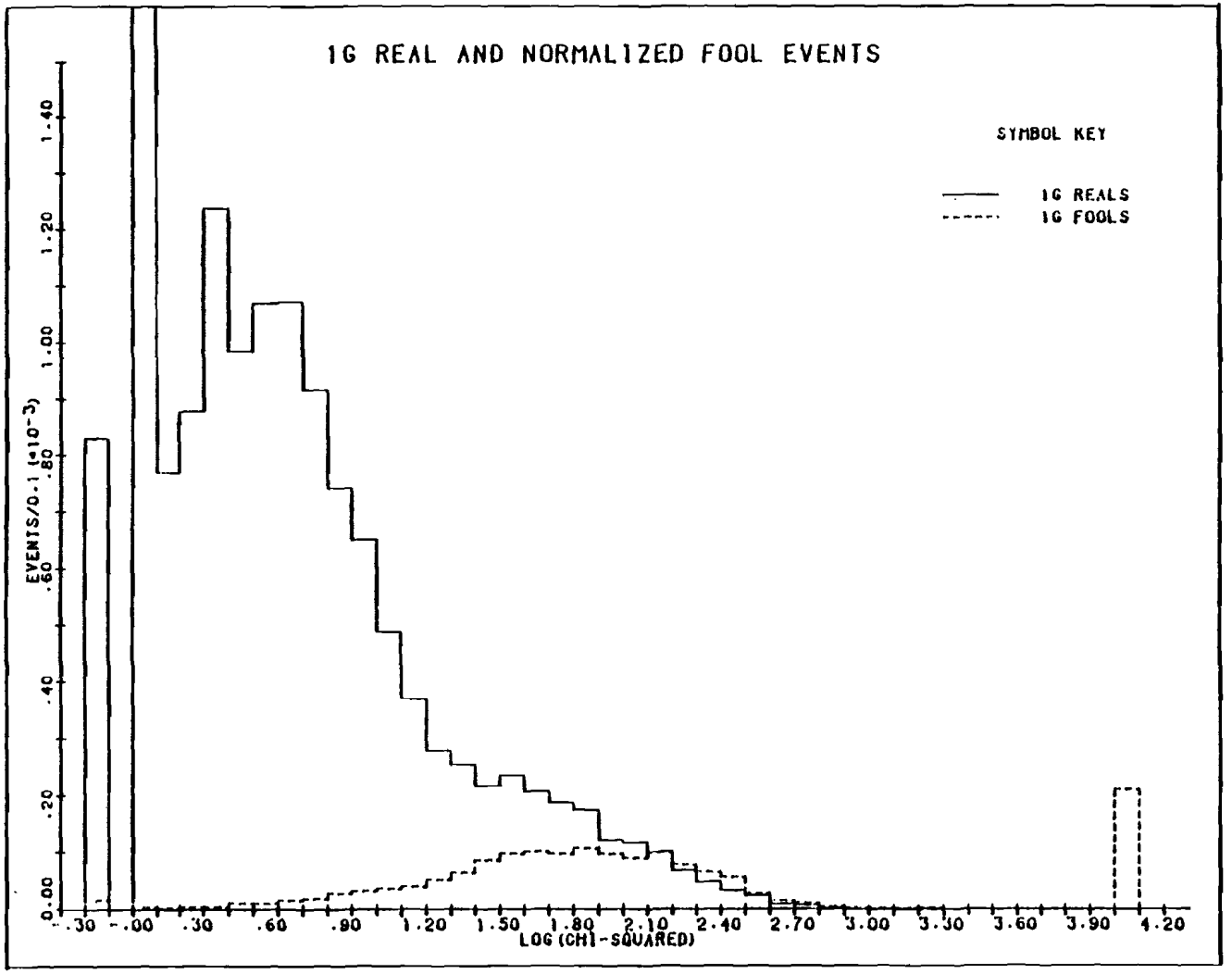

FIGURE (3.10.5) Log($\chi^2_{\Xi^0}$) for real and normalized fool 1G Ξ^0 events

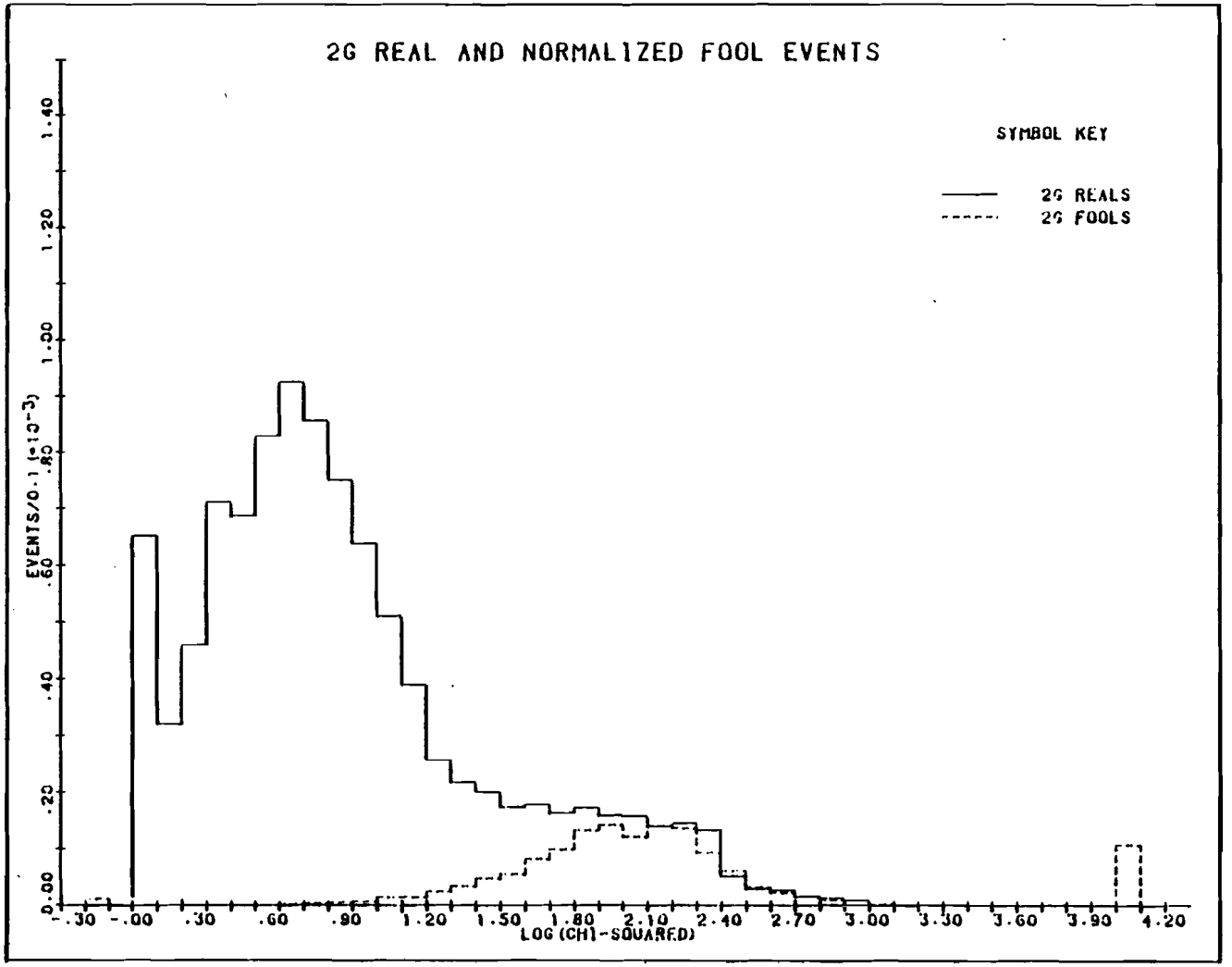

FIGURE (3.10.6) Log(χ^2_{Ξ}) for real and normalized fool 2G Ξ^0 events

CHAPTER 4

DATA ANALYSIS II: POLARIZATION ANALYSIS

4.1 Λ Polarization - Theoretical

The $\Lambda \rightarrow p\pi^-$ decay mode typifies the decay process of the type

spin 1/2 $\rightarrow$ spin 1/2 + spinless (4.1.1)

In such a decay the two-particle final state can have one of only two possible orbital angular momenta, with L=0 (S state), or L=1 (P state). The decay is completely described by the amplitudes s, p for the final state to be in the S, P states respectively. In expressions for decay rates, and transition amplitudes, the following combinations often occur:

$$\alpha = \frac{2\,\mathrm{Re}(s^{*}p)}{|s|^2+|p|^2}$$

$$\beta = \frac{2\,\mathrm{Im}(s^{*}p)}{|s|^2+|p|^2} \qquad (4.1.2)$$

$$\gamma = \frac{|s|^2-|p|^2}{|s|^2+|p|^2}$$

and $\alpha^2 + \beta^2 + \gamma^2 = 1$ (4.1.3)

These α, β, and γ are called the "decay parameters" for the process. The spin state of the daughter spin 1/2 particle is determined by these parameters.

For the decay (4.1.1) the distribution of either daughter particle in space is related to the polarization of the parent through an equation

$$\frac{dn}{d\Omega} = k\,(1 + \alpha P \cos\theta) \qquad (4.1.4)$$

where

n = no. of daughter particles (either one),

Ω = solid angle,

α = α decay parameter,

P = parent polarization,

θ = angle between direction of polarization and daughter momentum direction (see Fig. (4.1.1)),

k = normalization constant (e.g. requiring $\int dn = 1$ implies $k=1/(4\pi)$).

All these values are referred to the rest frame of the parent. For the case of $\Lambda \rightarrow p\pi^-$,

$$\frac{dn(p)}{d\Omega} = k(1 + \alpha_\Lambda P_\Lambda \cos\theta) \qquad (4.1.5)$$

with $\text{Cos}\,\theta = \dfrac{\vec{P}_\Lambda \cdot \hat{p}}{P_\Lambda}$

where $\vec{P}_\Lambda$ is the Λ polarization, and $\hat{p}$ is the unit proton momentum vector [25,26]. Integration over the ϕ variable gives

$$\frac{dn}{d\theta} = k(1 + \alpha_\Lambda \vec{P}_\Lambda . \hat{n}\ \hat{n} . \hat{p}) \qquad (4.1.6)$$

where $\hat{n}$ is a unit vector in any arbitary direction, and $\text{Cos}\,\theta = \hat{n} . \hat{p}$. This is only approximately true in practice because the acceptance may depend slightly on ϕ. Thus if α_Λ and P_Λ are non-zero (α_Λ is known to be ~0.65), there will be an asymmetrical proton (or pion) distribution in space, relative to (any) direction $\hat{n}$. If $\hat{n}$ is chosen successively as the x, y, and z axes then the components of $\vec{P}_\Lambda$ along these axes can be found. This is the convenient "self-analyzing" property of the weak parity-violating $\Lambda \rightarrow p\pi^-$ decay mode. In practice this is not trivial because the acceptance of the detecting apparatus distorts the apparent spatial distribution of the protons, and this may mask the asymmetry due to polarization.

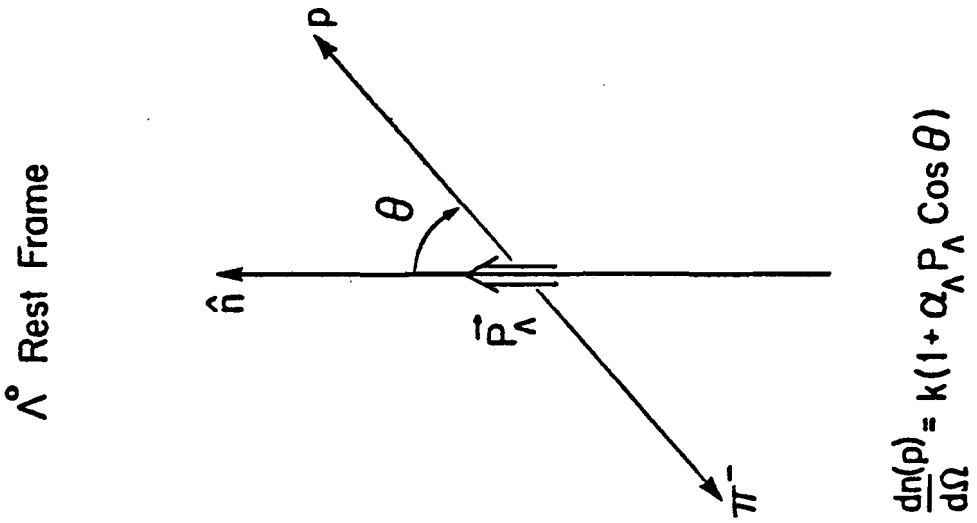

FIGURE (4.1.1) Definition of directions for Λ decay

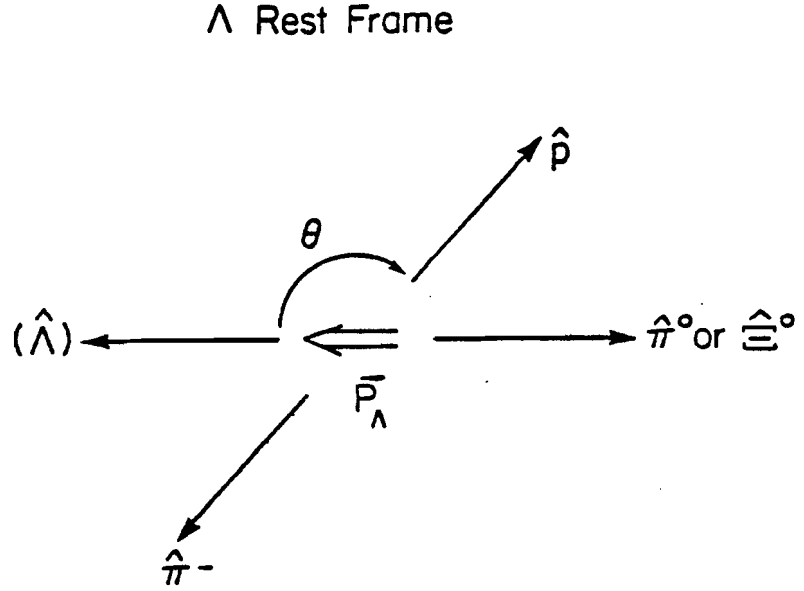

FIGURE (4.2.1) Definition of directions in α_{Ξ^0} analysis

4.2 Ξ^0 Polarization - Theoretical

For the $\Xi^0 \to \Lambda\pi^0$ decay an expression analogous to Eq. (4.1.5) describes the distribution of Λ's in the Ξ^0 rest frame:

$$\frac{dn(\Lambda)}{d\Omega} = k(1 + \alpha_{\Xi^0} \vec{P}_{\Xi^0} \cdot \hat{\Lambda}) \qquad (4.2.1)$$

where $\hat{\Lambda}$ is the unit 3-momentum vector of the Λ in the Ξ^0 rest frame (RF).

For decays of the type Eq. (4.1.1), the polarization of the daughter spin 1/2 particle can be related to that of the parent [27]. The expression written for the particular case of the $\Xi^0 \to \Lambda\pi^0$ decay is

$$\vec{P}_\Lambda = \frac{(\alpha_\Xi + \hat{\Lambda}.\vec{P}_\Xi)\hat{\Lambda} - \beta_\Xi(\hat{\Lambda} \times \vec{P}_\Xi) - \gamma_\Xi \hat{\Lambda} \times (\hat{\Lambda} \times \vec{P}_\Xi)}{1 + \alpha_\Xi \hat{\Lambda} \cdot \vec{P}_\Xi} \qquad (4.2.2)$$

where the terms on the right-hand-side are referred to the Ξ^0 RF (although of course the left-hand side, being a polarization, only has a simple interpretation in the Λ RF). Here $\vec{P}_\Lambda$, $\vec{P}_\Xi$ are 3-vector polarizations, $\hat{\Lambda}$ is the unit 3-vector momentum of the Λ, and α_Ξ, β_Ξ and γ_Ξ are the decay parameters for the $\Xi^0 \to \Lambda\pi^0$ mode. (A similar relation of course relates the decay proton polarization to that of the parent Λ for the $\Lambda \to p\pi^-$ decay).

For the measurement of the Ξ^0 polarization for the $\Xi^0 \rightarrow \Lambda\pi^0$ case the relation Eq. (4.2.2), used with Eq. (4.1.6), may be more convenient than the self-analyzing relation Eq. (4.2.1), because then only the Λ acceptance of the detection equipment must be understood.

It is important to note that Eq. (4.2.2) is unambiguously defined, so that the symbols mean "polarizations" in their standard sense, in the special Λ RF obtained from the Ξ^0 RF by a Lorentz boost along the Λ direction in the Ξ^0 RF.

Eq. (4.2.2) also shows how α_{Ξ^0} can be measured. For an unpolarized sample of Ξ's,

$$\vec{P}_\Lambda = \alpha_\Xi \hat{\Lambda} \qquad (4.2.3)$$

so the daughter Λ's are polarized longitudinally, with a magnitude α_Ξ. Since this is helicity, and helicity is invariant to Lorentz boosts along the momentum direction, it does not matter which Λ rest frame is used for the analysis, so that in contradistinction to the general case, the various measured quantities do not have to be transformed from the Lab frame to the Λ RF via the Ξ^0 RF. (See Fig. (4.2.1), which shows the relationship between the various momenta for the α_Ξ analysis).

The best experimental values for α_{Ξ^0}, β_{Ξ^0}, and γ_{Ξ^0} are given in terms of α_{Ξ^0} and a phase ϕ defined by

$$\beta = \sqrt{1 - \alpha^2}\ \mathrm{Sin}\ \phi$$

$$\gamma = \sqrt{1 - \alpha^2}\ \mathrm{Cos}\ \phi$$

Their best experimental values (before <u>this</u> experiment) were [1],

$$\alpha_{\Xi^0} = -0.44 \pm 0.08$$

$$\phi = (21 \pm 12)\ \mathrm{deg}$$

with the derived values

$$\gamma_{\Xi^0} = 0.84$$

$$\Delta = (216^{+13}_{-19})\ \mathrm{deg},\ \text{where}$$

$$= \frac{2|s||p|\mathrm{Cos}\,\Delta}{|s|^2 + |p|^2}$$

$$= \frac{-2|s||p|\mathrm{Sin}\,\Delta}{|s|^2 + |p|^2}$$

β is time-reversal-violating and should be zero except for the existence of final state interactions between the Λ and π^0 [28]. It is still so small that it is negligible for this experiment.

4.3 Λ Polarization Analysis

This section discusses the methods available for polarization analysis of lambdas. The following section expands the discussion to the cascade analysis.

4.3.1 General principles

The two most popular methods of polarization analysis are the Monte Carlo approach and the maximum likelihood method. In the Monte Carlo approach unpolarized Λ 's are generated and the experimental apertures are mocked as carefully as possible in the software. A comparision can then be made between the real event and the Monte Carlo event $\cos\theta$ distributions, and the Monte Carlo weighted by a $(1 + \alpha P \cos\theta)$ factor, with αP unknown but varied until the best fit is obtained between the distributions, according to some χ^2 criterion which is constructed in order to compare the two. In the maximum likelihood method a likelihood function is defined by

$$L = \prod_i L_i$$

where i indexes the real events, and

$L_i = 1 + \alpha P \cos\theta_i$ for perfect acceptance, or

$$L = \frac{1 + \alpha P \cos\theta_i}{\int_i (1 + \alpha P \cos\theta)\, d\cos\theta} \quad \text{for imperfect acceptance,}$$

and the integral is over the accepted region of $\cos\theta$-space for that real event i. The function L is the probability of observing the ensemble $\{i\}$, and the most likely value of αP is that for which L is maximized. Again, a Monte Carlo approach must be used to determine the accepted $\cos\theta$ regions. This time the real event parameters other than $\cos\theta$ can be fixed and $\cos\theta$ varied, and each of these Monte Carlo events tested for acceptance according to a software model of the experiment.

The first approach necessitates the use of a <u>perfect</u> Monte Carlo, something which can be notoriously difficult to obtain. The second approach has the disadvantage that no criterion for the quality of the resulting value of αP is obtained.

4.3.2 The hybrid Monte Carlo method [29]

A simple and convenient method has been found which combines features of both the aforementioned approaches, in which a Monte Carlo is based on the real data sample in such a way that only the $\cos\theta$-dependence of the acceptance

is studied and all other event parameters are taken from the data A chi-squared comparison can then be made between the real, presumably polarized, distribution, and the simulated distribution which can be arbitrarily polarized until the chi-squared is minimized.

These Monte Carlo events, called "fake events" to distinguish them from true Monte Carlo-generated events, are generated from the real data by replacing the $\cos\theta$ value $\cos\theta_i$ of the ith event with a randomly chosen $\cos\theta_{MC}$, while retaining all the other parameters of the real event (e.g. the decay vertex, the azimuthal angle of the proton, etc). Each fake event can be Lorentz-transformed into the Lab frame and traced through a sequence of software cuts designed to model the geometrical apertures and trigger logic of the experimental apparatus. These cuts are typically slightly more restrictive than the actual physical apertures, in order to reduce edge effects, where resolution and detection efficiencies may become very sensitive to small mismatches between the real and assumed geometry. Only those real events passing all the cuts are used as starting events for the procedure. The procedure is repeated until an arbitary fixed number (10 was actually used) of fake events has been accepted for each real event, or until some preset maximum number (200) of attempts has been made. (When such a failure occurs, both that real

event, and any accepted fakes generated from it, are discarded from the subsequent analysis). This approach ensures that the Λ parameter distributions of the fakes are identical to those of the real event sample (but with ten times the statistics), as would be required of a true Monte Carlo simulation of the experiment. The Monte Carlo fake events test only the $\mathrm{Cos}\,\theta$ acceptance of the spectrometer, in terms of the fake proton (and pion) distributions in the Lab, but have been constrained to have the same momentum and vertex distributions as the real data.

The fake event $\mathrm{Cos}\,\theta$ distribution can now be compared with the real event distribution. Since the fakes are generated <u>randomly</u> in $\mathrm{Cos}\,\theta$ they should be unpolarized; any $\mathrm{Cos}\,\theta$ -dependence must be due to the $\mathrm{Cos}\,\theta$ -dependence of the apparatus acceptance. However the real events are polarized, and this $\mathrm{Cos}\,\theta$ bias is reflected in the generated Monte Carlo events, again through the $\mathrm{Cos}\,\theta$ -dependence of the (software) acceptance. This bias must be removed from the fake $\mathrm{Cos}\,\theta$ distribution before it can be weighted by a polarization factor of the form $1 + \alpha P \mathrm{Cos}\,\theta_{MC}$ and αP adjusted until the two distributions match. To do this, a weight

$$W_{ij} = \frac{1 + \alpha P \mathrm{Cos}\,\theta_{ij}}{1 + \alpha P \mathrm{Cos}\,\theta_{i}}$$

is attached to each fake event j generated from real event i, which explicitly implements the $(1 + \alpha P \cos\theta_{MC})$ polarization, and removes the real event polarization bias $(1 + \alpha P \cos\theta_{R})$. (The form of this weight is discussed in more detail in the following section). In this weight the product αP is a priori unknown. The fake data weighted event by event by a term of this form, and normalized appropriately, can be compared to the real data by forming a χ^2 in each of 20 $\cos\theta$ bins (each of width 0.1), combining these to an overall χ^2, and minimizing this with respect to αP to obtain the most likely value for αP. In $\cos\theta$ bin I (I=1,...,20),

$$\chi^2_I = \frac{(n_I - n'_I/N_o)^2}{n_I}$$

where n_I is the number of real events with $\cos\theta$ falling in bin I, n'_I is the number of fake events with $\cos\theta$ falling in bin I, and N_o is a normalizing factor (=total no. of fakes/total no. of reals = 10). Each n'_I is given by

$$n'_I = \sum_{ij} W_{ij}(I)$$

where the sum is over each real event i, and for each Monte Carlo event j such that $\cos\theta_{MC}$ lies in bin I. The overall χ^2 is

$$\chi^2 = \sum_I \chi^2_I(\alpha P)$$

which can be minimized as a function of αP. The error associated with the αP obtained at the minimum χ^2 is found from the range of αP when allowing χ^2 to change

from its minimum value by one. Since 20 $\mathrm{Cos}\theta$ bins are used, and there is one parameter in the fit, there are 19 degrees of freedom (df).

The fake distribution of $\mathrm{Cos}\theta$ can be simply calculated and stored as it is generated by expanding the weight W_{ij} as a power series in αP

$$W_{ij} = \frac{1+\alpha P\mathrm{Cos}\theta_{ij}}{1+\alpha P\mathrm{Cos}\theta_i}$$

$$= (1+\alpha P\mathrm{Cos}\theta_{ij})(1+\alpha P\mathrm{Cos}\theta_i)^{-1}$$

$$= (1+\alpha P\mathrm{Cos}\theta_{ij})(1-\alpha P\mathrm{Cos}\theta_i+(\alpha P\mathrm{Cos}\theta_i)^2-\ldots)$$

$$= 1+\alpha P(\mathrm{Cos}\theta_{ij}-\mathrm{Cos}\theta_i)-(\alpha P)^2(\mathrm{Cos}\theta_{ij}-\mathrm{Cos}\theta_i)\mathrm{Cos}\theta_i$$

$$+(\alpha P)^3(\mathrm{Cos}\theta_{ij}-\mathrm{Cos}\theta_i)\mathrm{Cos}^2\theta_i+\ldots$$

Then with $C_i=\mathrm{Cos}\theta_i$ and $C_{ij}=\mathrm{Cos}\theta_{ij}$,

$$\sum W_{ij} = 1+(\alpha P)\sum(C_{ij}-C_i)-(\alpha P)^2\sum(C_{ij}-C_i)C_i+\ldots$$

The coefficients in this expansion can be calculated for each Monte Carlo event, and the sums accumulated as the Monte Carlo events are generated. This expansion for the distribution is also useful for calculating the χ^2 in a form suitable for minimization with respect to αP. The series converges for $|\alpha P\mathrm{Cos}\theta_i|\leq 1$, and quite rapidly for typical values of αP in this experiment. Four terms were found to provide a sufficiently precise estimate when $|\alpha P|\sim 0.1$.

It is clear that the method requires that αP be event-independent, as is of course true for the case of Λ polarization, but becomes a little more complicated for the Ξ^0 case.

The minimization of χ^2 can be carried out using Newton's method, in which the slope and intercept of the tangent to a function of a variable are evaluated at a first estimate for the value of the variable, and these used to calculate a second estimate of the variable, assuming the slope of the function is zero (as required at a maximum or minimum). The method can be iterated until it converges with sufficient precision.

The following section discusses the form of the weight W_{ij} in more detail before the generalization of this analysis method to the Ξ^0 case is discussed.

4.3.3 Formal discussion of hybrid Monte Carlo technique

The real event distribution in $\cos\theta$, where θ is the polar angle between the polarization vector and the direction under investigation, can be written in differential form as:

$$dn(\cos\theta) = kA(\cos\theta)(1+\alpha P\cos\theta)d\cos\theta \qquad (4.3.1)$$

where k is a normalization constant, $1+\alpha P\cos\theta$ expresses the polarization of the sample, and A is an acceptance function, with value 1 or 0, which signifies whether or not a particular event would be detected in the experimental apparatus.

A Monte Carlo distribution of fake events is generated by generating randomly in $\cos\theta$, from each real event, while keeping the other parameters of the real event fixed (at their actual values). In differential form,

$$d^2n'(\cos\theta', \cos\theta) = k'A'(\cos\theta')d\cos\theta' dn(\cos\theta) \qquad (4.3.2)$$

where the superscript ′ is used to denote fake event values, and otherwise the terms have the same meanings as in Eq. (4.3.1).

It is required to weight this Monte Carlo distribution so that it matches the real distribution, by attaching a weight W to each fake event; the last equation becomes

$$d^2n'(\cos\theta') = k'A'(\cos\theta')W(\cos\theta', \cos\theta)d\cos\theta' dn(\cos\theta) \qquad (4.3.3)$$

The overall Monte Carlo distribution is

$$dn'(\cos\theta') = k'A'(\cos\theta')d\cos\theta'\left[\int W(\cos\theta', \cos\theta)dn(\cos\theta)\right] \qquad (4.3.4)$$

where the integral is over all the real events. Since it is required that this distribution be polarized, just as is the real distribution,

$dn'(\cos\theta') \sim 1 + \alpha P \cos\theta'$, or

$d^1n'(\cos\theta') \sim 1 + \alpha P \cos\theta'$

Also, $dn(\cos\theta) \sim 1 + \alpha P \cos\theta$, so that the form

$$W(\cos\theta', \cos\theta) = \frac{1 + \alpha P \cos\theta'}{1 + \alpha P \cos\theta} \qquad (4.3.5)$$

will fulfil the requirements. In this equation the polarization P is a priori unknown, although it is the same for both the reals and fakes by construction. The overall normalization is $\int dn = N$ = total no. of real events, and $\int dn' = N' = 10 \times N$ = total no. of fake events.

The acceptance functions A and A' are assumed to be, and should be, identical. They are implemented by a software mock-up of the experimental geometric apertures and trigger requirements. Distributions over any of the event parameters (of the Λ's) will be identical for the reals and the fakes, again by construction.

4.4 Ξ^0 Polarization Analysis

4.4.1 General

As discussed previously, the Ξ^0 polarization may be calculated using Eq. (4.2.2) to obtain it from the measured daughter Λ polarization. This was the approach followed in this experiment. It is relatively easy and efficient (in computer time) to apply the hybrid method to the analysis of the daughter lambda sample, and this avoids the necessity of a detailed knowledge of the π^0 acceptance of the spectrometer which would be required to perform the analysis of the asymmetry of the $\Xi^0 \rightarrow \Lambda\pi^0$ decay in direct analogy to the $\Lambda \rightarrow p\pi^-$ case. It is clearly more complicated to model the π^0 acceptance (which is in fact the acceptance of the two daughter γ rays from the virtually immediate $\pi^0 \rightarrow 2\gamma$ decay) than that of the two charged particles from the $\Lambda \rightarrow p\pi^-$ decay. In particular this would require a detailed quantitative knowledge of the efficiency of each lead glass block in the array of 70, and their variation over the course of the experiment – a quite daunting prospect.

To use Eq. (4.2.2) everything must be calculated in the Ξ^0 RF, i.e. quantities measured in the Lab must first be transformed to the Ξ^0 RF where Eq. (4.2.2) holds, and then to the Λ RF where Eq. (4.1.6) can be used to find $\vec{P}_\Lambda$. The following sections treat the application of the hybrid method to the particular cases of Ξ^0 polarization measurement.

4.4.2 α_{Ξ^0} analysis

By analyzing the component of the daughter Λ polarization along the Λ momentum direction, Eq. (4.2.3) shows that α_Ξ is obtained if the parent Ξ^0 sample is unpolarized. The data at 0 mrad production angle must be unpolarized due to rotational symmetry, and so the daughter Λ's will be polarized due to α_{Ξ^0} alone. The decay distribution of the protons from the daughter Λ decays is

$$dn(\cos\theta) \sim 1 + \alpha_\Lambda \alpha_{\Xi^0} \cos\theta$$

where θ is the polar angle between the proton and the (negative) Λ momentum vector. The weight W in the hybrid method is then

$$W_{ij} = \frac{1+\alpha_\Lambda \alpha_\Xi \cos\theta_{ij}}{1+\alpha_\Lambda \alpha_\Xi \cos\theta_i} \qquad (4.4.1)$$

and the method applies directly in analogy with the

$\Lambda \to p\pi^-$ case discussed previously. This time the direction from which the proton polar angle is measured changes from event to event. The result is the product $\alpha_\Lambda \alpha_\Xi$, or α_Ξ once the known value of α_Λ is assumed.

For non-zero production angles, Eq. (4.2.2) shows that the component of Λ polarization measured is

$$\vec{P}_\Lambda \cdot \hat{\Lambda} = \frac{(\alpha_{\Xi 0} + \hat{\Lambda} \cdot \vec{P}_{\Xi 0})}{1 + \alpha_{\Xi 0} \hat{\Lambda} \cdot \vec{P}_{\Xi 0}} \qquad (4.4.2)$$

If $\vec{P}_\Xi$ is non-zero the α_Ξ term is modulated by terms involving $\hat{\Lambda} \cdot \vec{P}_\Xi$. These terms can be calculated for each event if $\vec{P}_\Xi$ is known. Typically, $|\vec{P}_\Xi| \sim 0.1$ in this experiment, and the magnitudes of the P_Ξ terms are further reduced by the cosine factor in the $\hat{\Lambda} \cdot \vec{P}_\Xi$ product, so that α_Ξ (~ 0.5) is still the dominant term. The hybrid method can be applied, with a weight

$$W_{ij} = \frac{1 + \alpha_\Lambda (\vec{P}_\Lambda \cdot \hat{\Lambda}) \cos\theta_{ij}}{1 + \alpha_\Lambda (\vec{P}_\Lambda \cdot \hat{\Lambda}) \cos\theta_i} \qquad (4.4.3)$$

and expanded as a (rapidly-convergent) series in $\alpha_\Lambda \alpha_\Xi$ as:

$$W_{ij} = \frac{1 + b_i C_{ij}}{1 + b_i C_i} + \frac{A[a_i (C_{ij} - C_i)]}{(1 + b_i C_i)^2} + \frac{A^2[-a_i^2 C_i (C_{ij} - C_i)]}{(1 + b_i C_i)^3} + \ldots$$

where $A = \alpha_\Lambda \alpha_\Xi$, $a_i = 1 - (\hat{\Lambda} \cdot \vec{P}_\Xi)$, and $b_i = \alpha_\Lambda (1 - \alpha_\Xi^2) \hat{\Lambda} \cdot \vec{P}_\Xi$. Here the α_Ξ terms associated with $\hat{\Lambda} \cdot \vec{P}_\Xi$ may be considered as small perturbations on the dominant α_Ξ term, and this value

iterated. In fact the results using Eq. (4.4.3) differed only slightly in value, and in χ^2 for the fits between fake and real data, from those using the approximation of Eq. (4.2.3) even when $\vec{P}_\Xi$ was not zero. (This was expected since the mean values $\langle \hat{\Lambda} \cdot \hat{x} \rangle$, $\langle \hat{\Lambda} \cdot \hat{y} \rangle$, and $\langle \hat{\Lambda} \cdot \hat{z} \rangle$ over all the data tended to be small. Assuming the polarization of all the data could be described by Eq. (4.2.3), all the data were analyzed together in order to check the overall value of α_{Ξ^0} obtained, and the χ^2 from the fit. Both were reasonable and consistent with the results obtained from Eq. (4.4.2).

4.4.3 P_Ξ analysis

To obtain a first approximation value for $\vec{P}_\Xi$, Eq. (4.2.2) was written as

$$\vec{P}_\Lambda \doteq \alpha_\Xi \hat{\Lambda} + \gamma_\Xi \vec{P}_\Xi \qquad (4.4.4)$$

which is quite a good approximation in practice, where $\alpha_\Xi \sim -0.5$, $\gamma_\Xi \sim 0.9$, and $|P_\Xi| \sim 0.1$. Using Eq. (4.4.4) in the decay proton distribution of the daughter lambdas, Eq. (4.1.6),

$$\vec{P}_\Lambda \cdot \hat{n} = \alpha_\Xi \hat{\Lambda} \cdot \hat{n} + \gamma_\Xi \vec{P}_\Xi \cdot \hat{n} \qquad (4.4.5)$$

for any direction $\hat{n}$ in space. Once a value of α_Ξ is known, this expression allows the component of P_Ξ along any $\hat{n}$ to

be obtained. In the hybrid method the corresponding weight is

$$W_{ij} = \frac{1 + (\alpha_A \alpha_\Xi \Lambda + \alpha_A \gamma_\Xi P_\Xi)\cos\theta_{ij}}{1 + (\alpha_A \alpha_\Xi \Lambda + \alpha_A \gamma_\Xi P_\Xi)\cos\theta_i} \qquad (4.4.6)$$

with the notation $\Lambda = \hat{\Lambda} \cdot \hat{n}$ and $P_\Xi = \vec{P}_\Xi \cdot \hat{n}$. In this equation, $\alpha_A \gamma_\Xi P_\Xi$ is event-independent, but $\alpha_A \alpha_\Xi \Lambda$ is not, although it can be calculated for each event. In fact W_{ij} can be expanded as a power series in $\alpha_A \gamma_\Xi P_\Xi$ alone, with coefficients which can be calculated event by event, and again only a few terms must be retained to give sufficient precision. With the notation

$$A_i = \alpha_A \alpha_\Xi \Lambda, \quad G = \alpha_A \gamma_\Xi P_\Xi, \quad C_i = \cos\theta_i, \quad C_{ij} = \cos\theta_{ij},$$

a simple calculation gives

$$W_{ij} = \frac{1+A_i C_{ij}}{1+A_i C_i} + \frac{(C_{ij} - C_i)G}{(1+A_i C_i)^2} - \frac{C_i (C_{ij} - C_i) G^2}{(1+A_i C_i)^3} + \ldots \qquad (4.4.7)$$

where i labels each real event, and j labels each fake event generated from real event i. Choosing $\hat{n}$ successively as the x, y, z Lab directions, the hybrid method then results in a value for $\alpha_A \gamma_\Xi \vec{P}_\Xi$. From this $\vec{P}_\Xi$ can be calculated.

Once this approximation has been obtained, Eq. (4.4.4) may be replaced by a second approximation

$$\vec{P}_\Lambda \doteq \frac{\alpha_\Xi \hat{\Lambda} + \gamma_\Xi \vec{P}_\Xi + (\vec{P}_\Xi)_\perp \cdot \hat{\Lambda}\,(1-\gamma_\Xi)\hat{\Lambda}}{1+\alpha_\Xi (\vec{P}_\Xi)_\perp \cdot \hat{\Lambda}} \qquad (4.4.8)$$

in which the first approximation $(\vec{P}_\Sigma)_1$ is used to estimate the perturbation on the dominant $\gamma_\Sigma \vec{P}_\Sigma$ term. The corresponding weight expansion to Eq. (4.4.7) becomes

$$W_{ij} = \frac{1+EC_{ij}}{1+EC_i} + \frac{(C_{ij}-C_i)FG}{(1+EC_i)^2} - \frac{C_i(C_{ij}-C_i)(FG)^2}{(1+EC_i)^3} + \ldots \qquad (4.4.9)$$

where A, G, C_i, C_{ij} have the same meanings, but

$$C=(1-\gamma_\Sigma)\,\alpha_\Lambda(\vec{P}_\Sigma)_1 \cdot \hat{\Lambda},$$

$$D=\alpha_\Sigma \hat{\Lambda}\cdot(\vec{P}_\Sigma)_1,$$

$$E=\frac{A+C}{1+D}, \quad F=\frac{1}{1+D}.$$

In fact this iterative procedure converges very rapidly, and the values of $\vec{P}_\Sigma$ obtained from even this second approximation are the same of those from Eq. (4.4.7). Other analysis directions $\hat{n}$ could also be used, but $\hat{\Lambda}$, x, y, and z were found most convenient and useful. The directions orthogonal to $\hat{\Lambda}$, e.g. $\hat{\Lambda}$ x z, were found not to be useful since they contain components of the polarization in combinations from which it is hard to extract the x, y, and z signals independently.

4.5 The Cancellation Of Experimental Biases

Any polarization determination essentially depends on measurement of left/right asymmetry. Any systematic experimental effect which favors detection in one hemisphere over the other introduces a spurious polarization due to instrumental bias. Such instrumental biases are very difficult to eliminate and it is important to design any polarization - determining experiment to be able to handle them. In this experiment we were able to reverse the sign of the polarization, leaving instrumental systematic effects unchanged. This will first be discussed for the well-understood case of beam (target-produced) Λ's.

4.5.1 The reversal of production angle

The direction of the polarization vector of Λ's produced in the target is known to be perpendicular to the production plane (defined by the incoming proton beam direction, and the outgoing neutral beam direction) in the parity-allowed direction [12, 15]. This is $-(\hat{p} \times \hat{\Lambda})$ where $\hat{p}$ is the unit vector along the proton beam direction, and $\hat{\Lambda}$ is that along the lambda momentum direction. The

conventional choice for the positive normal to this plane is the direction ($\hat{p}$ x $\hat{\Lambda}$), so the polarization is <u>negative</u> at production. Thus the Λ polarization direction was $-x$ for positive production angles, and $+x$ for negative production angles. The precessing magnetic field was along $+y$ for positive field integral, so the polarization vector precessed about the y direction (remaining in the horizontal, xz, plane). When the production angle was reversed the initial polarization direction was also reversed, although any asymmetries not accounted for by the internal Monte Carlo were not (and appeared as biases). To calculate the polarization components, the differences

$$\alpha P = \frac{\alpha P(+\theta) - \alpha P(-\theta)}{2} \qquad (4.5.1)$$

were formed. The sums

$$B = \frac{\alpha P(+\theta) + \alpha P(-\theta)}{2} \qquad (4.5.2)$$

are the <u>biases</u> along each direction. These can be of considerable size without adversely affecting magnetic moment measurements because of this method of cancellation. It was assumed that the biases were independent of production angle sign and magnitude; the experimental measurements support this assumption.

4.5.2 Checks of bias cancellation

There are several possible checks of bias cancellation.

1. By reversing the sign of the sweeping magnetic field, the precession direction of the polarization vector is reversed. For Λ's, which precess about 150° in the highest field integral used in this experiment, the z-component of the polarization is reversed in this way. This allows an independent calculation of the z-bias as

$$B_z = \frac{\alpha P_z(+Sw) + \alpha P_z(-Sw)}{2} \qquad (4.5.3)$$

for each production angle separately.

2. At a production angle of 0 mrad there is no preferred direction in space, so rotational invariance requires the transverse polarization to be zero, while parity invariance (of strong interactions) forbids the existence of longitudinal polarization. Any measured polarization signal must then be bias, which should be consistent with the bias determined in other ways.

3. The polarization in the y-direction (vertical) can only be non-zero if parity is not conserved in the Λ production process, if the collimator axis and the incident proton beam axis at finite production angle do not form a vertical plane, or if the precessing field is not vertical. Previous experience of the production angle-varying magnets and the Sweeper have shown that these effects are negligibly small. The Λ (and Ξ^0) production mechanisms are presumably strong interaction processes, so that parity is expected to be conserved.

These points were the motivation for taking Ξ^0 data under conditions of opposite signs of production angle and precessing field integral. The intention was to use Eqs. (4.5.1) and (4.5.2) for any measured Ξ^0 polarization, while allowing checks of the type expressed in Eq. (4.5.3) (although this of course depends on the actual size of the precession angle), in analogy with the inclusive Λ polarization. A priori, the direction of any Ξ^0 polarization was unknown, although the above points 2 and 3 are still valid. Without loss of generality the following discussion of the precession is restricted to motion in the (xz)-plane (horizontal).

In principle, data at different field integral values allow the resolution of lower order ambiguities in the precession angle of a polarization vector. These are of the form

$$\phi' = \phi + (m+2n)\pi \text{ rads } (m=0 \text{ or } 1;\ n=0,1,2,\ldots)$$

which are indistinguishable using measurements at one field integral alone. The index m represents lack of knowledge of the initial polarization direction (at production), which can in principle be measured by turning the sweeping field off. This was impractical in this experiment (due to the high beam intensities required), but the overall consistency of the data allows a reasonably unique set of conclusions to be drawn.

4.6 The Precession Analysis

The precession angle of a polarization vector is given by

$$\tan\phi = \frac{\alpha P_z}{\alpha P_x} \quad . \qquad (4.6.1)$$

By using Eq. (4.5.1) to calculate bias-removed polarization components, and inverting this equation, the precession angle ϕ can be calculated. The magnetic moment of the requisite particle follows from Eq. (1.5.1). This approach works for Λ's and Ξ^0's.

A more sophisticated method utilizes the available range of different data-taking conditions, and the expected behavior of the polarization under these various conditions, by construction of a chi-squared function which describes the data. This approach was known as the "Master χ^2 Fit". A χ^2 was formed involving the measured polarization components as a function of the unknown magnetic moment (or precession angle), polarization, and x and z biases. It was defined by

$$\chi^2 = \sum_{ijk} \left[\frac{(\alpha P_{xijk} - B_{xi} \pm \alpha P_{oi} \cos\phi_j)^2}{\sigma^2_{xijk}} + \frac{(\alpha P_{zijk} - B_{zi} \pm \alpha P_{oi} \sin\phi_j)^2}{\sigma^2_{zijk}} \right] \qquad (4.6.2)$$

where $i=1,\ldots,n$ runs over the n momentum bins into which the data was divided; $j=1,\ldots,6$ runs over the 6 field integral values (± 1, $\pm 7/9$, $\pm 2/3$); and $k=1,2$ runs over the 2 signs of production angle. The <u>lower</u> sign is taken with <u>positive</u> production angle. B_{xi} and B_{zi} are the biases which are cancelled by reversing the production angle, and are allowed to be functions of momentum. The six precession angles ϕ_j (in degrees) are all computed from the (unknown) magnetic moment parameter μ (in nuclear magnetons) using

$$\phi_j = -(18.30) \int B dl_j \times \mu \qquad (4.6.3)$$

where the field integral $\int B dl_j$ is expressed in Tesla-meters. The minus-sign correctly correlates the sign

of the precession angle with the sign of the field integral (according to the convention of the experiment). P_{xijk} and P_{zijk} are the data points in each momentum bin for each field integral and sign of the production angle. (These are the raw data points, i.e. measured polarization signals, without any bias cancellation technique applied). The χ^2 may be minimized by conventional techniques to obtain the unknown parameters μ, P_0, B_x, and B_z, as functions of momentum. (μ of course should turn out to be independent of momentum). This chi-squared automatically takes account of the biases which must be removed explicitly before the calculation of Eq. (4.6.1).

CHAPTER 5

RESULTS

5.1 Λ Polarization and Magnetic Moment

The polarization analysis of the prescaled Λ component of the data taken at 7.6 mrad was performed in detail. In this way the consistency of the experiment with previous experiments could be checked. The value of the Λ magnetic moment was calculated in the standard way discussed in the previous chapter, using the overall χ^2 fit to the several data-taking conditions.

For all the polarization analyses, including the Ξ^- and $\bar{\Lambda}_{\Xi^-}$ analyses, no distinction was made between samples taken with different targets. This was justified by previous experience that the polarization showed no A (=atomic weight) -dependence, at least for the Be, Cu, and

Pb targets used, and also by the fact that no such dependence was apparent in this data.

5.1.1 The measured signals

The signals measured were the products of ϕ_Λ with the polarization component along each of the three axes x, y, z. These values are given in Table 4, subdivided according to the sign of the production angle, and the value of the Sweeper current.

These results were obtained by analyzing the Λ information on the tapout tapes directly. A cut requiring R^2 of the Λ at the target to be ≤ 40 mm^2 was used, in order to reduce the effects of contamination from any sources but the target, including daughter Λ's from Ξ^0 decays. The cross-contamination of the beam Λ sample by Λ's from Ξ^0 decays was very small, due to the much lower Ξ^0 yield. The R^2_Λ cut removed essentially all these events.

The $(p\pi^-)$ invariant mass, the Λ momentum spectrum, decay vertex distribution, and R^2_Λ distribution, have already been presented for the 7.6 mrad Λ data.

It is immediately obvious that there was a large signal in the y-direction (a parity-violating direction). As it did not reverse sign under reverse of sign of the production angle it was a bias, which could be cancelled from the results by combining the different samples according to the discussion in the previous chapter. When this procedure was followed the true y-signal was consistent with zero, as it should be: $\alpha P_y = -0.018 \pm 0.012$ for Sw+, and $\alpha P_y = -0.007 \pm 0.010$ for Sw- samples.

Much study was devoted to searching for the origin of this y-bias. The difficulty was that in the y-view all the chambers, and counters, used in the trigger and/or reconstruction, shadowed each other, so that it was impossible to pinpoint unambiguously a small y inefficiency in one place. Fortunately, because this effect was indeed a bias, which could be cancelled by virtue of the experimental design, it could have no effect on the final polarization or magnetic moment measurements. A possibly related effect was the fact that poor χ^2 values were often obtained for the fits between the real and fake $\cos\theta$ distributions for the y-direction analysis. This mismatch was considerably worse at the center of the $\cos\theta_y$ distribution, where it appeared that real events were cut harder than expected from the fake event Monte Carlo. Such an effect was just that which would result from chamber

inefficiency problems. A sensitive consequence of lowered MWPC efficiencies is lowered reconstruction efficiency for events with small opening angle (between the p and π^-) upstream of the analyzing magnet. These events tend to populate the center of the $\mathrm{Cos}\,\theta_y$ distribution. The same effect appears as an increased number of vees of a specific failure-type in the vee pattern recognition analysis: those unreconstructable because there appears to be only one track in one or both of the x,y views upstream of the magnet. This problem was unavoidable during much of the data-taking due to the high background charged particle fluxes in the chambers, arising presumably from muons and gamma-conversions from the neutral beam, at the high proton intensities necessary to acquire Ξ^0 triggers at a reasonable rate. It is important to realize that such a mismatch at the center of a $\mathrm{Cos}\,\theta$ distribution usually cannot cause a polarization signal as it cannot weight the distribution with an overall slope. This hardly affected the x (or z) direction, mainly because the tracks are split in x downstream of the analyzing magnet. At 0 mrad production angle the effect was less evident, which supported the idea that it was primarily due to rate-dependence in the chambers. At small angles much lower proton beam intensities (with a corresponding decrease in the resulting neutral beam flux) were required to saturate the trigger. (Typically, 0 mrad data-taking

only required a few 10^7 protons per spill on the production target; at 10 mrad, intensities up to 2 x 10^{10} protons per spill were used).

For this Λ data an independent method of polarization analysis was also tried. This utilized the expected reversals of the different components of the Λ polarization under the various combinations of production angle sign and Sweeper field. It assumed that the acceptance of the spectrometer for Λ's under these reversals was unchanged. Then a ratio could be formed of the numbers of events detected in a particular $\mathrm{Cos}\theta$ bin (normalized appropriately) for both conditions, and this ratio fit by a linear expression in $\mathrm{Cos}\theta$ of slope αP. This followed from the simple calculation:

$$\frac{N_+ - N_-}{N_+ + N_-} = \frac{(1+\alpha P\mathrm{Cos}\theta)-(1-\alpha P\mathrm{Cos}\theta)}{(1+\alpha P\mathrm{Cos}\theta)+(1-\alpha P\mathrm{Cos}\theta)}$$

This approach yielded x and z signals entirely consistent with the full analysis (which did not require the quite strong assumption of equal acceptances for the opposite signs of production angle).

5.1.2 The fitted parameters: the magnetic moment μ_Λ

The measured polarization components were used in the master χ^2 to apply full analytic power in combining the various sets of different run conditions to the problem of extracting the Λ magnetic moment. This resulted in the values for the magnitude of the polarization, the magnetic moment, and the x and z biases, given in Table 5. The χ^2 for the fit is also presented; the value was much improved by removing one data point (contributed by a very small sample of the total data). The results of the fit without this point are also shown.

The precession analysis method was also used to obtain a value for the magnetic moment. The appropriate combinations of the measured signals were formed, following the discussion in the previous chapter. The Λ magnetic moment obtained,

$$\mu_\Lambda = -0.593 \pm 0.025 \ \mu_N$$

agrees with that obtained from the χ^2 fit,

$$\mu_\Lambda = -0.598 \pm 0.015 \ \mu_N \qquad (5.1.1)$$

and is in good agreement with our previous precision measurement [2], which gave

$$\mu_\Lambda = -0.6138 \pm 0.0047 \ \mu_N \ . \qquad (5.1.2)$$

This agreement gave some confidence that the behavior of the beam Λ polarization was understood. This result is itself the world's second most precise measurement of the Λ magnetic moment. Fig. (5.1.1) shows the precession angle corresponding to each field integral for the 7.6 mrad Λ data; the least squares fit straight line is shown. The slope gave the magnetic moment

$$\mu_\Lambda = -0.587 \pm 0.017 \ \mu_N$$

with a chi-squared of 10.5 for 4 d.f., where the error came from finding the range for the slope value when the chi-squared value changed by one from its minimum value.

The beam Λ polarization of the data at other production angles was also analyzed, although the full χ^2 method was not applied. In particular, the polarization components measured for the 0 mrad data (171K events), including the y-signal, were consistent with being due entirely to the biases, as expected. This 0 mrad data spanned the entire range of Sweeper field integral values used in the experiment.

The sign of the beam Λ polarization at production has been found to be negative for positive production angles, and positive for negative production angles. ('Positive' is defined in the sense that the vector product of the incoming proton momentum vector and the outgoing lambda

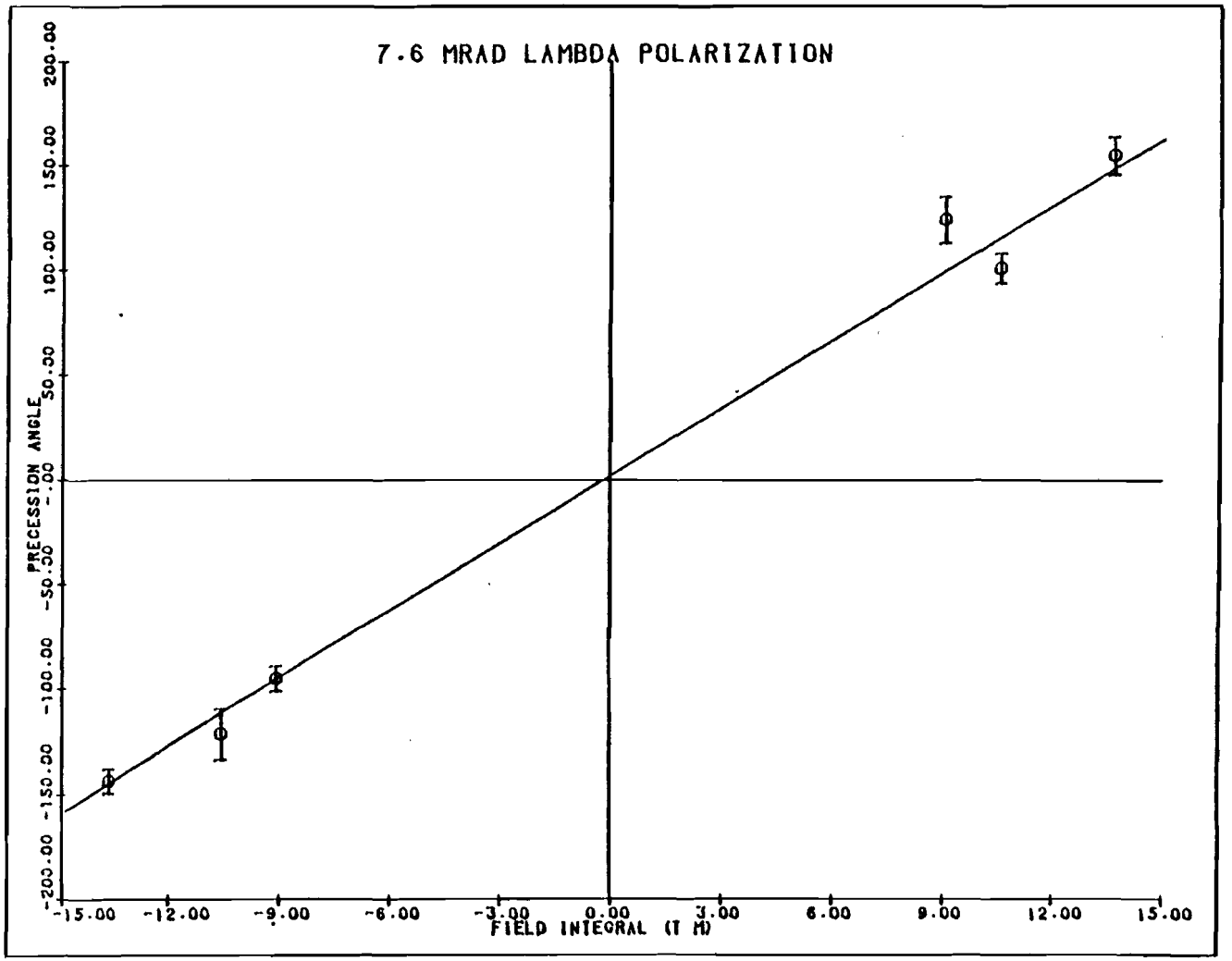

FIGURE (5.1.1) Precession angle versus field integral (for Λ's)

5.2 Ξ^0 Polarization and Magnetic Moment

5.2.1 The measured signals and the precession analysis

After checking the overall data quality by studying the beam Λ polarization, the polarization of the daughter Λ's from Ξ^0 decays was measured. The components $\alpha_\Lambda \gamma_\Xi P_\Xi$ along the x, y, and z axes were obtained for each production angle and Sweeper field, and are presented in Tables 6 - 11 for the 1G and 2G samples at each production angle. In these tables the symbol α denotes $\alpha_\Lambda \gamma_\Xi$ unless subscripted explicitly. Note the factors α_Λ and γ_Ξ which often occur in these values. In the calculations, β_Ξ was assumed to be zero, so that γ_Ξ was calculated from α_Ξ (which was measured independently to be -0.41; see Section 5.3.3) to be $\gamma_\Xi = 0.920 \pm 0.005$. The results were not sensitive to the precise value of γ_Ξ (in fact 0.91+0.01 was used for the calculation of the polarization from the measured components). The value 0.642 ± 0.013 was used for α_Λ [1]. The errors quoted are purely statistical; the effects of possible backgrounds are discussed later in this chapter. The 1G and 2G samples of Ξ^0's were kept separate through most of the analysis. Their acceptances were quite different, so the biases involved in their polarization

measurements could be different.

The precession analysis technique was applied directly to extract a precession angle at each Sweeper field, and hence the magnetic moment. This led to the informative plot of Fig. (5.2.1), which shows the dependence of the precession angle ϕ on the field integral $\int Bdl$. Only the 7.6 mrad data were used for this plot; the polarization signals are contained in Table 12, and the precession angles in Table 13. As expected, this was a straight line through the origin, with a slope related to the Ξ^0 magnetic moment through Eq. (1.5.1). The magnetic moment obtained from a least-squares straight-line fit to the six data points (but not constraining the fit at the origin), was

$$\mu_{\Xi^0} = -1.235 \pm 0.022\ \mu_N \quad (\ = 11.6/4\ \text{df}) \qquad (5.2.1)$$

where the error was estimated by finding the value of the moment which changed the χ^2 value from its minimum value by one. This fit is drawn in the figure.

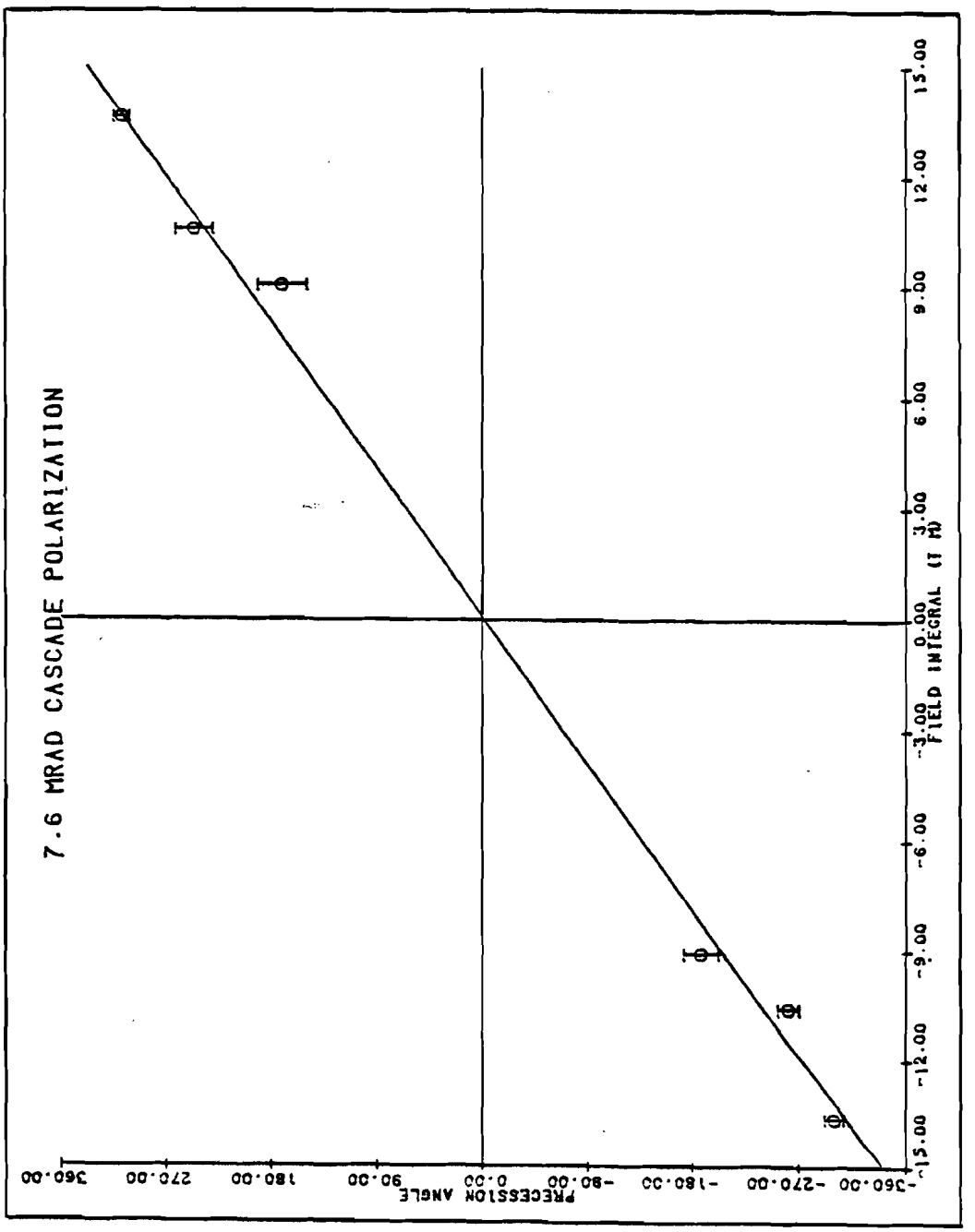

FIGURE (5.2.1) Precession angle versus field integral (for π^0's)

5.2.2 The Ξ^0 magnetic moment

In analogy with the 7.6 mrad Λ data (Table 5), the master χ^2 procedure was applied to the 7.6 mrad Ξ^0 data without momentum-binning; the results are shown in Table 14.

The data were then divided into several momentum bins according to the momentum of the parent Ξ^0 and these measured components fed into the master χ^2 procedure, for each production angle and each of the 1G and 2G samples separately. This led to values for the magnitude of the Ξ^0 polarization, the Ξ^0 magnetic moment, and the x and z biases, in each momentum bin. The momentum bins used, unless otherwise explicitly stated, were 0-120, 120-140, 140-160, 160-180, 180-200, 200-400 GeV/c. The fitted values are shown in Tables 15 - 20, according to production angle. The weighted averages of 1G and 2G results at each angle are listed in Tables 21 - 23.

Three separate analyses of the 7.6 mrad data were performed, using the first iteration, second iteration, and second iteration values with a cascade momentum cut requiring the momenta to be above 90 GeV/c. The differences between the results of these analyses were insignificant, so only one set of results is shown.

From the tables it is clear that indeed the biases in the Ξ^0 polarization measurements were quite different for the 1G and 2G samples. The momentum dependence of these biases is plotted in Figs. (5.2.2) - (5.2.13).

The overall value for the Ξ^0 magnetic moment obtained from weighted averages over all the data was

$$\mu_{\Xi^0} = -1.237 \pm 0.016 \ \mu_N \qquad (5.2.2)$$

where the error is purely statistical. This combination was implemented by taking weighted averages over the 1G and 2G results at each angle (obtained from a master χ^2 fit without momentum binning), and then an overall weighted average. 270 425 reconstructed $\Xi^0 \rightarrow \Lambda\pi^0$ events contribute to this value, with a mean cascade momentum of 134 GeV/c, and an average polarization of -0.108 ± 0.006. Combining the momentum-binned results gave the number

$$\mu_{\Xi^0} = -1.239 \pm 0.014 \ \mu_N \qquad (5.2.3)$$

for 269524 events. The number of events is less because some momentum bins did not contain enough events for meaningful results to be obtained. This number confirms the result we obtained for the Ξ^0 moment from our Λ magnetic moment experiment.

The Ξ^0 magnetic moment from the 4, 7.6, and 10 mrad data is plotted as a function of momentum for the 1G and 2G samples separately, in Figs. (5.2.14) - (5.2.19). In each

plot a straight line has been drawn at the value −1.25, as a reference. The combined data sets resulted in Fig. (5.2.20); the least-squares fit to a constant value is also shown. It gave the value

$$\mu_{\Xi^0} = -1.236 \pm 0.014 \ \mu_N \ (\chi^2 = 2.14/5 \text{ d.f.}) \qquad (5.2.4)$$

from 269524 events again. The momentum-independence of the moment, the consistency of the 1G and 2G values, and the very different biases in the two samples, are strong evidence that the biases have been properly cancelled in the fitting procedure.

The 0 mrad and 2 mrad data yielded polarization components which were not amenable to the χ^2 approach, because as it was not expected that there be any polarization (or for the case of 2 mrad, only very small polarization) there was no satisfactory way to define the χ^2. These data were combined according to the previously discussed prescriptions, and resulted in signals consistent with being due to the biases alone. The signals ($\alpha_\Lambda \gamma_\Xi P_\Xi$) from the data at 0 mrad and 2 mrad, after combining opposite production angles, are plotted in Figs. (5.2.21)−(5.2.30). In these plots, the ordinate is labelled "signal", which denotes the measured $\alpha_\Lambda \gamma_\Xi P_\Xi$ component.

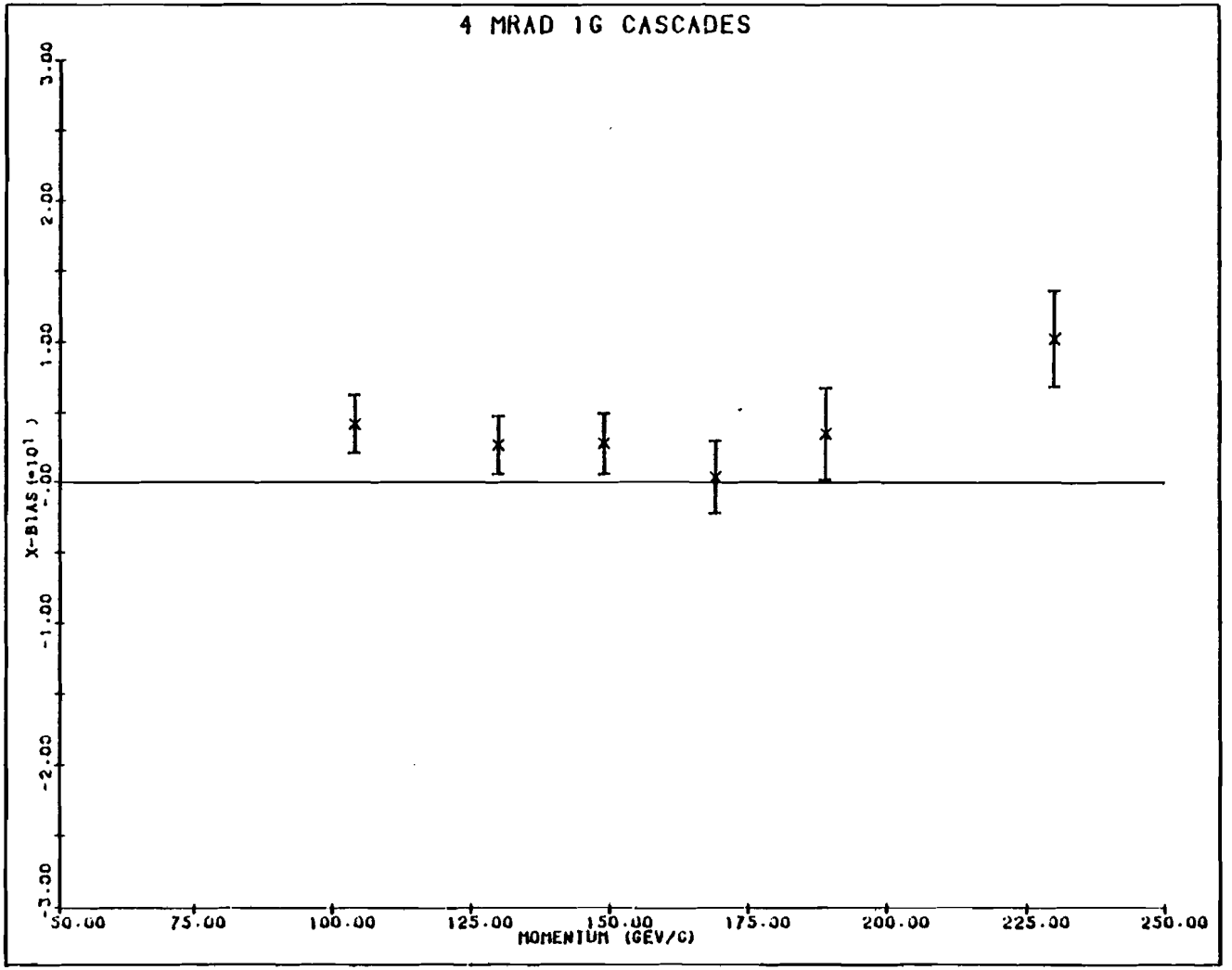

FIGURE (5.2.2) x-bias from 4 mrad 1G Σ^0's

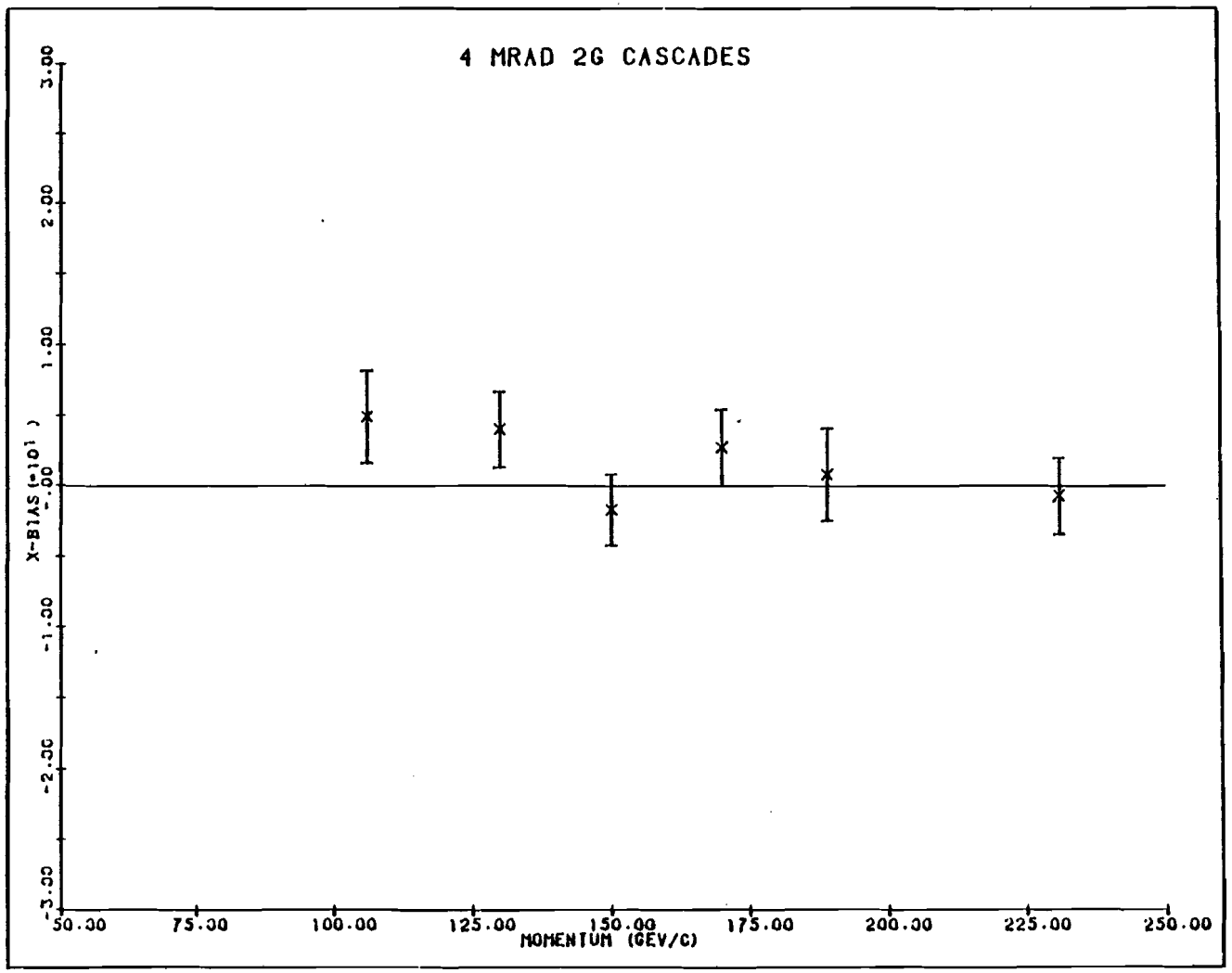

FIGURE (5.2.3) x-bias from 4 mrad 2G Ξ^0's

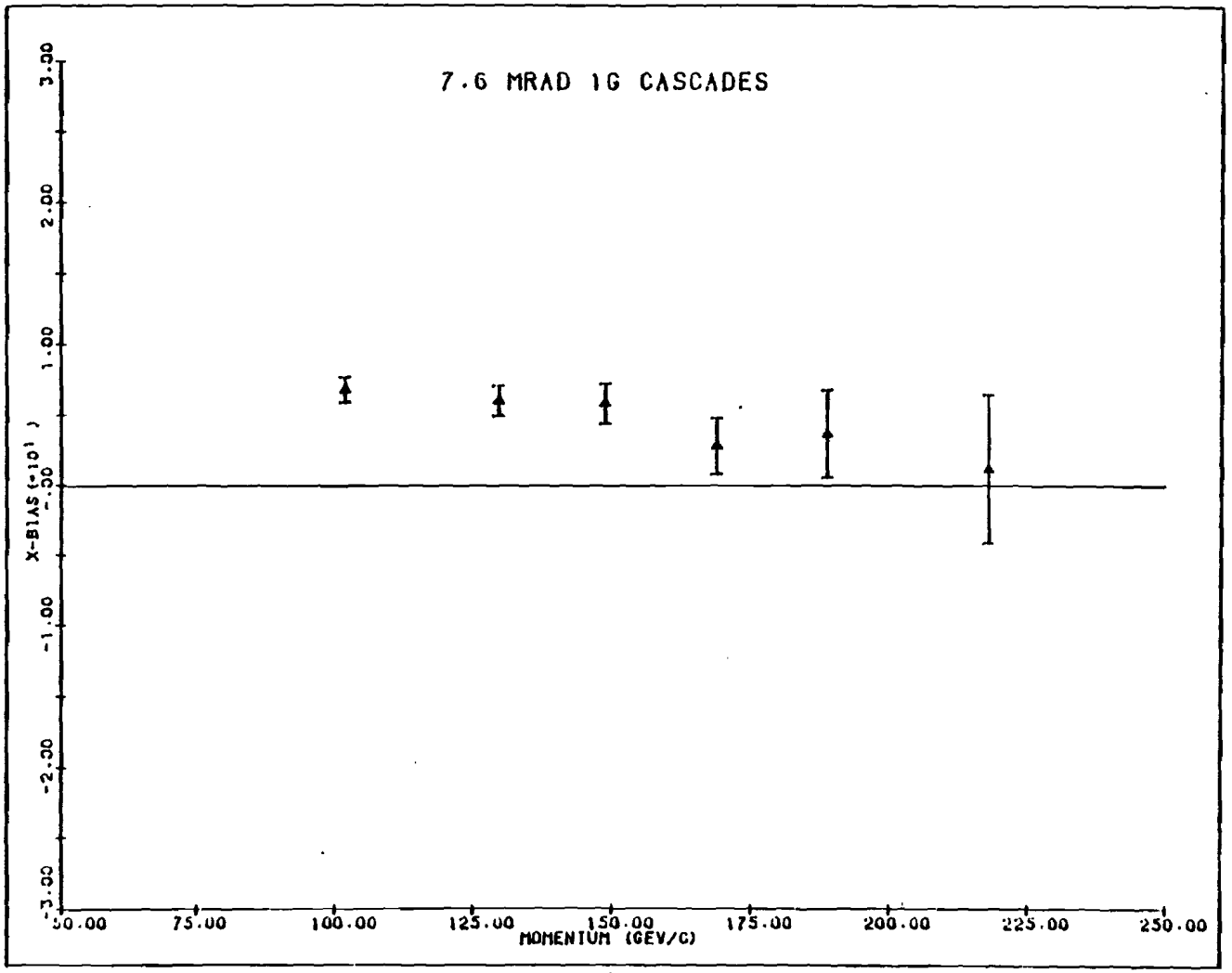

FIGURE (5.2.4) x-bias from 7.6 mrad 1G Ξ^0's

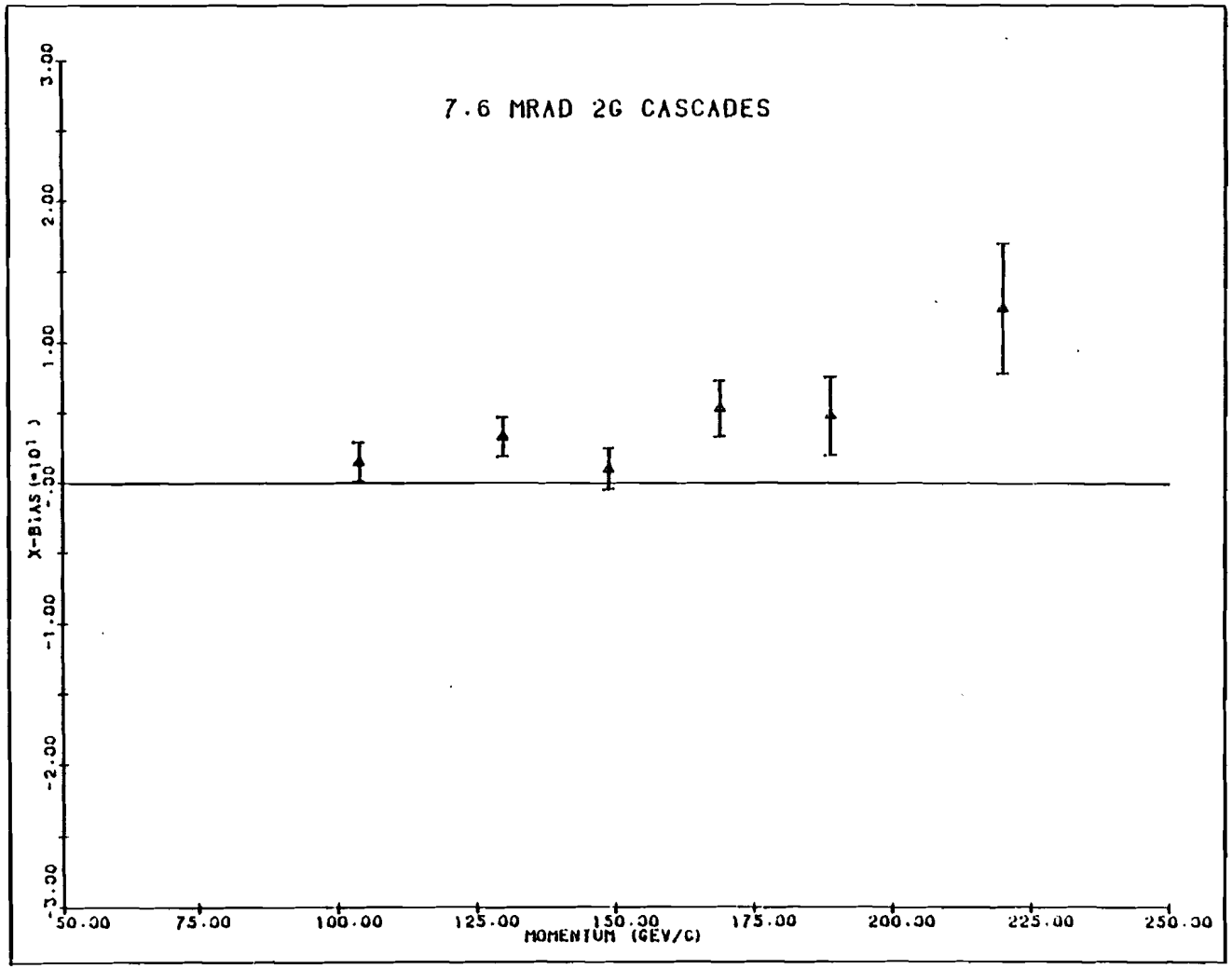

FIGURE (5.2.5) x-bias from 7.6 mrad 2G Ξ^0's

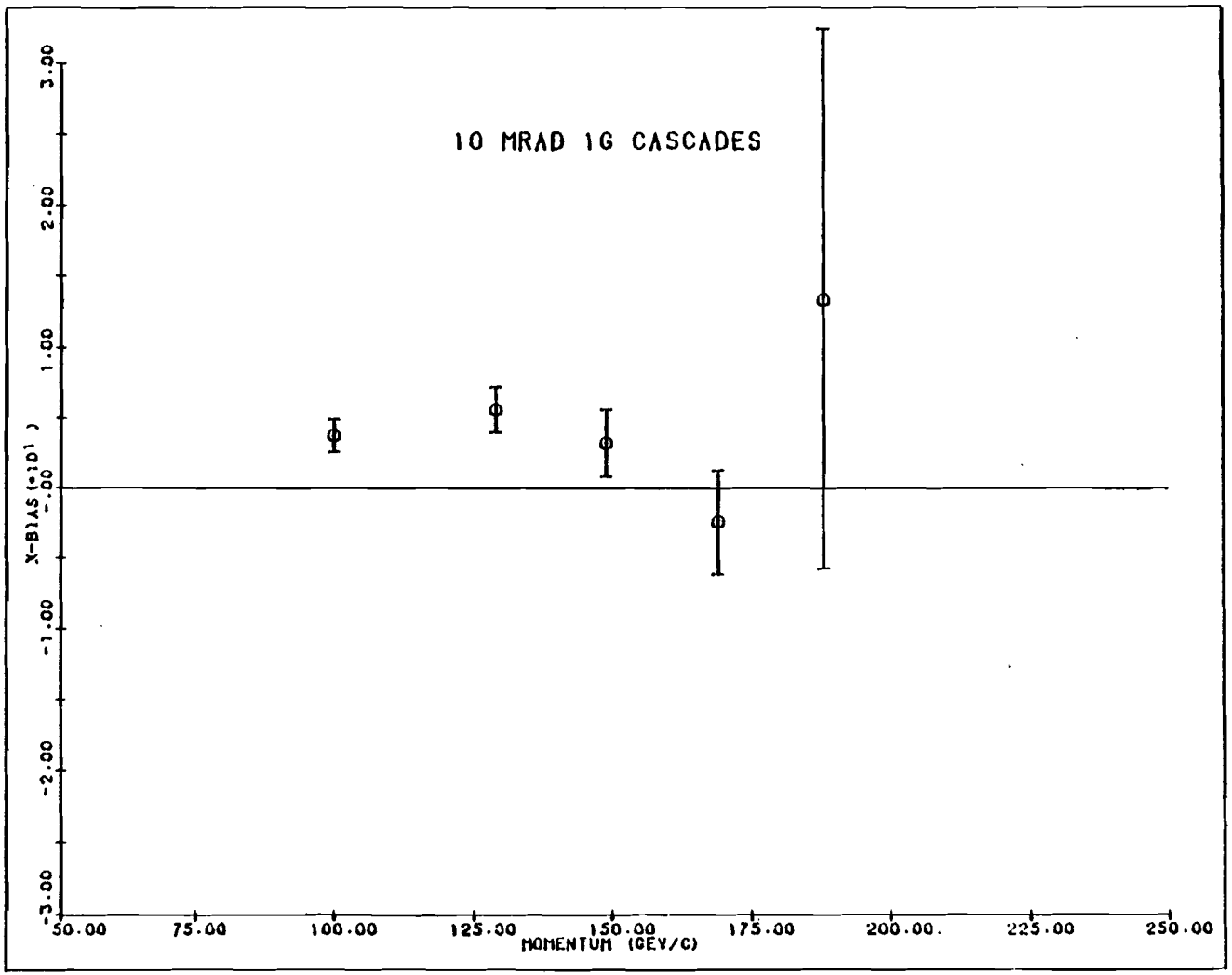

FIGURE (5.2.6) x-bias from 10 mrad 1G Ξ^0's

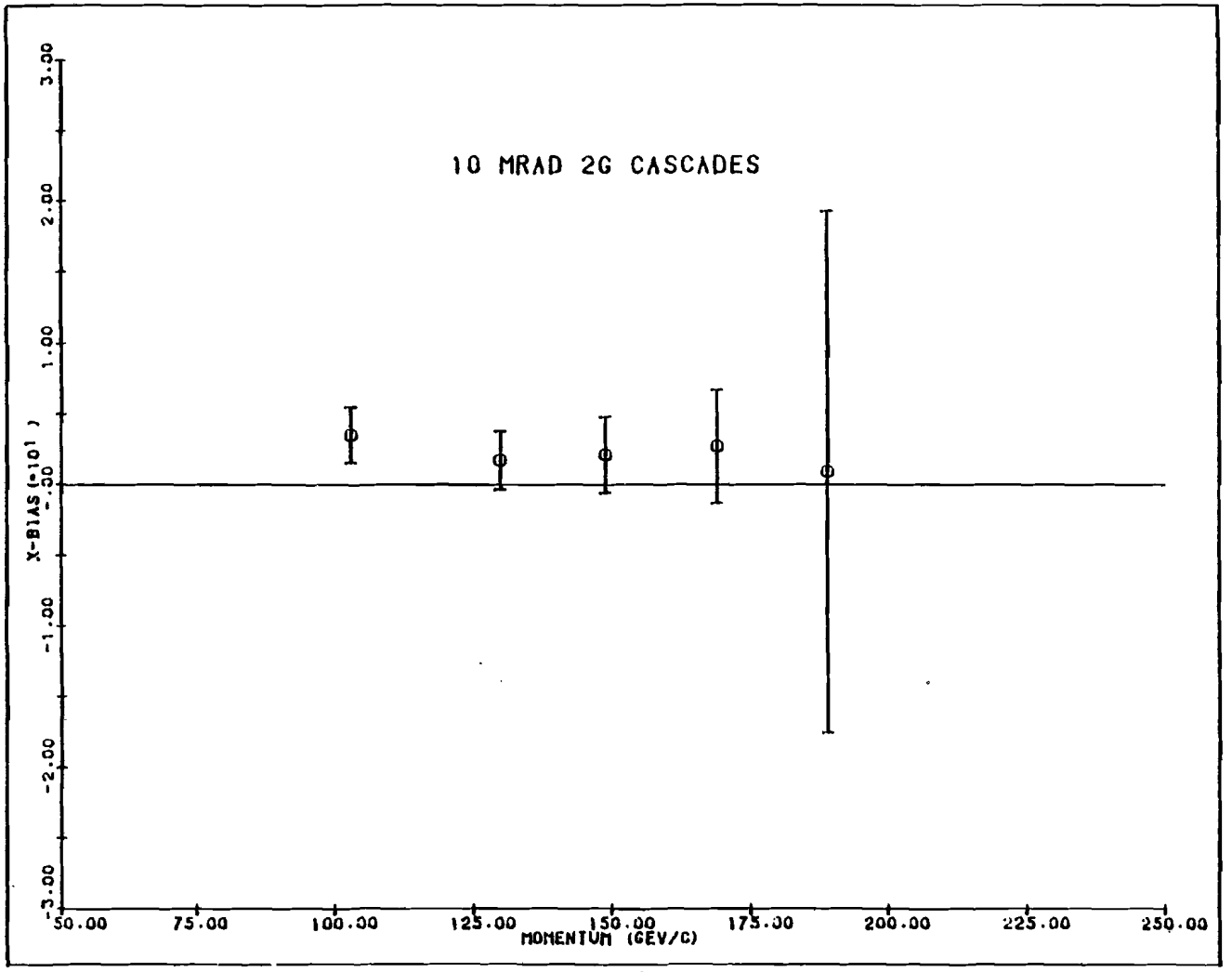

FIGURE (5.2.7) x-bias from 10 mrad 2G Ξ^0's

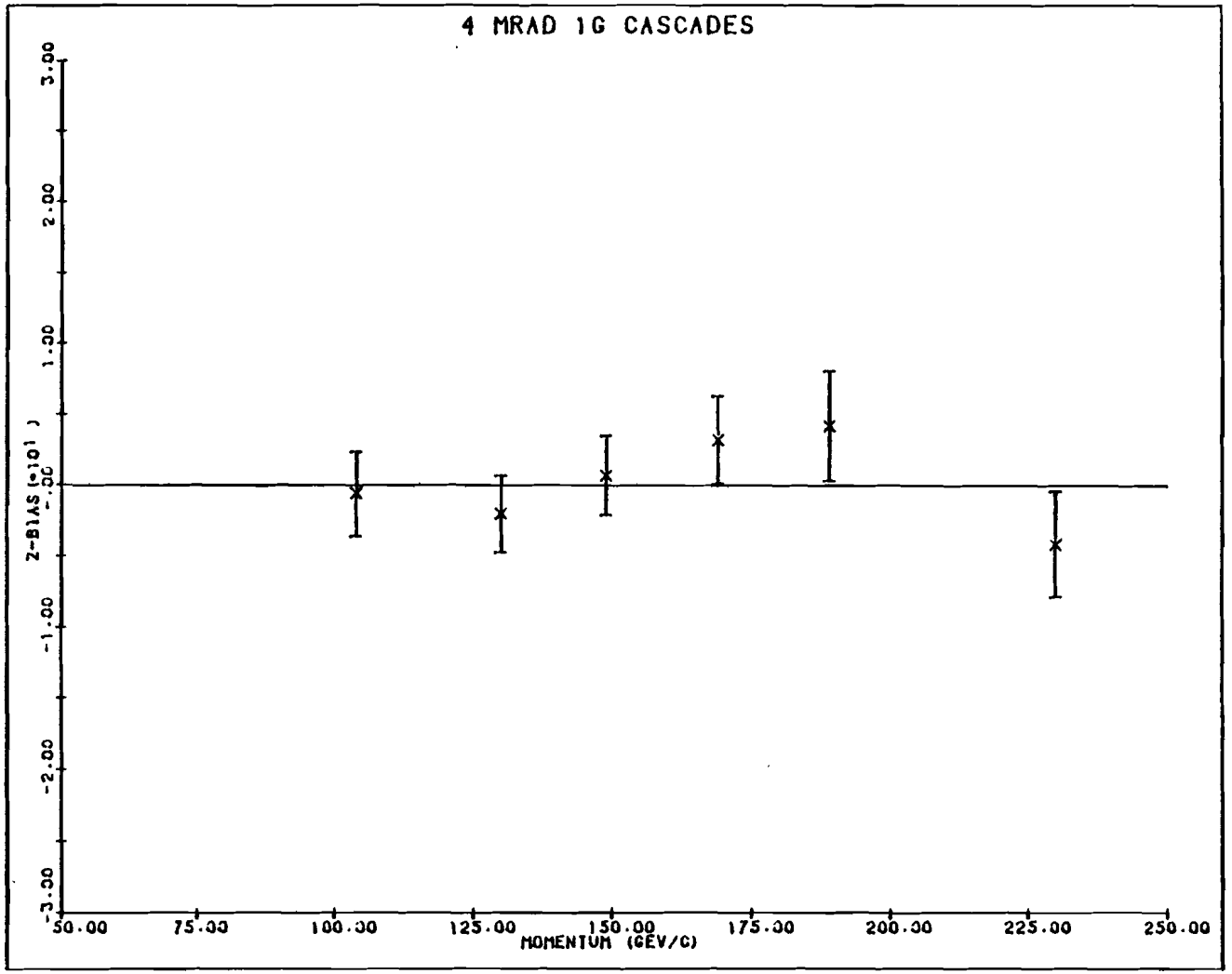

FIGURE (5.2.8) z-bias from 4 mrad 1G Ξ^0's

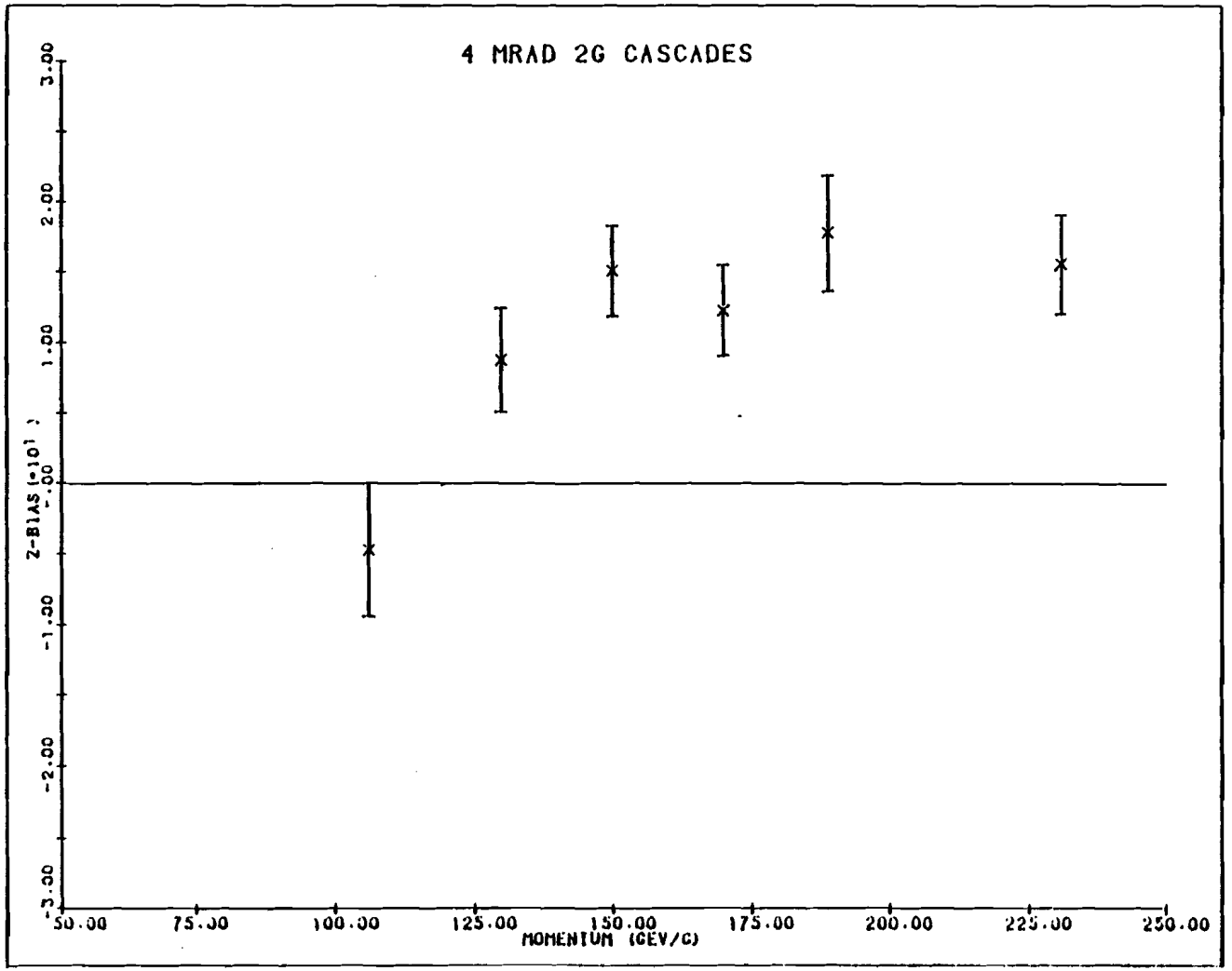

FIGURE (5.2.9) z-bias from 4 mrad 2G Ξ^0's

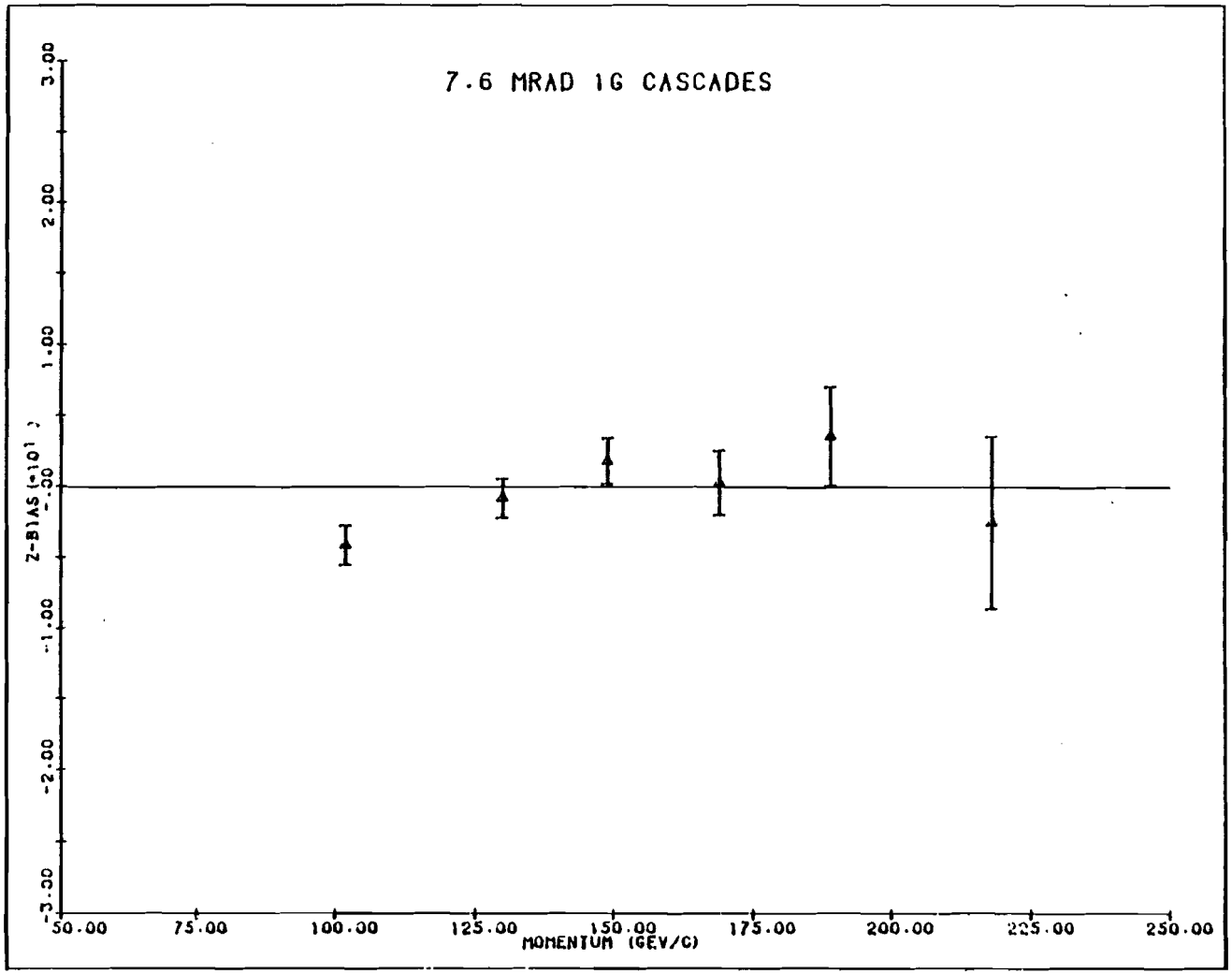

FIGURE (5.2.10) z-bias from 7.6 mrad 1G Ξ^0's

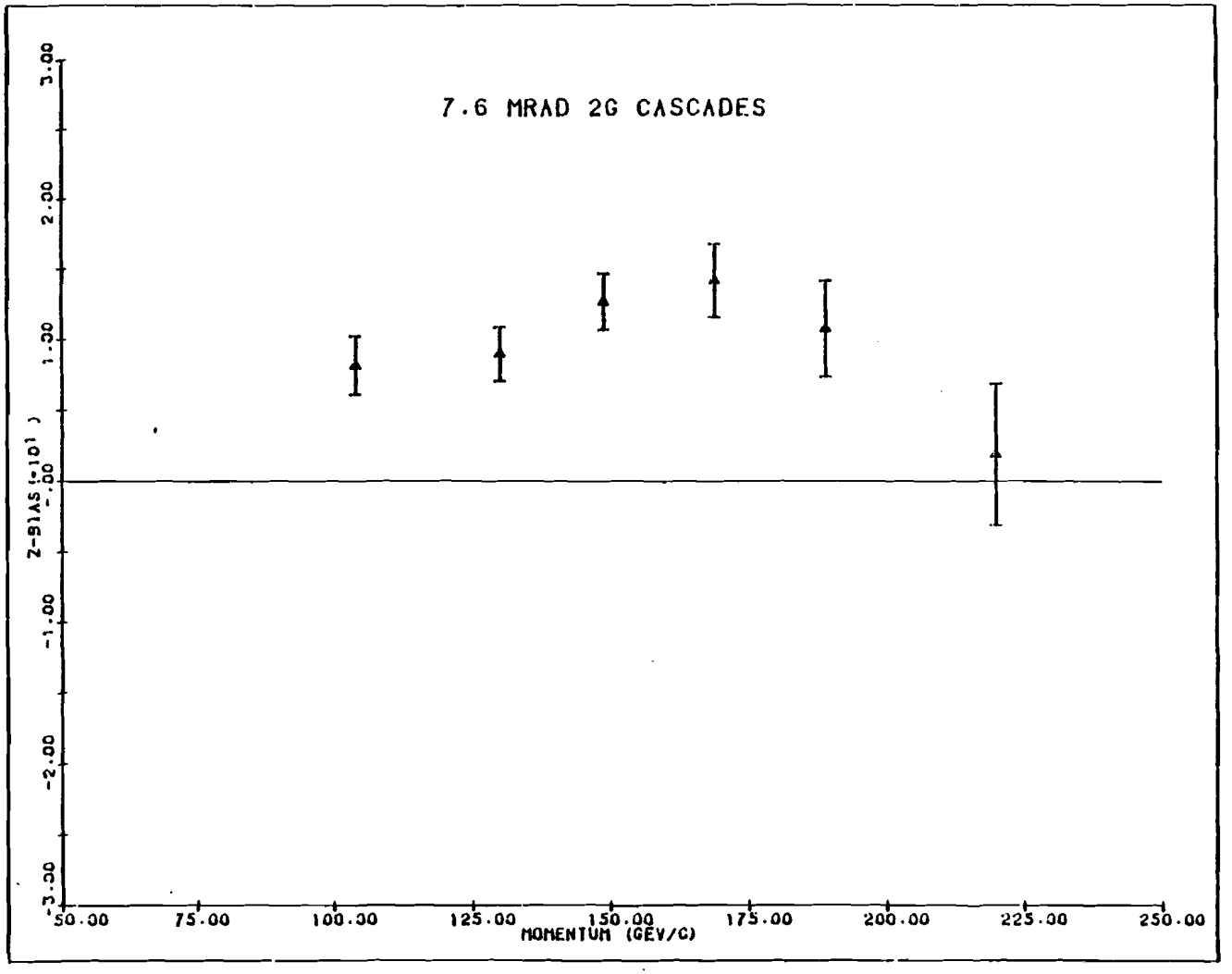

FIGURE (5.2.11) z-bias from 7.6 mrad 2G Ξ^0's

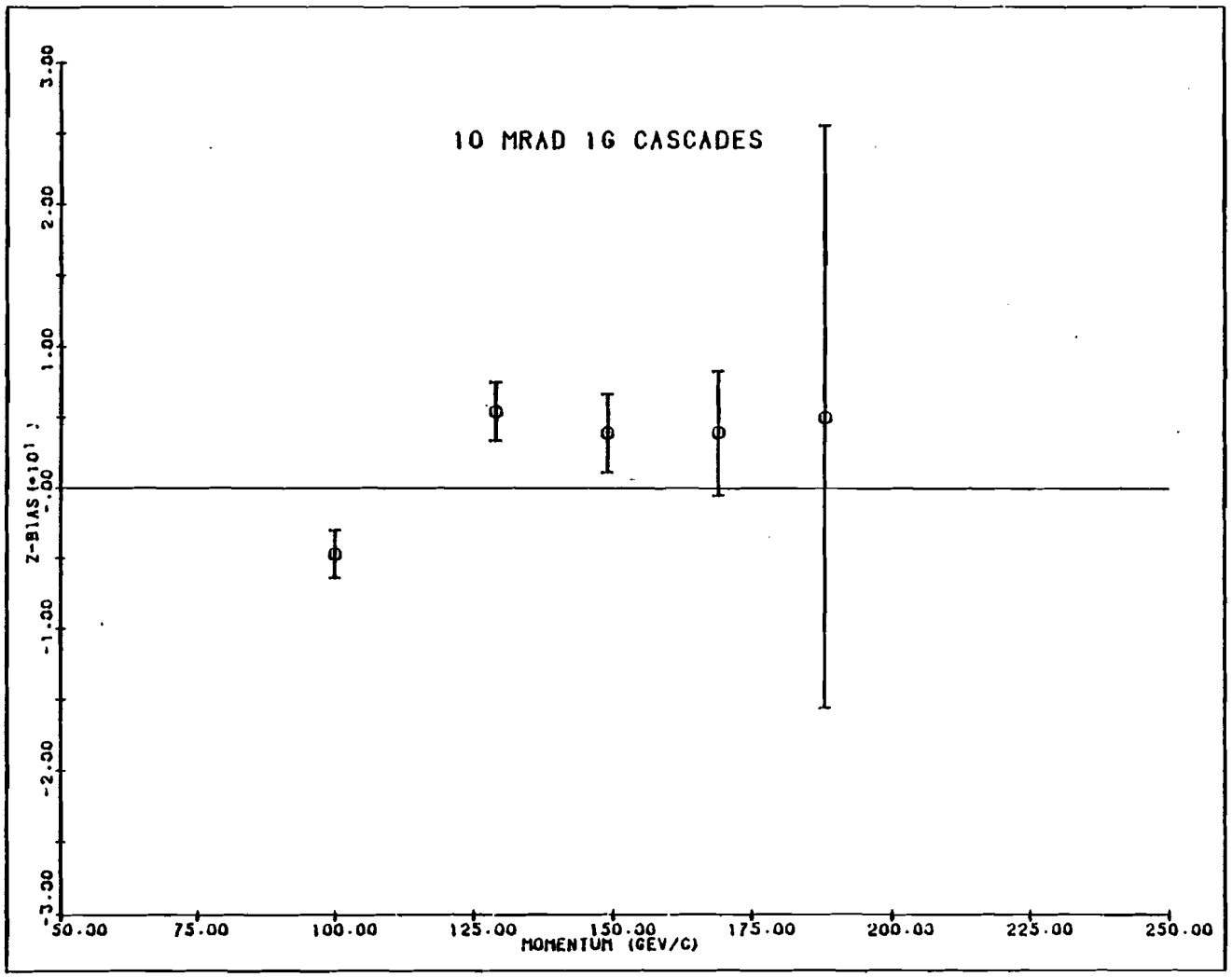

FIGURE (5.2.12) z-bias from 10 mrad 1G Ξ^0's

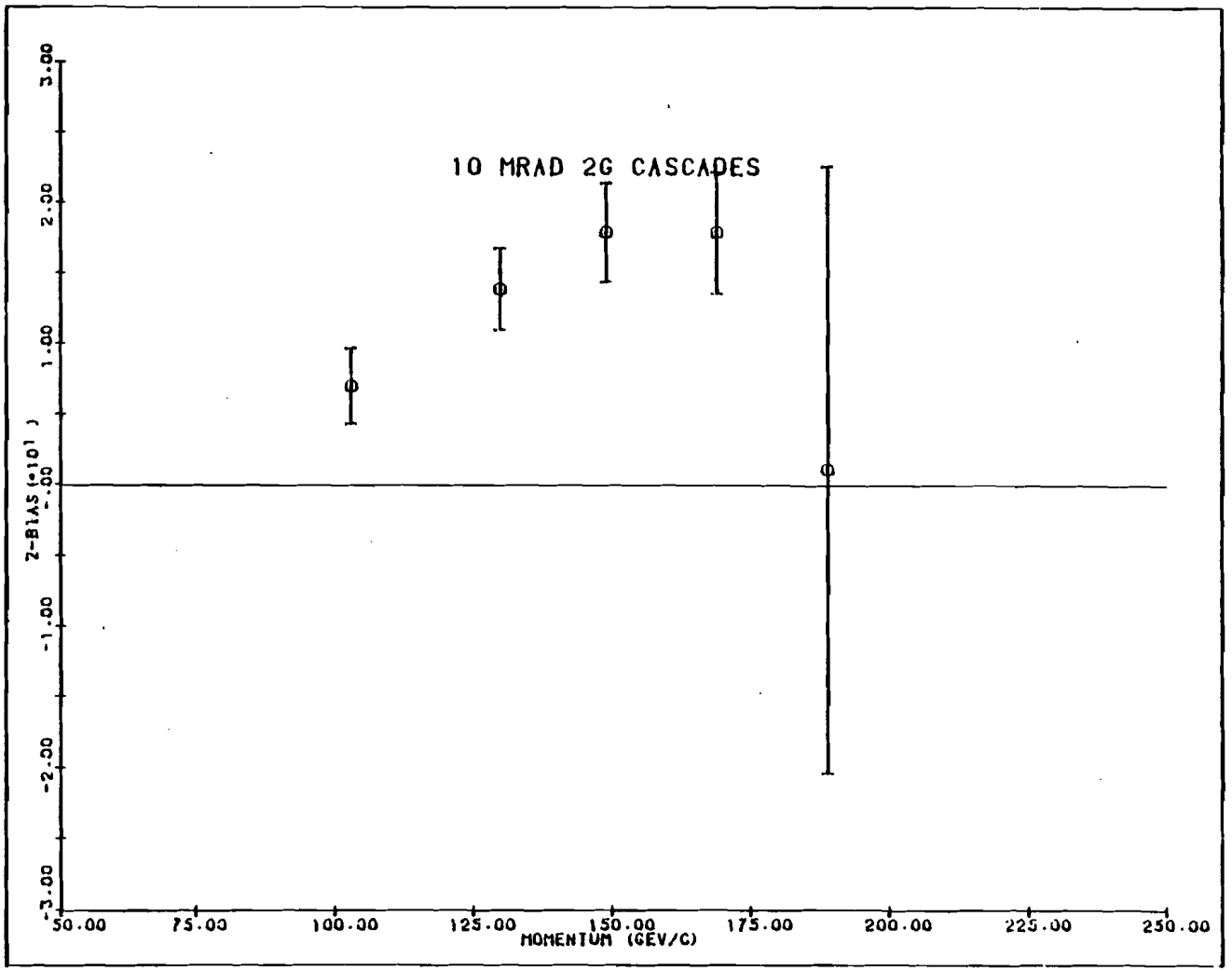

FIGURE (5.2.13) z-bias from 10 mrad 2G Ξ^0's

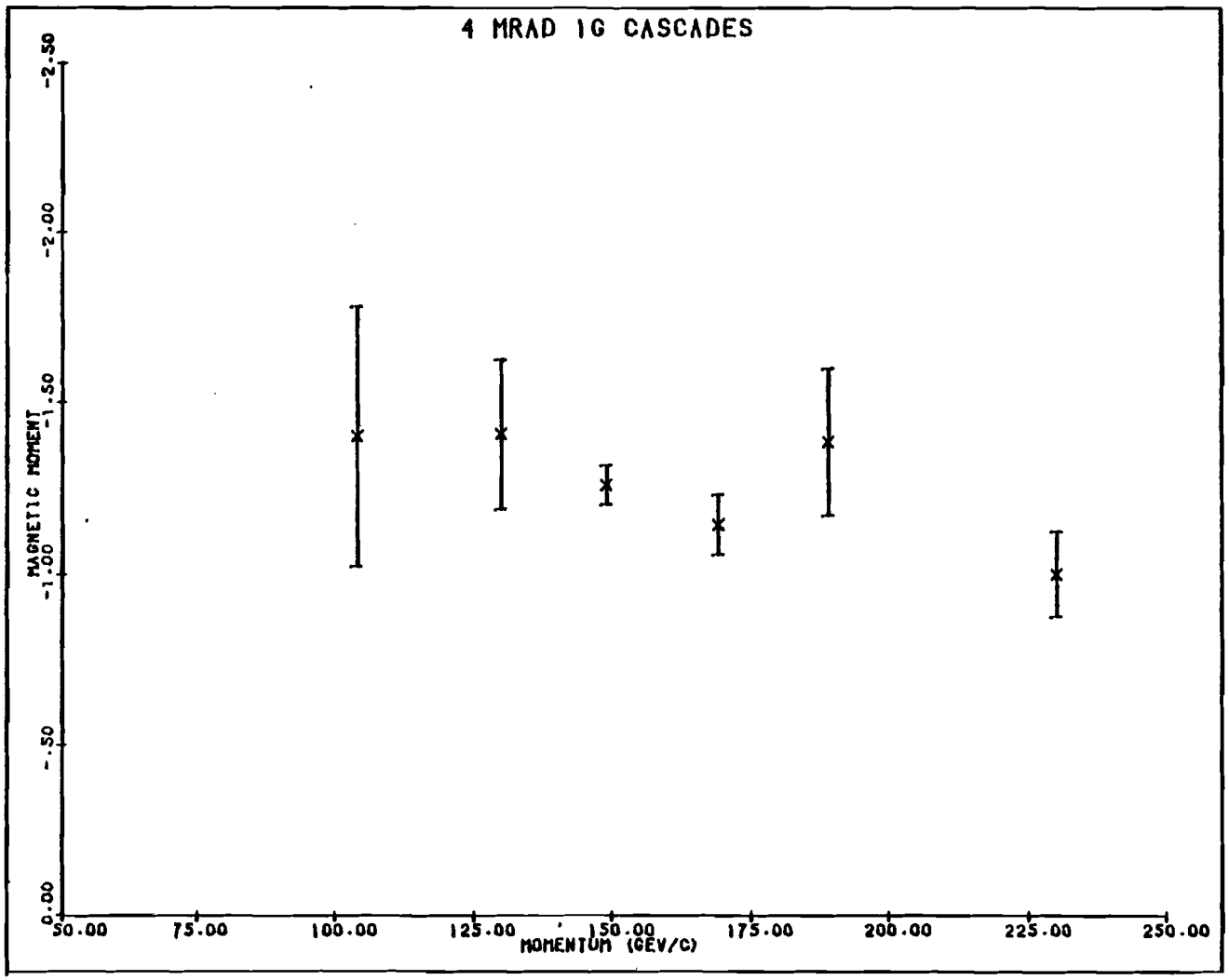

FIGURE (5.2.14) μ_{Ξ^0} from 4 mrad 1G Ξ^0's

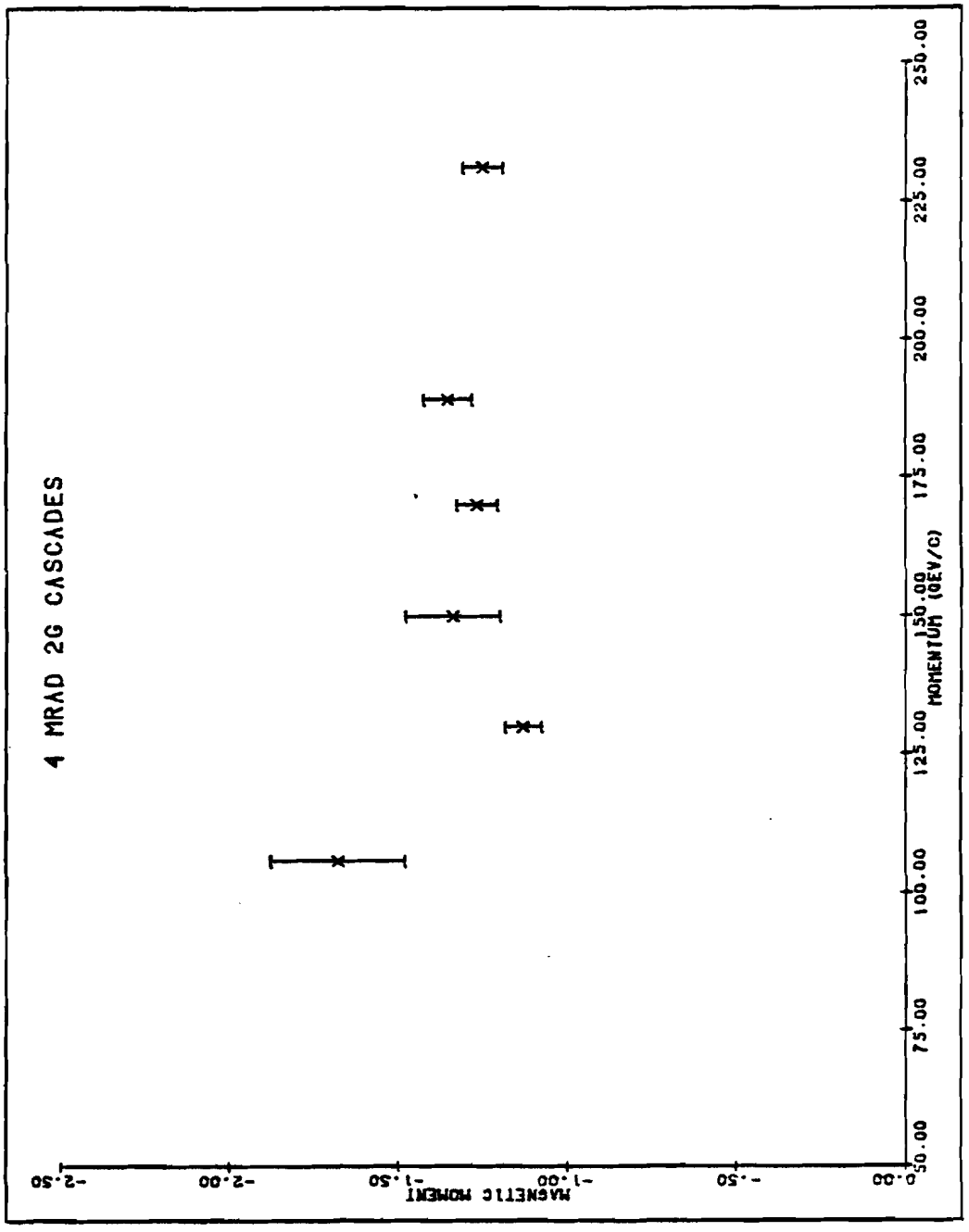

FIGURE (5.2.15) μ_{Ξ^0} from 4 mrad 2G Ξ^0's

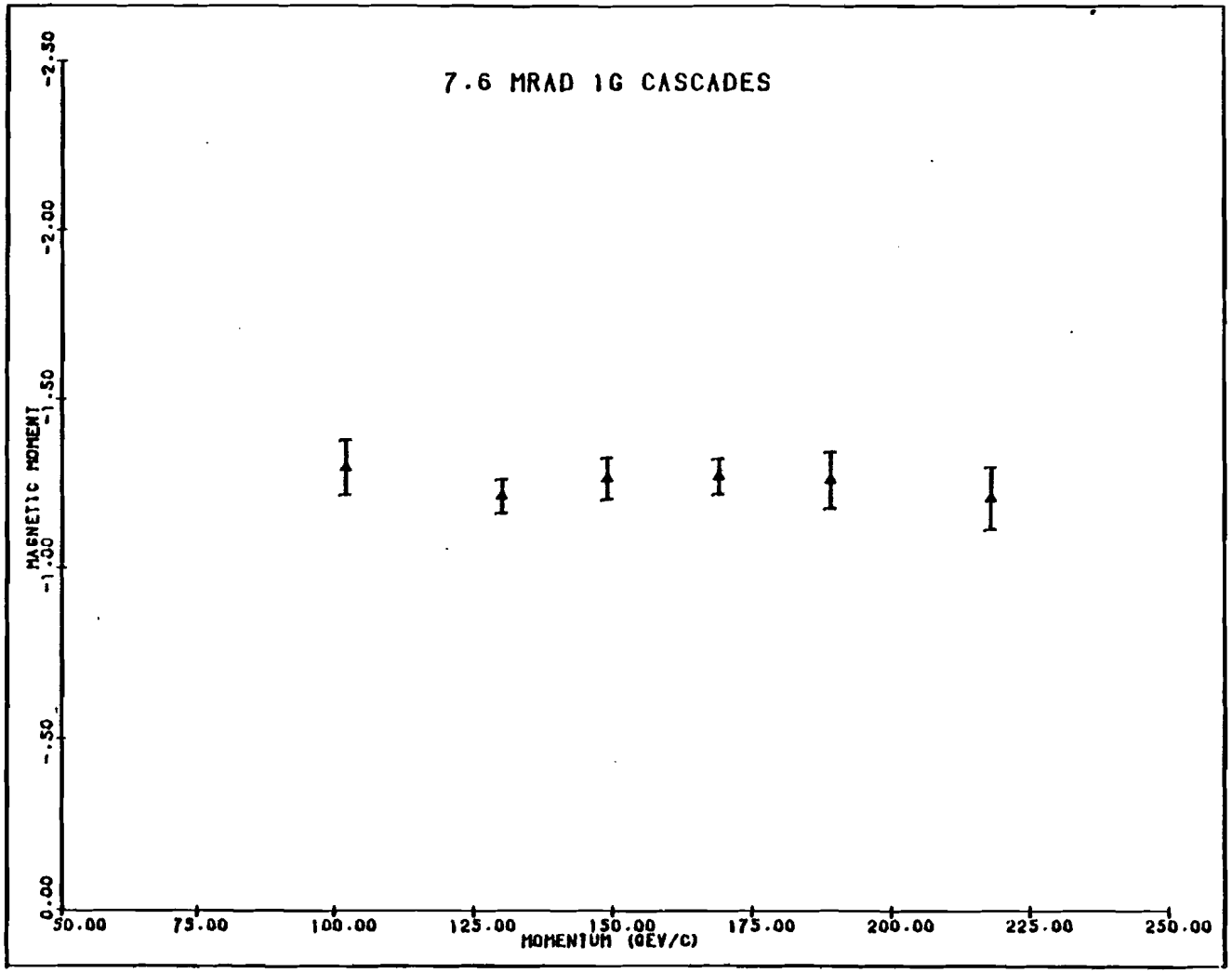

FIGURE (5.2.16) μ_{Ξ^0} from 7.6 mrad 1G Ξ^0's

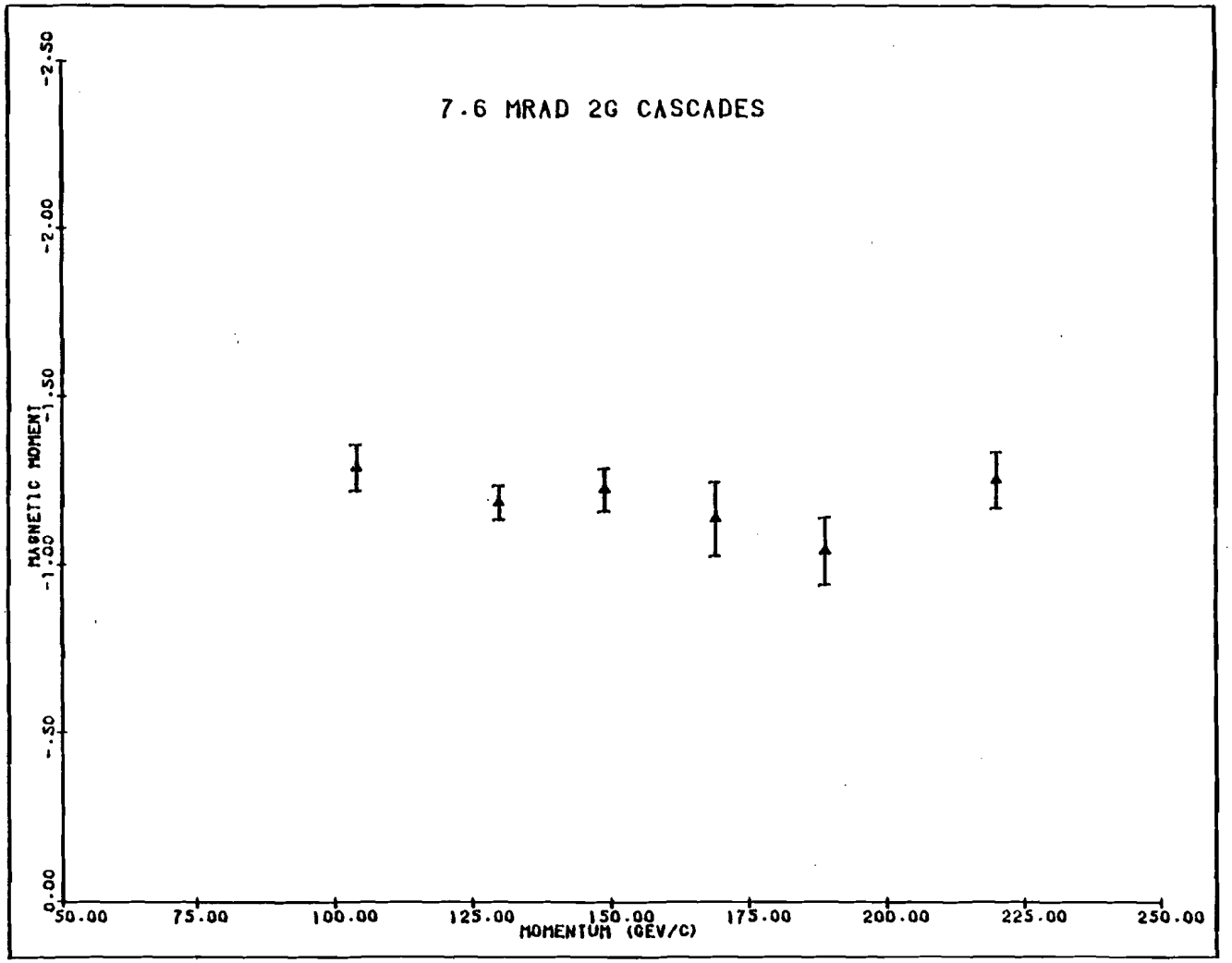

FIGURE (5.2.17) μ_{Ξ^0} from 7.6 mrad 2G Ξ^0's

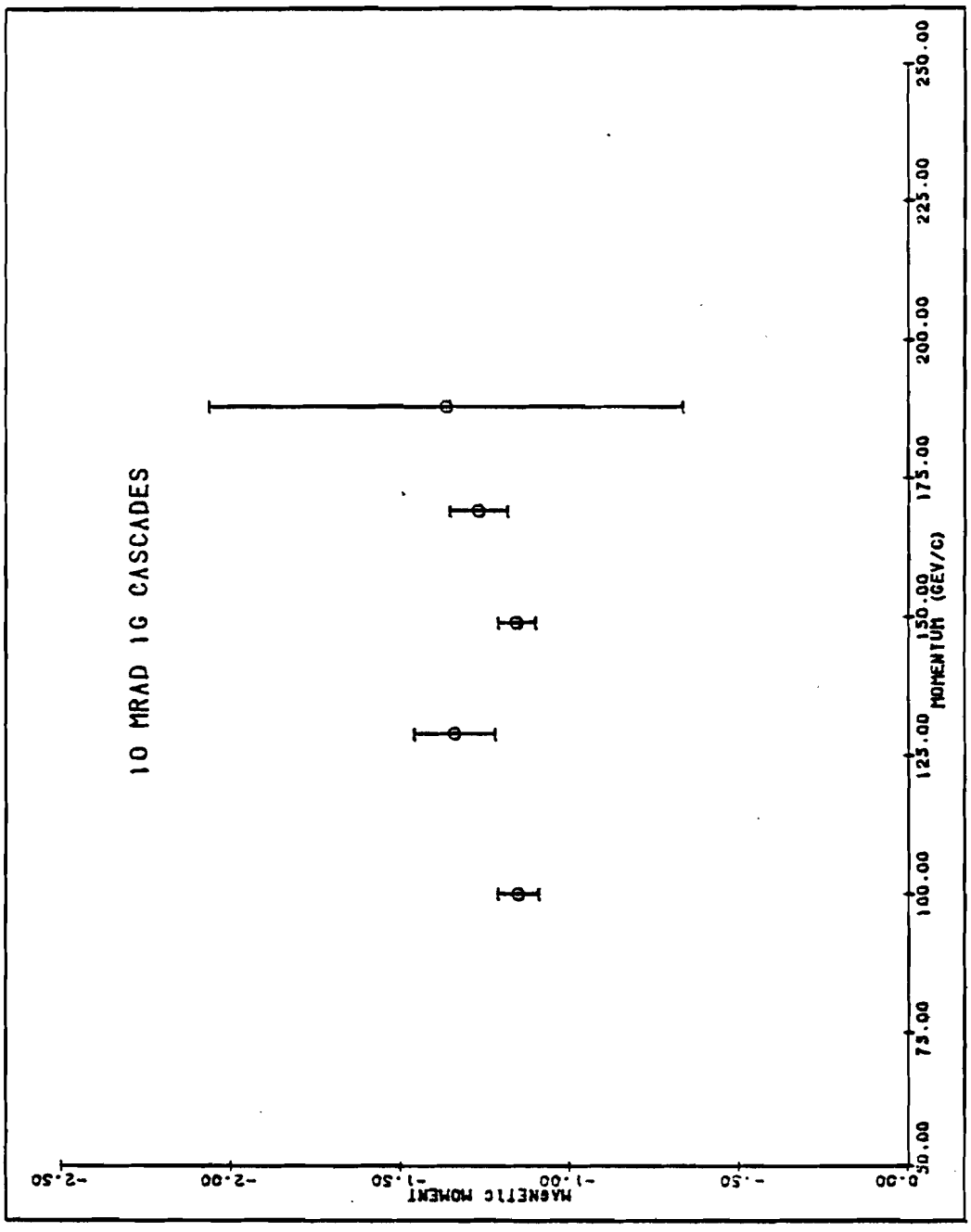

FIGURE (5.2.18) $M_{\gamma\gamma}$ from 10 mrad 1G π^0's

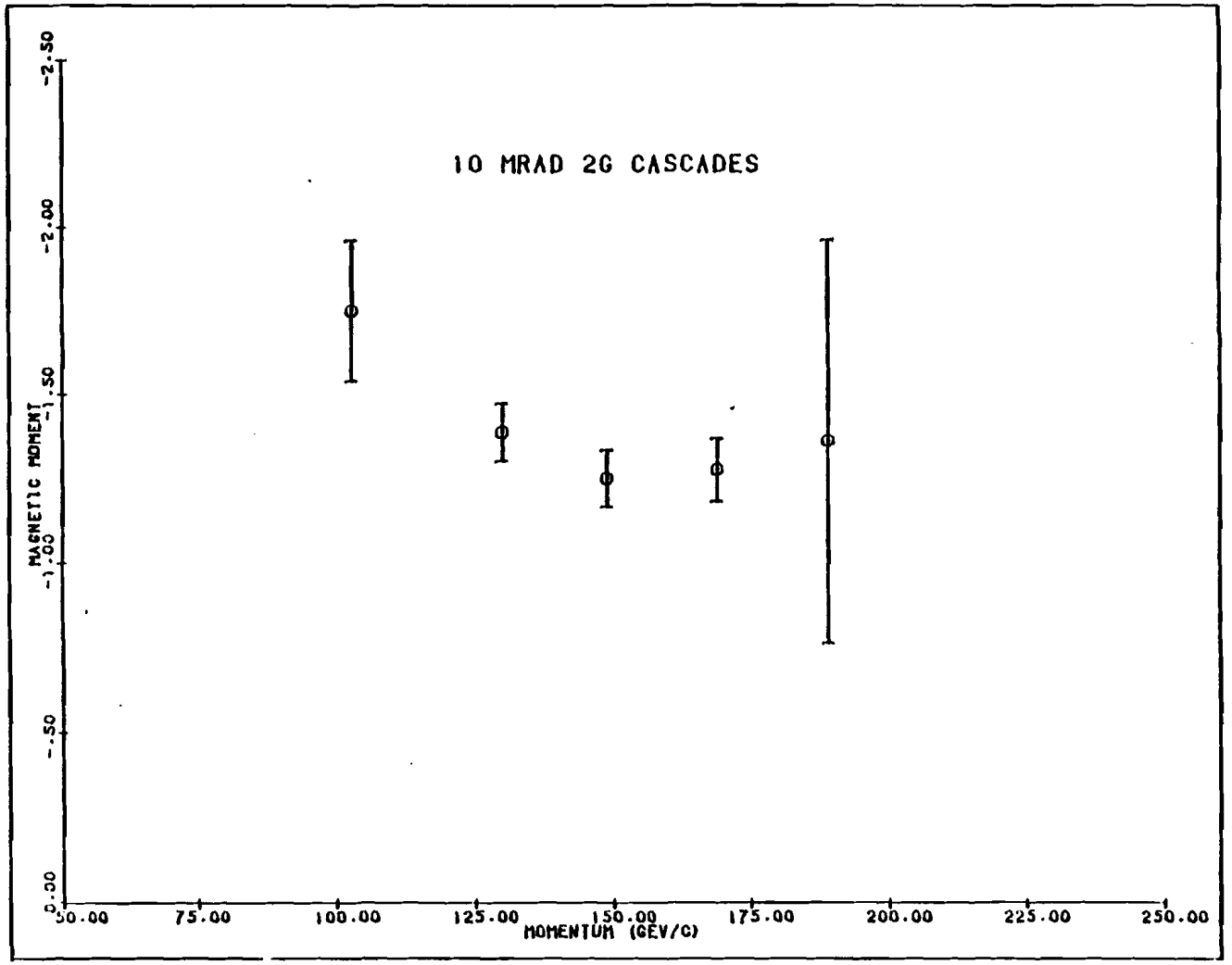

FIGURE (5.2.19) μ_{Ξ^0} from 10 mrad 2G Ξ^0's

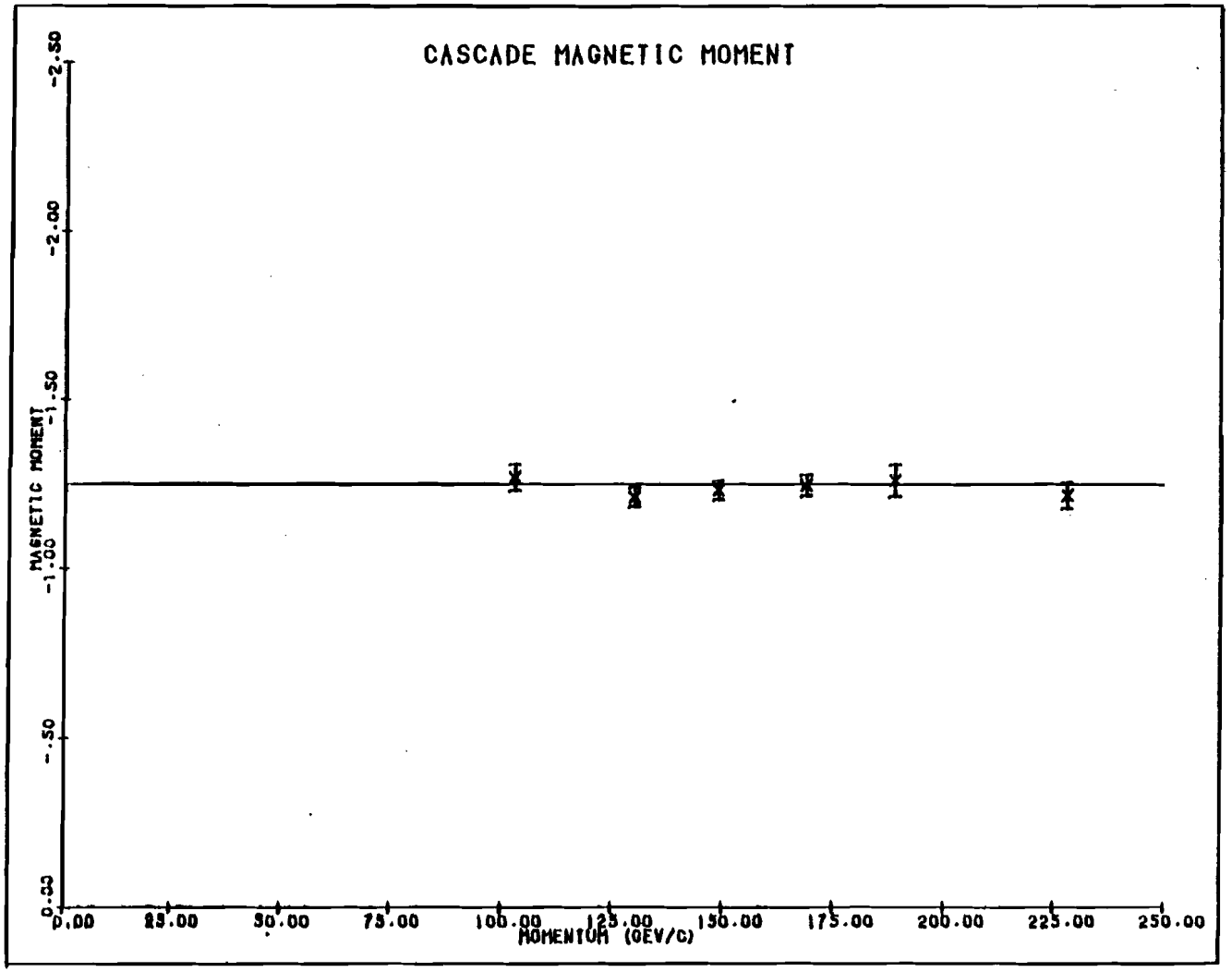

FIGURE (5.2.20) Momentum dependence of Ξ^0 magnetic moment, all data combined

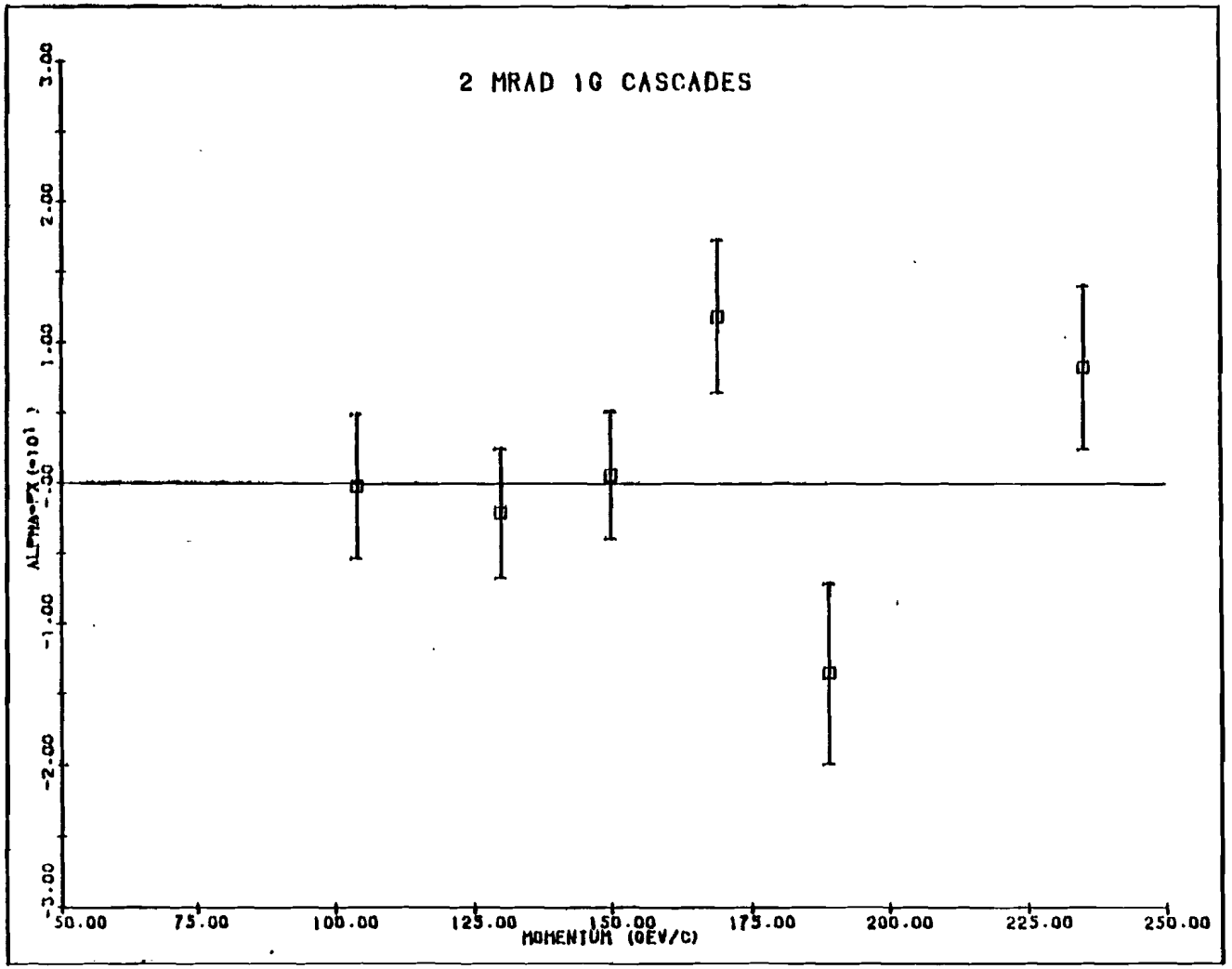

FIGURE (5.2.21) x-polarization of 2 mrad 1G Ξ^0's

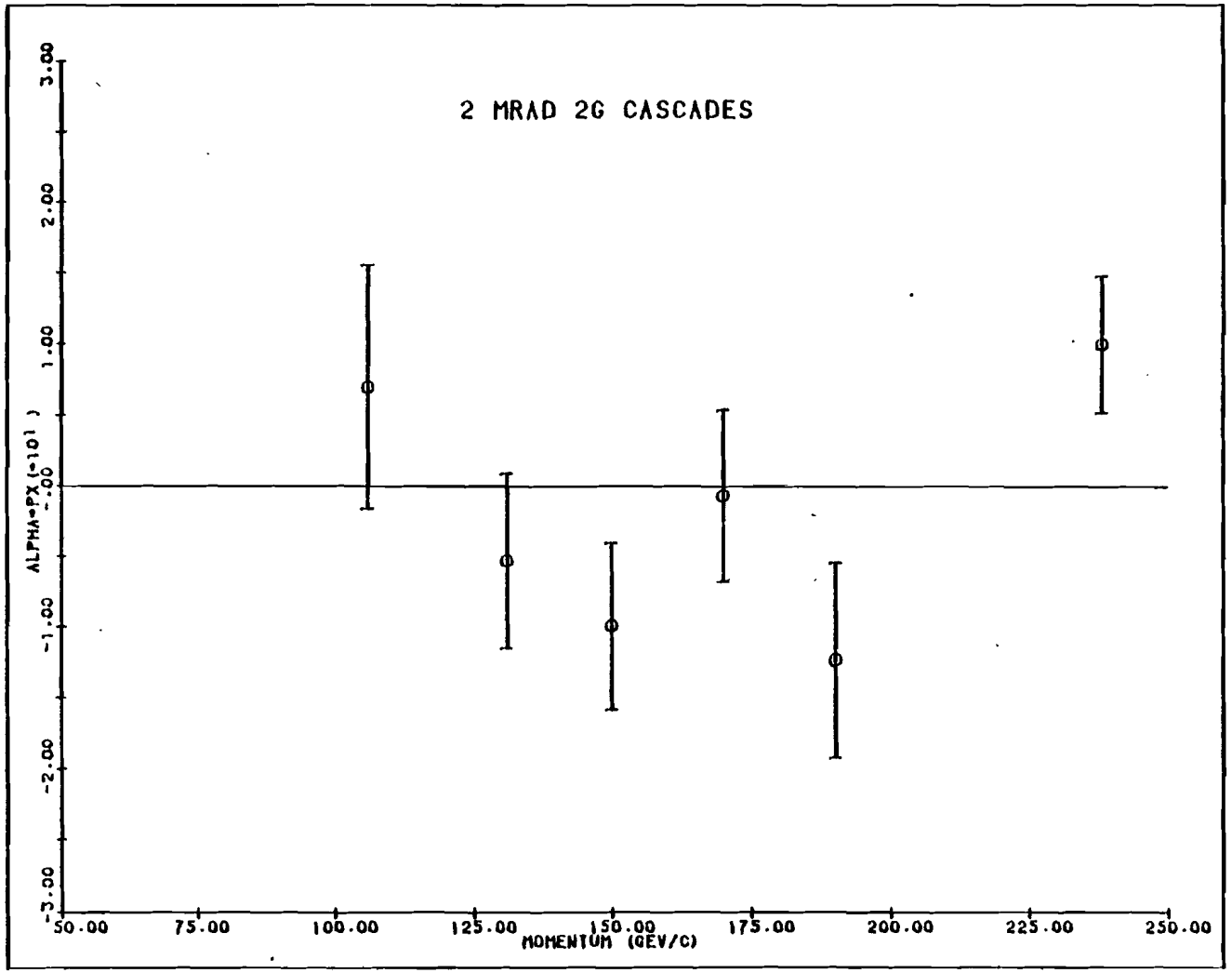

FIGURE (5.2.22) x-polarization of 2 mrad 2G Ξ^0's

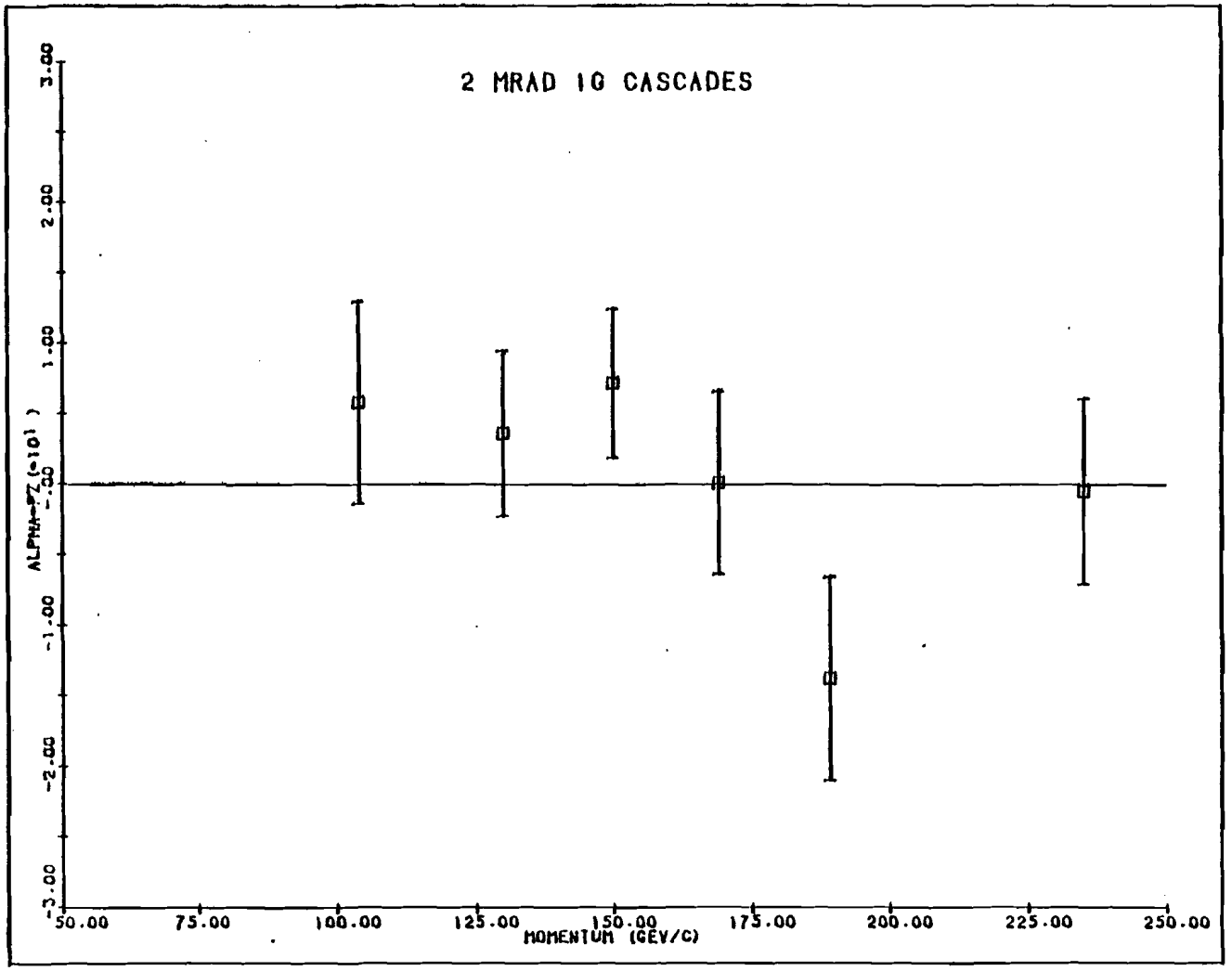

FIGURE (5.2.23) z-polarization of 2 mrad 1G Ξ^0's

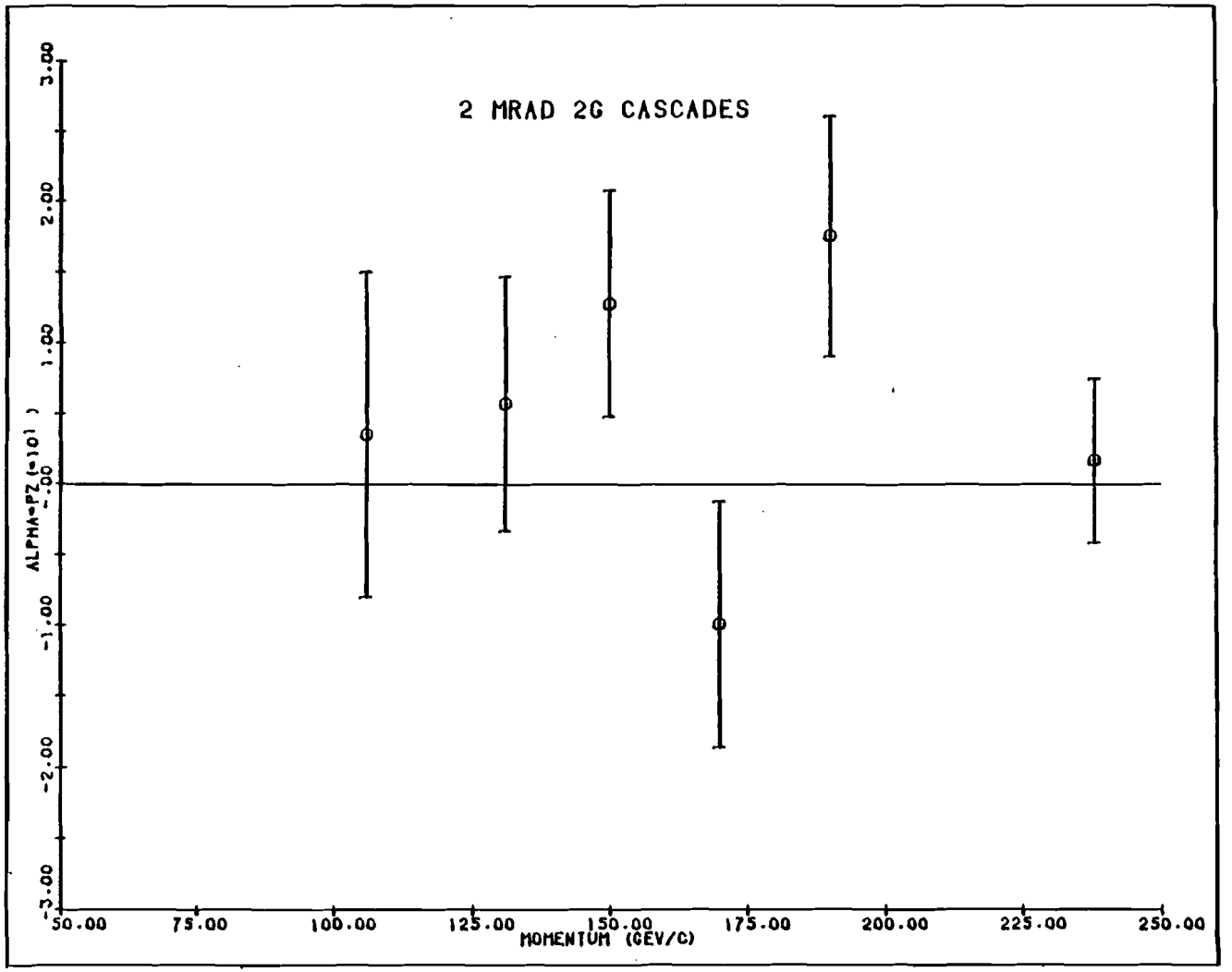

FIGURE (5.2.24) z-polarization of 2 mrad 2G Ξ^0's

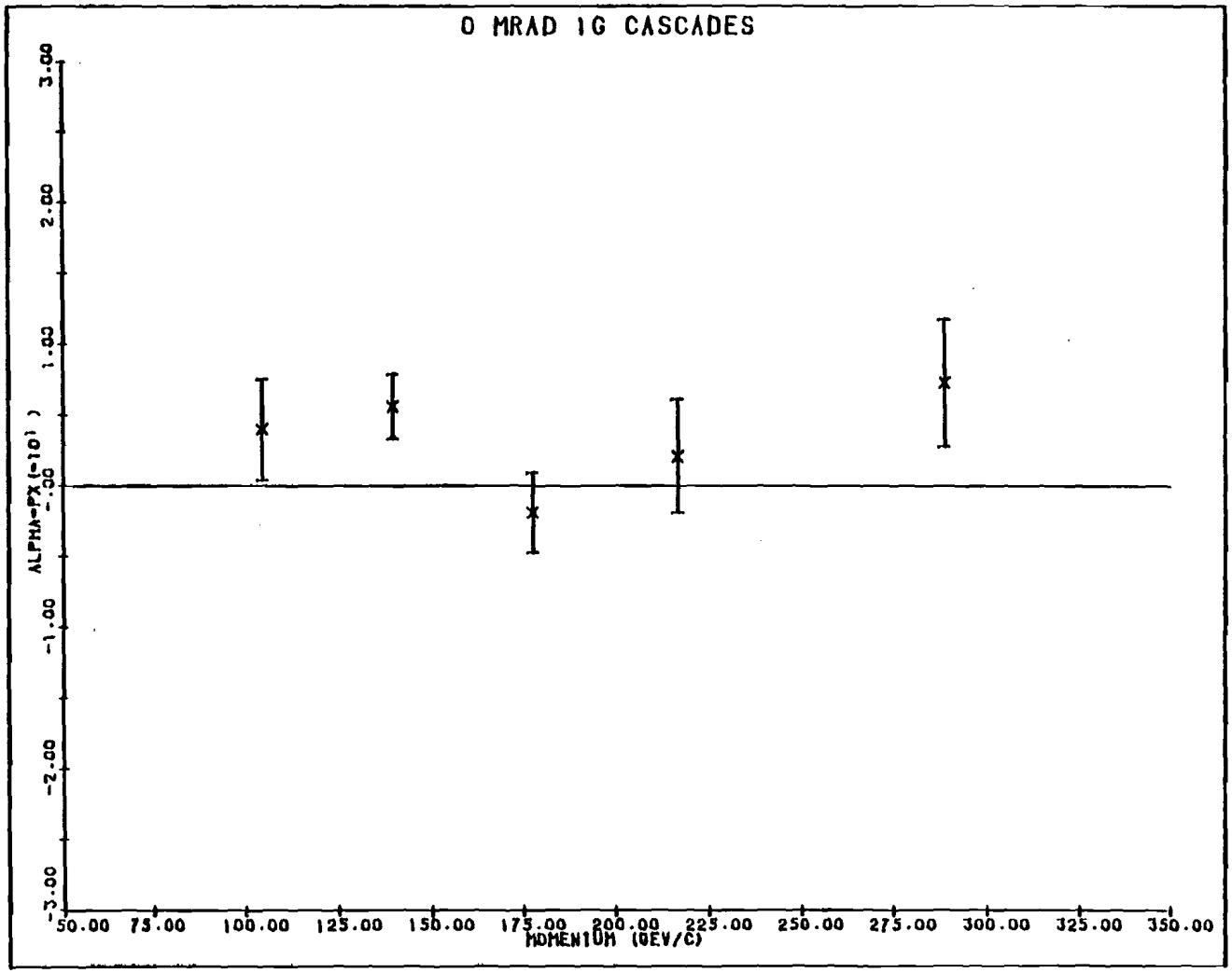

FIGURE (5.2.25) x-polarization of 0 mrad 1G Ξ^0's

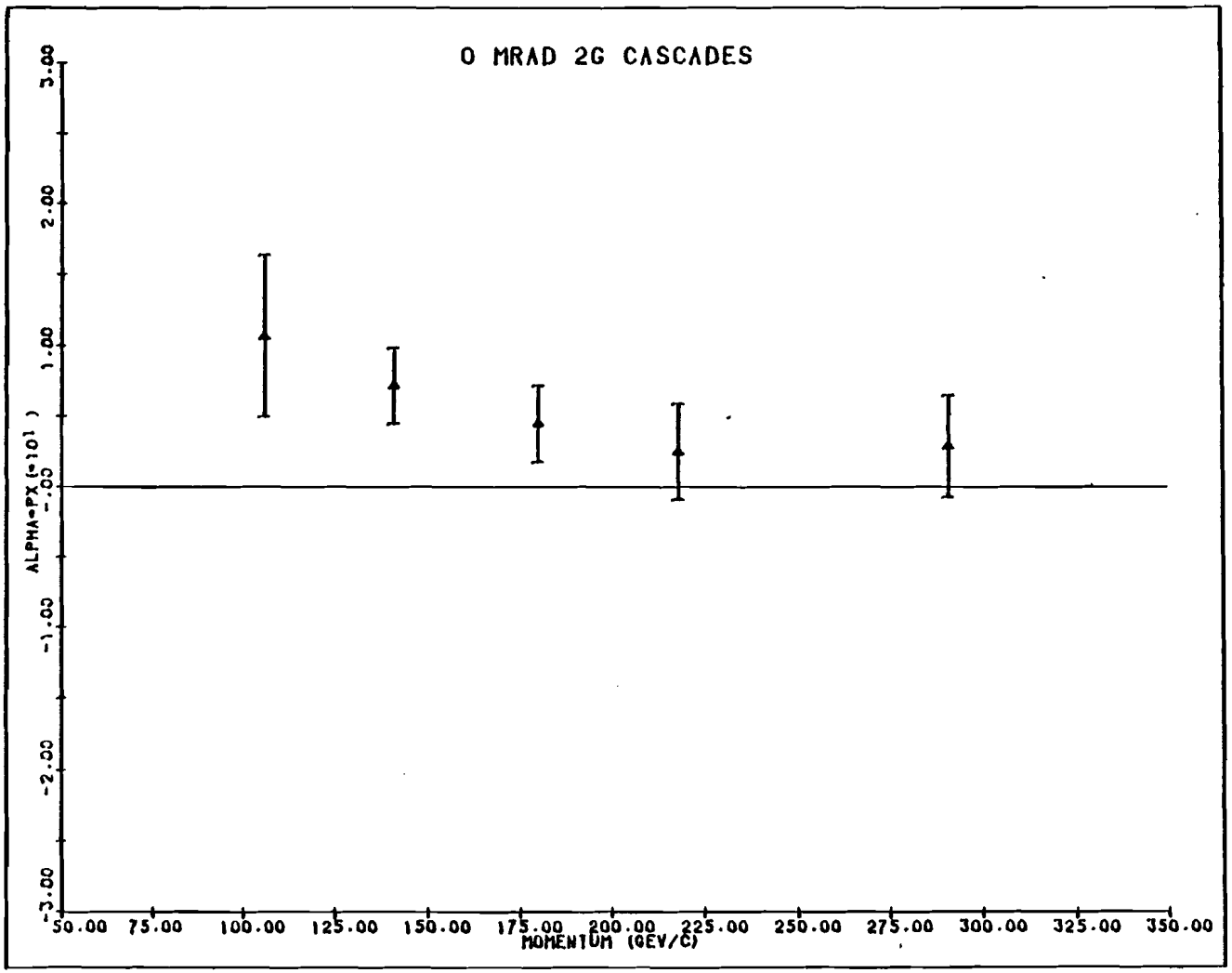

FIGURE (5.2.26) x-polarization of 0 mrad 2G Ξ^0's

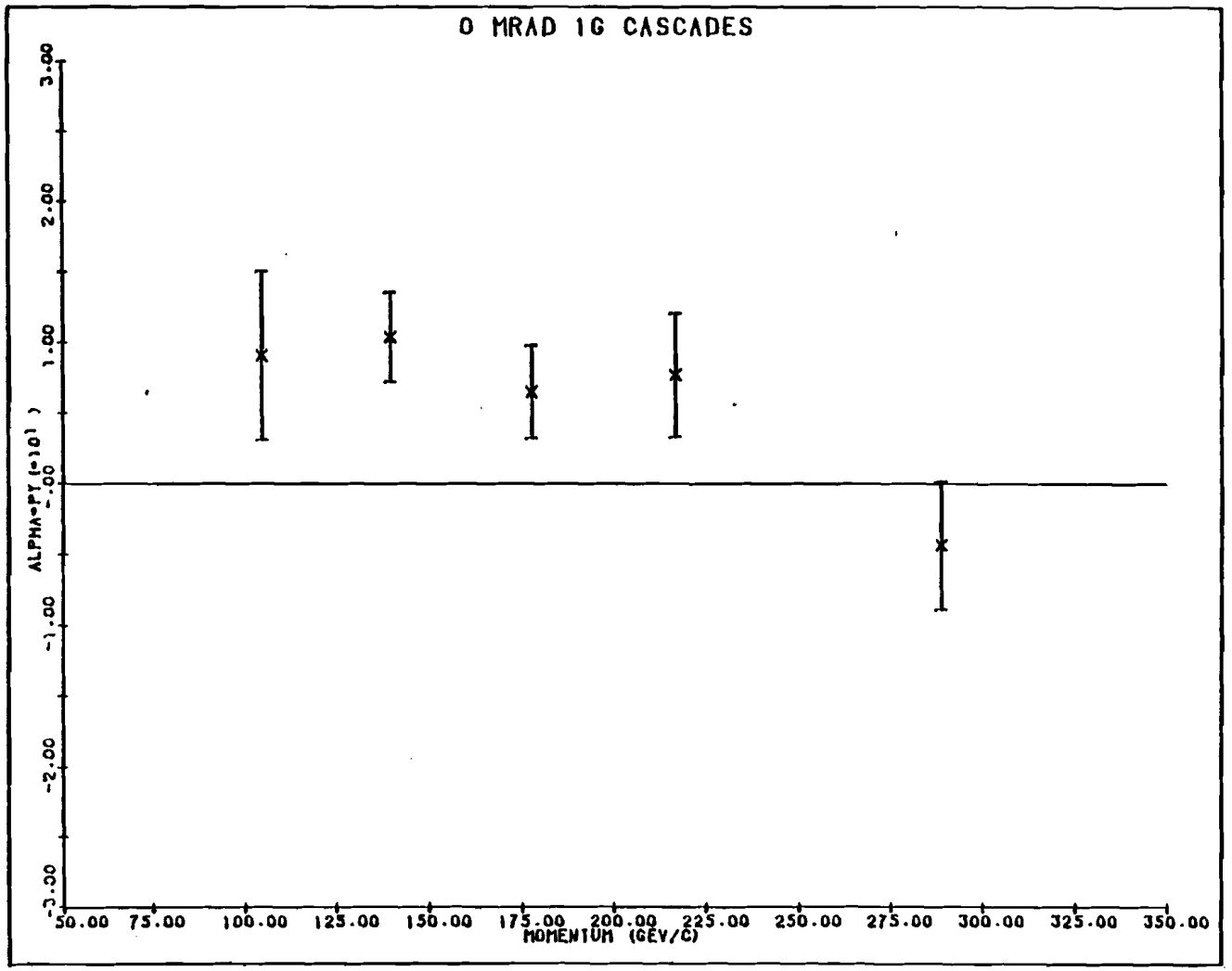

FIGURE (5.2.27) y-polarization of 0 mrad 1G Ξ^0's

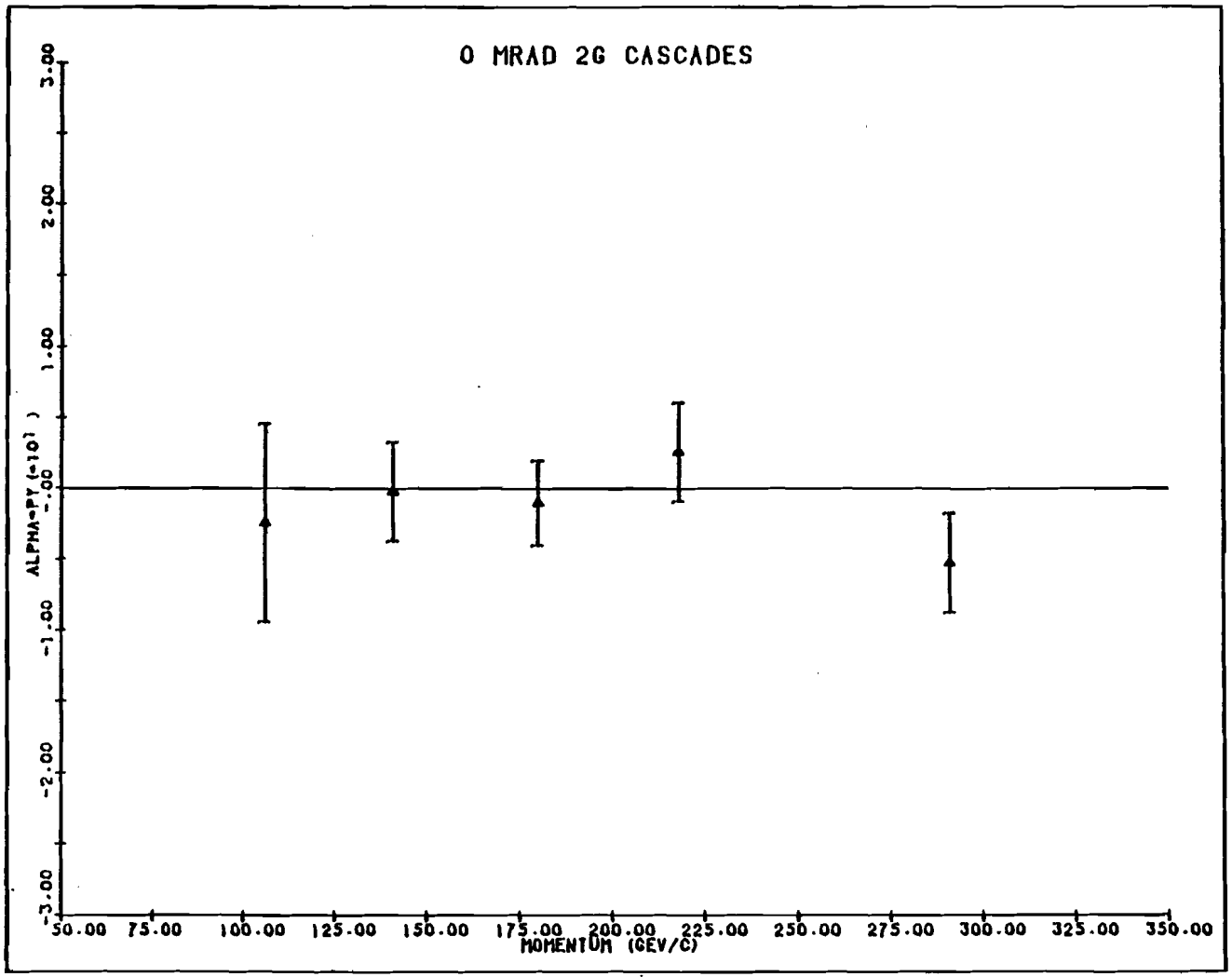

FIGURE (5.2.28) y-polarization of 0 mrad 2G Ξ^0's

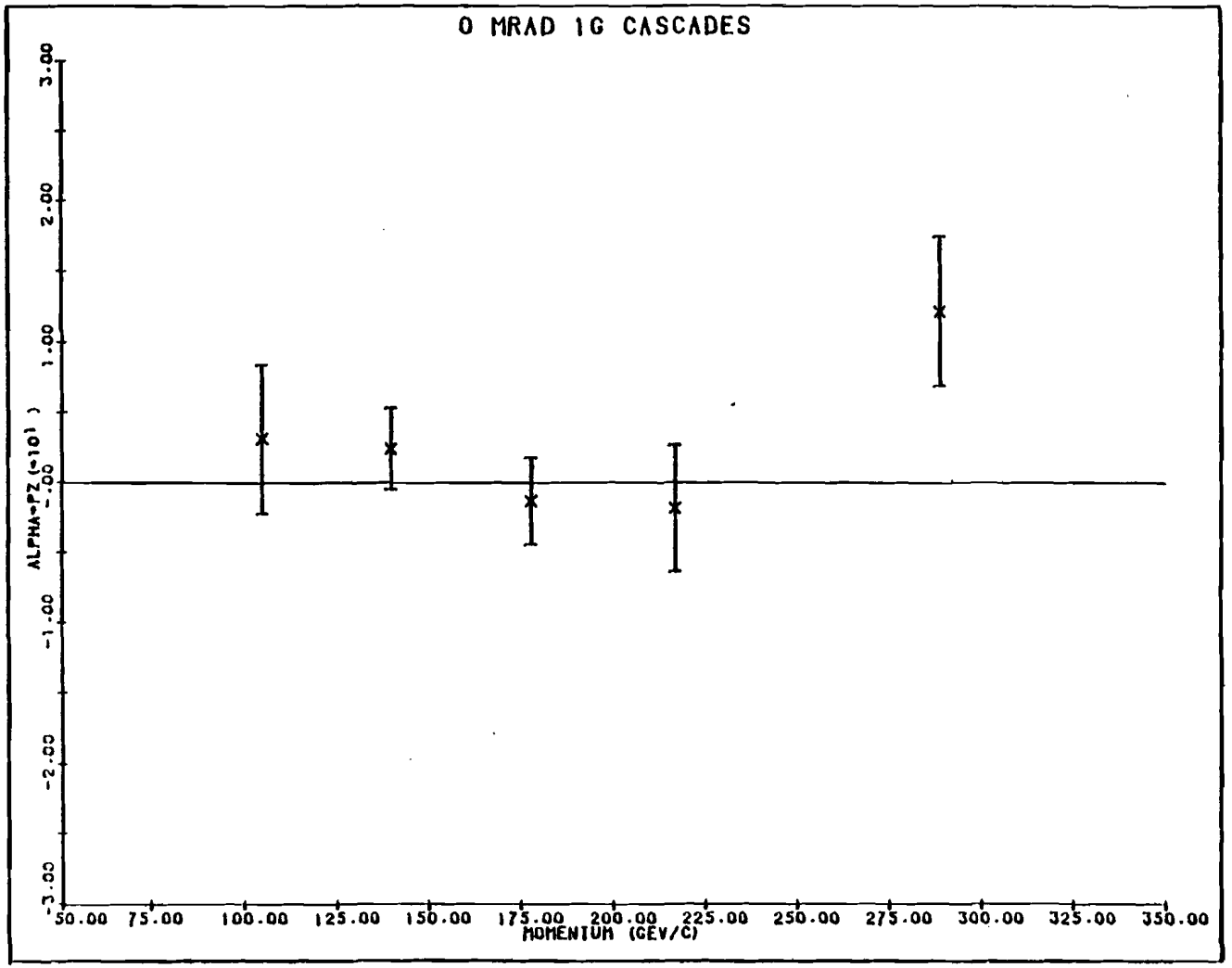

FIGURE (5.2.29) z-polarization of 0 mrad 1G Ξ^0's

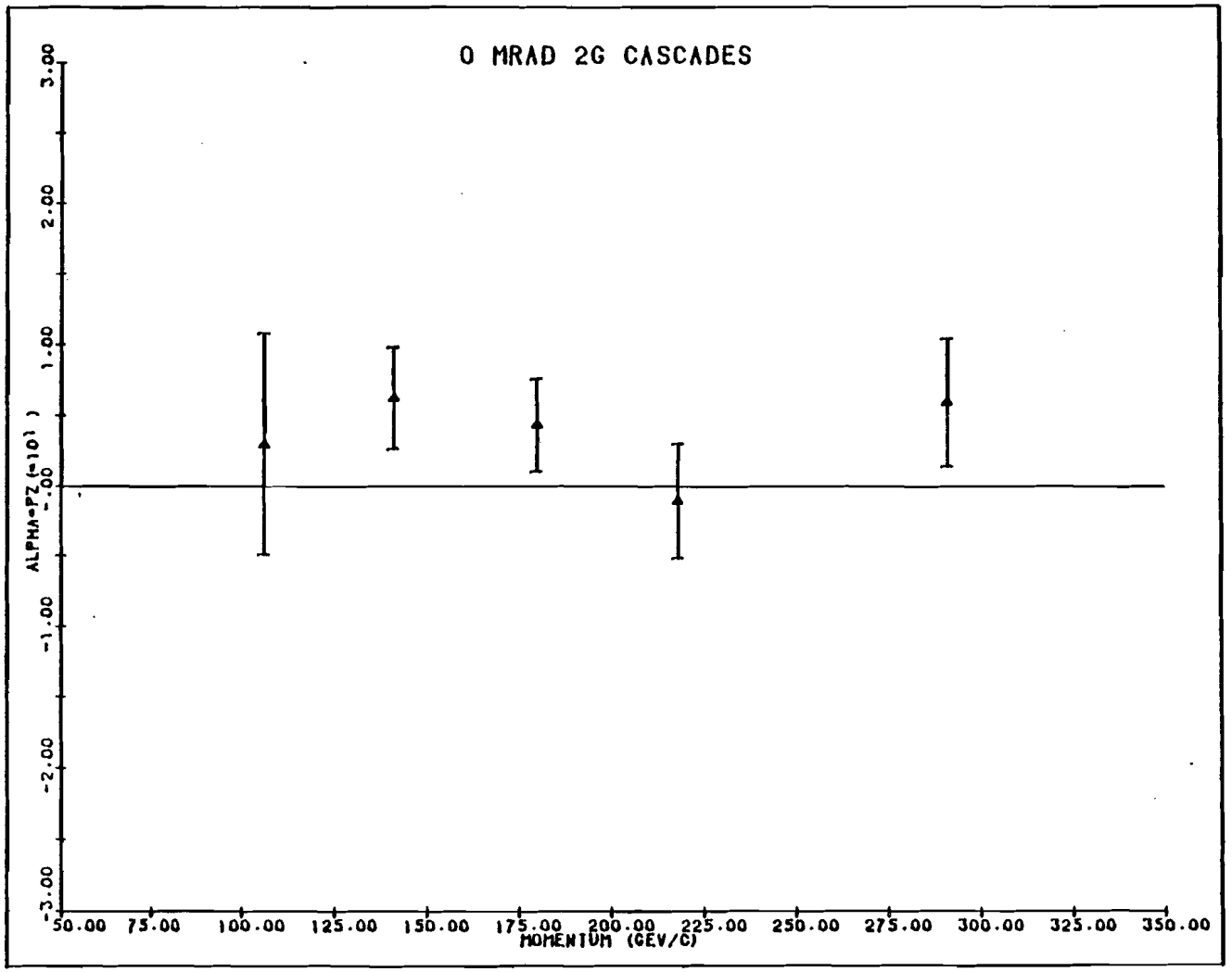

FIGURE (5.2.30) z-polarization of 0 mrad 2G Ξ^0's

The fitted results, using the combined momentum data sets, are presented for the separate 4, 7.6, and 10 mrad 1G and 2G samples in Table 24, which summarizes the overall polarization and magnetic moment obtained from each data set.

Since the data were taken at fixed Lab production angles, and binned according to the momentum of the parent Ξ^0 (or Λ for the beam Λ's), the average transverse momentum corresponding to each momentum bin was obtained from the product

$$p_T = p \times \theta \qquad (5.2.5)$$

where p is the momentum in GeV/c and θ is the production angle in mrad. Using this prescription the p_T values listed in the tables were obtained.

The sign of the Ξ^0 polarization for the 4, 7.6, and 10 mrad data was consistent with being the same as that for the corresponding beam Λ polarization, i.e. negative at positive production angle.

The Ξ^0 polarization for the 7.6 mrad data is plotted as a function of p_T in Fig. (5.2.31), together with the Λ polarization of the 7.2 mrad data from reference [2] for comparison purposes. The $\bar{\Lambda}$ data from this reference are also shown. Clearly the Ξ^0 and Λ polarizations agree very closely.

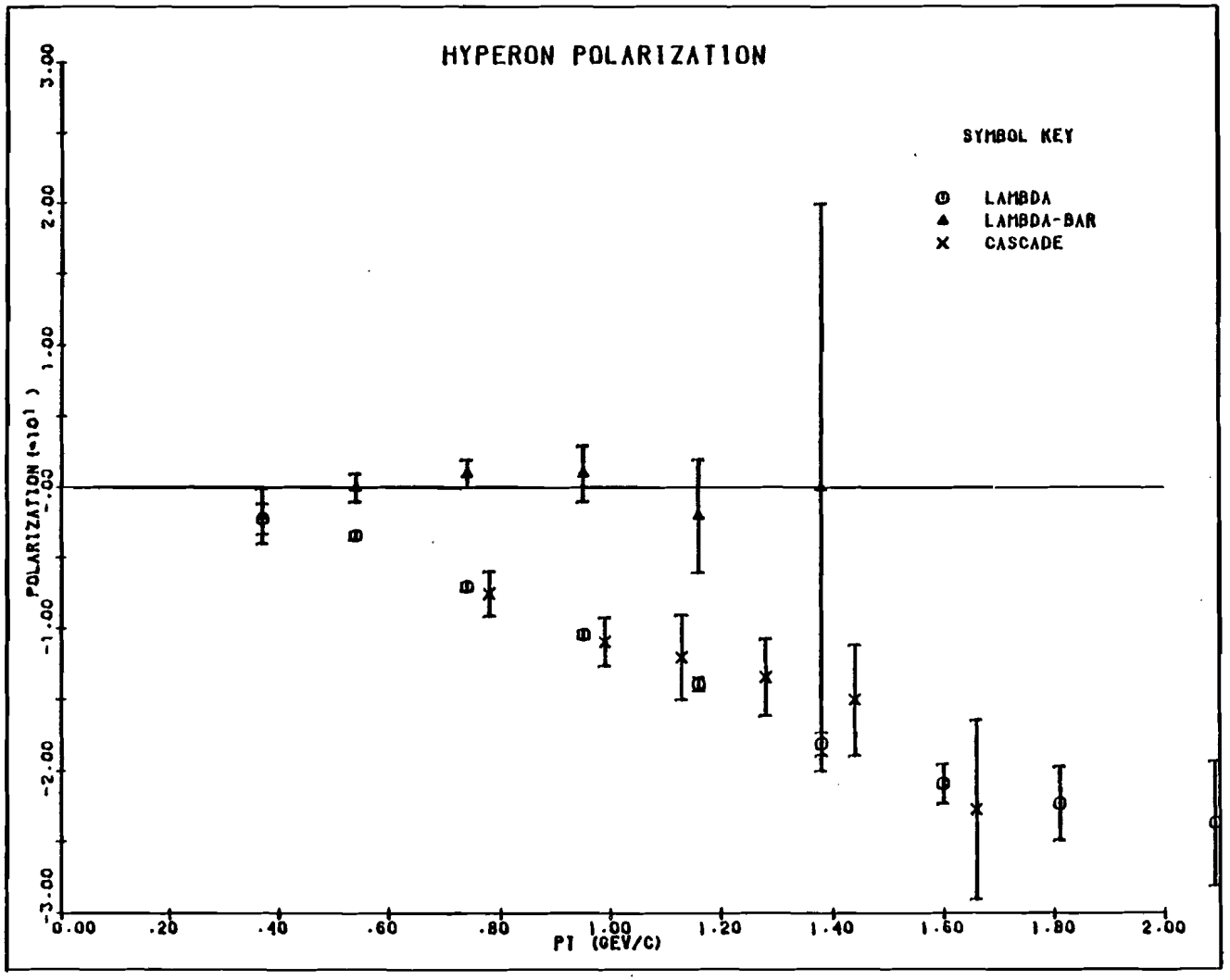

FIGURE (5.2.31) Transverse-momentum dependence of hyperon polarizations (at ∿7½ mrad LAB production angle)

The Ξ^0 polarization is plotted separately for each of the 4, 7.6, and 10 mrad data sets, as a function of p_T in Fig. (5.2.32). There is an obvious tendency for the polarization at a fixed value of p_T to be larger at the lower production angle. This is presumably an x-dependence, where the Feynman x-variable is defined as

$$x = p_L / p \qquad (5.2.6)$$

and p_L is the longitudinal momentum (effectively the z-component of momentum in this experiment, where $p_z >> p_x$ or p_y). Because of this dependence, the different production angle samples cannot be combined directly in terms of the p_T -binning already discussed. It seems most reasonable to combine the samples in terms of the Ξ^0 momentum bins directly, which gives Fig. (5.2.33).

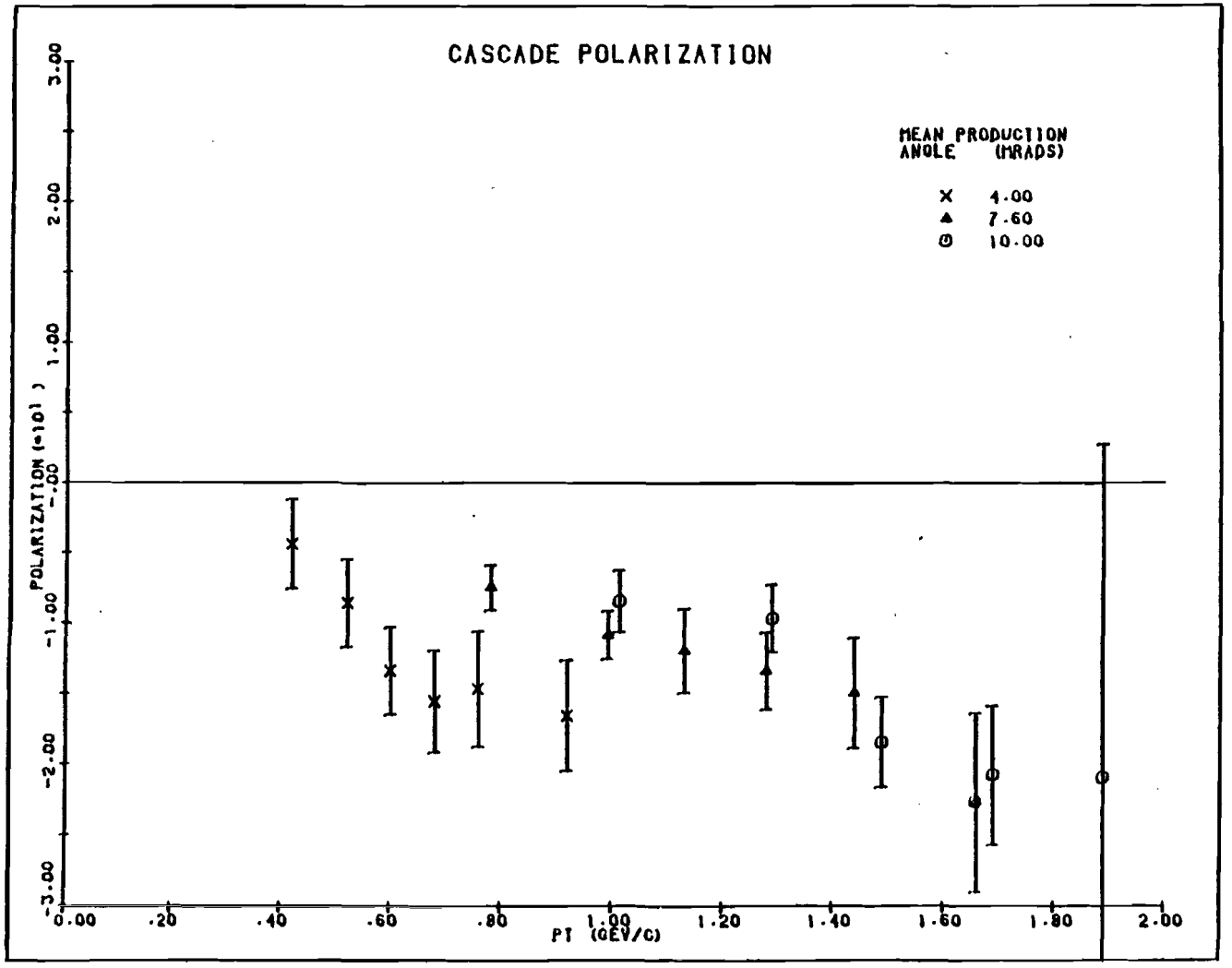

FIGURE (5.2.32) Transverse-momentum dependence of Ξ^0 polarization at each fixed LAB production angle

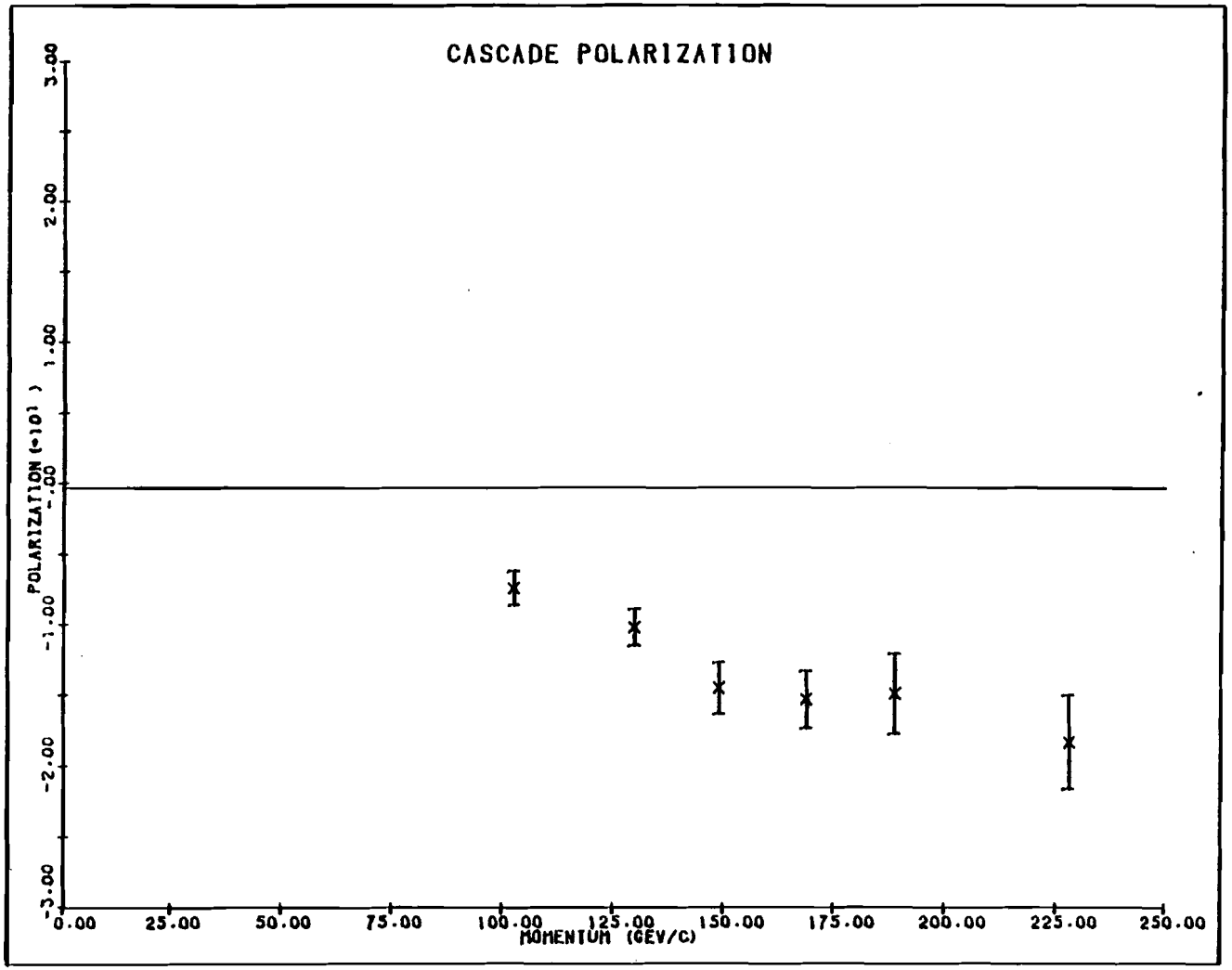

FIGURE (5.2.33) Momentum dependence of Ξ^0 polarization, all production angles combined

5.3 The Measurement of α_{Ξ^0}.

5.3.1 The 0 mrad data

The 0 mrad data were analyzed first, since for these the daughter lambda polarization is due only to the alpha term of the decay. The outstanding problem with these data is that they were more susceptible to background contamination than those at non-zero production angles. To purify the sample an R_Λ^2 cut was applied. The cut required that $R_\Lambda^2 \geq 30$ mm^2 for the daughter Λ's. This was justified by examination of the ($\Lambda\pi^0$) invariant mass plots, and the χ^2_Ξ distributions. Scatter-plots of the R_Λ^2 against the χ^2_Ξ showed clearly that high χ^2_Ξ events tended to correlate with small R_Λ^2 values, as would be expected for contamination of the Ξ^0 sample by beam Λ's, presumably with accidental γ signals. This can be seen in Figs. (5.3.1) and (5.3.2), which are typical scatter-plots (from 7.6 mrad data) before any cuts. From these plots it was decided that $R_\Lambda^2 \geq 30$ was a satisfactory compromise to the problem of maximizing the background Λ's cut, while minimizing the true Ξ^0 events cut. Comparison of the various parameter distributions of the Ξ^0's before and after this cut with those of Monte Carlo Ξ^0 events, with

similar momentum spectra, confirmed this decision. The results of the α_{Ξ^0} analysis of the 0 mrad data, with this cut applied, are presented in Tables 25 and 26 for the 1G and 2G momentum-binned samples. The results from the combined 0 mrad data are given in Table 27 . The combined value of

$$\alpha_\Lambda \alpha_{\Xi^0} = -0.275 \pm 0.014 \qquad (5.3.1)$$

agrees with that obtained as the weighted average of the separate samples

$$\alpha_\Lambda \alpha_{\Xi^0} = -0.275 \pm 0.015$$

This number resulted from 21 000 events; as usual the error quoted is entirely statistical. The momentum-binned results are shown in Fig. (5.3.3) . The highest and lowest momentum bins were discarded from the analysis, as being most likely to be affected by poorly-understood biases, and the weighted averages obtained for the 1G and 2G samples. Again, the weighted average of these two values was, over the cascade momentum range 120-240 GeV/c,

$$\alpha_\Lambda \alpha_{\Xi^0} = -0.275 \pm 0.016 \qquad (5.3.2)$$

so all the results are consistent. Assuming a value of $\alpha_\Lambda = -0.642 \pm 0.013$ in Eq. (5.3.1) gave

$$\alpha_{\Xi^0} = -0.428 \pm 0.024 \qquad (5.3.3)$$

The 1G and 2G values are consistent and momentum-independent over the range 120-240 GeV/c. The $\alpha_\Lambda \alpha_{\Xi^0}$ value of each sample stabilized after a cut of about $R_\Lambda^2 > 15$ mm^2, although 30 mm^2 was used. Cutting events for

which the energy of the γ in chamber 3 was less than 3 GeV (instead of the usual 1 GeV cut) did not affect the 1G results at all.

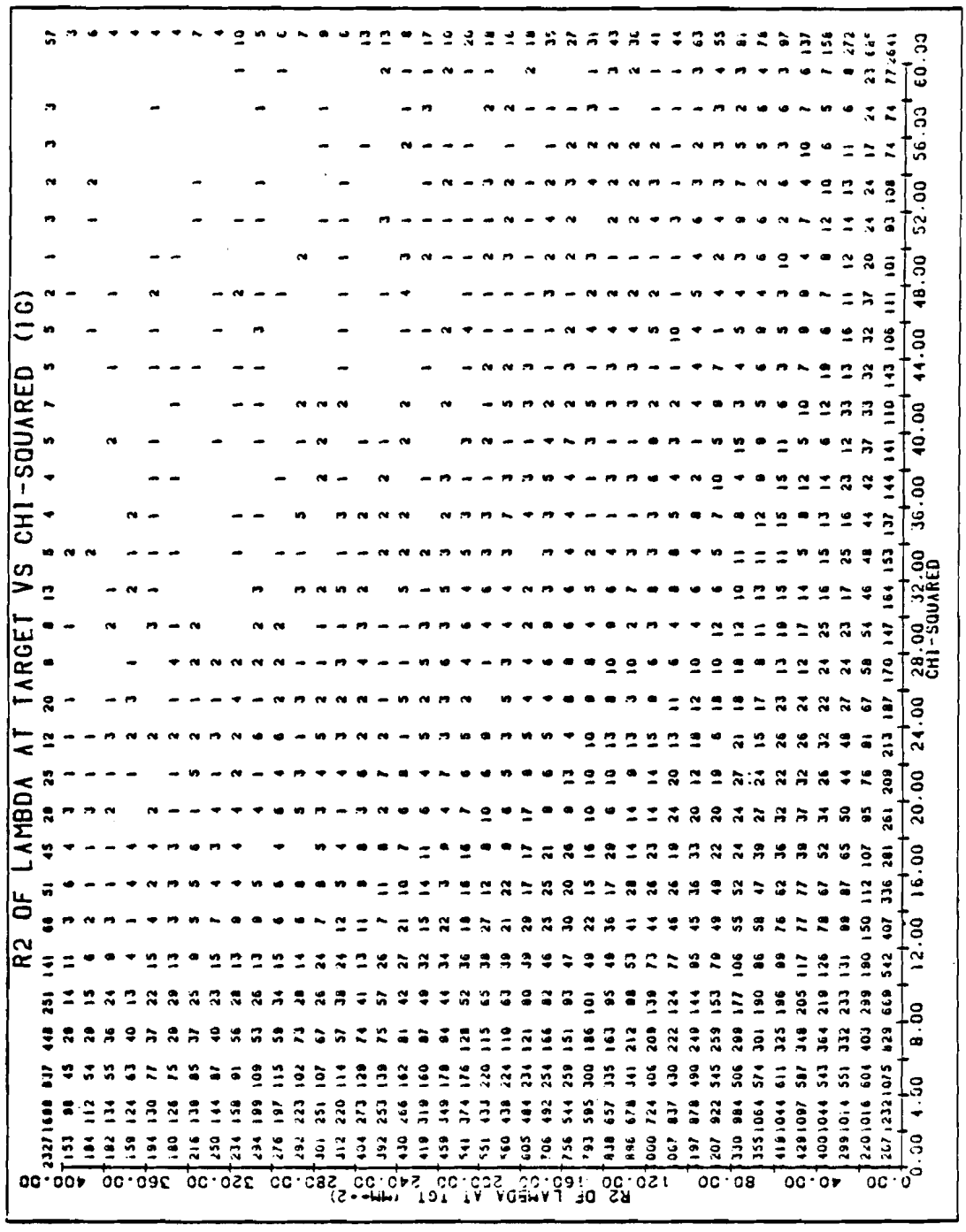

FIGURE (5.3.1a) Scatter plot of R^2_Λ of daughter Λ's versus χ^2_Ξ for 1G Ξ^0's

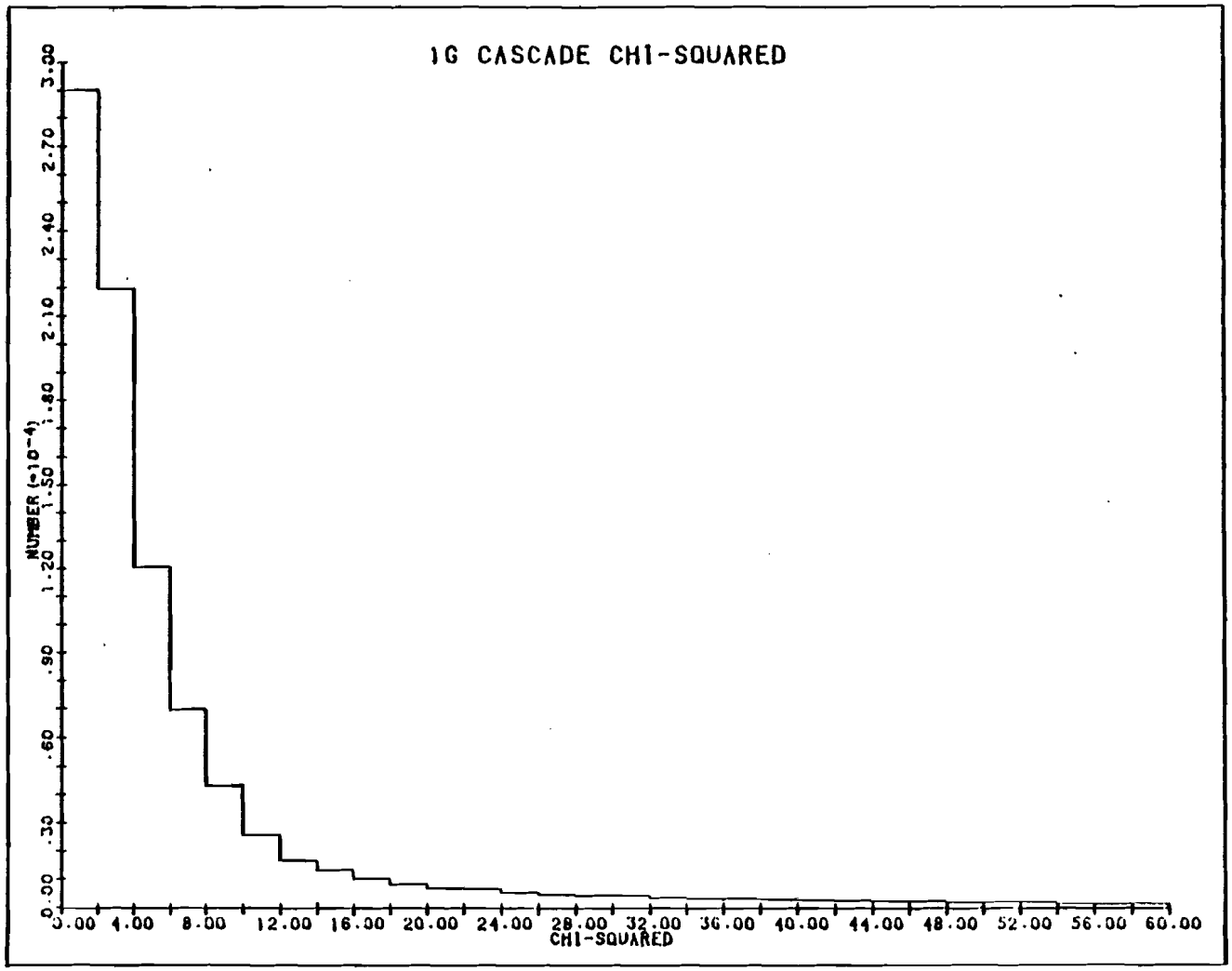

FIGURE (5.3.1b) Projection of scatterplot on χ^2_{Ξ} axis

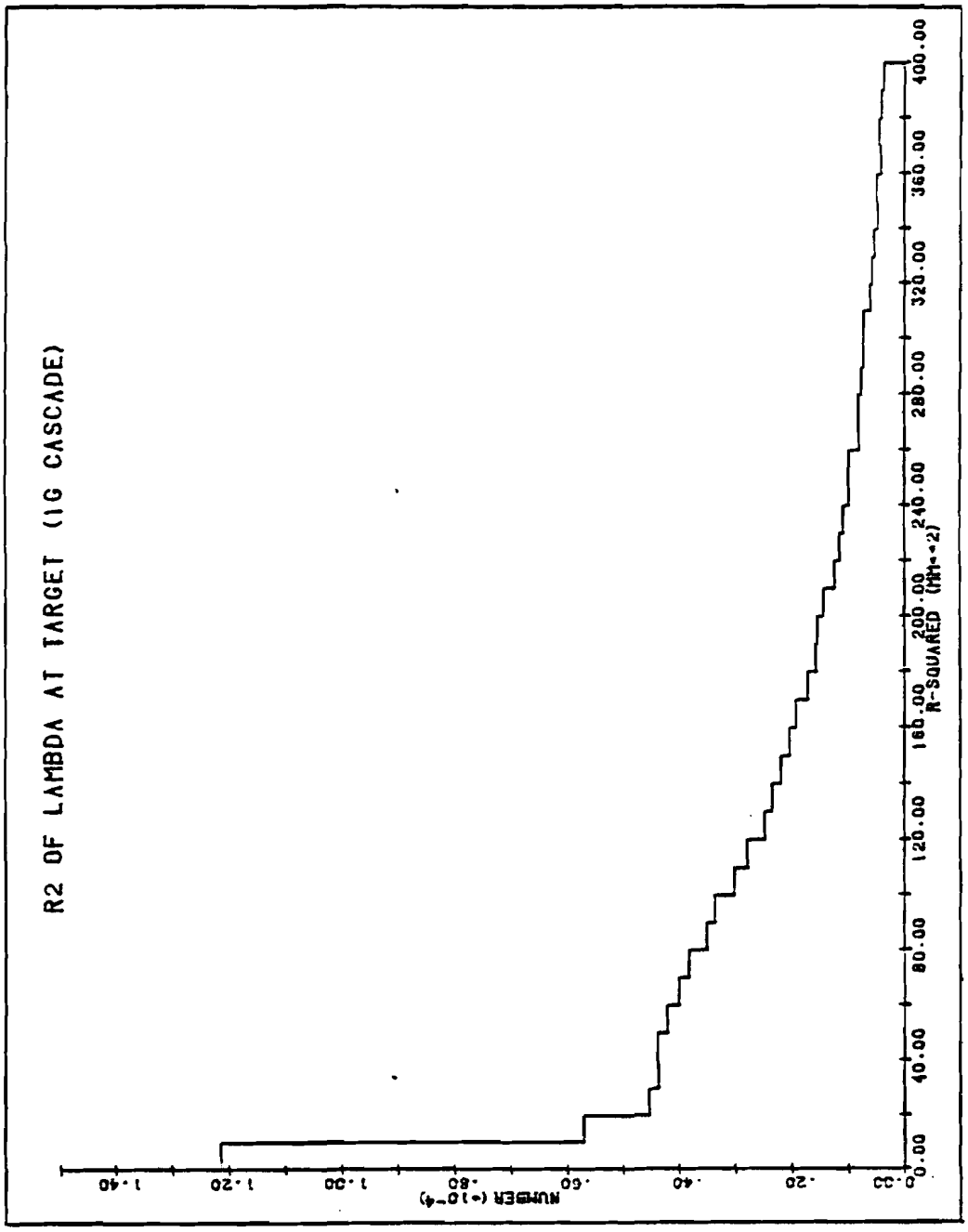

FIGURE (5.3.1c) Projection of scatterplot on R^2_Λ axis

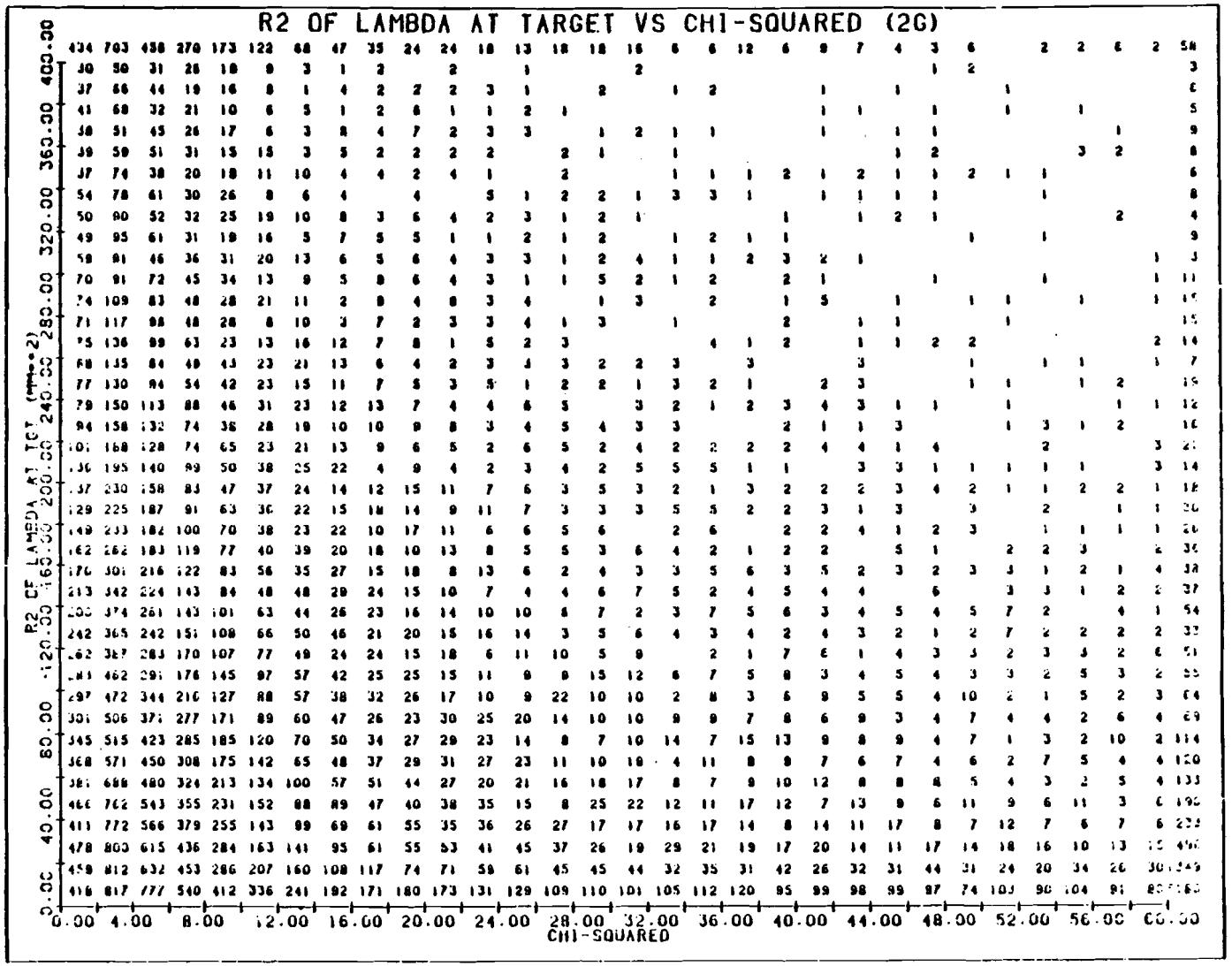

FIGURE (5.3',2a) Scatter plot of R^2_Λ of daughter Λ's versus $\chi^2_{\Xi^0}$ for 2G Ξ^0's

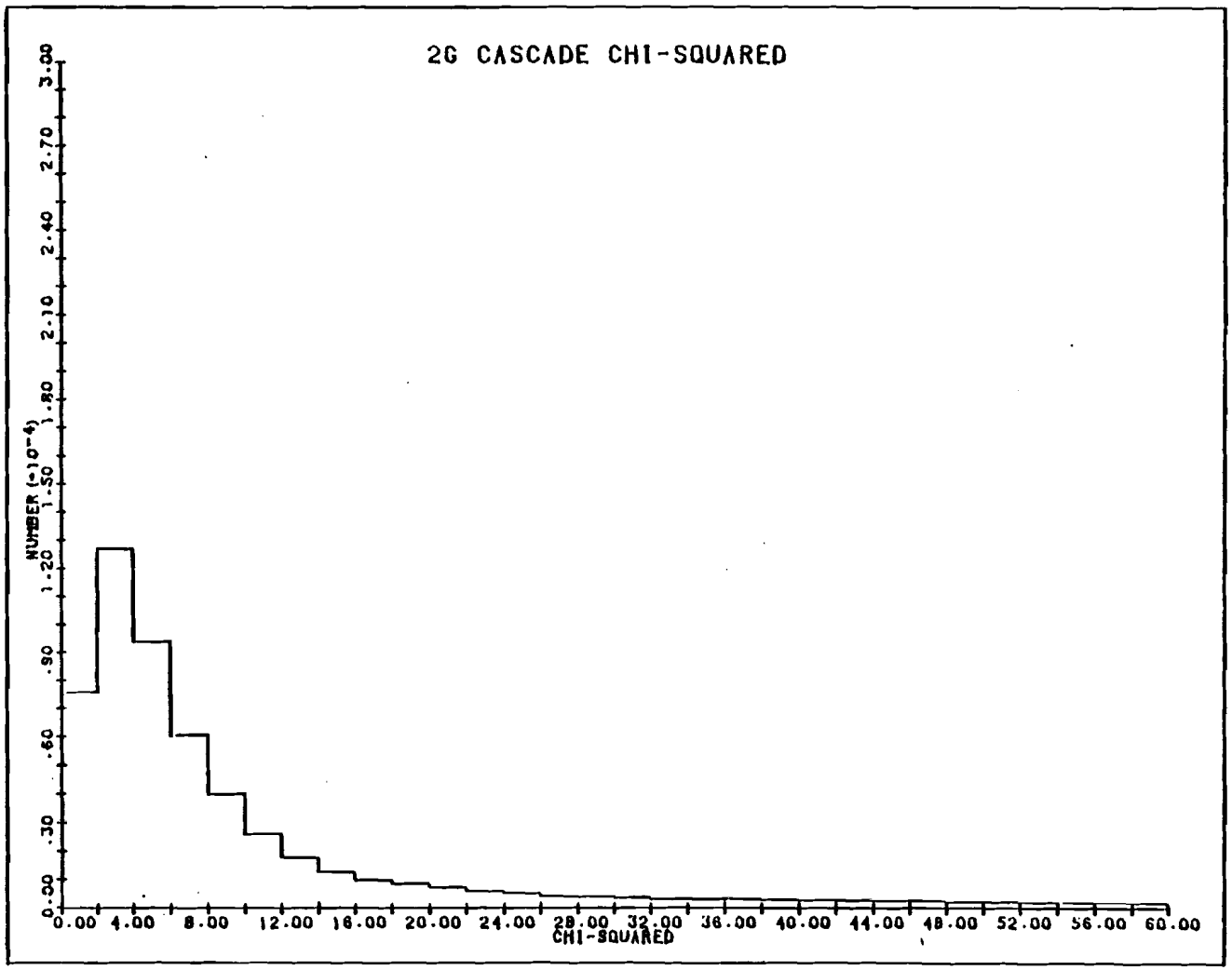

FIGURE (5.3.2b) Projection of scatterplot on $\chi^2_{\Sigma\Sigma}$ axis

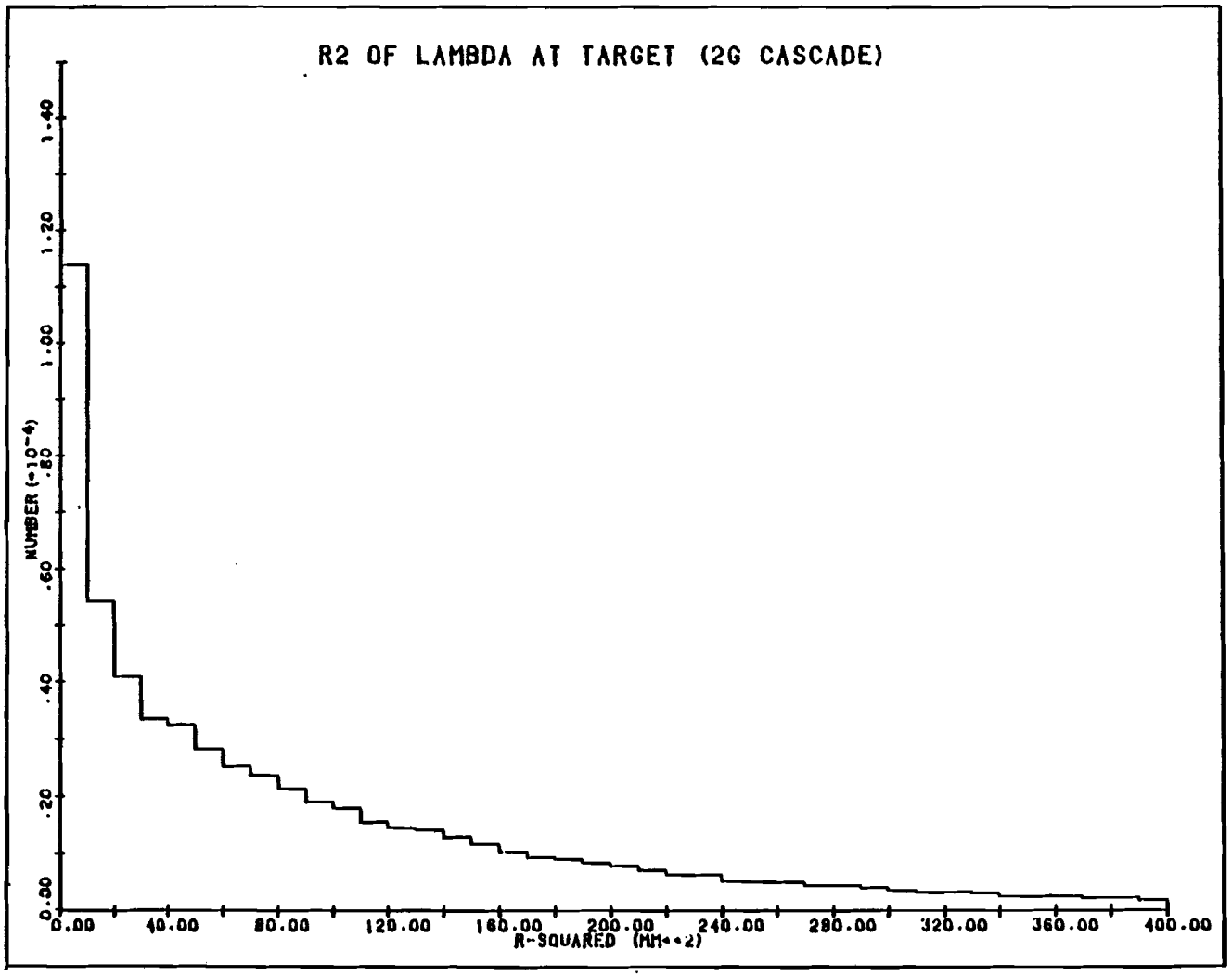

FIGURE (5.3.2c) Projection of scatterplot on R^2_Λ axis

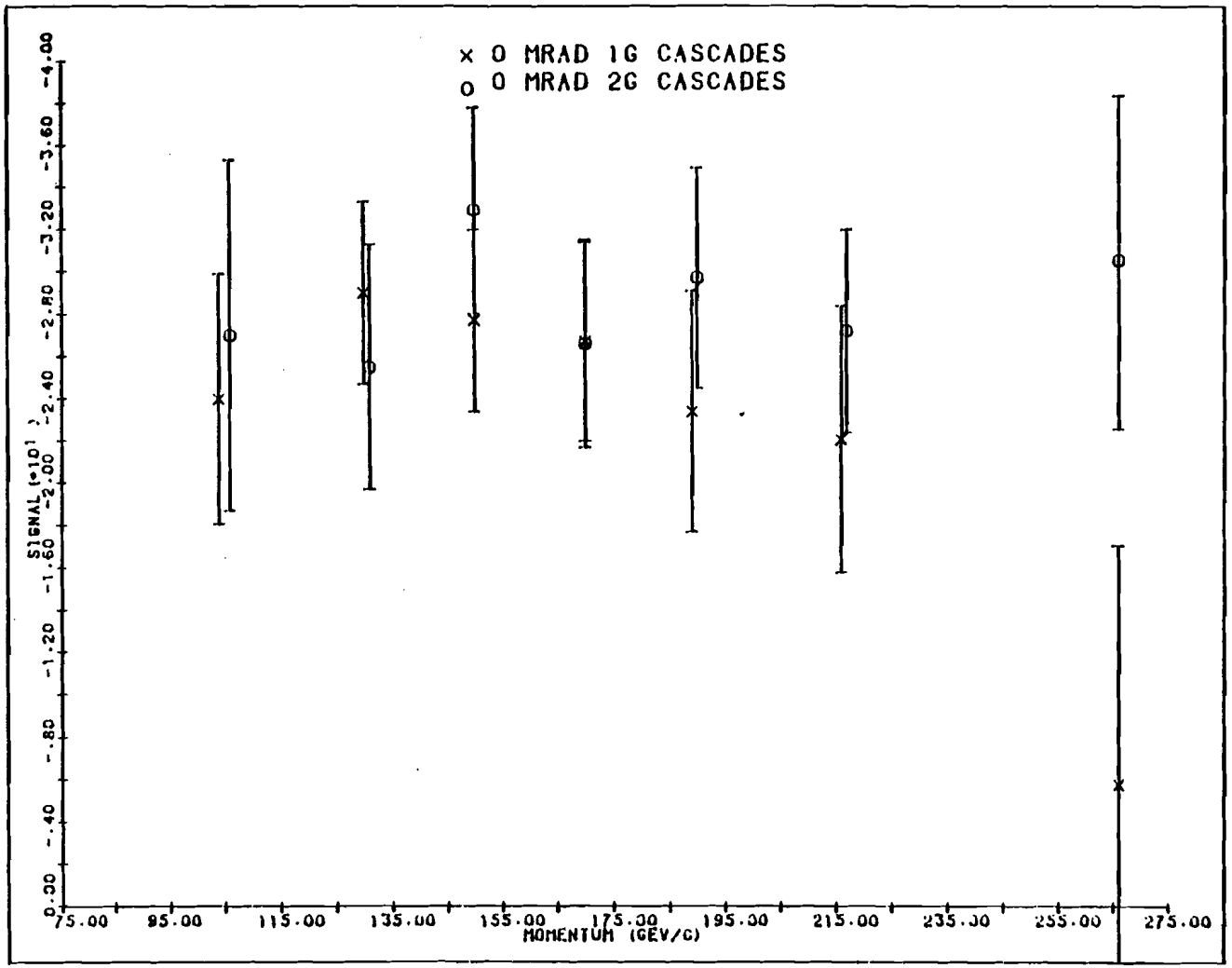

FIGURE (5.3.3) Momentum dependence of $\alpha_\Lambda \alpha_{\Xi^0}$ from 0 mrad Ξ^0 data

5.3.2 The non zero production angle data

The same α_{Ξ^0} analysis program as that used for the 0 mrad data could be applied to the non zero production angle data. This was equivalent to assuming that the effect of any terms involving $\vec{P}_\Xi$ or $\hat{\Lambda}$ was negligible on the dominant α_{Ξ^0} term in the daughter Λ polarization. However, once values were known for α_{Ξ^0}, from the 0 mrad analysis, and for $\vec{P}_\Xi$, they could be used in an iterative procedure to measure α_{Ξ^0} without these assumptions. It turned out that using the full expression, Eq. (4.4.2), led to values for α_{Ξ^0} identical to those using the approximation Eq. (4.2.3). The results presented are those from the 2nd iteration value, i.e. approximating α_{Ξ^0} by the 0 mrad number in any terms involving $\vec{P}_\Xi$. The analysis was necessarily performed for each separate (Sw, θ) combination, using a value for $\vec{P}_\Xi$ from the polarization master χ^2 fit, and the corresponding precession angle to obtain the relevant x and z components. A weighted average over each momentum bin was then performed which led to the results of Table 28 . Taking a weighted average of this data over the momentum-range 120-220 GeV/c gave

$$\alpha_\Lambda \alpha_{\Xi^0} = -0.263 \pm 0.005 \ . \qquad (5.3.4)$$

(This came from 155213 events, $\langle p_\Lambda \rangle$ =125 GeV/c, $\langle p_\Xi \rangle$ =151 GeV/c). These data are plotted in Fig. (5.3.4) .

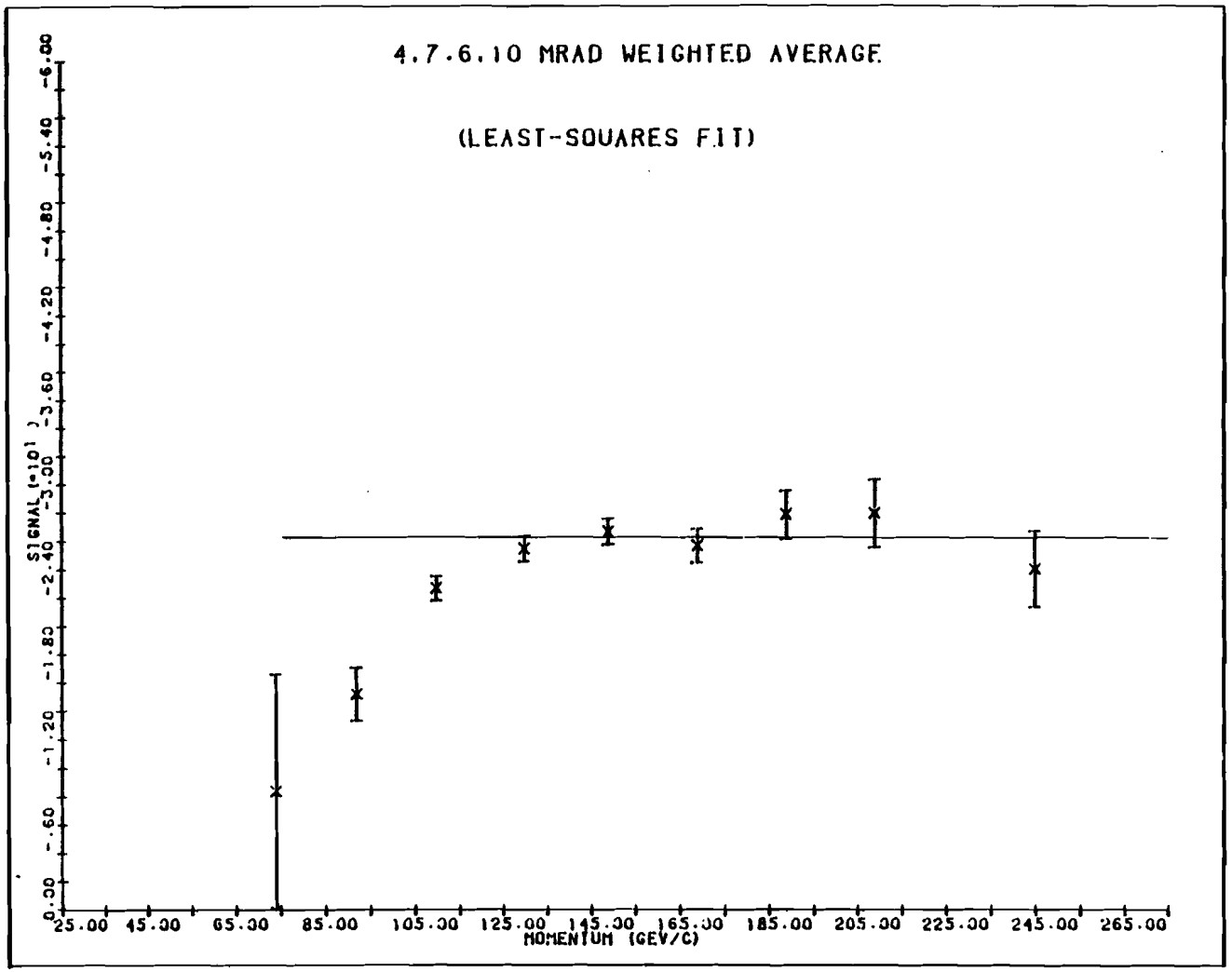

FIGURE (5.3.4) Momentum dependence of $\alpha_A \alpha_{\Xi^0}$ from combined 4, 7.6, and 10 mrad Ξ^0 data, and least squares fit straight line over 120-240 GeV/c momentum range

A least-squares fit to a constant over this momentum range gave the same value, with χ^2=2.6/4 df; this is shown in the figure too. The low values of $\alpha_\Lambda\alpha_{\Xi^0}$ in the lower momentum bins were understood to result from biases in the Λ polarization determination. (At low Λ momenta, below about 120 GeV/c, the spectrometer acceptance falls rapidly, and asymmetry measurements become sensitive to large biases). For the α_{Ξ^0} analysis such biases cannot be removed by combining data taken at opposite production angles since the daughter Λ polarization is along the momentum direction of the Λ, which is not affected by the production angle. Over the range 120-240 GeV/c these biases were negligibly small (see section (5.4.3)). The momentum independence of the result, and the consistency of the values from the 1G and 2G samples, demonstrated that there were no remaining biases.

Various possible influences on the α_{Ξ^0} result were investigated. The analysis was repeated for the 10 mrad data using the <u>measured</u> Ξ^0 polarization components instead of the <u>fitted</u> ones used so far in the 2nd iteration. These values inherently involved the P_Ξ biases; it was hoped that this approach would remove the effects of these biases from the $\alpha_\Lambda\alpha_{\Xi^0}$ obtained. Unfortunately this is not completely justified since the biases depend to some extent on the approximations and transformations involved in the analysis

method, and cannot take account of the errors involved in an acceptable way. The results are shown in Tables 30 and 31 for the 1G and 2G samples, and in Table 32 for the weighted average of the two. For comparison, Table 33 shows the corresponding results using the fitted components. Almost none of the momentum dependence was removed, although over the 120-240 GeV/c range the values were unchanged, hence checking the stability of the answer over this range. Repeating the 10 mrad analysis with a cut on all Λ momenta below 75 GeV/c (which in effect removed the lowest cascade-momentum bin) did not affect the values in momentum bins above 100 GeV/c at all, but slightly increased the value in the 80-120 GeV/c bin. This is consistent with the subsequent understanding that the momentum dependence was due entirely to the biases in the Λ polarization measurement.

As a check of the overall quality of fits obtained by the polarization analysis programs the 4, 7.6, and 10 mrad data sets were combined together and analyzed assuming that $P_\Lambda = \alpha_\Xi$. This led to the values in Table 29; it is apparent that the lower momentum bins still have low values. For comparison purposes this fit was studied to investigate the sensitivity to the χ^2 of the value of $\alpha_\Lambda \alpha_\Xi$ used:

χ^2=38 for $\alpha_\Lambda \alpha_\Xi$ =-0.248 (at the minimum χ^2), whereas

χ^2=165 for $\alpha_\Lambda \alpha_\Xi$ =-0.31 (the current world average),

and χ^2 ~3000 for $\alpha_\Lambda \alpha_\Xi$ =0 (no polarization),

which showed that the χ^2 was quite sensitive to this value. The "high" value of χ^2=38 for 19 d.f. was due mainly to the poor fits in the low momentum bins, which had not been excluded.

Typical $Cos(\hat{p},-\hat{\Xi})$ distributions for 1G and 2G cascade samples from a subsample of the 7.6 mrad data are shown in Figs. (5.3.5) and (5.3.6) . Also shown in these figures are the distributions for the corresponding Monte Carlo fake event samples, before they were polarized (i.e. with α_{Ξ^0}=0). Since the fakes events were generated isotropically the $Cos(\hat{p},-\hat{\Xi})$ distribution would be flat, apart from acceptance effects. Some of the asymmetry visible in the real events is due to the α_{Ξ^0} polarization, and the rest is due to the effect of detection efficiency (i.e. apparatus acceptance). In Figs. (5.3.7) and (5.3.8) the same real distributions are shown, overlaid with the fake distributions polarized by the α_{Ξ^0}-value picked for the best fit in the analysis. The chi-squared per degree-of-freedom (19 d.f. in each Cos comparison) for the polarized fits was 0.71 for the 1G and 0.73 for the 2G data shown here, giving the $\alpha_\Lambda\alpha_{\Xi^0}$ values of -0.250 ± 0.009 and -0.232 ± 0.011 . For the unpolarized fits the corresponding χ^2/d.f. were 36.0 and 20.9 respectively!

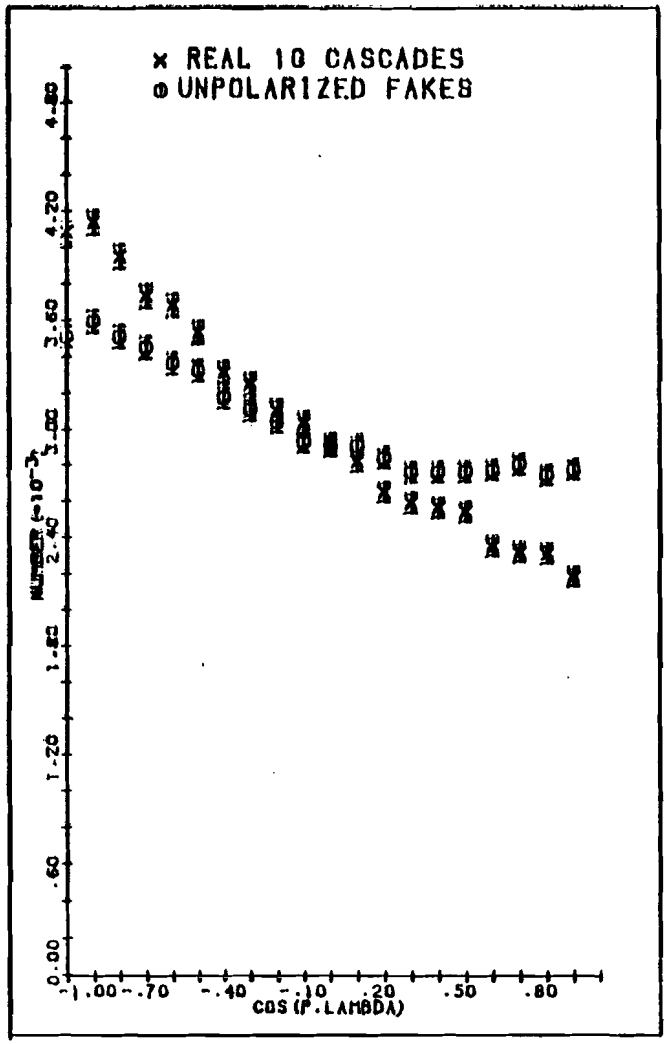

FIGURE (5.3.5) $\cos(\hat{p},\hat{\Lambda})$ for real and unpolarized fake 1G Ξ^0 events

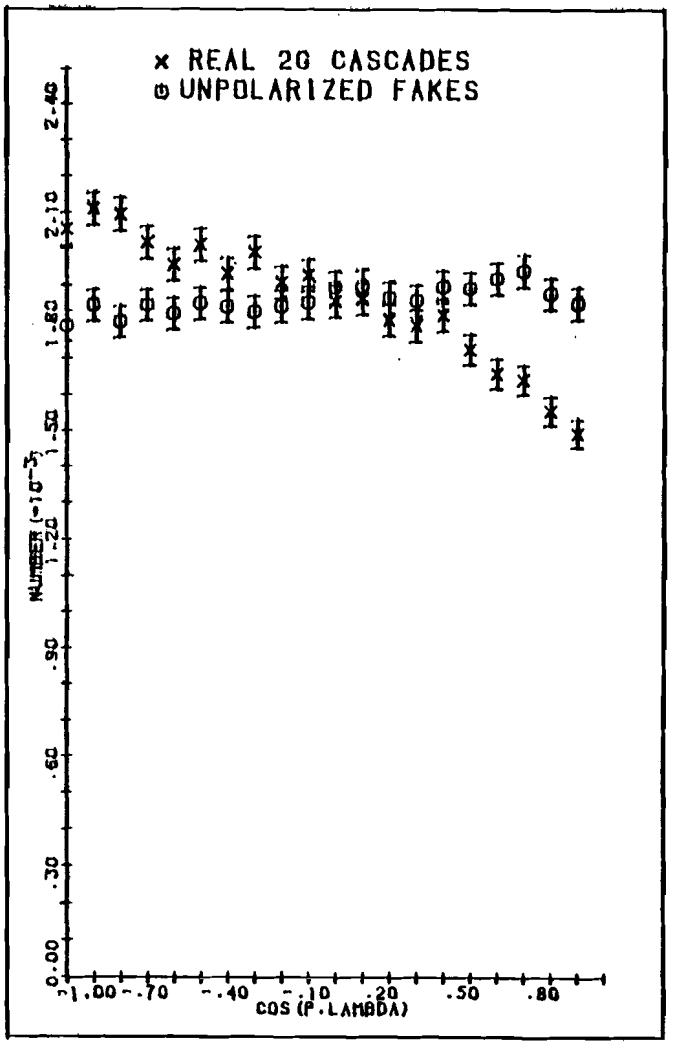

FIGURE (5.3.6) $\cos(\hat{p},\hat{\Lambda})$ for real and unpolarized fake 2G Ξ^0 events

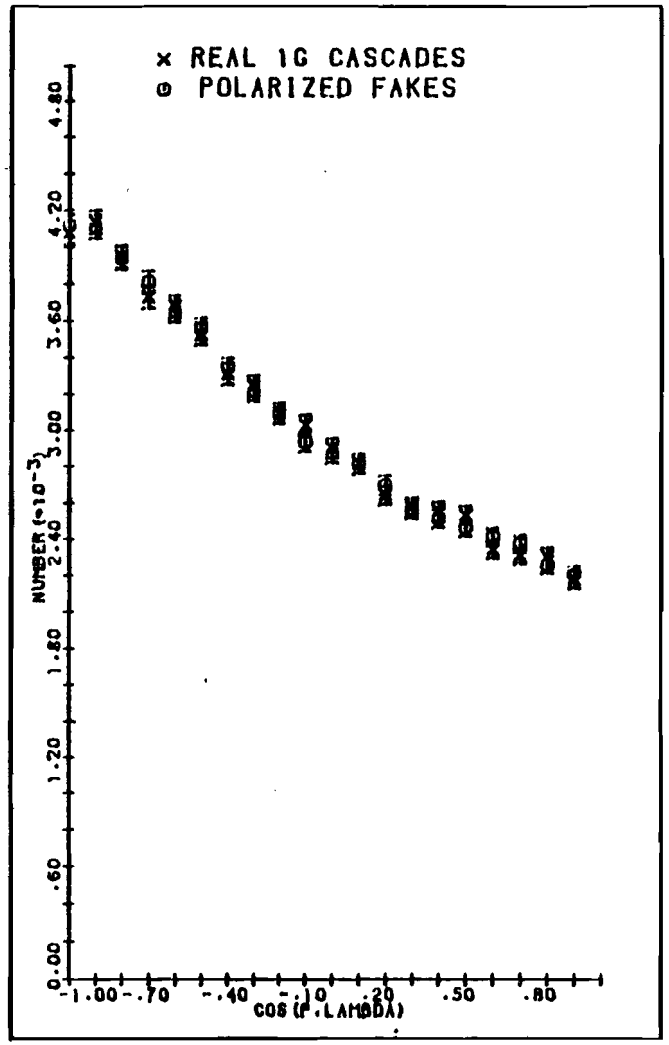

FIGURE (5.3.7) $\cos(\hat{p},\hat{\Lambda})$ for real and polarized fake 1G Ξ^0 events

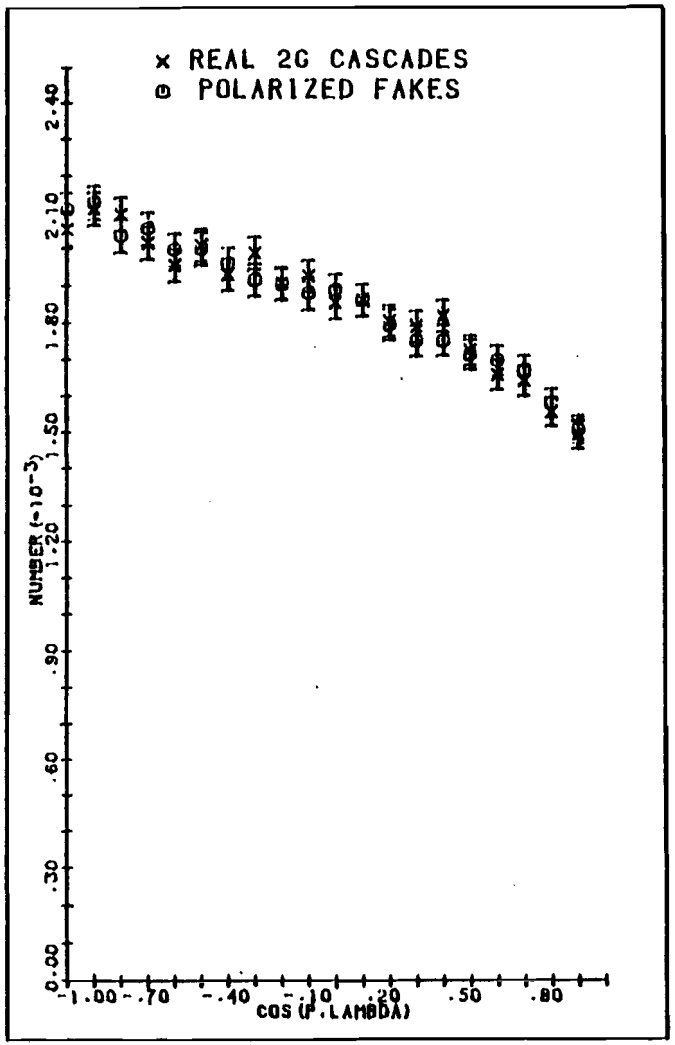

FIGURE (5.3.8) $\cos(\hat{p},\hat{\Lambda})$ for real and polarized fake 2G Ξ^0 events

5.3.3 Result for α_{Ξ^0}.

The overall result for the product $\alpha_\Lambda\alpha_{\Xi^0}$ was obtained by taking a weighted average of the five useful data sets listed in Table 34 . Note that the 0 and 2 mrad data have R^2_Λ cuts on them, as discussed, but the other three sets do not, since applying one did not change the values, or seem required from studies of the $\chi^2_{\Xi^0}$ or invariant mass distributions. The weighted average of the 4, 7.6, and 10 mrad data gave

$$\alpha_\Lambda\alpha_{\Xi^0} = -0.264 \pm 0.005$$

whereas combining all five sets gave

$$\alpha_\Lambda\alpha_{\Xi^0} = -0.265 \pm 0.005 \quad . \qquad (5.3.5)$$

A least-squares fit to a constant value for these five points gave the same $\alpha_\Lambda\alpha_{\Xi^0}$ with a $\chi^2 = 4.72/4$ df.

From this α_{Ξ^0} was calculated to be

$$\alpha_{\Xi^0} = -0.413 \pm 0.011 \qquad (5.3.6)$$

where α_Λ was assumed to be 0.642 ± 0.013 . It is interesting to point out that the limit in precision to which α_{Ξ^0} could be obtained in this experiment was due to the precision with which α_Λ is known.

5.4 Backgrounds and Systematics

This section presents the results of the various estimates of background and systematic effects on the measured values. The stability of the quoted numbers to many different cuts and variations in the cuts was investigated; any significant changes have been noted where relevant. In particular the χ^2_Ξ and R^2_Λ cuts were examined in great detail, and the comparison between real and Monte Carlo data carefully studied. Quantitative estimates of the background contamination in the zero and non-zero mrad data samples were obtained from the fool event studies discussed in Section (3.10.3).

Background corrections due to Ξ^0 production from sources other than the production target were unimportant. The background was estimated by the ratio of Ξ^0 yields from data taken with and without a solid target (the so-called target-in/target-out ratio). This ratio was typically ~4 % at 0 mrad <u>before cuts</u> and less than ~1 % at non-zero angles; after cuts it was negligibly small.

5.4.1 Results of the fool event studies

At 7.6 mrad, the ratio of the normalized number of fool to the number of real events falling within the λ^2_Ξ cut-offs (2O for 1G and 3O for 2G) was between 0.019 and 0.020. Thus a 2% accidental background was estimated in both the 1G and 2G Ξ^0 data. This was consistent with estimates based on the R^2_Λ distributions, and with comparisons to Monte Carlo distributions.

At O mrad, as expected, the ratios were much larger, reflecting the much higher contamination of the data by accidentals. The background in the 1G sample was estimated to be ~6%, and in the 2G sample ~13%. Studies of the R^2_Λ distributions of the fool events showed that this background was reduced to ~<1.5%, in both samples, by cutting events with R^2_Λ <3O mm^2, as was done for the real data used in subsequent analysis. In fact, cutting R^2_Λ <15 mm^2 already reduced the background to ~2.5 to 3%.

These background estimates were obtained starting from real data which had not been passed through the set of further loose cuts listed in section (3.1O.1). Even without the R^2_Λ cuts, these cuts removed between 65% and 75% of the fool background, so that the remaining

contamination in the data subjected to polarization analysis was certainly less than 2%.

The effect of any remaining background of this type on the polarization results was negligible. The polarization of beam Λ's is different from that of daughter Λ's, but due to the different rest frame, the contribution to the Ξ^0 polarization is effectively that of an unpolarized sample. The fool events were measured to have α_{Ξ^0} consistent with zero, so that this was an unpolarized background to the α_{Ξ^0} measurement too. This also tested for bias due to any correlation between the χ^2_Ξ obtained from the Ξ^0 fit and the decay proton direction.

It is important to emphasize that daughter Λ's from Ξ^0 decays are polarized in the Ξ^0 rest frame, whereas beam Λ's are polarized in the Λ rest frame, so that the influence of beam Λ polarization on Ξ^0 polarization is small.

5.4.2 Background studies using the χ^2 fit

The master χ^2 was used to estimate the effects of backgrounds on the fitted values of the moment and polarization. Only the 7.6 mrad data were used since all the non-zero angle data were of similar purity. The 1G and 2G samples were kept separate. It was important to choose the order in which various parameters were fitted, because only one iteration was made on each of the other parameters once a particular value had been chosen by the minimization. The approach taken was to fit first the bias terms, and then the polarization and moment, in order that the biases were allowed as much freedom as possible to fit the data. When generalizing this to search for various backgrounds, additional terms were added to the χ^2, and were fitted <u>after</u> the above four, so that such backgrounds were forced to remain less important in the fit than the primary terms.

To implement this background search a term was added to the master chi-squared which behaved as $P_B \cos\phi_B$ in x and $P_B \sin\phi_B$ in z, with a background moment μ_B and polarization P_B. Several different sources of background were considered by trying different values of μ_B and P_B.

1. A value of $\mu_B = -0.61$ was assumed (beam lambda background) and the fit was performed as before, which led to values for P_Ξ (actually $\alpha_\Lambda \gamma_\Xi P_\Xi$), μ_Ξ, x_b, and z_b, as usual, but also a value for P_B. The results are given in Tables 35 and 36. The original values from the fit are also shown for purposes of comparison.

2. The fit was repeated assuming $\mu_B = 0.$; these results are also shown in the tables.

Since there were 24 data points, and 5 parameters in the fit, there were 19 degrees-of-freedom. From this it is seen that the biases were unchanged, and the moment and cascade polarization virtually unchanged, by the addition of this extra parameter. To check the stability of the results to the presence of such backgrounds a similar procedure was followed in which both μ_B and P_B were input, but only the four usual parameters were fitted. The magnitude of the background polarization assumed was the same as that of the real (lambda) polarization of the cascades, i.e. about 5 %. The amount of background contamination was assumed to be 10 %, since this was certainly an overestimate of the <u>real</u> lambda background in the data sample used in the analysis; (see the previous section). Consequently a value of $|P_B| = 0.005$ was used.

The following cases were tried:

1. $\mu_B = -0.61$ and $P_B = +0.005$,

2. $\mu_B = -0.61$ and $P_B = -0.005$,

3. $\mu_B = 0.$ and $P_B = +0.005$, and

4. $\mu_B = 0.$ and $P_B = -0.005$

The results are shown in Table 37 , with the chi-squared values (for 20 degrees-of-freedom). It is evident that even such large assumed backgrounds do not affect the value of the magnetic moment severely, the 1G value remaining in the range from -1.27 to -1.23, and the 2G one in the range -1.23 to -1.20. These numbers presumably can be taken as maximum estimates of possible systematic effects on the quoted magnetic moment. In all the cases the statistical error covers this range of values, i.e. the change was always $<1\sigma$.

5.4.3 Backgrounds and systematic effects in α_{Ξ^0} analysis.

The alpha-cascade analysis suffered from the problem that biases in the measurement could not be explicitly cancelled by means of the experimental design, as could be done for the polarization measurements. This is because the polarization of the decay lambda is correlated with the momentum in the cascade rest frame, a direction which changes from event to event. There was no corresponding reversal of the sign of the polarization which could be effected. The fact that the polarization is in the Ξ^0 rest frame, means that any biases (which are presumably in the Lab) will correlate only weakly with the momentum of the Λ direction, and so should not have a large effect on the result. However, biases in the Λ rest frame may affect the α_{Ξ^0} determination. This may be seen by considering the structure of the measured signal, $(\vec{P}_\Lambda \cdot \hat{\Lambda})$, which has a "physics" component $(\alpha_\Xi + \hat{\Lambda} \cdot \vec{P}_\Xi)$, but also the additional possibility of a "bias" component $\hat{\Lambda} \cdot \vec{B}$. Here $\vec{P}_\Xi$ includes the biases in the $\vec{P}_\Xi$ measurement, but $\vec{B}$ represents the biases in the $\vec{P}_\Lambda$ measurement. It has been demonstrated that the $\vec{P}_\Xi$ biases (which are virtually momentum-independent) do not affect the α_{Ξ^0} values obtained. The contribution of the $\vec{B}_\Lambda$ term will now be discussed.

To study systematic errors due to the biases in the Λ polarization measurement, the average values over the data at each production angle, $\langle \vec{B}_\Lambda \cdot \hat{\Lambda} \rangle$, were estimated from the known values $\langle \hat{\Lambda} \cdot \hat{x} \rangle$, $\langle \hat{\Lambda} \cdot \hat{y} \rangle$, and $\langle \hat{\Lambda} \cdot \hat{z} \rangle$ (which were usually small but could be large e.g. at low momentum) and the measured $\vec{B}_\Lambda$ (bias in polarization measurement of <u>beam</u> Λ's) to find an upper limit on the effect this term could have on the final $\alpha_\Lambda \alpha_{\bar{\Xi}^+}$ answer. The three bias functions B_x, B_y, and B_z were obtained from analysis of beam Λ polarization, as discussed in section (4.5.1). As mentioned there was a fairly constant y bias ~+0.07. The x bias decreased from about +0.12 at 60 GeV/c to zero at $\geq$220 GeV/c. The z bias was negative, decreasing from zero at $\geq$220 GeV/c to $<$-0.25 at 60 GeV/c. This severe z bias agreed with that measured previously in our precision μ_Λ experiment; it was not fully understood but does not affect the polarization or moment results <u>after bias cancellation</u>. The measured signal in the alpha analysis was then assumed to be

$$\alpha_\Lambda P_{meas.} = \alpha_\Lambda \alpha_{\bar{\Xi}^+} + \hat{\Lambda} \cdot \alpha_\Lambda \vec{B}_\Lambda$$

where $\vec{B}_\Lambda$ is the bias in the beam Λ polarization (this is <u>measured in the Λ rest frame</u>). Applying this correction the severe momentum dependence in the measured signal was removed. Fortunately, over the range 120-240 GeV/c, the contribution of this bias term was negligible ($\leq \pm 0.003$ in each bin) thus justifying the results quoted over this range. Since this is a lambda-controlled bias it also

explains why both the 1G and 2G Ξ^0 data showed the same dependence. It was decided not to quote the "corrected" $\alpha_\Lambda\alpha_{\Xi^0}$ value over the full momentum range ~60-~360 GeV/c because the actual magnitudes of the large correction terms were quite sensitive to the precise values picked for the estimates.

Finally, an unpolarized lambda background would contribute an effective value of $\alpha_{\Xi^0}=0$ to the overall measurement, and hence would reduce the magnitude of the observed α_{Ξ^0}. This type of contamination might occur at the highest momenta, where the spectrometer resolution is worst due to small opening angles between the proton and pion from lambda decays, and possibly contributes to the decrease in the alpha value seen in the highest momentum bin. Any such contribution over the 120-240 GeV/c momentum range was estimated to be negligible.

CHAPTER 6

IMPLICATIONS

6.1 Status of Baryon Magnetic Moments

The importance of magnetic moments arises from the following reasons (apart from their obvious role in the static interaction of a spin system with the electromagnetic field):

- They are measurable quantities;
- They may reflect internal structure of particles;
- They give realistic meaning to the term "quark mass";
- There is some (apparent) success in their theoretical prediction.

There are now four baryon magnetic moments which have been determined with high precision. The experiment described in this thesis has measured the magnetic moment of the cascade-zero to be

$$\mu_{\Xi^0} = -1.236 \pm 0.014 \ \mu_N \qquad (6.1.1)$$

which is almost a 1% measurement, from a sample of 270 000 reconstructed $\Xi^0 \rightarrow \Lambda\pi^0$ decays. This value confirms our previous measurement of the Ξ^0 moment. According to simple SU(6) and quark models, which in effect attempt to relate any property of the eight octet baryons to three parameters (corresponding to the u, d, and s quarks), the parameters describing magnetic moments should now be overconstrained. Since 1978 the Σ^+ moment has been newly obtained from a revised analysis [30], so that the current (April 1980) octet baryon moments are as shown in Table 38, together with typical broken SU(6) predictions.

It is clear that the agreement between theory and experiment is not as close as might have been hoped after the successful prediction of the lambda moment. The quark moments may be defined by

$$\mu_q = \frac{g_q e_q \hbar}{4 m_q c} . \qquad (6.1.2)$$

Then setting g =2 (for the reasonable assumption that quarks are pointlike) leads to

$$\mu_q = \frac{e_q \hbar}{2 m_q c} , \qquad (6.1.3)$$

where the quark charges e_q are given by $e_q = Qe$ in Table 2. Expressing the baryon moments in terms of the quark moments μ_u, μ_d, μ_s (assuming SU(6) wavefunctions as described in Chapter 1) gives:

$$\mu(p) = \tfrac{4}{3}\mu_u - \tfrac{1}{3}\mu_d ,$$
$$\mu(n) = \tfrac{4}{3}\mu_d - \tfrac{1}{3}\mu_u ,$$
$$\mu(\Lambda) = \mu_s ,$$
$$\mu(\Xi^0) = \tfrac{4}{3}\mu_s - \tfrac{1}{3}\mu_u .$$

Using the measured magnetic moments of the proton, neutron, and lambda to determine the μ_q gives

$$\mu_u = 1.852\ \mu_N ,$$
$$\mu_d = -0.972\ \mu_N ,$$
$$\mu_s = -0.614\ \mu_N ,$$

which in turn imply that $\mu(\Xi^0) = -1.436\ \mu_N$, which is 12σ from the experimental value ! An alternative expression of this disagreement can be obtained by calculating the s-quark magnetic moments from the measured Λ and measured Ξ^0 moments independently. Forming the difference

$$\mu_s(\Xi^0) - \mu_s(\Lambda) = (-0.465 \pm 0.015) - (-0.614 \pm 0.005)\ \mu_N$$
$$= 0.15 \pm 0.02\ \mu_N ,$$

shows that there is a 7σ disagreement.

Notice that the <u>exact</u> SU(6)-limit (or SU(3)) prediction [31] of $\mu(\Xi^0)/\mu(\Lambda) = 2$ is experimentally true to high accuracy (~1%) (although the other SU(3) relations are grossly violated).

Several authors have attempted to fit the measured moments using three input parameters, typically chosen to be the realistic quark masses m_q defined by Eq. (6.1.3). Very poor fits are obtained; for example Teese and Settles [32] obtained a $\chi^2=28/5$ df for their best fit (which used $\mu(\Xi^0)=-1.20\pm0.06\,\mu_N$) giving:

m_u = 338 MeV ,
m_d = 322 MeV ,
m_s = 512 MeV .

It can be argued that intrinsic magnetons, rather than nuclear magnetons, should be used to make these comparisons (which means scaling the values given by m_p/m_B where m_B=the baryon mass), but this does not help the overall fit. Franklin has reached similar conclusions [33]. Allowing the quarks to have $g_q \neq 2$ will not improve the quality of the fits either, but will only change the values of the masses obtained. The outstanding question is that of the importance of relativistic effects, and interactions between the quarks, which probably complicate these simple predictions.

De Rujula, Georgi, and Glashow in their seminal paper [7] on the application of quantum chromodynamics to hadron properties also assumed pointlike Dirac quarks, and obtained magnetic moment predictions tantamount to those from broken SU(6) models. Considerable work has been done relating baryon magnetic moments through SU(6) sum-rules

[34, 35, 36, 37] which are argued to be more reliable than absolute predictions, based on experience with mass-splittings. None of these theories seems capable of obtaining predictions close to all the experimental values in a simple and self-consistent way [38, 39].

With the advent of more precision measurements of baryon magnetic moments these theories will be even more severely constrained. Since this experiment was completed, the Neutral Hyperon Group at Fermilab has taken data on charged hyperon inclusive production in the hope that they too will be polarized and allow precision moment measurements. At the time of writing these data are undergoing analysis.

6.2 Application of the new α_{Ξ^0} value to tests of $\Delta I = 1/2$ rule

The weak non-leptonic decays of hyperons are described by isospin-changing s- and p-wave amplitudes (see Section (4.1)). Clebsch-Gordan coefficients of the isospin-changing amplitudes connect the experimental observables (decay widths, lifetimes, asymmetry parameters etc.) of decays within the same isospin family. It is an experimental fact that $\Delta I = 1/2$ terms dominate these hyperon

decays [40]; the theoretical reason for this is not understood. Recent theoretical attempts to understand weak non-leptonic decays have been based on quantum chromodynamics, in which radiative corrections (including gluon and W-boson corrections) have been estimated using renormalization group techniques. Unfortunately these approaches have not met with overwhelming success, at least for the decays involving light quarks (u, d, and s), and the $\Delta I = 1/2$ enhancement in hyperon decays is still not understood [41]. Consequently it is of interest to test experimentally the validity of the " $\Delta I = 1/2$ Rule" as severely as possible.

The standard notation [40] $s_{2\Delta I}$, $p_{2\Delta I}$ can be used for the s and p wave amplitudes with isospin change $2\,\Delta I$, or equivalently the dimensionless amplitudes $A_{2\Delta I}$, $B_{2\Delta I}$, which are related by

$$\frac{p}{s} = \left[\frac{(M-m)^2 - \mu^2}{(M+m)^2 - \mu^2}\right]^{1/2} \frac{B}{A} \quad ,$$

where s, p or A, B describe the decay $B_1 \rightarrow B_2 + \pi$ of baryon B_1 (mass M) to baryon B_2 (mass m), and μ is the mass of the pion. The amplitude ratios s_3/s_1, p_3/p_1 (which are equal to the corresponding A_3/A_1, B_3/B_1) can be related to the ratios of the decay rates, and the α asymmetry parameters, for the different charged modes in the requisite decays. It is convenient to express the

experimental values of these ratios in terms of the deviations from the values predicted by the $\Delta I=1/2$ rule.

For Λ (and Ξ) decay, the $\Delta I=1/2$ rule predicts

$$\frac{\Gamma_0(\Lambda)}{\Gamma_-(\Lambda)} = \frac{1}{2} \quad \left(\text{or } \frac{\tau_0}{\tau_-} = 2\right),$$

$$\frac{\alpha_0(\Lambda)}{\alpha_-(\Lambda)} = 1,$$

where the subscripts refer to the sign of the charge of the final-state pion. Overseth and Pakvasa [42] write linear expressions for $\Delta I=3/2$ amplitudes in terms of $\Delta\alpha = (\alpha_0/\alpha_-)-1$ and $\Delta\Gamma = (\Gamma_0/\Gamma_-)-0.5$, from which the ratios of the amplitudes can be obtained once the decay rates and asymmetry parameters are known. For Λ decay, $s_3/s_1 = 0.027\pm0.008$, i.e. a small $\Delta I=3/2$ s-amplitude, which is controlled mainly by the ratio of the decay rates (of the $\Lambda\to n\pi^0$ and $\Lambda\to p\pi^-$ modes). The ratio of the asymmetry parameters (which is less accurately measured) does contribute to the p-wave ratio, giving $p_3/p_1 = 0.030\pm0.037$, consistent with the $\Delta I=1/2$ rule. The limits to the precision with which the rule may be tested in Λ decay are the experimental difficulties in detecting the neutral decay mode $\Lambda\to n\pi^0$, and the uncertainties in the calculation of the radiative corrections [43].

Σ decays are complicated by the involvement of three decays, and the possible presence of $\Delta I = 5/2$ amplitudes, but Ξ decays are well-suited to $\Delta I = 1/2$ tests. There are no $\Delta I = 5/2$ amplitudes possible, and both final states ($\Lambda\pi^-$ and $\Lambda\pi^0$) have the same isospin so that knowledge of final state interaction phase shifts is not required (as <u>is</u> in the Λ case).

The $\Delta I = 1/2$ rule for Ξ decays predicts

$$\frac{\alpha_0}{\alpha_-} = 1, \quad \frac{\tau_0}{\tau_-} = 2,$$

which are modified by phase space corrections to

$$\frac{\alpha_0}{\alpha_-} = 0.975, \quad \frac{\tau_0}{\tau_-} = 2.067 .$$

Other radiative corrections are apparently smaller, but in the same direction. The linear expressions for the differences $\Delta\alpha, \Delta\Gamma$ are [40]

$$\Delta\alpha = 1.38(s_3/s_1) - 1.38(p_3/p_1)$$

$$\Delta\Gamma = -1.44(s_3/s_1) - 0.06(p_3/p_1) .$$

The previous world average values for the decay rates and asymmetry parameters [1] led to the differences

$$\Delta\Gamma = 0.070 \pm 0.021$$

$$\Delta\alpha = 0.12 \pm 0.21$$

and implied

$$s_3/s_1 = -0.043 \pm 0.015$$

$$p_3/p_1 = -0.13 \pm 0.15 .$$

With a more recent value for the lifetime of the Ξ^0 [44], $\tau_{\Xi^0} = 2.89 \pm 0.10 \times 10^{-10}$ sec, and the most recent measurement of α_{Ξ^0} previous to this experiment, $\alpha_{\Xi^0} = -0.490 \pm 0.042$ [45], the ratios are

$$s_3/s_1 = -0.041 \pm 0.014$$

$$p_3/p_1 = -0.22 \pm 0.09 ,$$

(without phase space corrections).

The new value of α_{Ξ^0} obtained from this experiment enables a more precise determination of the ratio p_3/p_1 to be made. The result from this experiment was

$$\alpha_{\Xi^0} = -0.413 \pm 0.011 .$$

The current best value for α_{Ξ^-} has been taken as the weighted average of the most recent published value [46] with the previous world average. This number is

$$\alpha_{\Xi^-} = -0.413 \pm 0.019 .$$

These numbers imply $\Delta\alpha = (1.000 \pm 0.053) - 1 = 0.000 \pm 0.053$ (without phase space corrections), and -0.025 ± 0.053 (with phase space corrections). With the new value of τ_{Ξ^0} [44] quoted above, $\Delta\Gamma$ is 0.072 ± 0.021 (without phase space corrections), and 0.088 ± 0.021 (with the corrections). Solving for s_3/s_1 and p_3/p_1 gives

$$s_3/s_1 = -0.048 \pm 0.014 ,$$

$$p_3/p_1 = +0.048 \pm 0.040 ,$$

with no phase space corrections. With corrections the ratios are

$s_3/s_1 = -0.059 \pm 0.014$,

$p_3/p_1 = -0.041 \pm 0.040$,

where the error in the s ratio is contributed entirely by the decay rate ratio, but the error in the p ratio comes mainly from the α ratio. Thus the p-wave ratio is now consistent with the $\Delta I = 1/2$ rule.

6.3 Summary

In summary we have obtained the following measurements:

1. The magnetic moment of the Λ hyperon

   $\mu_\Lambda = -0.598 \pm 0.015\ \mu_N$,

   from 202627 reconstructed $\Lambda \to p\pi^-$ decays;

2. The magnetic moment of the Ξ^0 hyperon

   $\mu_{\Xi^0} = -1.236 \pm 0.014\ \mu_N$,

   from 269524 reconstructed $\Xi^0 \to \Lambda\pi^0$ decays;

3. A new value for the product

   $\alpha_\Lambda \alpha_{\Xi^0} = -0.265 \pm 0.005$,

   from 182450 $\Xi^0 \to \Lambda\pi^0$ decays; and

4. The inclusive polarization of Ξ^0 hyperons (at production angles of 4, 7.6, and 10 mrad), as shown in Figs. (5.2.32) and (5.2.33). The mean polarization of these 270000 events was -0.108 ± 0.006, with an average Ξ^0 momentum of 134 GeV/c.

APPENDIX

TABLE 1. Experimental values for magnetic moments of stable leptons and baryons (at April 1978)

Particle	Magnetic Moment	
e	1.001 159 652 41 (20)	i m
μ	1.001 165 922 (9)	i m
p	2.792 845 6 (11)	n m
n	−1.913 042 11 (88)	n m
Λ	−0.613 8 (47)	n m
Σ^+	2.83±0.25	n m
Σ^-	$-1.48\overline{+}0.37$	n m
Ξ^-	$-1.85\overline{+}0.75$	n m
$\Sigma^0 \to \Lambda\gamma$	$1.82^{\overline{+}0.8}_{\overline{-}0.7}$	n m

1 n m $= \mu_N = \frac{e\hbar}{2m_p c} = 3.152\ 451\ 5\ (53) \times 10^{-8}$ MeV gauss

1 i m (electron) $= \frac{e\hbar}{2m_e c} = 0.578\ 837\ 85\ (95) \times 10^{-4}$ MeV gauss

1 i m (muon) $= \frac{e\hbar}{2m_\mu c}$

TABLE 2. Quantum numbers of up, down and strange quarks

Quantum Number	u	d	s
Q/e	+2/3	−1/3	−1/3
I_3	+1/2	−1/2	0
S	0	0	−1

TABLE 3. Baryon magnetic moments predicted by various simple models

Baryon	Exact SU(6) $m_u=m_d=m_s$	Broken SU(6) $m_u=m_d\neq m_s$	Broken SU(6) $m_u\neq m_d\neq m_s$
p	input 2.79	input 2.79	input 2.79
n	-1.86	-1.86	input -1.91
Λ	-0.93	-0.60	input -0.61
Σ^+	2.79	2.67	2.67
Σ^0	0.93	1.05	0.79
Σ^-	-0.93	-1.05	-1.09
Ξ^0	-1.86	-1.39	-1.44
Ξ^-	-0.93	-0.46	-0.49
$(\Sigma^0\rightarrow\Lambda\gamma)$	1.66		1.63

TABLE 4. Results of Λ polarization analysis, 7.6 mrad data

θ	Sw	events	αP_z	αP_x	αP_y
+1	+1	28584	$-0.002 \pm .013$	$0.078 \pm .010$	$0.045 \pm .015$
+1	+7/9	19333	$0.044 \pm .016$	$0.058 \pm .013$	$0.040 \pm .018$
+1	+2/3	19304	$0.022 \pm .016$	$0.065 \pm .013$	$0.049 \pm .017$
+1	-2/3	20130	$-0.097 \pm .016$	$0.045 \pm .012$	$0.031 \pm .016$
+1	-7/9	15702	$-0.081 \pm .017$	$0.065 \pm .014$	$0.035 \pm .020$
+1	-1	46240	$-0.074 \pm .010$	$0.091 \pm .008$	$0.063 \pm .011$
-1	+1	66634	$-0.040 \pm .008$	$-0.002 \pm .007$	$0.081 \pm .008$
-1	+7/9	18775	$-0.094 \pm .016$	$0.030 \pm .013$	$0.100 \pm .016$
-1	+2/3	26198	$-0.055 \pm .014$	$0.013 \pm .011$	$0.093 \pm .013$
-1	-2/3	20873	$0.082 \pm .015$	$0.030 \pm .012$	$0.072 \pm .015$
-1	-7/9	20236	$0.004 \pm .013$	$0.014 \pm .013$	$0.085 \pm .015$
-1	-1	61169	$0.002 \pm .009$	$-0.010 \pm .007$	$0.076 \pm .009$

TABLE 5. Results from master χ^2 fit, 7.6 mrad Λ polarization, with $R_\Lambda^2 \leq 40$ mm^2.

Sample	$\alpha_\Lambda P_\Lambda$	μ_Λ (μ_N)	x-bias	z-bias	χ^2 20df
All (203K)	-0.056±0.003	-0.598±0.015	0.040±0.003	-0.024±0.004	36.3
w/o Sw-$\frac{2}{3}$,θ-	-0.053±0.003	-0.603±0.016	0.040±0.003	-0.027±0.004	23.7

TABLE 6. Results of Ξ^0 polarization analysis, 4 mrad 1G, all momenta

p	Sw	θ	αP_z	αP_x	αP_y
1	-1	+1	0.034±.030	0.004±.023	0.064±.031
1	+1	+1	-0.008±.026	0.024±.021	0.124±.031
1	-1	-1	-0.044±.024	0.065±.019	0.019±.024
1	+1	-1	0.043±.025	0.071±.021	0.021±.025

TABLE 7. Results of Ξ^0 polarization analysis, 4 mrad 2G, all momenta

p	Sw	θ	αP_z	αP_x	αP_y
1	-1	+1	0.180±.035	-0.027±.026	0.010±.032
1	+1	+1	0.053±.036	-0.082±.026	-0.006±.035
1	-1	-1	0.084±.025	0.082±.020	0.020±.024
1	+1	-1	0.196±.027	0.064±.021	0.020±.025

TABLE 8. Results of Ξ^0 polarization analysis, 7.6 mrad 1G, all momenta

p	Sw	θ	αP_z	αP_x	αP_y
1	-1	-1	-0.018±0.019	0.088±0.014	0.028±0.019
1	-7/9	-1	-0.120±0.036	0.035±0.026	-0.016±0.037
1	-2/3	-1	-0.001±0.036	-0.039±0.026	0.065±0.036
1	+2/3	-1	-0.047±0.032	0.015±0.024	0.027±0.033
1	+7/9	-1	0.083±0.039	0.043±0.029	0.063±0.040
1	+1	-1	0.043±0.018	0.118±0.014	0.033±0.019
1	-1	+1	0.027±0.020	0.025±0.015	0.104±0.022
1	-7/9	+1	0.064±0.036	0.075±0.028	0.120±0.039
1	-2/3	+1	0.102±0.032	0.105±0.024	0.126±0.034
1	+2/3	+1	-0.016±0.033	0.114±0.025	0.128±0.035
1	+7/9	+1	-0.063±0.034	0.088±0.026	0.110±0.035
1	+1	+1	-0.081±0.027	0.028±0.020	0.144±0.030

TABLE 9. Results of Ξ^0 polarization analysis, 7.6 mrad 2G, all momenta

p	Sw	θ	αP_z	αP_x	αP_y
1	-1	-1	0.054±0.022	0.043±0.017	0.031±0.021
1	-7/9	-1	0.047±0.045	-0.020±0.032	0.045±0.041
1	-2/3	-1	0.116±0.042	-0.044±0.031	-0.108±0.038
1	+2/3	-1	0.141±0.036	-0.005±0.028	0.006±0.035
1	+7/9	-1	0.122±0.043	-0.004±0.032	0.090±0.042
1	+1	-1	0.196±0.022	0.091±0.017	0.024±0.020
1	-1	+1	0.205±0.027	-0.002±0.019	0.042±0.026
1	-7/9	+1	0.260±0.055	-0.008±0.037	0.072±0.052
1	-2/3	+1	0.137±0.042	0.105±0.032	0.008±0.043
1	+2/3	+1	0.133±0.044	0.089±0.032	0.015±0.041
1	+7/9	+1	0.083±0.046	0.039±0.033	0.081±0.045
1	+1	+1	0.051±0.038	-0.032±0.028	0.020±0.038

TABLE 10. Results of Ξ^0 polarization analysis, 10 mrad 1G, all momenta

p	Sw	θ	αP_z	αP_x	αP_y
1	+1	+1	-0.049±0.044	-0.002±0.032	0.084±0.047
1	+2/3	+1	0.021±0.036	0.114±0.027	0.147±0.038
1	-2/3	+1	0.019±0.029	0.068±0.022	0.087±0.032
1	-1	+1	0.077±0.037	0.031±0.027	0.119±0.040
1	+1	-1	0.068±0.026	0.087±0.020	-0.001±0.027
1	+2/3	-1	-0.028±0.051	-0.071±0.039	0.015±0.051
1	-2/3	-1	-0.010±0.045	-0.023±0.032	0.069±0.045
1	-1	-1	-0.049±0.024	0.074±0.018	0.046±0.025

TABLE 11. Results of Ξ^0 polarization analysis, 10 mrad 2G, all momenta

p	Sw	θ	αP_z	αP_x	αP_y
1	+1	+1	0.122±0.059	0.014±0.045	-0.004±0.057
1	+2/3	+1	0.119±0.049	0.132±0.037	-0.007±0.046
1	-2/3	+1	0.251±0.038	0.086±0.031	-0.038±0.040
1	-1	+1	0.187±0.049	-0.055±0.038	0.075±0.052
1	+1	-1	0.168±0.034	0.078±0.027	-0.022±0.033
1	+2/3	-1	0.179±0.071	0.093±0.053	-0.011±0.059
1	-2/3	-1	0.087±0.061	-0.101±0.044	0.083±0.053
1	-1	-1	0.127±0.031	0.037±0.023	0.035±0.029

TABLE 12. Bias-removed Ξ^0 polarization signals, 7.6 mrad, all momenta

	1G			2G	
Sw	αP_z	αP_x	Sw	αP_z	αP_x
-1	0.023±0.014	-0.032±0.010	-1	0.076±0.017	-0.023±0.013
-7/9	0.092±0.026	0.020±0.019	-7/9	0.107±0.035	0.006±0.024
-2/3	0.007±0.024	0.072±0.018	-2/3	0.011±0.030	0.075±0.022
+2/3	0.016±0.023	0.050±0.017	+2/3	-0.004±0.028	0.047±0.021
+7/9	-0.073±0.026	0.023±0.019	+7/9	-0.020±0.031	0.022±0.023
+1	-0.062±0.015	-0.045±0.012	+1	-0.073±0.019	-0.062±0.015

TABLE 13. Weighted average of 1G and 2G bias-removed Ξ^0 polarization signals, 7.6 mrad, all momenta, and corresponding precession angles.

Sw	αP_z	αP_x	$\int$Bdl T m	$\tan^{-1}(\alpha P_z/\alpha P_x)$ deg	ϕ deg
-1	0.052±0.010	-0.029±0.008	-13.64	-61± 8	-299± 8
-7/9	0.097±0.021	0.015±0.015	-10.55	81± 9	-261± 9
-2/3	0.009±0.019	0.073±0.014	-9.05	7±15	-187±15
+2/3	0.008±0.018	0.049±0.013	9.05	9±21	171±21
+7/9	-0.051±0.020	0.023±0.015	10.55	-66±16	246±16
+1	-0.066±0.012	-0.052±0.009	13.64	52± 7	308± 7

TABLE 14. Results from master χ^2 fit, 7.6 mrad Ξ^0 polarization

Sample	$\alpha_\Lambda \gamma_\Xi P_\Xi$	μ_Ξ (μ_N)	x-bias	z-bias	χ^2 20df
All 1G	-0.056±0.007	-1.278±0.036	0.061±0.007	-0.012±0.009	20.5
All 2G	-0.069±0.008	-1.215±0.029	0.026±0.007	0.126±0.010	17.8
All (130K)	-0.064±0.006	-1.234±0.023	0.045±0.005	0.048±0.007	22.5
All, R_Λ^2 cut	-0.063±0.006	-1.251±0.024	0.042±0.005	0.042±0.005	34.3

TABLE 15. Results from master χ^2 fit, 4 mrad 1G Ξ^0 polarization

p_Ξ Gev/c	#	$\alpha_\Lambda \gamma_\Xi P_\Xi$	μ_Ξ (μ_N)	x-bias	z-bias	χ^2 4df
104	7773	-0.018+0.022	-1.406+0.380	0.042±0.021	-0.006±0.030	2.87
130	6032	-0.029∓0.021	-1.412∓0.219	0.027±0.021	-0.020±0.027	4.41
149	5287	-0.101∓0.024	-1.264∓0.057	0.028±0.022	0.007±0.028	8.99
169	3867	-0.070∓0.030	-1.149∓0.088	0.004±0.026	0.032±0.031	1.85
189	2404	-0.043∓0.034	-1.391∓0.215	0.035±0.033	0.042±0.039	4.07
230	2844	-0.064∓0.036	-1.004∓0.125	0.103±0.034	-0.041±0.037	2.32

TABLE 16. Results from master χ^2 fit, 4 mrad 2G Ξ^0 polarization

p_Ξ Gev/c	#	$\alpha_\Lambda \gamma_\Xi P_\Xi$	μ_Ξ (μ_N)	x-bias	z-bias	χ^2 4df
106	3388	-0.046+0.036	-1.680+0.200	0.049±0.033	-0.047±0.047	8.27
130	3811	-0.117∓0.036	-1.132∓0.054	0.040±0.027	0.088±0.037	4.91
150	4195	-0.054∓0.026	-1.340∓0.140	-0.017±0.025	0.151±0.032	0.267
170	3903	-0.114∓0.029	-1.269∓0.061	0.027±0.027	0.123±0.032	1.58
189	2898	-0.130∓0.034	-1.357∓0.072	0.008±0.033	0.178±0.041	2.45
231	4155	-0.121∓0.030	-1.253∓0.059	-0.007±0.027	0.156±0.035	3.29

TABLE 17. Results from master χ^2 fit, 7.6 mrad 1G Ξ^0 polarization

p_Ξ GeV/c	#	$\alpha_\Lambda \gamma_\Xi P_\Xi$	μ_Ξ (μ_N)	x-bias	z-bias	χ^2 20df
102	43702	-0.037+0.011	-1.300+0.082	0.068±0.009	-0.041±0.014	18.9
130	23072	-0.061∓0.012	-1.215∓0.051	0.060±0.011	-0.008±0.014	15.9
149	14589	-0.061∓0.015	-1.268∓0.063	0.058±0.014	0.018±0.016	13.5
169	7259	-0.101∓0.021	-1.274∓0.053	0.028±0.020	0.003±0.023	28.3
189	3196	-0.102∓0.033	-1.264∓0.085	0.037±0.031	0.036±0.035	9.8
218	1072	-0.138∓0.058	-1.209∓0.094	0.012±0.053	-0.025±0.061	3.45

TABLE 18. Results from master χ^2 fit, 7.6 mrad 2G Ξ^0 polarization

p_Ξ GeV/c	#	$\alpha_\Lambda \gamma_\Xi P_\Xi$	μ_Ξ (μ_N)	x-bias	z-bias	χ^2 20df
104	18168	-0.062+0.017	-1.291+0.069	0.015±0.014	0.082±0.021	17.0
130	14407	-0.069∓0.016	-1.186∓0.051	0.033±0.014	0.090±0.019	22.8
149	11434	-0.071∓0.017	-1.225∓0.065	0.010±0.015	0.127±0.020	17.8
169	7297	-0.053∓0.023	-1.138∓0.110	0.053±0.020	0.142±0.026	22.2
189	3818	-0.076∓0.031	-1.044∓0.099	0.048±0.028	0.108±0.034	18.2
220	1582	-0.131∓0.048	-1.254∓0.085	0.124±0.046	0.019±0.050	2.3/4

TABLE 19. Results from master χ^2 fit, 10 mrad 1G Ξ^0 polarization

p_Ξ Gev/c	#	$\alpha_\Lambda \gamma_\Xi P_\Xi$	μ_Ξ (μ_N)	x-bias	z-bias	χ^2 12df
100	26659	-0.056±0.015	-1.152±0.061	0.038±0.012	-0.047±0.017	7.56
129	10222	-0.040∓0.017	-1.341∓0.121	0.056±0.016	0.054±0.021	12.0
149	5017	-0.117∓0.026	-1.157∓0.055	0.032±0.024	0.039±0.028	7.82
169	2099	-0.120∓0.039	-1.270∓0.086	-0.024±0.037	0.039±0.044	18.6
188	425	-0.120∓0.198	-1.367∓0.700	0.134±0.191	0.050±0.206	0.0/2

TABLE 20. Results from master χ^2 fit, 10 mrad 2G Ξ^0 polarization

p_Ξ Gev/c	#	$\alpha_\Lambda \gamma_\Xi P_\Xi$	μ_Ξ (μ_N)	x-bias	z-bias	χ^2 12df
103	10482	-0.030±0.026	-1.753±0.210	0.035±0.020	0.070±0.027	13.1
130	6094	-0.086∓0.022	-1.389∓0.086	0.017±0.021	0.139±0.029	14.6
149	3944	-0.100∓0.029	-1.253∓0.084	0.021±0.027	0.179±0.035	7.46
169	1958	-0.127∓0.043	-1.279∓0.094	0.027±0.040	0.179±0.043	5.30
189	471	-0.127∓0.198	-1.367∓0.600	0.009±0.184	0.011±0.215	0.0/2

TABLE 21. Weighted averages of 1G and 2G fitted 4 mrad Ξ^0 polarization

events	p_Ξ GeV/c	p_T GeV/c	x	$\alpha_\Lambda P_\Xi$	P_Ξ
11161	105	0.42	0.26	-0.028 ± 0.021	-0.044 ± 0.032
9843	130	0.52	0.33	-0.055 ∓ 0.020	-0.086 ∓ 0.031
9482	149	0.60	0.37	-0.086 ∓ 0.020	-0.134 ∓ 0.031
7770	170	0.68	0.43	-0.101 ∓ 0.023	-0.156 ∓ 0.036
5302	189	0.76	0.47	-0.095 ∓ 0.026	-0.147 ∓ 0.041
6999	231	0.92	0.58	-0.107 ∓ 0.025	-0.166 ∓ 0.039

TABLE 22. Weighted averages of 1G and 2G fitted 7.6 mrad Ξ^0 polarization

events	p_Ξ GeV/c	p_T GeV/c	x	$\alpha_\Lambda P_\Xi$	P_Ξ
61870	103	0.78	0.26	-0.048 ± 0.010	-0.075 ± 0.015
37479	130	0.99	0.33	-0.070 ∓ 0.011	-0.109 ∓ 0.017
26023	149	1.13	0.37	-0.077 ∓ 0.019	-0.120 ∓ 0.030
14556	169	1.28	0.42	-0.086 ∓ 0.017	-0.134 ∓ 0.027
7014	189	1.44	0.47	-0.096 ∓ 0.025	-0.150 ∓ 0.039
2654	219	1.66	0.55	-0.146 ∓ 0.040	-0.227 ∓ 0.063

TABLE 23. Weighted averages of 1G and 2G fitted 10 mrad Ξ^0 polarization

events	p_Ξ GeV/c	p_T GeV/c	x	$\alpha_\Lambda P_\Xi$	P_Ξ
37141	101	1.01	0.25	-0.054 ± 0.014	-0.085 ± 0.022
18316	129	1.29	0.32	-0.062 ∓ 0.015	-0.097 ∓ 0.024
8961	149	1.49	0.37	-0.119 ∓ 0.021	-0.185 ∓ 0.032
4057	169	1.69	0.42	-0.134 ∓ 0.032	-0.208 ∓ 0.049
896	189	1.89	0.47	-0.135 ∓ 0.152	-0.210 ∓ 0.237

TABLE 24. Results from master χ^2 fit, Ξ^0 polarization, all momenta.

Sample	P_Ξ	μ_Ξ (μ_N)	χ^2/df
4 mrad,1G	-0.043±0.012	-1.235±0.062	1.55/4
4 mrad,2G	-0.087∓0.013	-1.272∓0.035	3.26/4
7.6 mrad,1G	-0.059∓0.007	-1.252∓0.029	20.7/20
7.6 mrad,2G	-0.069∓0.008	-1.214∓0.029	18.0/20
10 mrad,1G	-0.064∓0.010	-1.190∓0.039	7.89/12
10 mrad,2G	-0.061∓0.013	-1.291∓0.066	17.8/12

TABLE 25. Results of α_{Ξ^0} analysis 0 mrad, 1G sample, with $R^2_\Lambda > 30$ mm^2, momentum-binned.

p_Ξ GeV/c	p_Λ GeV/c	events	$\alpha_\Lambda\alpha_{\Xi^0}$	χ^2 (19 df)
104	87	2526	-0.240 ± 0.059	21
130	110	2359	-0.290 ∓ 0.043	22
150	128	2273	-0.277 ∓ 0.043	19
170	145	1663	-0.267 ∓ 0.047	21
189	164	1158	-0.234 ∓ 0.057	27
216	187	1038	-0.221 ∓ 0.063	27
266	234	329	-0.058 ∓ 0.113	12

TABLE 26. Results of α_{Ξ^0} analysis 0 mrad, 2G sample, with $R^2_\Lambda > 30$ mm^2, momentum-binned.

p_Ξ GeV/c	p_Λ GeV/c	events	$\alpha_\Lambda\alpha_{\Xi^0}$	χ^2 (19 df)
106	84	1048	-0.270 ± 0.083	21
131	105	1355	-0.255 ∓ 0.058	11
150	122	1649	-0.329 ∓ 0.049	24
170	139	1671	-0.266 ∓ 0.049	29
190	156	1392	-0.297 ∓ 0.052	21
217	181	1586	-0.272 ∓ 0.048	18
266	224	710	-0.305 ∓ 0.079	20

TABLE 27. Results of α_{Ξ^0} analysis, all 0 mrad data

Conditions	events	$\alpha_\Lambda\alpha_{\Xi^0}$	χ^2
All 1G	14661	-0.237 ± 0.017	36
All 1G, $R^2_\Lambda > 30$ mm^2	11346	-0.261 ∓ 0.020	21
All 2G	13984	-0.253 ± 0.017	37
All 2G, $R^2_\Lambda > 30$ mm^2	9411	-0.291 ∓ 0.021	32
1G and 2G, $R^2_\Lambda > 30$ mm^2	20757	-0.275 ∓ 0.014	29

TABLE 28. Results of α_{Ξ^0} analysis, separate 4, 7.6, and 10 mrad data, 1G and 2G combined, momentum-binned, weighted average of the three angles.

p_{Ξ} GeV/c	p_{Λ} GeV/c	events	$\alpha_{\Lambda}\alpha_{\Xi^0}$	Bin GeV/c
74	60	5854	-0.084 ± 0.082	0-80
92	75	37552	-0.152 ∓ 0.019	80-100
110	91	67551	-0.227 ∓ 0.009	100-120
130	107	63788	-0.255 ∓ 0.009	120-140
149	124	44538	-0.267 ∓ 0.009	140-160
169	141	26419	-0.257 ∓ 0.012	160-180
189	158	13859	-0.279 ∓ 0.017	180-200
209	176	6609	-0.280 ∓ 0.024	200-220
245	209	5688	-0.241 ∓ 0.027	220-400

TABLE 29. Results of α_{Ξ^0} analysis, combined 4, 7.6, and 10 mrad data, 1G and 2G combined, momentum-binned, including χ^2 values from fit.

Bin GeV/c	p_{Ξ} GeV/c	events	$\alpha_{\Lambda}\alpha_{\Xi^0}$	χ^2 (19 df)
0-80	74	5854	-0.101 ± 0.081	13
80-100	92	37552	-0.152 ∓ 0.019	36
100-120	110	67551	-0.226 ∓ 0.009	22
120-140	130	63788	-0.255 ∓ 0.008	38
140-160	149	44538	-0.266 ∓ 0.009	17
160-180	169	26419	-0.256 ∓ 0.012	8
180-200	189	13859	-0.275 ∓ 0.016	17
200-220	209	6609	-0.276 ∓ 0.024	14
220-400	245	5688	-0.237 ∓ 0.026	25

TABLE 30. Results of α_{Ξ^0} analysis, 10 mrad 1G data, momentum-binned, 2nd iteration using measured P_Ξ, weighted average over each (Sw,θ) set.

P_Ξ GeV/c	P_Λ GeV/c	events	$\alpha_\Lambda\alpha_{\Xi^0}$	Bin GeV/c
100	83	26952	-0.199 ± 0.019	0-120
129	109	10243	-0.290 ∓ 0.023	120-140
149	126	5033	-0.307 ∓ 0.031	140-160
169	144	1989	-0.249 ∓ 0.049	160-180
196	170	863	-0.212 ∓ 0.080	180-400

TABLE 31. Results of α_{Ξ^0} analysis, 10 mrad 2G data, momentum-binned, 2nd iteration using measured P_Ξ, weighted average over each (Sw,θ) set.

P_Ξ GeV/c	P_Λ GeV/c	events	$\alpha_\Lambda\alpha_{\Xi^0}$	Bin GeV/c
103	82	10616	-0.206 ± 0.029	0-120
130	104	6106	-0.271 ∓ 0.030	120-140
149	120	3949	-0.310 ∓ 0.039	140-160
169	137	1872	-0.281 ∓ 0.052	160-180
198	163	979	-0.166 ∓ 0.017	180-400

TABLE 32. Results of α_{Ξ^0} analysis, 10 mrad data, momentum-binned, 2nd iteration using measured P_Ξ, weighted average over 1G and 2G bins.

P_Ξ GeV/c	P_Λ GeV/c	events	$\alpha_\Lambda\alpha_{\Xi^0}$	Bin GeV/c
101	83	37568	-0.201 ± 0.016	0-120
130	107	16349	-0.283 ∓ 0.018	120-140
149	124	8982	-0.308 ∓ 0.024	140-160
169	140	3861	-0.264 ∓ 0.036	160-180
197	167	1842	-0.186 ∓ 0.053	180-400

TABLE 33. Results of α_{-0} analysis, 10 mrad data, 1G and 2G combined, momentum binned.

p_{Ξ} GeV/c	p_{Λ} GeV/c	events	$\alpha_{\Lambda}\alpha_{\Xi^0}$	χ^2 (19 df)
74	60	2305	0.001 ± 0.144	18
92	75	13773	-0.182 ∓ 0.032	24
110	90	21490	-0.208 ∓ 0.017	16
129	107	16349	-0.269 ∓ 0.017	24
149	124	8982	-0.287 ∓ 0.021	12
169	141	4066	-0.289 ∓ 0.030	11
188	158	1526	-0.304 ∓ 0.052	42
208	175	524	-0.202 ∓ 0.082	10
234	197	223	-0.140 ∓ 0.130	20

TABLE 34. Results of α_{-0} analysis, overall value from each angle, over p_{Ξ} range 120-240 GeV/c, momentum-binned, mean momenta quoted, 1G and 2G combined.

Angle mrad	p_{Ξ} GeV/c	p_{Λ} GeV/c	events	$\alpha_{\Lambda}\alpha_{\Xi^0}$	Conditions
0	167	139	16144	-0.275 ± 0.016	Cut $R_{\Lambda}^2<30$ mm^2
2	164	137	11093	-0.277 ∓ 0.022	Cut $R_{\Lambda}^2<20$ mm^2
4	160	133	35625	-0.249 ∓ 0.011	No R_{Λ}^2 cut
7.6	149	124	88141	-0.263 ∓ 0.007	No R_{Λ}^2 cut
10	144	120	31447	-0.288 ∓ 0.013	No R_{Λ}^2 cut

TABLE 35. Results from background studies using master χ^2 allowing free P_B, 1G 7.6 mrad data

B_x	B_z	P_Ξ	μ_Ξ	P_B	χ^2 (20df)
0.060+0.006	-0.007+0.008	-0.059+0.007	-1.252+0.029	-	20.7
-0.061∓0.006	-0.007∓0.008	-0.061∓0.007	-1.259+0.028	-0.005+0.007	20.3
0.060∓0.006	-0.007∓0.008	-0.059∓0.007	-1.256+0.029	0.001+0.006	20.7

TABLE 36. Results from background studies using master χ^2 allowing free P_B, 2G 7.6 mrad data

B_x	B_z	P_Ξ	μ_Ξ	P_B	χ^2 (20df)
0.026+0.007	0.127+0.010	-0.069+0.008	-1.214+0.029	-	18.0
0.025∓0.007	0.127∓0.010	-0.067∓0.008	-1.204+0.030	0.008+0.008	17.4
0.025∓0.007	0.127∓0.010	-0.069∓0.008	-1.196+0.029	-0.011+0.007	16.3

TABLE 37. Results from background studies using master χ^2, fixed input P_B and μ_B, 7.6 mrad data.

Sample	P_B(in)	μ_B(in)	$\mu_{=0}$	χ^2 (20 df)
1G	0.005	-0.61	-1.239±0.030	21.5
1G	-0.005	-0.61	-1.264±0.028	20.2
1G	0.005	0.00	-1.271±0.029	20.7
1G	-0.005	0.00	-1.233±0.029	21.2
2G	0.005	-0.61	-1.202±0.030	17.4
2G	-0.005	-0.61	-1.225±0.028	18.7
2G	0.005	0.00	-1.229±0.029	19.5
2G	-0.005	0.00	-1.198±0.029	16.9

TABLE 38. Experimental values for octet baryon magnetic moments (April 1980)

Particle	Experimental (n m)	Theoretical (typical)
p	2.793	input
n	-1.913	-1.86
Λ	-0.614±0.005	-0.61
Σ^+	2.33 ∓0.13	2.67
Σ^0		
Σ^-	-1.48 +0.37	-1.05
Ξ^-	-1.85 ∓0.75	-0.46
Ξ^0	-1.24 ∓0.02	-1.39
$\Sigma^0 \to \Lambda\gamma$	$1.82\ ^{+0.25}_{-0.18}$	1.63

REFERENCES

REFERENCES

1. Particle Data Group, Review Of Particle Properties, Phys. Lett. 75B, 1 (1978)

2. L. Schachinger, G. Bunce, P. T. Cox, T. Devlin, J. Dworkin, B. Edelman, R. T. Edwards, R. Handler, K. Heller, R. March, P. Martin, O. E. Overseth, L. Pondrom, M. Sheaff, and P. Skubic, Phys. Rev. Lett. 41, 1348 (1978)

3. See, for example, B. T. Feld, "Models Of Elementary Particles", (Blaisdell Pub. Co. 1968)

4. M. A. B. Beg, B. W. Lee, and A. Pais, Phys. Rev. Lett. 13, 514 (1964)

5. G. Morpurgo, Physics 2, 95 (1965)

6. L. Schachinger, Ph. D. thesis, "The Magnetic Moment of the Lambda Hyperon", (Rutgers University, 1978, unpublished)

7. A. De Rujula, H. Georgi, and S. L. Glashow, Phys. Rev. D12, 147 (1975)

8. H. J. Lipkin, Phys. Rev. Lett. 41, 1629 (1978)

9. T. DeGrand, R. L. Jaffe, K. Johnson, and J. Kiskis, Phys. Rev. D12, 2060 (1975)

10. G. Bunce, O. E. Overseth, P. T. Cox, J. Dworkin, K. Heller, T. Devlin, B. Edelman, R. T. Edwards, L. Schachinger, P. Skubic, R. Handler, R. March, P. Martin, L. Pondrom, and M. Sheaff, Phys. Lett. 86B, 386 (1979)

11. V. Bargmann, L. Michel, and V. L. Telegdi, Phys. Rev. Lett. 2 , 435 (1959)

12. G. Bunce, R. Handler, R. March, P. Martin, L. Pondrom, M. Sheaff, K. Heller, O. E. Overseth, P. Skubic, T. Devlin, B. Edelman, R. Edwards, J. Norem, L. Schachinger, and P. Yamin, Phys. Rev. Lett. 36, 1113 (1976)

13. For a review, see C. Bourrely, E. Leader, and J. Soffer, "Polarization Phenomena In Hadronic Reactions", Phys. Rep. 59 , 95 (1980)

14. K. Heller, O. E. Overseth, G. Bunce, F. Dydak, and H. Taureg, Phys. Lett. 68B, 480 (1977)

15. K. Heller, P. T. Cox, J. Dworkin, O. E. Overseth, P. Skubic, L. Schachinger, T. Devlin, B. Edelman, R. T. Edwards, G. Bunce, R. Handler, R. March, P. Martin, L. Pondrom, and M. Sheaff, Phys. Rev. Lett. 41, 607 (1978)

16. S. Erhan, W. Lockman, M. Medinnis, T. Meyer, J. Rander, P. Schlein, R. Webb, A. Boehm, H. Foeth, A. Staude, R. Ellis, B. Naroska, P. Strolin, and J. Zsembery, Phys. Lett. 82B, 301 (1979)

17. F. Lomanno, D. Jensen, M. N. Kreisler, R. Poster, M. S. Z. Rabin, M. Way, J. Wise, J. Humphrey, Phys. Rev. Lett. 43, 1905 (1979)

18. K. Raychaudhuri, D. Jensen, F. Lomanno, D. McIntyre, M. Rabin, G. Bunce, S. P. Yamin, P. T. Cox, J. Dworkin, O. E. Overseth, K. Heller, and Y. Makdisi, Phys. Lett. 90B, 319 (1980)

19. R. Grobel, Ph. D. thesis, (University of Wisconsin, 1980, unpublished)

20. G. Kane and Y. P. Yao, Nucl. Phys. B137, 313 (1978)

G. L. Kane, J. Pumplin, and W. Repko, Phys. Rev. Lett. 41, 1689 (1978)

21. R. O. Polvado, S. C. Ems, S. W. Gray, R. M. Lepore, H. A. Neal, H. O. Ogren, D. R. Rust, and G. A. Walters, Phys. Rev. Lett. 42, 1325 (1979)

22. P. Skubic, Ph. D. thesis, "Neutral Strange Particle Production From Nuclear Targets", (University of Michigan, 1977, unpublished)

23. P. Martin, Ph. D. thesis, "Lambda-Proton Elastic Scattering At Fermilab", (University of Wisconsin, 1978, unpublished)

24. P. Skubic, O. E. Overseth, K. Heller, M. Sheaff, L. Pondrom, P. Martin, R. March, R. Handler, G. Bunce, P. Yamin, L. Schachinger, J. Norem, R. T. Edwards, B. Edelman, and T. Devlin, Phys. Rev. D18, 3115 (1978)

25. T. D. Lee, J. Steinberger, G. Feinberg, P. K. Kabir, and C. N. Yang, Phys. Rev. 106, 1367 (1957)

See, for example, R. P. Feynman, R. G. Leighton, and M. Sands, "The Feynman Lectures On Physics", Vol. III, (Addison-Wesley Pub. Co. 1965)

26. See, for example, J. J. Sakurai, "Advanced Quantum Mechanics" (Addison-Wesley Pub. Co. 1967)

27. T. D. Lee and C. N. Yang, Phys. Rev. 108, 1645 (1957)

See, for example, G. Kallen, "Elementary Particle Physics", (Addison-Wesley Pub. Co. 1964)

28. O. E. Overseth and R. E. Roth, Phys. Rev. Lett. 19, 391 (1967)

29. G. Bunce, "A Monte Carlo/Data Hybrid", BNL 26479-R, submitted to Nucl. Instr. Meth.

30. R. Settles, A. Manz, W. Matt, T. Hansl, I. Herynek, N. Doble, G. Wolf, S. Reucroft, J. Marraffino, J. Waters, M. Webster, and C. E. Roos, Phys. Rev. D20, 2154 (1979)

31. S. Coleman and S. L. Glashow, Phys. Rev. Lett. 6, 423 (1961)

32. R. B. Teese and R. Settles, Phys. Lett. 87B, 111 (1979)

33. J. Franklin, Phys. Rev. D20, 1742 (1979)

34. H. R. Rubinstein, F. Scheck, and R. H. Socolow, Phys. Rev. 154, 1608 (1967)

35. J. Franklin, Phys. Rev. 172, 1807 (1968)

36. J. Franklin, Phys. Rev. 182, 1607 (1969)

37. Y. Tomozawa, Phys. Rev. D19, 1626 (1979)

38. H. Lipkin, "Magnetic moments of quarks, leptons, and hadrons: a serious difficulty for composite models", Fermilab-Conf-79/60-THY (July 1979)

39. N. Isgur and G. Karl, "Ground state baryon magnetic moments", submitted to Phys. Rev. D

40. O. E. Overseth, in Particle Data Group, Review Of Particle Properties, Phys. Lett. 75B, 1 (1978)

41. For example, J. Finjord and M. K. Gaillard, preprint LAPP-TH-11 (1979), submitted to Phys. Rev. D

42. O. E. Overseth and S Pakvasa, Phys. Rev. 184, 1663 (1969)

43. G. W. Intemann, Phys. Rev. D10, 3753 (1974)

44. G. Zech, F. Dydak, F. L. Navarria, O. E. Overseth, P. Steffen, H. Wahl, E. G. H. Williams, C. Geweniger, K. Kleinknecht, and H. Taureg, Nucl. Phys. B124, 413 (1977)

45. G. Bunce, R. Handler, R. March, P. Martin, L. Pondrom, M. Sheaff, K. Heller, O. E. Overseth, P. Skubic, T. Devlin, B. Edelman, R. T. Edwards, L. Schachinger, and S. P. Yamin, Phys. Rev. D18, 633 (1978)

46. W. E. Cleland, W. E. Cooper, M. Dris, E. Engels, M. L. Herbert, D. E. Kraus, D. Lowenstein, and J. A. Thompson, Phys. Rev. D21, 12 (1980)